THERMAL EXPANSION, COMPRESSIBILITY, AND LOCAL STRUCTURE OF FLUORIDES AND OXYFLUORIDES WITH THE RHENIUM TRIOXIDE STRUCTURE

A Thesis
Presented to
The Academic Faculty

by

Cody Reeves Morelock

In Partial Fulfillment
of the Requirements for the Degree
Doctor of Philosophy in the
School of Chemistry and Biochemistry

Georgia Institute of Technology
December 2014

THERMAL EXPANSION, COMPRESSIBILITY, AND LOCAL STRUCTURE OF FLUORIDES AND OXYFLUORIDES WITH THE RHENIUM TRIOXIDE STRUCTURE

Approved by:

Professor Angus P. Wilkinson, Advisor
School of Chemistry and Biochemistry
Georgia Institute of Technology

Professor Christopher W. Jones
School of Chemical and Biomolecular Engineering
Georgia Institute of Technology

Professor Joseph W. Perry
School of Chemistry and Biochemistry
Georgia Institute of Technology

Professor Mary Anne White
Department of Chemistry
Dalhousie University

Professor Z. John Zhang
School of Chemistry and Biochemistry
Georgia Institute of Technology

Date Approved: 05 August 2014

Dedicated to the glory of God,

to my parents and grandparents,

to Julianna,

and to all others who had some part in making this thesis possible.

ACKNOWLEDGEMENTS

Despite appearing first in this document, these acknowledgements were written last chronologically because I wanted to have time to reflect on my graduate school experiences and the many people that made this thesis possible. Graduate school has been an especially challenging time for me, both academically and personally, but I am glad that I have persevered to see the completion of this thesis. Scientific research is indeed a collaborative endeavor, and this work is no exception. I have sought to be as inclusive as possible in the acknowledgements listed here, and I apologize for any omissions.

I am first and foremost thankful to God for His guidance and for enabling me to complete this achievement. During my time in graduate school, my faith has definitely been tested more than ever, but I am pleased to say that I emerge with a stronger faith than when I entered. I also appreciate the prayers of my family, church family, and friends during these challenging years.

My family is one of my greatest blessings, and I certainly could not have completed my Ph.D. without them. My education began at home with my parents, Jeff and Lisa Morelock, and I am indebted to them for their love and support. My beloved sisters, Caitlyn and Cassidy Morelock, have always been there for me, and it means so much to have them as my cheerleaders. My grandparents have also been a source of much strength and inspiration. I have been blessed to know both grandmothers, Joan Morelock and Marie Sparks, as an adult, and I know that they are so proud of me for this accomplishment. My grandfathers, George Morelock and Gene Sparks, are no longer here on Earth, but I feel their presence in everything that I do. My extended family is one of my greatest blessings, and I am grateful for the support of my aunts and uncles, my cousins, and other relatives, both living and deceased. I hope that I have made you all proud!

I am thankful to my girlfriend of three years, Julianna Hendley, for her constant love and support. I met Julianna at a time in graduate school when I was a bit lost and unsure

of my future. She has given me something to work for and has made me happier than I have ever been. I am certain that this thesis could not have been completed without her support and patience...sorry for all of the trips to Argonne and conferences!

Outside of work, my friends have been a source of happiness and relief. During my time at Georgia Tech, I played a great deal of pub trivia at Rocky Mountain Pizza, and I want to acknowledge my team mates. The core of my first team (Sexual Tyrannosauruses) were fellow chemistry graduate students Matt Kennedy, Rob Brown, and Brian Snyder. On my current team (Gym, Trivia, Laundry), I want to thank Kristen Welch, Kristin Agostini, Christina and Ben Pack, Jay Forsythe, and my cousin Andy Large and his wife Rachel. I am also grateful for the people I got to know at Smyrna First United Methodist Church, especially Pastor Steve Lyle, Kim Duggins, and the other members of the orchestra in which I played viola. There are many other people, too many to list, who have touched my life and made my graduate school years more pleasant, and I thank you all.

This thesis marks the completion of not only five years of graduate school but a total of twenty-two years of formal education. I was very fortunate to have a strong educational background before coming to Georgia Tech. I wish to acknowledge some of my greatest teachers from Kingsport City Schools who gave me such a solid academic basis and encouraged my development: Mrs. Jonelle Stephens, Mrs. Sylvia Wright, Ms. Betty Deakins, Mrs. Phyllis Bloomer, Mr. Dwight Monday, Mr. Kenn Naegele, Mrs. Jennifer Jensen, Mrs. Libby Harbin, and especially Mrs. Nancy Bovender, my AP Chemistry teacher who first taught me to love chemistry (I still think of her every Mole Day). My undergraduate training at Furman University was also phenomenal; I want to thank the whole chemistry department at Furman, but especially my undergraduate advisor Prof. Laura Wright, who taught me how to keep a good lab notebook, approach scientific problems, and think critically. I also wish to acknowledge Profs. Jeff Petty, Lon Knight, Noel Kane-Maguire, and Tim Hanks, and thanks to Prof. Karen Buchmueller for making me struggle through Biochemistry I and preparing me for graduate school classes!

In graduate school, I have been lucky to have a Ph.D. advisor, Prof. Angus Wilkinson, who has not only supported my research in every way possible but has also been a friendly

presence. I came to Georgia Tech with little knowledge of solid-state chemistry or crystallography, and Angus has helped me every step of the way. I am so appreciative of the many skills I have learned from him, ranging from theoretical solid-state physics to general skills like plumbing and working with tools, as well as his great patience, especially when I had to call him at 3 AM to tell him a rupture disk had blown in our high-pressure setup! Angus always amazes me with his knowledge and experience, and I have appreciated learning from him.

I acknowledge the members of my thesis committee, Profs. Joe Perry, John Zhang, Chris Jones, and Mary Anne White, whose signatures were required to complete this thesis. I greatly appreciate their time and patience during all of the major requirements for the Ph.D., including my candidacy exam, data review, and thesis defense, as well as their helpful suggestions for the improvement of this document. I should also acknowledge the late Prof. Bob Snyder, who was an original member of my committee but passed away in the time between my candidacy exam and data review.

The other members of the Wilkinson group have been a source of friendship and mutual assistance. I am grateful to Dr. Benjamin Greve for his help and friendship when I first arrived; I learned a great deal about synthesis and synchrotron experiments from Ben, and I will not forget many of our times together, from our long nights at Argonne to our three trips to New Orleans. Ben initiated the ScF_3 solid solution project and performed some analysis of the TaO_2F local structure data. Although I never met him, I should acknowledge Dr. Mehmet Cetinkol for beginning the TaO_2F project several years ago. I also want to thank Leighanne Gallington for her assistance on our many trips to Argonne as well as at Georgia Tech, where she was my go-to person for computer problems, probably more often than she liked. Dr. Andrew Jupe provided me with so much help when I first arrived; I still miss Andrew's humor and wit and his vast knowledge of all things Linux. In addition, two Masters students, Chad Ruschman and Ryan Josefsberg, and two phenomenal undergraduates, Justin Hancock and Chris Monaco, were great to work with and assisted me in various ways. Finally, I thank our newest students, Brett Hester and Ben Kaplan, and our visiting student, Daniel Stewart, for their encouragement as I completed and defended

this thesis and wish them all the best in their future careers.

Nearly all of the data presented in this thesis were collected somewhere besides Georgia Tech. During my time as a graduate student, I traveled to Argonne National Laboratory some sixteen times (I think); I am grateful for the assistance of Dr. Greg Halder at 1-BM/17-BM for his awesome help with variable-temperature measurements, Drs. Karena Chapman and Peter Chupas at 11-ID-B for their support and assistance with most of my projects, especially the BRIM-related work and TaO_2F supercell design, Dr. Matthew Suchomel at 11-BM for guidance with the ScF_3/varnish work (Chapter 5), and the great support staff at all of these beamlines, especially Kevin Beyer and Charles Kurtz at Sector 11. Thanks also to the people who made my visits to Argonne more pleasant, especially Larry, the friendly waiter in the Argonne Guest House restaurant. I also wish to thank our collaborators at Dalhousie University, Prof. Mary Anne White and her associates Carl Romao and Mike Johnson, for the heat capacity work in Chapter 7. I traveled to Dalhousie in June 2013, and they were gracious hosts and wonderful people. Finally, although I do not present any neutron data here, I did spend some time at Oak Ridge National Laboratory and am grateful for the advice and assistance of several scientists there, including Drs. Ashfia Huq (POWGEN at the Spallation Neutron Source) and Clarina de la Cruz (HP-2A at the High Flux Isotope Reactor).

Funding for this work was provided by National Science Foundation grants DMR-0605671 and DMR-0905842. Use of the Advanced Photon Source at Argonne National Laboratory was supported by the United States Department of Energy, Office of Science, Office of Basic Energy Sciences, under Contract no. DE-AC02-06CH11357.

TABLE OF CONTENTS

LIST OF TABLES

LIST OF FIGURES

SUMMARY

The cubic ReO_3 framework is the simplest structure with all of the key features required for negative thermal expansion (NTE) arising from the transverse thermal motion of bridging atoms and rotation of rigid polyhedra. Rhenium trioxide itself displays low NTE below ambient temperature, but there is a potentially large family of isostructural fluorides and oxyfluorides that could display NTE. However, the coefficients of thermal expansion (CTEs) of ReO_3-type materials range from strongly positive to strongly negative. This thesis examines the thermal expansion of several ReO_3-type fluorides and oxyfluorides, demonstrating the effects on CTE and related properties of both cation and anion substitution and the disorder produced by these structural changes, as well as the effects of stress on these properties. Variable-temperature/pressure X-ray diffraction is used extensively for characterization of the materials.

Before examining disordered materials, two simple, non-disordered ReO_3-type metal trifluorides are discussed in Chapter 4: α-AlF_3 and InF_3. At ambient temperature, both materials have a rhombohedrally distorted form of the ReO_3 structure that becomes cubic on heating. This phase transition occurs at ~713 K in α-AlF_3, while in InF_3, there is a rather large temperature range (approximately 680 to 795 K) with rhombohedral and cubic phase co-existence. In both fluorides, the rhombohedral phase displays strongly positive volume thermal expansion. Cubic α-AlF_3 continues to display strong positive thermal expansion (volume CTE, α_V, at 900 K $\approx$ 25 ppm$\cdot$K^{-1}), while the thermal expansion of cubic InF_3 changes from positive to zero (~850 to 950 K) to negative (above ~950 K).

The work in Chapter 5 presents a cautionary message concerning thermal expansion mismatch and suggests limitations of ScF_3 during use in composites, a potential application of materials displaying NTE. Cubic ReO_3-type ScF_3 is known to display strong isotropic NTE over a wide temperature range; the NTE is most pronounced at low temperatures. When ScF_3 powder is mixed with a polyvinyl phenolic varnish, an unexpected

cubic-to-rhombohedral phase transition in ScF_3 is observed at ∼50 K, exhibiting smaller low-temperature unit cell volumes than samples without the varnish matrix. Experimental observations and quantitative estimates suggest that these anomalies are the result of stress induced by a thermal expansion mismatch between the varnish matrix (large positive CTE) and ScF_3 (quite large negative CTE).

Solid solution formation is investigated in an effort to control the strongly negative thermal expansion of ScF_3 without forming a composite; thermal expansion studies of $Sc_{1-x}M_xF_3$ (M = Ti, Y, and Al) solid solutions are the focus of three chapters (6, 7, and 8, respectively). The effects on both thermal expansion and compressibility of substituting differently sized cations into the ScF_3 framework are explored. In the case of $Sc_{1-x}Ti_xF_3$, Sc^{3+} and Ti^{3+} are closely size-matched, allowing full solubility of TiF_3 in ScF_3 at the synthesis temperature of 1338 K. The temperature for the cubic-to-rhombohedral phase transition in $Sc_{1-x}Ti_xF_3$ varies linearly with composition (above 100 K), and, at high Ti content, the transition is clearly first-order. The rhombohedral phase for each composition examined exhibits strongly positive thermal expansion, while the expansion of the cubic phase (between 420 and 500 K) is negative or low positive for all compositions, with a small degree of CTE tunability (average α_V between 350 and 470 K varies from ∼-16 to ∼+4 ppm·K^{-1} with increased Ti content).

The solubility limit of YF_3 in ScF_3 is restricted by the significant difference in ionic radius between Sc^{3+} and Y^{3+}. Insertion of the relatively large Y^{3+} ion into ScF_3 results in a subtle cubic-to-rhombohedral phase transition upon cooling from ambient temperature to 100 K, even at low substitution levels (5%). The CTE of the rhombohedral phase is strongly dependent on both composition and temperature; however, above 400 K, where all samples are cubic, the CTE appears to be largely independent of composition. The isothermal bulk modulus and CTE of ScF_3, but not those of the solid solutions, are independent of temperature and pressure, respectively. Yttrium substitution lowers the bulk modulus, even at temperatures where the samples are cubic; the solid solutions also stiffen upon heating. From heat capacity measurements, no evidence is given for a phase transition in ScF_3 between 0.35 and 390 K at ambient pressure, while the subtle nature of the phase

transition in the solid solutions is visible. In addition, the low-temperature heat capacities of $Sc_{1-x}Y_xF_3$ are much different than those of ScF_3.

The ionic radius of Al^{3+} is significantly smaller than that of Sc^{3+}; thus, the solubility limit of α-AlF_3 in ScF_3 is limited to ~50% at 1338 K. A second-order cubic-to-rhombohedral phase transition is again observed, the temperature of which increases smoothly with Al substitution, approaching 500 K at the solid solubility limit, and also upon compression for a given composition. The slope of the pressure-temperature phase boundary (~0.5 $K \cdot GPa^{-1}$) is steeper than that of most symmetry-lowering phase transitions in perovskites. The volume CTE of rhombohedral $Sc_{1-x}Al_xF_3$ is strongly positive, while the cubic-phase CTE (>600 K) varies from negative ($x < 0.15$) to near zero ($x = 0.15$) to positive ($x > 0.20$). The cubic solid solutions elastically stiffen on heating, while Al^{3+} substitution causes softening at a given temperature.

Finally, a local structural study of anion-disordered cubic ReO_3-type TaO_2F is presented in Chapter 9. Local distortions away from the ideal cubic structure, associated with the need to accommodate the different bonding requirements of the disordered O and F, contribute to the occurrence of near-zero thermal expansion in TaO_2F rather than NTE. The local structure of TaO_2F is poorly described by an ideal cubic ReO_3-type model with O and F randomly distributed over the available anion sites, but a supercell model featuring –Ta–O–Ta–O–Ta–F– chains along <1 0 0>, with different Ta–O and Ta–F distances and O/F off-axis displacements, gives much better agreement with pair distribution functions (PDFs) derived from X-ray total scattering data for small separations (<8 Å). Analyses of PDFs derived from variable-temperature measurements (80 to 487 K), over different length scales, indicate an average linear expansion coefficient of close to zero, with similar contributions from the geometrically distinct Ta–O–Ta and Ta–F–Ta links in TaO_2F.

CHAPTER 1

INTRODUCTION

Most materials, including solids, expand when heated; this positive thermal expansion (PTE) is a ubiquitous phenomenon. However, some materials exhibit negative thermal expansion (NTE), or contraction on heating, in one or sometimes multiple directions over some temperature range. These thermomiotic (from the Greek, "thermo" for "heat" and "mio" for "contract") materials are not only interesting as scientific curiosities due to their anomalous nature but also potentially useful in certain applications [1]. This thesis primarily focuses on the thermal expansion of materials with ReO_3-type connectivity. The role and effects of structural disorder on the thermal expansion and related properties of these materials are also explored.

In this introductory chapter, the origins and measurement of thermal expansion, proposed mechanisms for NTE, the effects of pressure on NTE, and known families of thermomiotic materials are discussed. Thermomiotic behavior arising from lattice vibrations is of particular note. Previous work on the thermal expansion of ReO_3-type materials is introduced, followed by a brief overview of the work presented in subsequent chapters.

1.1 Thermal expansion

The thermal expansion behavior of solids is critical to many industrial processes and other applications. Good control of thermal expansion is necessary for the thermal matching of materials in close contact with one another and the precision positioning of objects such as optical instruments. Although differences in thermal expansion behavior between materials can be useful, as in thermostatic bimetals, they are generally problematic and may cause interfacial cracking. Also, materials with large coefficients of thermal expansion show poor thermal shock resistance; rapid heating or cooling of such materials creates temperature gradients that can result in cracking and eventually material failure. Thus, low thermal expansion is generally desirable because it imparts both dimensional stability and good

thermal shock resistance; the most preferred case is zero thermal expansion, a lack of dimensional change with temperature. Furthermore, materials displaying isotropic thermal expansion (equal expansion/contraction in all directions) are also preferred, as anisotropic thermal expansion can cause internal microcracking and mechanical failure in polycrystalline bodies even when monophasic [1, 2, 3, 4, 5, 6, 7, 8]; in a material with isotropic thermal expansion, orientation does not affect properties.

In this section, the general origins, measurement, and classification of thermal expansion (both positive and negative) are discussed.

1.1.1 Bond anharmonicity

The principle of thermal expansion is well understood [1, 6, 7, 9, 10, 11] and can be illustrated by the interatomic potential curves in Figure 1.1. The potential energy of a simple harmonic oscillator (Figure 1.1a) decreases as the two atoms are brought closer together, and a bond is formed. However, as the atoms move closer together, the repulsion of the electrons in each atom causes a sharp increase in potential at low interatomic distances. The interatomic distance resulting in the minimum potential energy is the average bond distance; however, due to the parabolic shape of the harmonic potential curve, an increase in temperature from T_1 to T_2, with which higher-energy vibrational levels (modes) may be accessed, does not affect the average distance $\langle r \rangle$. At higher temperatures, the parabola becomes wider, so the harmonic oscillator is able to explore a broader range of interatomic distances. Nevertheless, the average distance remains the same at all temperatures, and the harmonic oscillator does not experience thermal expansion.

In most solids, however, the potential energy of a single bond is only harmonic at very low temperatures. The potential energy curve of such bonds is asymmetric, resulting in anharmonic behavior (Figure 1.1b). Atoms may not move very close to one another; hence, the potential energy of these bonds approaches infinity as interatomic distance approaches zero. In this case, the oscillator is still able to explore a wider range of interatomic distances r with an increase in temperature from T_1 to T_2; however, due to the asymmetry of the potential energy curve, longer interatomic distances are more easily explored than

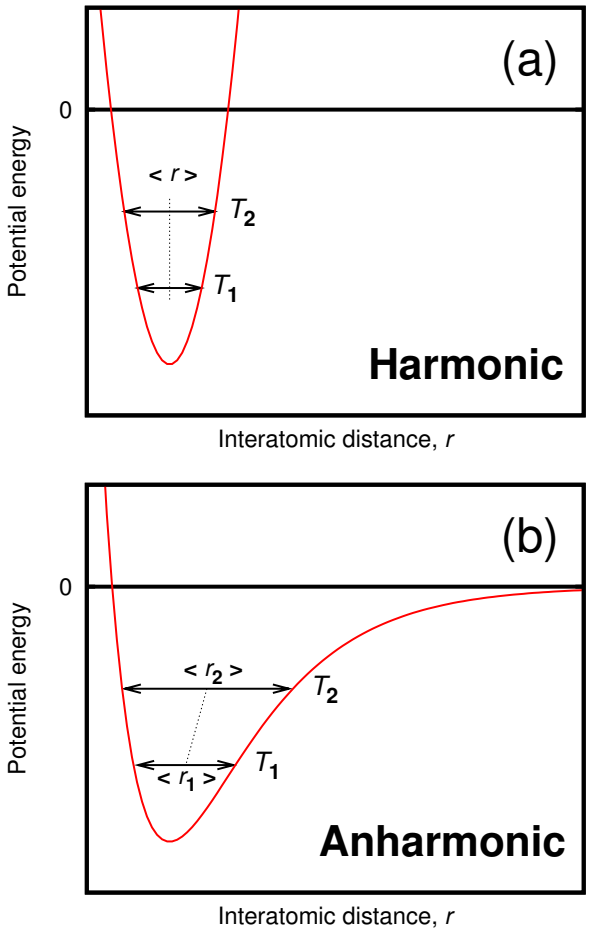

Figure 1.1: Potential energy of (a) harmonic and (b) anharmonic oscillators as a function of interatomic distance. A harmonic oscillator has the same average distance $\langle r \rangle$ for all temperatures T, whereas the average distance for an anharmonic oscillator increases from $\langle r_1 \rangle$ at T_1 to $\langle r_2 \rangle$ at T_2.

shorter distances. Therefore, the average distance increases at higher temperatures, and the bond experiences positive thermal expansion. Strong bonds typically have potential curves that are harmonic in nature, deepening the potential well and accessing more symmetric vibrational modes; at low temperatures, the thermal expansion of very strong bonds may approach zero [4].

In complex systems such as crystalline solids, the interdependent thermal expansion of all interatomic bonds, changes in bond angles, and population of the entire phonon density of states as a function of temperature must be considered. Although crystalline solids are more complex than diatomic molecules, thermal expansion still arises from the population of higher-energy vibrational modes. In a few categories of materials, however, the positive thermal expansion of individual bonds may be dominated by other factors, leading to thermal contraction over some temperature range; some of these factors are discussed in Section 1.2.2 [5].

1.1.2 Coefficient of thermal expansion (CTE), bulk modulus, and heat capacity

Thermal expansion is typically expressed in terms of the coefficient of thermal expansion (CTE), which indicates the relative amount by which a material expands (or contracts) with a given change in temperature at constant pressure; as the CTE of most solids is on the order of 10^{-6}, the most common unit for CTE is ppm·K^{-1}. The linear coefficient of thermal expansion (α_L) at constant pressure (P) is defined as

$$\alpha_L = \left(\frac{\partial \ln L}{\partial T}\right)_P = \frac{1}{L}\left(\frac{\partial L}{\partial T}\right)_P \approx \frac{L - L_0}{L_0(T - T_0)}, \tag{1.1}$$

where L and L_0 are unit cell edge lengths at temperatures T and T_0, respectively. The thermal expansion of anisotropic (non-cubic) materials is completely described by a second-rank CTE tensor [1]:

$$\boldsymbol{\alpha} = \begin{pmatrix} \alpha_{11} & \alpha_{12} & \alpha_{13} \\ \alpha_{21} & \alpha_{22} & \alpha_{23} \\ \alpha_{31} & \alpha_{32} & \alpha_{33} \end{pmatrix}. \tag{1.2}$$

If the three principal axes of $\boldsymbol{\alpha}$ coincide with the crystallographic axes, then $\alpha_{11} = \alpha_a$, $\alpha_{22} = \alpha_b$, and $\alpha_{33} = \alpha_c$, and the off-diagonal elements α_{ij} vanish. However, the off-diagonal elements in orthogonal coordinates are non-zero in systems with non-orthogonal axes, leading to shear strain during thermal expansion.

The volume coefficient of thermal expansion (α_V) at constant P is defined as

$$\alpha_V = \left(\frac{\partial \ln V}{\partial T}\right)_P = \frac{1}{V}\left(\frac{\partial V}{\partial T}\right)_P \approx \frac{V - V_0}{V_0(T - T_0)}, \tag{1.3}$$

where V and V_0 are unit cell volumes at temperatures T and T_0, respectively. In systems with orthogonal axes, α_V is merely the sum of the individual α_L (or α_{ii}):

$$\alpha_V = \alpha_a + \alpha_b + \alpha_c = \alpha_{11} + \alpha_{12} + \alpha_{13}. \tag{1.4}$$

Equation 1.4 implies that, for a cubic material in which $a = b = c$,

$$\alpha_V = 3\alpha_a. \tag{1.5}$$

As the CTE is a function of temperature, the temperature range over which it is calculated should be specified. Also, as defined here, the CTE at a given temperature is an intrinsic property that is not dependent on the bulk form of the material; experimental methods for CTE measurement are discussed in Section 1.1.4.

Positive thermal expansion implies an increase in entropy S on volume increase by the following Maxwell relations of Equation 1.3:

$$\alpha_V = \frac{1}{V}\left(\frac{\partial V}{\partial T}\right)_P = -\frac{1}{V}\left(\frac{\partial S}{\partial P}\right)_T = \frac{1}{K_T}\left(\frac{\partial S}{\partial V}\right)_T, \tag{1.6}$$

where K_T is the isothermal bulk modulus, or the inverse of compressibility, defined as:

$$K_T = -V\left(\frac{\partial P}{\partial V}\right)_T, \tag{1.7}$$

and always positive; therefore, the signs of α_V and $\left(\frac{\partial S}{\partial V}\right)_T$ are always the same. Thus, for positive α_V (PTE), entropy increases with volume at constant temperature, while negative α_V (NTE) involves increased entropy with contraction, or alternatively, decreased entropy on expansion [10]. Also, to connect CTE to the interatomic potential curve (Figure 1.1), as $T \to 0$ K, the potential becomes increasingly harmonic in nature and $\alpha \to 0$ K^{-1}. This

requirement is true for all materials as a result of the third law of thermodynamics, which states that the entropy of a system is zero at 0 K [12].

Thermal expansion may also be expressed as the elastic response to thermally induced stress by further transforming Equation 1.6:

$$\alpha_V = \frac{1}{K_T}\left(\frac{\partial S}{\partial V}\right)_T = \frac{1}{K_T}\left(\frac{\partial P}{\partial T}\right)_V = \left(\frac{\partial P}{\partial T}\right)_V \left(\frac{-\partial \ln V}{\partial P}\right)_T . \tag{1.8}$$

Thus, the process of thermal expansion can be envisioned as occurring in two stages: an initial change in pressure as the material is heated at constant volume, followed by a change in volume as the material relaxes to the original pressure at the new higher temperature [10].

The thermal expansion of a material is related to its heat capacity, the amount of energy required to change temperature by a certain amount. The $\left(\frac{\partial P}{\partial T}\right)_V$ term in Equation 1.8 may be expressed as the product of the heat capacity at constant volume per unit volume (C_V/V), which is the amount of energy gained during a given temperature increase, and the thermodynamic (bulk) Grüneisen parameter (γ_{th}), the effectiveness of that energy in changing pressure, originally proposed by Grüneisen in the 1920s [13]:

$$\left(\frac{\partial P}{\partial T}\right)_V = \left(\frac{C_V}{V}\right)\gamma_{th}, \tag{1.9}$$

where

$$\gamma_{th} = \left(\frac{\partial P}{\partial (U/V)}\right)_V = -\left(\frac{\partial \ln T}{\partial \ln V}\right)_S \tag{1.10}$$

and U is internal energy. A combination of Equations 1.8 and 1.9 yields the following expression:

$$\gamma_{th} = \frac{\alpha_V K_T V}{C_V}. \tag{1.11}$$

As K_T, V, and C_V are always positive, the signs of α_V and the dimensionless thermodynamic Grüneisen parameter are the same [10].

1.1.3 Lattice vibrations

As suggested above, lattice vibrations (phonons) are critical to thermal expansion. The quasi-harmonic approximation is often used to explain how lattice vibrations cause thermal expansion. By this approximation, the frequencies of phonons are considered volume-dependent but otherwise treated as harmonic [10]. Each vibrational mode contributes to

thermal expansion; the volume derivative of each phonon mode frequency ω_i is known as the mode Grüneisen parameter [14]:

$$\gamma_i = -\frac{d \ln \omega_i}{d \ln V}. \tag{1.12}$$

In a harmonic solid, each ω_i is volume-independent; thus, γ_i for all modes is zero. The magnitude of the mode Grüneisen parameter is therefore an indicator of the anharmonicity of the interactions within the solid. For negative γ_i, the frequency of a mode must decrease with decreasing volume (*i.e.*, the mode must soften).

The thermodynamic Grüneisen parameter γ_{th} is merely an average of the individual γ_i, weighted by the heat capacity contributions c_i of the individual modes:

$$\gamma_{th} = \frac{\sum c_i \gamma_i}{\sum c_i}. \tag{1.13}$$

For overall negative thermal expansion at a given temperature, there must be a sufficient number of excited modes with negative γ_i to outweigh those with positive γ_i [10]. Transverse modes generally have lower energies than longitudinal modes and become excited at lower temperatures; therefore, transverse modes typically dominate γ_{th} at low temperatures in thermomiotic materials (Section 1.2.2.1).

Finally, a distinction must be made between apparent and true bond lengths. The apparent bond length, determined from X-ray or neutron diffraction, is the distance between the mean positions of two atoms, while the true bond length is the mean distance between the atoms. The true bond length is always longer than the apparent bond length as a result of libration, a particular vibrational motion in a specific direction relative to the bond axis [1, 6, 10].

1.1.4 Experimental measurement

Two primary methods for experimental measurement of thermal expansion are diffraction (microscopic or intrinsic CTE) and dilatometry (macroscopic or extrinsic CTE). Diffraction is used exclusively in this thesis, so this method is discussed in greater detail.

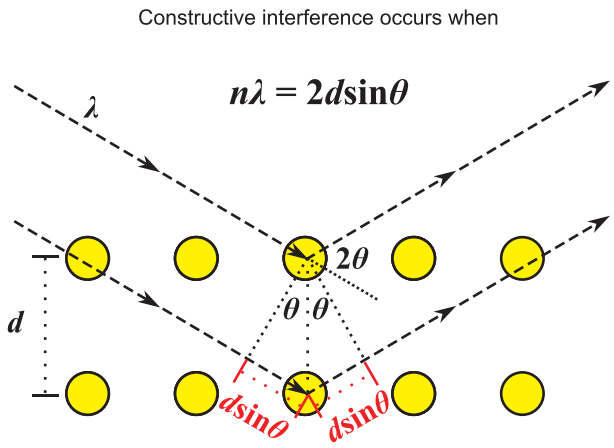

Figure 1.2: Illustration of Bragg's Law. Radiation of wavelength λ scatters from atomic planes with lattice spacing d. The angle between the incident and scattered beams is 2θ. By geometry, the path length difference between two adjacent atoms in adjacent planes is $2d\sin\theta$; for constructive interference of the two diffracted beams, this path length difference must equal an integral multiple of λ.

1.1.4.1 Diffraction

Diffraction with X-rays and/or neutrons is used to examine average or local structures and measure the thermal evolution of lattice constants and hence the intrinsic CTE. With current synchrotron and neutron sources, lattice parameters can be determined with high accuracy and precision; thus, with accurate temperature measurement, diffraction can yield reliable CTE values.

The fundamental law describing diffraction is Bragg's Law, derived by Sir William L. Bragg a century ago:

$$n\lambda = 2d\sin\theta, \tag{1.14}$$

where n is an integer, λ is the wavelength of the incident beam, d is the spacing between atomic lattice planes, and θ is the angle between the incident beam and scattering planes (Figure 1.2). The angle between the incident and scattered beams is 2θ. The d-spacing of a material is intrinsic, but 2θ is wavelength-dependent. Constructive interference of two diffracted beams occurs when their path length difference ($2d\sin\theta$) is an integral multiple of their wavelength λ.

Diffraction measurements typically use either X-rays or neutrons to probe materials. The

wavelengths of X-rays, discovered by W. C. Röentgen in 1895 (for which he was awarded the first Nobel Prize for Physics in 1901), are on the order of 0.1-1.0 Å, the same length scale as interatomic distances and chemical bonds. X-rays for modern diffraction experiments are produced either in the laboratory by an X-ray tube or at a synchrotron facility. In an X-ray tube, a metal target (such as Cu, Mo, or Ag) is bombarded with high-energy electrons that excite the electrons in the metal atoms to higher energy levels; upon transitioning to lower energy levels, photons are emitted. With the proper collimation and monochromator, X-rays with a specified wavelength reach the sample for diffraction. At a synchrotron facility, however, high-intensity and high-energy X-rays are produced by rapidly accelerating electrons. X-rays interact with the electrons in an atom, so the atomic X-ray scattering factor varies smoothly with atomic number Z. Therefore, X-ray diffraction is best applied to the study of materials containing high-Z elements, although low-Z elements may be observed in the absence of high-Z ones. Diffracted X-rays were historically detected by photographic film, but such detection is now uncommon. Modern X-ray detectors include scintillation, solid-state semiconductor, and image plate varieties.

Neutrons were discovered by Chadwick in 1932 [15], for which he was awarded the Nobel Prize for Physics three years later. Unlike X-rays, neutrons have a magnetic moment and are thus useful for diffraction studies of magnetic structure. Neutrons interact with the nuclei of atoms, and their scattering power is dependent on nuclear structure. However, there is no smooth variation of neutron scattering factor with Z; hence, neutron diffraction can be used to probe low-Z elements (like C, N, or O) even in the presence of high-Z elements. In many cases, the highest accuracy is obtained by combining neutron and X-ray data. Neutron diffraction cannot be performed in a typical home laboratory; neutrons are currently only produced at nuclear fission-based reactors or at spallation sources, primarily at national laboratory facilities. The fluxes available at these sources, however, are quite low, even when compared to those from X-ray tube sources. Thus, much larger samples are required for neutron diffraction than for X-ray diffraction.

Diffraction measurements (both X-ray and neutron) may use either a single crystal at a particular orientation or a powder, consisting of many individual crystallites in different

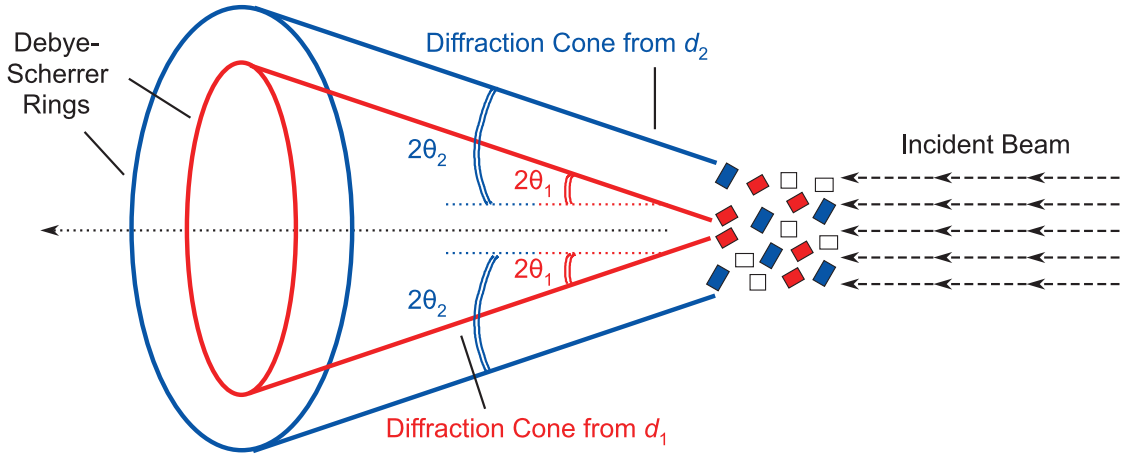

Figure 1.3: Schematic illustration of powder diffraction, showing two Debye-Scherrer cones from crystallites with d-spacings d_1 and d_2 and the Debye-Scherrer rings formed by their intersection with a plane perpendicular to the incident beam.

random orientations. Single-crystal diffraction is preferred for structure solution; however, in some cases, growth of single crystals can be difficult, especially if large crystals are required, as in neutron diffraction. Powder diffraction may be used for structure solution but is better applied to structure refinement. In addition, crystalline materials can be identified based on their powder patterns. For single-crystal diffraction, the crystal must be arranged at a particular orientation for Bragg's Law to be satisfied; if this condition is not met, the crystal must be rotated to a proper angle for diffraction. However, such rotation is unnecessary in a powder sample, in which all crystallite orientations are (ideally) equally likely. In a powder, for any given d-spacing, there are many crystallites with the correct angular orientation for satisfaction of Bragg's Law. These correctly aligned crystals all have orientations about the incident beam, so the diffracted beams form a cone with half-apex angle of 2θ. For every d-spacing, there is a so-called Debye-Scherrer cone, and the rings formed by the intersection of the cone with a plane perpendicular to the incident beam are called Debye-Scherrer rings [16]; these rings are relevant to powder diffraction with an area detector (Section 2.4.2.1). Some of the basic principles of powder diffraction are illustrated in Figure 1.3. X-ray powder diffraction techniques (discussed in more detail in Chapter 2) were used to collect most of the data presented in this thesis.

1.1.4.2 Dilatometry

Mechanical dilatometric techniques can be used to measure the extrinsic CTE in bulk specimens and observe change in microstructure. During a dilatometric measurement, the linear change in sample length is measured as a function of temperature. In general, this measurement is accomplished by mechanically transmitting the displacement of a sample at increased temperature to a sensor located away from the heat [17]. Dilatometric data are typically reported as $\Delta L/L_0$ *versus* temperature, where ΔL and L_0 are the change and original sample length, respectively. Dilatometric measurements may be done in the laboratory with either commercial or custom-built instruments [1, 17].

Push rod dilatometers are the most common method of dilatometry. In this setup, the sample is housed in a furnace, and two rods are in contact with opposite faces of the sample, parallel to the direction of expansion. The rods are attached (outside the furnace) to the ferromagnetic core of a linear variable differential transformer, which measures displacement of the rods as a function of temperature based on the voltage change of the ferromagnetic core [17]. In this instrument, the rods and other parts in contact with the sample must be made from a material with both low CTE and high melting temperature, such as fused silica [1]. Another variety is the capacitance dilatometer, in which the sample dictates the distance between the plates of a capacitor and capacitance is measured as a function of temperature. Capacitance has an inverse dependence on the separation of the plates, so the dimensions of the sample can be determined accurately as a function of temperature [18]. A more thorough review of dilatometric methods can be found in ref. [17].

1.1.4.3 Diffraction vs. dilatometry

The thermal expansion coefficients determined from diffraction (intrinsic) and dilatometry (extrinsic) can sometimes differ greatly. This problem is especially notable for thermomiotic ceramics with anisotropic thermal expansion. For example, the intrinsic volume CTE of $Al_2W_3O_{12}$ was reported to be low positive, while dilatometry suggested NTE [19]. In the related material $Sc_2W_3O_{12}$, both measurements yielded negative CTEs with significantly different magnitudes; this difference was attributed to microcracks in the ceramic bar [20].

However, the CTEs of cubic (and hence isotropic) thermomiotic materials, such as members of the ZrW_2O_8 family [21], are independent of the measurement technique employed.

Unless otherwise stated, all coefficients of thermal expansion reported in this thesis are estimated using diffraction.

1.1.5 Classification

Materials have been arbitrarily classified in the following groups based on their linear coefficient of thermal expansion [2]:

High Thermal Expansion:	$\alpha_L > 8$ ppm·K^{-1}
Intermediate Thermal Expansion:	$2 < \alpha_L < 8$ ppm·K^{-1}
Low Thermal Expansion:	$0 \leq \alpha_L < 2$ ppm·K^{-1}
Negative Thermal Expansion:	$\alpha_L < 0$ ppm·K^{-1}

The linear CTEs of various materials are listed in Table 1.1; the CTEs of many engineering materials have been known for decades.

1.2 Negative thermal expansion (NTE)

Although materials exhibiting high and intermediate thermal expansion are certainly useful for innumerable applications, materials with low and especially negative thermal expansion behaviors are the focus of this thesis. In this section, thermomiotic materials are introduced, including their applications and various mechanisms to explain thermomiotic behavior.

1.2.1 Applications

Negative thermal expansion behavior is of interest for both fundamental and practical reasons [1, 2, 3, 4, 5, 6, 7, 8]. Thermomiotic materials can in principle be used in composites to compensate for the positive thermal expansion of other materials [40, 41, 42, 43]. Composites consisting of both NTE and PTE components can be tailored to have near-zero thermal expansion, making them potentially useful in such devices as high-precision optical mirrors [5, 7]. However, the formation of such composites often leads to stresses from CTE mismatch between the components of the composite, which can induce deleterious phase

Table 1.1: Linear coefficients of thermal expansion (α_L) for various materials at either a single temperature or over a temperature range.

Material	**Average α_L (ppm·K^{-1})**	**Temperature (K)**	**Ref.**
H_2O (s)	+52.7	273	[22]
NaCl	+39.86	300	[23]
NaCl	+22.78	85	[23]
Al	+22.75	297	[23]
Ag	+18.73	283-338	[24]
Cu	+16.79	295	[23]
Au	+13.4	283-338	[24]
Cu	+12.03	120	[23]
NbO_2F	+10.4	20-300	[25]
Al	+8.81	85	[23]
$SnMo_2O_8$	+7.9	12-500	[26]
Pyrex® 7740 glass	+3.25	0-300	[27]
Si	+2.5	239.15	[28]
Hg	+1.8	295	[29]
Diamond	+0.97	273-296	[30]
H_2O (s)	+0.8	73	[22]
Diamond	+0.58	194-273	[30]
SiO_2 glass	+0.5	298-1273	[2]
Invar ($Fe_{65}Ni_{35}$)	+0.07	293	[31]
$Zr_{0.4}Sn_{0.6}Mo_2O_8$	-0.06	12-500	[26]
ReO_3	-0.6	2-200	[32]
$Ni[Pt(CN)_6]$	-1.02	100-400	[33]
$Fe[Co(CN)_6]$	-1.47	4.2-300	[34]
$Sc_2W_3O_{12}$	-2.2	50-450	[20]
H_2O (s)	-6.1	23	[22]
ScF_3	$\sim$-8	295	[35]
ZrW_2O_8	-9.1	0-300	[36]
$Cd[Pt(CN)_6]$	-10.02	100-400	[33]
ScF_3	$\sim$-14	60-110	[35]
$Zn(CN)_2$	-16.9	25-375	[37]
$Cd(CN)_2$	-20.4	150-375	[37]
$SrCu_3Fe_4O_{12}$	-22.6	200-230	[38]
$Bi_{0.95}La_{0.05}NiO_3$	-82	320-380	[39]

transitions [41, 42, 43, 44], discussed further in Section 1.2.3.1 and Chapter 5. Tuning the CTE of a single-phase material avoids such problems.

1.2.2 Mechanisms

The earliest and most common observation of thermomiotic behavior is likely the "density anomaly of water" between 273 and 277 K, which has been known for centuries [8]. Thermal contraction in a solid was first reported by Scheel over a century ago for quartz and vitreous silica at low temperatures [45, 46]. After World War II, NTE was observed over certain temperature ranges in several oxide systems, such as cordierite ($Mg_2Al_4Si_5O_{18}$) [47, 48, 49], β-eucryptite ($LiAlSiO_4$) and other lithium aluminum silicates (LAS) [50, 51, 52, 53], and the $NaZr_2(PO_4)_3$ (NZP) family [2]. These early examples of thermomiotic behavior, however, were over a small temperature range, and contraction was generally small and anisotropic. For example, in the case of NZP, thermal expansion in the c-direction is coupled with thermal contraction in the other two directions [2, 3, 4]. The low-x members of the $ZrV_{2-x}P_xO_7$ series were later reported to show isotropic NTE but only above 373 K [54].

Until the mid-1990s, studies of NTE remained somewhat sporadic, and the phenomenon was generally viewed as a novelty. However, the 1996 report of pronounced isotropic negative thermal expansion in ZrW_2O_8 between 0.3 and 1050 K [55] and subsequent connection of the behavior to structure [56, 57] sparked considerable (and ongoing) interest in materials displaying NTE over a broad temperature range. ZrW_2O_8 and related materials have since been widely studied, and many other thermomiotic materials, including oxides, cyanides, fluorides, and metal-organic frameworks, have been reported in the last couple of decades.

Several valid mechanisms for thermomiotic behavior in various types of solids have been suggested. In general, thermomiotic behavior occurs when some phenomenon outweighs the inherent lengthening of individual bonds so that the thermodynamic Grünesien parameter becomes negative. In this subsection, various mechanisms for NTE and relevant examples are introduced; a general overview of negative thermal expansion is intended rather than a comprehensive review.

1.2.2.1 Lattice vibrations and rigid unit modes

Negative thermal expansion in open-framework (non-magnetic) solids usually arises from lattice vibrations. Open-framework materials feature low-density, three-dimensional networks of polyhedra (typically, but not limited to, tetrahedra or octahedra) linked by a two-coordinate moiety (often, but not necessarily, an oxygen atom). The atomic displacements associated with lattice vibrations (phonons) through such networks can be either along the direction of propagation (longitudinal) or across it (transverse) [1]. Figure 1.4 shows the effect of both longitudinal and transverse vibrations on the metal–metal separation in a simple metal–oxygen–metal linkage. Upon heating, longitudinal vibrations cause an increase in the length of each M–O bond due to anharmonicity (Section 1.1.1). However, transverse vibrations that move the oxygen atom off the M–M axis result in contraction of the distance between the metal atoms. Transverse modes typically are lower in energy than longitudinal ones and can be excited at lower temperatures; therefore, transverse modes may dominate the thermodynamic Grüneisen parameter and cause NTE or low PTE (Equation 1.13), as discussed in Section 1.1.3. In a three-dimensional framework, the effect of transverse modes on thermal expansion also depends on the rigidity of the polyhedra and the strength of the metal–anion bonds linking them [5].

The transverse thermal motion of the oxygen atom shown in the simple cartoon in Figure 1.4 may also have an effect in real framework solids. In open-framework materials with anion-connected rigid polyhedra, the transverse thermal motion of the M–X–M unit results in coupled rocking of the polyhedra. In the rigid-unit mode (RUM) model, the polyhedra are treated as "rigid units" that, when heated, rock without distortion and give rise to the transverse motion of the bridging atoms [56, 58, 59]. This model is illustrated in Figure 1.5 by a top-down view of rigid, corner-sharing octahedra; heating the system causes the octahedra to rock back and forth and the unit cell volume (magenta box) to decrease in a time-averaged sense. The distortion of the linkages requires less energy than distortion of the rigid polyhedra; therefore, framework contraction outweighs polyhedral expansion and allows for overall NTE. There are some cases in which polyhedral rotations do cause small distortions in the polyhedra themselves; these so-called "quasi-RUMs" (qRUMs) [60] have

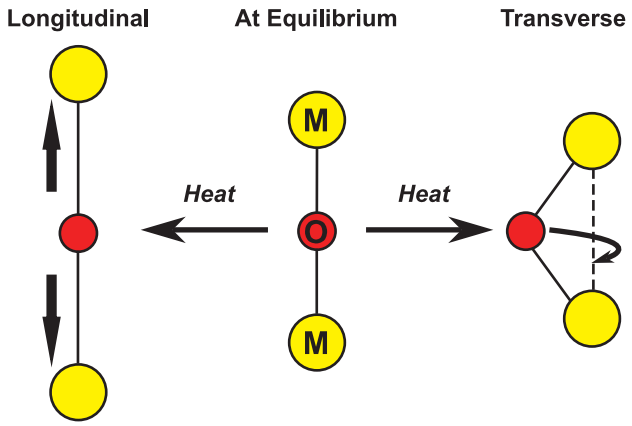

Figure 1.4: Effect of longitudinal and transverse vibrational modes on the metal–metal separation in a simple metal–oxygen–metal (M–O–M) linkage at elevated temperature. Upon heating, longitudinal vibrations of the linkage result in expansion due to anharmonicity, while transverse vibrations result in contraction of the $M \cdots M$ distance. Redrawn from refs. [1, 5].

been reported in the AM_2O_7 [61] and $A_2M_3O_{12}$ [62] families.

Several families of materials that are thermomiotic as a result of lattice vibrations are introduced in Section 1.2.4 below.

1.2.2.2 Changes in symmetry or bond length

In some cases, individual bond distances can decrease in a material, perhaps due to polyhedral distortion. One classic example of this phenomenon is the ferroelectric perovskite material $PbTiO_3$, which contains highly distorted TiO_6 octahedra below its ferroelectric-paraelectric phase transition at 763 K. At ambient conditions, the Ti–O bond lengths differ greatly (1.766, 4 × 1.979, and 2.390 Å) [63], and the crystal structure is tetragonal; upon heating, the octahedra regularize (crystal structure becomes cubic), and the average Ti–O bond length decreases. The a- and b-axes both show PTE, but the c-axis shrinks rapidly enough on heating for overall volume contraction below 763 K (normalized α_L = -3.3 ppm·K^{-1}) [4, 5]. Negative thermal expansion in $PbTiO_3$-based materials arising from the spontaneous polarization displacement of cations continues to be studied [64, 65, 66, 67, 68].

As mentioned above, the anisotropic thermomiotic behaviors of several lithium aluminum silicate (Li_2O–Al_2O_3–SiO_2) phases, including β-spodumene ($Li_2Al_2Si_nO_{4+2n}$) [53],

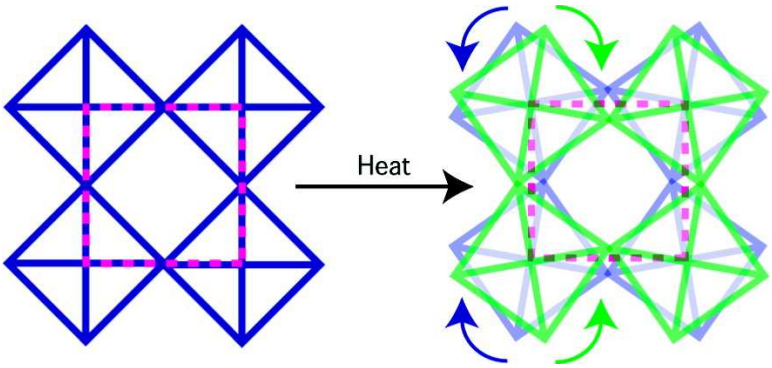

Figure 1.5: Top-down view of rigid, corner-sharing octahedra, with the unit cell outlined in magenta. Heating the system causes the octahedra to rock back and forth, and the unit cell volume decreases in a time-averaged sense. Reprinted with permission from B. K. Greve *et al. J. Am. Chem. Soc.*, 132(44):15496-15498, 2010. Copyright 2010, American Chemical Society.

β-eucryptite [52], and cordierite [47], have been known for several decades, as well as that of the NZP family [2]. In each of these materials, PTE in one or two dimensions is coupled with NTE in the other dimension(s) [3]. In corderite and β-eucryptite, the a- and b-axes display PTE, while the c-axis shows NTE; however, in NZP, PTE along the c-axis is coupled with contraction along a and b. The overall volume expansion of these materials can be either negative or positive in principle. The thermal expansion behavior of these materials arises from their structure; the materials consist of two-dimensional sheets composed of ionic bonds (such as Li–O, Mg–O, and Na–O) that are connected by strong covalent bonds like Al–O, Si–O, P–O, and Zr–O. The ionic bonds lengthen with increasing temperature, so the sheets expand two-dimensionally; however, the rigidity of the linking covalent bonds causes the sheets to be pulled closer together, and there is significant NTE in the direction normal to the sheets [3, 4, 7].

The family of sodium super-ionic conductors (NaSICON) is based on NZP; various substitutions of the metal ions can lead to a variety of thermal expansion properties [69, 70]. The thermal expansion of this family is anisotropic and can be negative along either the a- or c-axis, depending on the space group [71]. For example, in $NbTi(PO_4)_3$, α_a is negative between 293 and 973 K, while α_c is positive; the overall α_V is negative [72].

ZERODUR® (Schott AG, Mainz, Germany) is a commonly used LAS-related material

with very low thermal expansion that consists of a crystalline phase in an amorphous matrix. The crystalline phase is thermomiotic and has a high-temperature quartz structure; the amorphous phase, however, exhibits low PTE. Hence, the overall CTE can be controlled by changing the crystalline/amorphous composition [73].

1.2.2.3 Charge transfer

Thermomiotic behavior in some materials results from charge transfer between atoms. In this mechanism, electron-accepting species expand, while electron-donating species shrink. In practice, however, atomic or ionic radius variation depends on the elements and their electronic configurations. For overall volume contraction, the contraction of the electron-donating atoms must outweigh the expansion of the electron-accepting atoms [7].

An example of NTE arising from thermally induced charge transfer is $Sm_{2.75}C_{60}$ [74]. Some perovskite oxides also display NTE as a result of atomic radius contraction. One example, $Bi_{0.95}La_{0.05}NiO_3$, shows "colossal" NTE ($\alpha_L \approx$ -82 ppm·K^{-1}, 320-380 K) that results from charge transfer from Ni to Bi upon heating, with an accompanying first-order phase transition [39]. Strong NTE has also been reported for $LaCu_3Fe_4O_{12}$ [75, 76] and $SrCu_3Fe_4O_{12}$ [38] ($\alpha_L \approx$ -22.6 ppm·K^{-1}, 200-230 K), which feature charge transfer from Fe to Cu upon heating. Zero thermal expansion (and NTE in the *a*-*b* plane) was reported in YbGaGe between 100 and 400 K as a result of electronic charge transfer (Yb to Ga) [77].

1.2.2.4 Magnetic transitions

In some cases, magnetostriction can cause thermomiotic behavior, as changes in magnetic structure can compensate for thermal lengthening of bonds [5]. One classic example of such materials is Invar ($Fe_{65}Ni_{35}$) [31], an alloy discovered in 1897 by Guillaume (for which he was awarded the Nobel Prize in Physics in 1920) that shows low thermal expansion below its Curie temperature. The "Invar effect" has also been reported in magnetic metals such as Lu_2Fe_{17} and Y_2Fe_{17} [78] and intermetallics such as YMn_2 [79], $Y_2Al_3Fe_{11}Mn_3$ ($\alpha_V \approx$ -75 ppm·K^{-1}, 185-200 K) [80], and $Tm_2Fe_{16}Cr$ [81].

In recent years, antiperovskite manganese nitrides, Mn_3AN, have attracted interest for their highly thermomiotic behavior over a broad temperature range, accompanied by a

first-order phase transition from antiferromagnetic to paramagnetic phases [7]. Several A cations have been explored, including Cu, Ga, Zn, Sn, both separately and in combination [82, 83, 84, 85]. Nanometric $Mn_3(Cu_{1-x}Ge_x)N$ has more pronounced NTE than the bulk material [86].

1.2.3 Effects of pressure

The effects of pressure on the crystal structure and thermal expansion properties of thermomiotic materials are of both technological and fundamental importance. The same characteristics that lead to NTE in open-framework materials (enhanced flexibility and low-energy transverse modes) also lead to interesting pressure-related effects. In this subsection, the effects of pressure on NTE are discussed in terms of both applications and thermodynamics.

1.2.3.1 Technological considerations

The formation of composites combining materials with PTE and NTE can lead to stresses due to thermal expansion mismatch, which, coupled with the typically open-framework structures of thermomiotic materials, can induce deleterious phase transitions and, correspondingly, significant changes in thermal expansion behavior [40, 41, 42, 43, 44]. The thermomiotic material ZrW_2O_8 has been widely explored for use in composites; however, a phase transition in ZrW_2O_8 at approximately 0.2 GPa causes a reduction in the negative CTE by an order of magnitude [57, 87], which adversely affects the use of the material in composites with tailored thermal expansion, such as those with Cu [40, 88, 89]. In Chapter 5, the behavior of another thermomiotic material, ScF_3, is examined in a varnish matrix at low temperature, where stress associated with thermal expansion mismatch induces a phase transition and CTE sign change [44].

Pressure-induced phase transitions have been reported in several thermomiotic framework oxide materials, such as cubic $ZrMo_2O_8$ [90, 91, 92, 93], cubic $HfMo_2O_8$ [92], cubic ZrW_2O_8 [57, 93, 94], HfW_2O_8 [95], $Sc_2W_3O_{12}$ [96, 97], and $Al_2W_3O_{12}$ [98, 99]; these materials are discussed in Section 1.2.4. Generally, these phase transitions involve tilting of rigid polyhedral units, a decrease in unit cell volume, and lowering of symmetry. In Chapters 7

and 8, the effects of pressure on solid solutions of the thermomiotic compound ScF_3 with YF_3 and α-AlF_3, respectively, are explored.

1.2.3.2 Pressure dependence of CTE

The isothermal bulk modulus (K_T, Equation 1.7) is the reciprocal of isothermal compressibility and a measure of elastic stiffness. Hence, materials with high bulk moduli are stiffer than those with low ones. The bulk modulus, which has units of pressure, can be as high as 442 GPa for a highly stiff material like diamond [100], but, for many common engineering metals, like steel or copper, K_T is on the order of 100 GPa [11]. Softer materials such as some glasses and polymers have much lower bulk moduli, on the order of a few GPa.

The temperature dependence of K_T is related to the pressure dependence of α_V [101, 102]:

$$\left(\frac{\partial \alpha_V}{\partial P}\right)_T = \frac{1}{K_T^2}\left(\frac{\partial K_T}{\partial T}\right)_P. \tag{1.15}$$

As initially proposed by Wachtman *et al.* [103] based on empirical observations and later justified theoretically by Anderson [104],

$$K_T = K_0 - bTe^{-T_0/T}, \tag{1.16}$$

where K_0 is the bulk modulus at 0 K and b and T_0 are constants. From this relationship, the temperature derivative of bulk modulus at constant pressure is

$$\left(\frac{\partial K_T}{\partial T}\right)_P = -be^{-T_0/T}\left(1 + \frac{T_0}{T}\right). \tag{1.17}$$

The T_0/T term is always positive; thus, the sign of the above derivative depends only on the sign of parameter b. Anderson demonstrated that most materials have positive b; hence, $\left(\frac{\partial K_T}{\partial T}\right)_P$ is negative (most materials soften on heating) [104]. As K_T is always positive, Equation 1.15 thus suggests that most materials experience decreased CTE on compression.

Fang and Dove have recently suggested that pressure-induced softening (*i.e.*, $\left(\frac{\partial K_0}{\partial P}\right) < 0$) would be a feature of many thermomiotic materials; this behavior has been observed in ZrW_2O_8 [105], $ZrMo_2O_8$ [92], HfW_2O_8 [95], $Zn(CN)_2$ [106], and various thermomiotic zeolites [107, 108, 109]. The same authors have subsequently demonstrated that pressure-induced softening is temperature-dependent [110].

1.2.4 Examples

As introduced in Section 1.2.2.1, NTE may arise from lattice vibrations in open-framework solids. Since the mid-1990s, much of the work on thermomiotic materials has focused on this mechanism. These materials share some common features: strong metal–anion bonds with high covalency, two-coordinate bridging atoms, and low-density and flexible framework structures [111]. In this subsection, various families of thermomiotic materials, including oxides, cyanides, and metal-organic frameworks (MOFs), and the use of solid solutions for thermal expansion control are summarized. For some of the materials, behavior under pressure is also discussed.

1.2.4.1 AM_2O_8 family

The most widely studied thermomiotic framework material is undoubtedly ZrW_2O_8. The compound was first synthesized in 1959 by Graham *et al.* [112], and thermomiotic behavior was actually reported nine years later by Martinek and Hummel [113] but not further explored for many years afterward. However, the report of strong isotropic NTE between 0.3 and 1050 K by Mary *et al.* [55] inspired a large body of subsequent research on thermomiotic materials, particularly ZrW_2O_8 and its relatives. The AM_2O_8 structure (Figure 1.6) consists of corner-sharing AO_6 octahedra and MO_4 tetrahedra; each AO_6 octahedron is connected to six MO_4 tetrahedra, but each tetrahedron is only connected to three octahedra, leaving a single terminal O atom per tetrahedron.

Although ZrW_2O_8 shows strong isotropic NTE from 0.3 to 1050 K, the magnitude of its CTE changes significantly at 448 K (α_L = -9.1 ppm·K^{-1} below 350 K and -5.0 ppm·K^{-1} above 450 K) as a result of an orientational order-disorder phase transition [21]. The two phases, both of which are cubic, are illustrated in the bottom panels of Figure 1.6. The low-temperature phase, α-ZrW_2O_8 (space group $P2_13$), features orientationally ordered WO_4 tetrahedra; as α-ZrW_2O_8 is heated, the population of WO_4 pairs with the initial orientation decreases, and the population of WO_4 pairs with the opposite orientation increases. At the phase transition temperature, the populations of the two different orientations become equivalent. In the high-temperature phase, β-ZrW_2O_8 (space group $Pa\bar{3}$), the WO_4

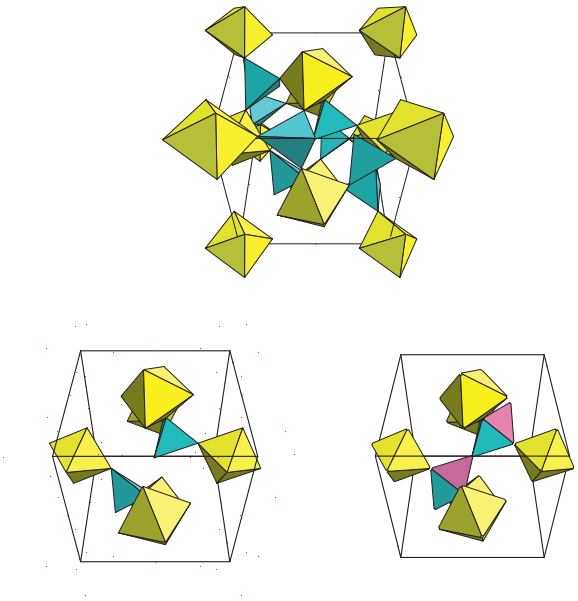

Figure 1.6: (top) A unit cell of completely orientationally ordered α-ZrW_2O_8, in which WO_4 tetrahedra are blue and ZrO_6 octahedra are yellow. (bottom left) A pair of WO_4 tetrahedra (blue) aligned along the [1 1 1] direction in completely orientationally ordered ZrW_2O_8. (bottom right) As α-ZrW_2O_8 is heated, the population of WO_4 pairs with the initial orientation (blue) decreases, and the population of WO_4 pairs with the opposite orientation (magenta) increases. At the $\alpha \rightarrow \beta$ phase transition temperature, the populations of the two different orientations become equivalent. Reproduced from ref. [93] by permission of the PCCP Owner Societies.

tetrahedral orientation is disordered.

Other materials with the AM_2O_8 structure have been studied extensively. Soon after its discovery in ZrW_2O_8, NTE was reported in $ZrMo_2O_8$ [114] and HfW_2O_8 [21]. HfW_2O_8 shows thermal expansion behavior that is similar to that of ZrW_2O_8 and has a similar order-disorder phase transition temperature (463 K) [21, 115]. However, metastable cubic $ZrMo_2O_8$ adopts the oxygen-disordered $Pa\bar{3}$ structure below 673 K [114] and exhibits NTE. The magnitude of NTE changes at around 200 K (from approximately -8 to -5 ppm·K^{-1}) due to a transition from dynamic to static oxygen disorder [116]. The complete range of $Zr_{1-x}Hf_xW_{2-y}Mo_yO_8$ solid solutions has been prepared, all of which show NTE; the magnitude of NTE depends primarily on the phase (α or β) and not as much on composition [117].

Attempts at substitution of other elements in the AM_2O_8 structure have had mixed success. Introduction of Sn^{4+} has been attempted in ZrW_2O_8, but solubility is limited to approximately 30% ($Zr_{0.7}Sn_{0.3}W_2O_8$) [118]. Sn-substitution in ZrW_2O_8 results in a decrease in the $\alpha \rightarrow \beta$ phase transition temperature but little change in CTE. The thermal expansion behavior of the full range of Sn-substituted $ZrMo_2O_8$ was recently reported; average α_L of the solid solutions vary between -5.9 and +7.9 ppm·K^{-1} for the end members, $ZrMo_2O_8$ and $SnMo_2O_8$, respectively, and near-zero thermal expansion was observed for $Zr_{0.4}Sn_{0.6}Mo_2O_8$ (α_L = -0.06 ppm·K^{-1}) [26]. The solubility of Ti^{4+} is significantly lower than that of Sn^{4+} (about 5%) because of its much smaller ionic radius. As with Sn, substitution of Ti in ZrW_2O_8 does not change CTE substantially but lowers the $\alpha \rightarrow \beta$ phase transition temperature [119]. Finally, there have been reports of trivalent metal substitution on the A site by a number of metals, including Sc, In, Y, Eu, Er, and Yb, which have limited solubility but can strongly affect the phase transition temperature [120, 121, 122, 123, 124].

The high-pressure behavior of the AM_2O_8 family has been studied extensively. Although no solid solutions have been examined to date, ZrW_2O_8 [57, 87, 93, 94, 125, 126], HfW_2O_8 [95, 127], $ZrMo_2O_8$ [90, 91, 92, 93, 128], and $HfMo_2O_8$ [92] have all been studied at high pressure. ZrW_2O_8 and HfW_2O_8 both undergo phase transitions on compression ($\sim$0.2 and 0.63 GPa, respectively) to an orthorhombic (γ) polymorph [87, 127]; no such transition has been observed for the molybdates at comparable pressures [92]. All four materials

undergo pressure-induced amorphization (PIA) at sufficiently high pressures [91, 125, 128]. ZrW_2O_8 is examined at high pressure (and temperature) in Section 3.3.1.

1.2.4.2 AM_2O_7 family

The AM_2O_7 family is another commonly studied class of thermomiotic materials. This family contains a large number of members; while M is mainly limited to P, V, or As, the A cation can be any tetravalent cation that can adopt octahedral coordination [1]. The archetypal member of the family is ZrV_2O_7, in which NTE was first reported in the mid-1990s [54]. The AM_2O_7 structure consists of corner-shared AO_6 octahedra and MO_4 tetrahedra. The high-temperature phase is cubic ($Pa\bar{3}$) and shows NTE. This structure is similar to the high-temperature phase of the AM_2O_8 family, but there are no terminal oxygen atoms in AM_2O_7. Instead, MO_4 tetrahedra share three vertices with neighboring AO_6 octahedra and the fourth with another MO_4. Unlike in the AM_2O_7 family, the transverse vibrations of corner-sharing O atoms that may give rise to NTE involve polyhedral distortions. Therefore, such vibrations cannot be described by the RUM model but are instead quasi-RUMs [59]. The low-temperature AM_2O_7 phase always displays PTE and often adopts a rather complicated $3 \times 3 \times 3$ cubic superlattice [54]. However, the low-temperature structures of some AM_2O_7 have been suggested to have lower symmetry, including monoclinic (GeP_2O_7 [129] and SnP_2O_7 [130]), orthorhombic (HfP_2O_7 and ZrP_2O_7 [131, 132]), and triclinic (CeP_2O_7 [133] and AnP_2O_7 (An = Th, U, Np, Pu) [134]).

Of the many members of the AM_2O_7 family, only TiP_2O_7 [135, 136], ZrP_2O_7 [135, 137], CeP_2O_7 [133], ZrV_2O_7 [135, 138], and HfV_2O_7 [139] have been examined under pressure. Neither TiP_2O_7 nor ZrP_2O_7 (both of which show PTE) shows evidence for pressure-induced phase transitions or amorphization, compressing smoothly up to 40.3 and 20.5 GPa, respectively, the highest investigated pressures [135]. However, CeP_2O_7, ZrV_2O_7, and HfV_2O_7 undergo symmetry-lowering high-pressure phase transitions at 0.65, 1.6, and 3.7 GPa, respectively [133, 138, 139]. A second reversible phase transition has been observed in CeP_2O_7 at $\sim$5 GPa [133]. ZrV_2O_7 and HfV_2O_7 both amorphize upon sufficient compression; for

ZrV_2O_7, complete amorphization occurs above 4.0 GPa [138], while HfV_2O_7 gradually undergoes amorphization that is still not complete at 41.7 GPa [139].

1.2.4.3 $A_2M_3O_{12}$ family

Another widely studied family of framework oxides with interesting thermal expansion properties is $A_2M_3O_{12}$ [19, 140]. Many $A_2M_3O_{12}$ phases of interest have orthorhombic [20, 141, 142] or monoclinic [143] structures (Figure 1.7); the A cation in these phases is a small trivalent metal (such as Al or In) or rare earth (Ho to Lu), and M is W or Mo [1, 8]. In both forms of this structure, AO_6 octahedra share vertices with six MO_4 tetrahedra, and each MO_4 is connected to four AO_6; there are no terminal oxygen atoms. Many (but not all) of the orthorhombic phases transform to monoclinic symmetry at lower temperatures, the latter of which only shows PTE. The temperature of this phase transition varies widely with composition; some compounds do not show the transition at the lowest temperatures examined, while $Fe_2Mo_3O_{12}$ is monoclinic up to 772 K [143]. The phase transition temperature is directly related to the electronegativity of the A cation and tends to be higher for molybdates than for tungstates [143].

Several compounds with the orthorhombic structure show anisotropic negative thermal expansion (a and c contract while b expands on heating). There are no RUMs in this structure, but NTE may still arise from transverse oxygen vibrations [59]. The polyhedra in $A_2M_3O_{12}$ are increasingly distorted with increasing temperature, with less rigid octahedra leading to more negative CTEs [62]. The archetypal compound of this family, $Sc_2W_3O_{12}$, is thermomiotic from 10 to 1300 K [20, 144], with an average α_L of -2.2 ppm·K^{-1} between 50 and 450 K estimated from X-ray diffraction data [20]. However, as mentioned in Section 1.1.4.3, dilatometric measurements of thermal expansion revealed more negative CTEs (-6 to -11 ppm·K^{-1}) because of microcracks in the ceramic bars. In a similar manner, the thermal expansion of polycrystalline $Al_2W_3O_{12}$ was initially unclear: dilatometry suggested low NTE, while neutron diffraction suggested low PTE [19]. A later dilatometric study of a single crystal of $Al_2W_3O_{12}$ reported PTE along the b-axis, NTE along

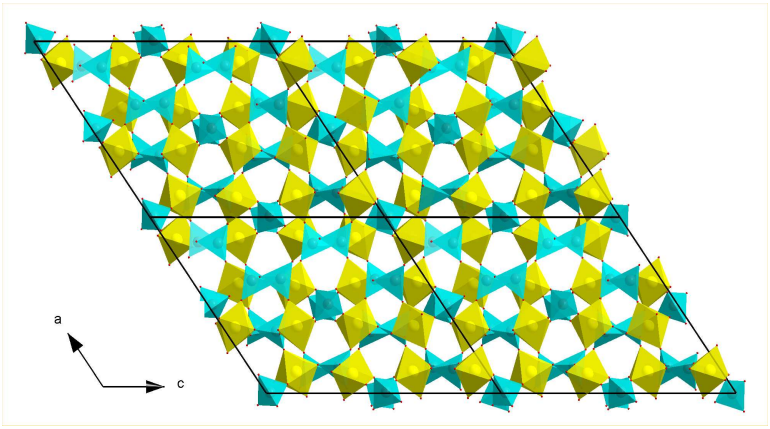

(a)

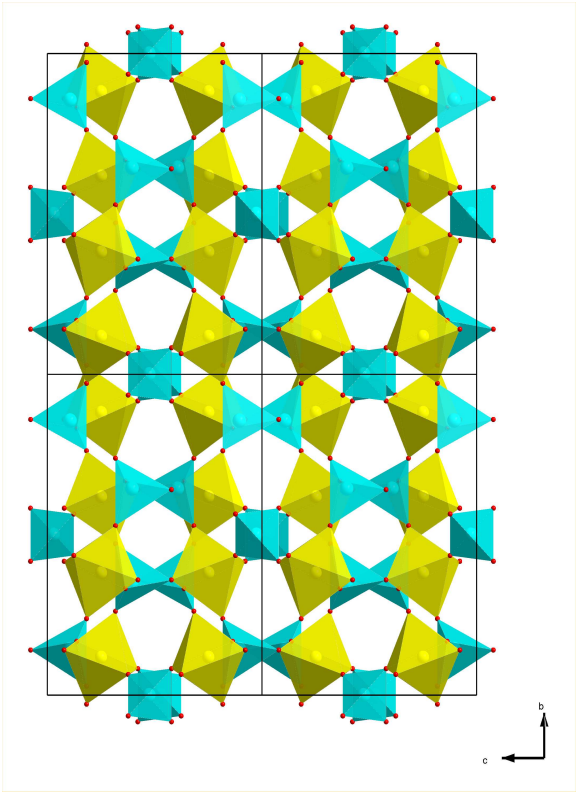

(b)

Figure 1.7: Two forms of $A_2M_3O_{12}$: (a) monoclinic ($P2_1/a$) and (b) orthorhombic ($Pbcn$). In both structures, MO_4 tetrahedra are blue, AO_6 octahedra are yellow, and O atoms are red.

a, and near-zero thermal expansion along c [145]. The polyhedra in the $A_2M_3O_{12}$ structure are more easily distorted when larger A cations are used, resulting in more negative CTEs. For example, $Y_2W_3O_{12}$ [146] and $Y_2Mo_3O_{12}$ [62] have average linear CTEs of -7.0 and -9.02 ppm·K^{-1}, respectively. Also, a number of solid solutions have been prepared, some of which show near-zero thermal expansion, such as $Al_{1.68}Sc_{0.02}In_{0.30}W_3O_{12}$ [140] and $Al_{0.30}(HfMg)_{0.85}W_3O_{12}$ [147].

Many $A_2M_3O_{12}$ compounds also undergo a symmetry-lowering phase transition on modest compression. For example, $Sc_2W_3O_{12}$, which remains orthorhombic ($Pnca$) down to the lowest temperatures studied [20], becomes monoclinic ($P2_1/a$) when compressed to between 0.25 and 0.3 GPa [96, 97]. Similarly, $Sc_2Mo_3O_{12}$ becomes monoclinic ($P2_1/a$) upon cooling below ∼178 K [148] and also upon compression to ∼0.25 GPa [99]. The orthorhombic-to-monoclinic transition is usually associated with a dramatic decrease in the bulk modulus of the material [149], and for some materials, the orthorhombic phase displays highly anisotropic compressibility. $Al_2W_3O_{12}$, which becomes monoclinic on cooling to 267 K at ambient pressure [143], has previously been studied by *in situ* diffraction at high pressure using a diamond anvil cell (DAC); however, the onset pressure of the orthorhombic-to-monoclinic transition was so low (<0.08 GPa) compared with the uncertainty of the pressure measurement and the precision of the pressure control that is possible in a DAC that the behavior of orthorhombic $Al_2W_3O_{12}$ on compression could not be determined with a high level of confidence [99]. This phase transition is examined with finer pressure control in Section 3.3.2.

1.2.4.4 AMO_5 family

Negative thermal expansion has been reported in two forms of $NbOPO_4$, a member of the AMO_5 family of framework oxides. Tetragonal $NbOPO_4$ ($P4/n$ below ∼473 K and $P4/nmm$ above) shows NTE only along the a-axis in the high-temperature form [150]. The monoclinic form ($P2_1/c$), which transforms to orthorhombic symmetry ($Pnma$) at ∼565 K, also shows NTE only along the a-axis; however, the high-temperature orthorhombic form displays isotropic NTE [151]. All forms of this material are composed of NbO_6 octahedra

and PO_4 tetrahedra with the following corner-sharing connectivity: NbO_6 are connected to four PO_4 and two other NbO_6, and PO_4 are connected to four NbO_6 [150, 151]. Other members of the AMO_5 that show NTE include $NbVO_5$ [152] and $TaVO_5$ [153].

1.2.4.5 M_2O family

A somewhat unusual oxide family is the cuprites, M_2O, of which the M = Cu and Ag forms have been reported to display NTE. The cubic structure of the cuprites features two-coordinate cations (Cu^{2+} or Ag^{2+}), while the O^{2-} are four-coordinate; the overall structure consists of a pair of independent but interpenetrating OM_4 networks [8]. However, the mechanism for NTE is similar to that in other framework oxides. Ag_2O displays NTE over its thermal stability range, while Cu_2O is only thermomiotic below approximately 200 K, where it changes to PTE [154]. This change from NTE to PTE in Cu_2O has been explained by the domination of cuprophilic interactions when Cu atoms are brought in sufficiently close proximity; these same interactions do not occur in Ag_2O [155].

1.2.4.6 ReO_3 family

Materials with ReO_3-type connectivity, which include oxides, oxyfluorides, and fluorides, are the primary focus of this thesis. These materials and their properties are discussed in greater detail in Section 1.3.

1.2.4.7 Zeolites and aluminophosphates

The final families of thermomiotic framework oxides to be discussed are zeolites (microporous aluminosilicates) and aluminophosphates (AlPOs). The structures of these materials consist of alternating, corner-sharing SiO_4 (or PO_4) and AlO_4 tetrahedra. NTE was predicted in zeolites and AlPOs in the 1990s [156] and has since been measured experimentally in several zeolite-related materials, including Na-zeolite X [157], siliceous faujasite (isotropic NTE, α_L = -4.2 ppm·K^{-1}, 25-573 K) [158], $AlPO_4$-17 (α_V = -35 ppm·K^{-1}, 18-300 K) [159], and ferrierite (anisotropic NTE, average α_V = -24 ppm·K^{-1}, 420-560 K) [160]. Many other zeolite-type materials have been studied, and Lightfoot *et al.* have suggested that NTE in these microporous oxides is the "norm rather than the exception" [161]. Furthermore, Fang

and Dove have recently shown via molecular dynamics simulations that most cubic zeolites show NTE accompanied by pressure-induced softening [107].

1.2.4.8 Cyanides ($M(CN)_2$ and $A_x[M(CN)_6]$)

The flexibility of framework cyanides is greater than that of metal oxides because M–C≡N–M linkages allow for a greater number of low-energy RUMs than do M–O–M linkages. The additional atom allows each rigid unit to rotate independently, giving the structure RUMs at a wide range of wave vectors [37]. As a result, some cyanide-based framework materials show thermomiotic behavior that is much more pronounced than that of oxide-based materials.

Pronounced isotropic NTE has been observed in the simple single-network cyanides $Zn_{1-x}Cd_x(CN)_2$ ($0 \leq x \leq 1$), with α_L in the range of -17 to -20 ppm·K^{-1} between 150 and 375 K, increasing with x (Cd substitution) [37, 162]. Another study reported a linear CTE of -33.5 ppm·K^{-1} for $Cd(CN)_2$ between 170 and 375 K [163]. The network of these simple cyanides consists of cyanide bridges tetrahedrally coordinated to M. Pair distribution function analysis of the NTE mechanism in these materials has shown that the average transverse displacement of the cyanide bridge increases with temperature, which counteracts the PTE of individual Zn–(C/N) bond lengths [164]. A later computational study reported low-energy, nearly dispersionless, transverse acoustic modes with negative mode Grüneisen parameters that arise from translation motion of all atoms in one direction, coupled with CN translation in the other two directions [165, 166]. A pressure-dependent CTE for $Zn(CN)_2$ has been reported, implying a modest temperature dependence to the bulk modulus (Equation 1.15) [106]. Fang and Dove have recently reported temperature-dependent, pressure-induced softening in $Zn(CN)_2$ [108, 109].

Thermomiotic behavior was also reported in $Ni(CN)_2$, which features a two-dimensional framework in which the cyanide units bind to Ni in a square-planar geometry to form a layered structure. In the plane of the sheets, NTE was observed between 28 and 300 K (α_L = -6.5 ppm·K^{-1}), but the weak interactions between individual sheets result in strong PTE in the direction perpendicular to the sheets (α_L = +61.8 ppm·K^{-1}) and a large positive volume CTE of +48.5 ppm·K^{-1} [167].

Other metal cyanides are also known to exhibit NTE. The Prussian Blue analogs, $M^{2+}[Pt(CN)_6]$ (M = Mn, Fe, Co, Ni, Cu, Zn, Cd), which have a cubic ReO_3-type structure (see Section 1.3) with alternating corner-sharing MN_6 and PtC_6 octahedra, are thermomiotic, with greater NTE occurring for larger M. For example, the linear CTE of $Ni[Pt(CN)_6]$ between 100 and 400 K is nearly zero (-1.02 ppm·K^{-1}), while that of $Cd[Pt(CN)_6]$ over the same temperature range is an order of magnitude more negative (-10.02 ppm·K^{-1}) [33]. These differences in thermal expansion arise from differences in M–cyanide bond strengths; larger M form weaker bonds and thus more flexible lattices in which transverse vibration of the cyanide bridges (the cause of NTE) requires less energy [33]. Incorporation of water molecules into the nanopores of $Zn[Pt(CN)_6]$ and $Cd[Pt(CN)_6]$, however, has been shown to increase the CTE by dampening transverse vibrations [168]. In addition, very low NTE (average α_L = -1.47 ppm·K^{-1}) was reported for the Prussian Blue analog $Fe[Co(CN)_6]$ between 4.2 and 300 K [34].

Other Prussian Blue analogs with formula unit $M_3[Co(CN)_6]_2$ (M = Mn, Fe, Co, Ni, Cu, Zn) also show strong isotropic NTE, with α_L ranging from -19.6 ppm·K^{-1} for $Fe_3[Co(CN)_6]_2{\cdot}14H_2O$ to -48.0 ppm·K^{-1} for $Mn_3[Co(CN)_6]_2{\cdot}12H_2O$. The hexacyanoferrate form $M_3[Fe(CN)_6]_2$ shows a wider range of linear CTEs, from +47.8 ppm·K^{-1} for $Mn_3[Fe(CN)_6]_2{\cdot}14H_2O$ to -39.6 ppm·K^{-1} for $Zn_3[Fe(CN)_6]_2{\cdot}14H_2O$ [169]. In these materials, the waters of hydration can partially replace some of the cyanide bridges, resulting in unlinked vertices on the octahedra that enhance the framework flexibility and potentially enhance NTE [169].

The first material reported to have "colossal" positive and negative thermal expansion ($|\alpha_L| \geq$ 100 ppm·K^{-1}) over a broad temperature range was $Ag_3[Co(CN)_6]$ [170]. The material has a layered structure; upon heating, the layers show colossal PTE (α_L = +140 ppm·K^{-1}), while colossal NTE occurs in the direction perpendicular to the layers (α_L = -125 ppm·K^{-1}). The resulting α_V is large and positive. The mechanism for this interesting behavior is believed to be driven by Ag^+ repulsions [170], as substitution on the Ag site reduces the CTE by an order of magnitude [171].

1.2.4.9 Metal-organic frameworks (MOFs)

MOF materials feature metal-oxygen clusters connected by organic linkers and have attracted much attention in recent years for such applications as gas adsorption because of their large surface areas and easily tunable pore sizes [172]. However, the open-framework structure and flexible polyhedra of MOFs also makes strong NTE possible in such materials. NTE in MOF-5 [Zn_4O(1,4-benzenedicarboxylate)$_3$] was first predicted [173], later simulated [174, 175], and then measured experimentally ($\alpha_L \approx$ -10 to -16 ppm·K^{-1}, 4-600 K) [176]. The pronounced thermomiotic behavior of MOF-5 is attributed to RUMs in which ZnO_4 tetrahedra and phenyl rings serve as rigid units and carboxyl groups are the bridges with large-amplitude transverse vibrations that lead to NTE [176].

Thermomiotic behavior has also been observed in the MOF Cu_3(btc)$_2$ (btc = 1,3,5-benzenetricarboxylate), which consists of Cu_2(carboxylate)$_4$ "paddle-wheel" units bridged by btc [177, 178, 179]. Cu_3(btc)$_2$ shows NTE from 50 to 500 K, with α_L = -4.1 ppm·K^{-1} over this range [178]. The unique mechanism for NTE involves two components: transverse vibration of planar (rather than linear) btc linkers and local dynamic deformation of the "paddle-wheel" nodes [178, 179].

Very recently, thermomiotic behavior arising from another new mechanism has been reported in MOF-14 [Cu_3(btb)$_2$; btb = 4,4′,4″-benzene-1,3,5-triyl-tribenzoate] [180]. The linear CTE of MOF-14 increased in magnitude from -4 to -13 ppm·K^{-1} between 3 and 400 K. MOF-14 features two interpenetrating networks that, upon heating, have an increasingly repulsive interaction, resulting in greater framework distortion; the overall result of this distortion is isotropic contraction of the unit cell.

1.2.5 Solid solutions

Solid solution formation can be used to control thermal expansion. Interstitial solid solutions, in which a small solute occupies a hole in the lattice, are not known to display NTE [1]. However, substitutional solid solutions have shown more promise for thermomiotic behavior. These materials are formed when some fraction of one type of atoms in a lattice are replaced by another type of atoms, in either a disordered or ordered manner.

For maximum solubility, substitutional solid solutions follow the Hume-Rothery rules [181]: solute and solvent atomic radii must not differ by more than 15%; solute and solvent crystal structures must match; and solute and solvent must have similar electronegativities and similar valences [18].

Much prior work has involved solid solutions of thermomiotic materials, some of which is discussed above. Korthuis *et al.* reported that solid solution formation in the $ZrV_{2-x}P_xO_7$ and $HfV_{2-x}P_xO_7$ systems suppressed an order-disorder phase transition. In the middle range of these solid solutions, $x \geq 0.3$, the phase transitions above ambient temperature were completely suppressed [54]. $ZrW_{2-x}Mo_xO_8$ solid solutions improve both thermal and mechanical properties of ZrW_2O_8; incorporation of Mo in ZrW_2O_8 lowers the temperature of the order-disorder phase transition [182, 183]. More recently, tunable thermal expansion was reported for $Zr_{1-x}Sn_xMo_2O_8$ ($0 \leq x \leq 1$) between 12 and 500 K, with average α_L varying between -5.9 and +7.9 ppm·K^{-1} for the end members, $ZrMo_2O_8$ and $SnMo_2O_8$, respectively; near-zero thermal expansion was observed for $Zr_{0.4}Sn_{0.6}Mo_2O_8$ (α_L = -0.06 ppm·K^{-1}) [26]. The control of thermal expansion with solid solutions is further explored in Chapters 6, 7, and 8.

1.3 ReO_3 family

As suggested in the above sections (for example, in Figures 1.6 and 1.7), many thermomiotic framework materials have rather complicated crystal structures. However, the cubic ReO_3 structure (Figure 1.8) features the simplest arrangement of polyhedra to illustrate NTE in framework solids; the transverse motion of the anion results in rocking of the rigid polyhedral units [59] and a time-averaged reduction in the distance between neighboring metal centers (Figure 1.5). This primitive cubic structure is a simpler version of the common perovskite structure ABX_3 in which the A site is vacant, creating a large amount of free space in the crystal structure for transverse motion of the anion. This simple illustration might suggest that all ReO_3-type materials are thermomiotic, but, as discussed below, not all members of this family show negative or even low positive thermal expansion. In this section, several members of the ReO_3 structural family, including oxyfluorides and fluorides,

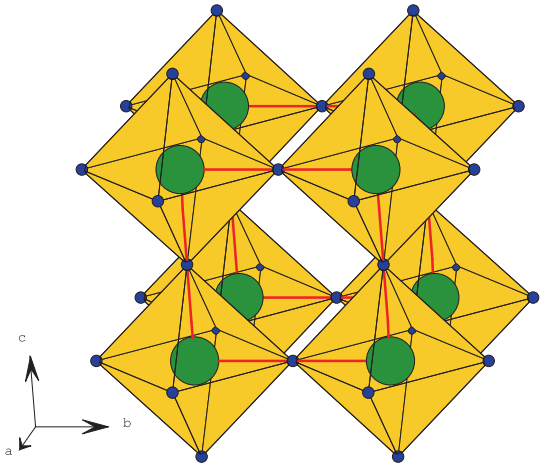

Figure 1.8: The cubic ReO_3 structure, related to the ABX_3 perovskite structure with a vacant A site, consists of corner-sharing ReO_6 octahedra. Green (blue) spheres represent Re (O) atoms, and the unit cell is outlined in red. Reprinted from *Journal of Solid State Chemistry*, 219, C. R. Morelock *et al.*, Thermal expansion and phase transitions of α-AlF_3, 143-147, Copyright 2014, with permission from Elsevier.

and previous research on their thermal expansion properties are introduced; studies of this family comprise the bulk of this thesis.

1.3.1 Rhenium trioxide

Although its structure is often the archetype for NTE in open-framework solids (Figure 1.5), ReO_3 itself demonstrates very complex thermal expansion [32, 184, 185, 186]. ReO_3 is an unusual framework oxide due to its excellent electrical conductivity; the low resistivity of ReO_3 at ambient conditions is close to that of a metal like Ag [187, 188]. Matsuno *et al.* in 1978 initially reported low negative thermal expansion in ReO_3 below 340 K [189]. However, Taylor subsequently reported low but positive thermal expansion between 123 and 486 K [190]; the frequent citation of this paper left ReO_3 unrecognized as a thermomiotic material. More recently, Chatterji *et al.* reported that ReO_3 displays low NTE between 2 and 200 K ($\alpha_L \approx -0.6$ ppm·K^{-1}) [32] and possibly around 600 K [185] but strong PTE near ambient temperature [185]. In a thorough neutron powder diffraction study of ReO_3, Rodriguez *et al.* demonstrated the strong dependence of thermal expansion on crystal structural defects and specifically static disorder of O atoms transverse to the Re$\cdots$Re axis [186].

The void spaces in the framework of the cubic ReO_3 structure allow for accommodation of tilting of the rigid octahedra upon modest compression. A pressure-induced phase transition in ReO_3 was first observed by Razavi *et al.* in 1978 [191]; a slightly later study reported the critical pressure to be 0.24 GPa at 2 K [192]. Upon compression at ambient temperature, ReO_3 undergoes a structural phase transition to another cubic phase ($Im3$) at ∼0.5 GPa [193, 194]. An intermediate phase transition to tetragonal ($P4/mbm$) symmetry was observed by some workers [195, 196] but not by others [197]. The $Im3$ phase further transforms to other phases at even higher pressures [198, 199, 200, 201, 202]. ReO_3 experiences a "compressibility collapse," in which its compressibility increases by an order of magnitude in the high-pressure phase [192]. A similar change in compressibility was observed in the cubic (δ) polymorph of UO_3 [203].

Despite the lack of pronounced NTE in ReO_3, there are potentially many isostructural oxyfluorides (MO_2F and MOF_2) and fluorides (MF_3) with thermomiotic behavior.

1.3.2 Oxyfluorides (MO_2F and MOF_2)

The ReO_3-type oxyfluorides TaO_2F and NbO_2F, both initially synthesized and characterized in 1956 by Frevel and Rinn [204], have been studied recently as potential thermomiotic materials. Tao and Sleight reported strong PTE in NbO_2F between 20 and 300 K ($\alpha_L \approx$ 10.4 ppm·K^{-1}) and very low, near-zero thermal expansion in TaO_2F between 20 and 773 K ($-1 < \alpha_L < +1$ ppm·K^{-1}) [25]. The PTE in NbO_2F has been found to be dependent on both sample preparation and thermal history [205]. The very low thermal expansion of TaO_2F has led to interest in the material for application in infrared-transparent, thermal-shock-resistant components [206]. Both NbO_2F and TaO_2F adopt the cubic ReO_3 structure at ambient conditions, and neither features long-range ordering of O and F across the available anion sites. The lack of O/F ordering is not atypical; none of the perovskites $KTiO_2F$ [207], $BaScO_2F$ [208], $BaFeO_2F$ [209], $SrFeO_2F$ [210], $PbScO_2F$ [211], or $PbFeO_2F$ [212] are known to be anion-ordered. Brink, Withers, and co-workers have published several studies examining O/F ordering in NbO_2F and related compounds [213, 214, 215, 216, 217]. Furthermore, analysis of the atomic displacement parameters of TaO_2F suggests anion static disorder [25]

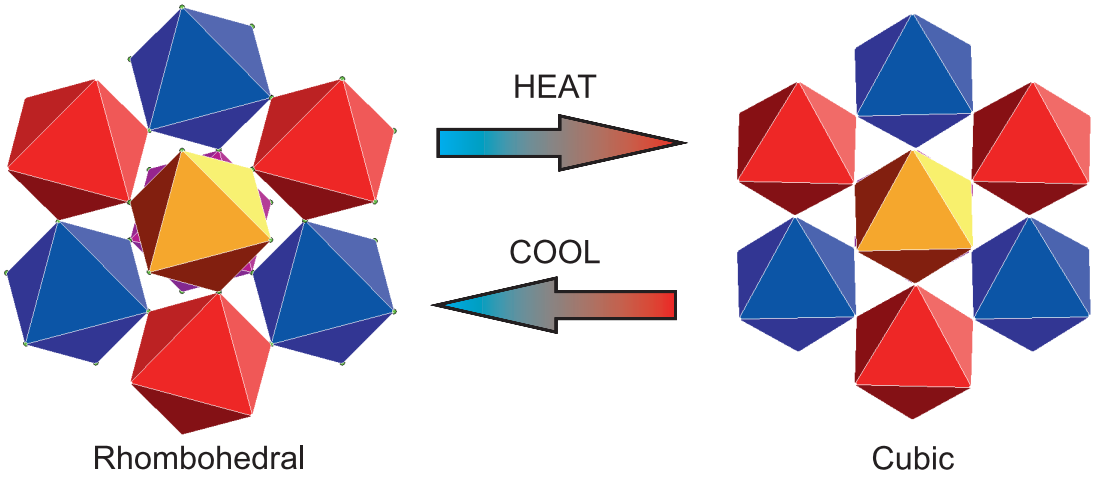

Figure 1.9: Transformation of the ReO_3 structure from rhombohedral (space group $R\bar{3}c$) to cubic ($Pm\bar{3}m$) symmetry upon heating (or compression), as viewed down the cubic (1 1 1) axis. This phase transformation can be conceptualized as the rotation of MX_6 octahedra around the threefold rotation axis. The orange octahedron is in the plane closest to the viewer, followed by the red, blue, and then magenta octahedra. Reprinted with permission from C. R. Morelock *et al. Chem. Mater.*, 26(5):1936-1940, 2014. Copyright 2014, American Chemical Society.

that is similar to that observed for ReO_3 itself [186]. The lack of NTE in TaO_2F and NbO_2F has prompted further investigation; the near-zero thermal expansion of TaO_2F as a result of O/F site disorder is explored in Chapter 9 [218].

The high-pressure behavior of both NbO_2F and TaO_2F has been examined. NbO_2F was studied using a diamond anvil cell and synchrotron radiation up to 40.1 GPa [219, 220]. Carlson *et al.* determined that NbO_2F transforms from ambient cubic ($Pm\bar{3}m$) to rhombohedral (VF_3-type, $R\bar{3}c$) symmetry at 0.47 GPa, with amorphization observed above 18.5 GPa [219]; the bulk modulus (K_0) of the cubic phase is 24.8 GPa, which drops by a factor of two to 9.6 GPa in the rhombohedral phase [220]. This phase transformation was attributed to tilting of the octahedra around the cubic threefold rotation axis (Figure 1.9), and compression and slight distortion of the $Nb(O/F)_6$ octahedra was also observed [219]. More recently, Cetinkol *et al.* studied TaO_2F using a DAC and synchrotron radiation and observed a transformation to rhombohedral symmetry in this material as well. The phase transition begins around 0.7 GPa and is completed by 4 GPa; a bulk modulus of 36 GPa was measured for cubic TaO_2F, and an average bulk modulus of 60 GPa was measured

for the rhombohedral phase on decompression from 8 to 4 GPa [221]. A very recent high-pressure Raman spectroscopy study of TaO_2F has confirmed the co-existence of both cubic and rhombohedral phases between 0.7 and 4 GPa [222]. In a variable-pressure/temperature study, it was also determined that, upon compression, the CTE of TaO_2F becomes more positive, and the bulk modulus increases upon heating; these effects are possibly due to local structural disorder in the material and the phase transformation at modest pressures [223].

Another ReO_3-type oxyfluoride, $TiOF_2$, was also initially synthesized and characterized several decades ago [224]. Like the above oxyfluorides, $TiOF_2$ also features anion site disorder. The material displays positive thermal expansion, with a transformation from rhombohedral to cubic symmetry on heating to ∼340 K [225].

1.3.3 Metal trifluorides (MF_3)

Many metal trifluorides (MF_3; M = Al, Cr, Fe, Ga, In, Ti, V) are only cubic at elevated temperatures; upon cooling, they adopt a rhombohedrally distorted form of the ReO_3 structure (VF_3-type) [226, 227, 228, 229]. The VF_3-type structure was initially solved by Jack and Gutmann in 1951 [230]. The temperature of the phase transition in MF_3 varies from ∼340 K in TiF_3 to ∼1250 K in CrF_3 [227]. As in the oxyfluorides discussed above, this phase transformation involves the coupled rotation of the constituent MF_6 octahedra (Figure 1.9). The exception to this trend is ScF_3, which remains cubic down to at least 10 K [35].

The thermal expansion behavior of a few ReO_3-type MF_3 has been studied. The unfolding of the rhombohedral phase on heating is accompanied by strongly positive thermal expansion, while the cubic phase shows much lower or even negative thermal expansion. TiF_3 is cubic above ∼340 K [226, 228], and the CTE of the cubic phase is nearly zero [228]. The rhombohedral-to-cubic phase transition in α-AlF_3 (∼730 K [231]) has been studied extensively [227, 231, 232, 233, 234, 235], but its thermal expansion has not been reported in detail. Ravez *et al.* provided some information on the temperature dependence of unit cell volume but did not report expansion coefficients [236]; they reported that both cubic and rhombohedral phases display positive thermal expansion. Chaudhuri *et al.* studied

the mechanism of the cubic-to-rhombohedral phase transition using molecular dynamics simulations and suggested local distortions and NTE above the phase transition temperature [234]. The thermal expansion of α-AlF_3 [237] and InF_3 is further explored in Chapter 4, and that of TiF_3 [238] is discussed in Chapter 6. Materials with the rhombohedral VF_3-type structure are typically highly compressible but do not undergo phase transitions on modest compression [239, 240, 241, 242]. In this structure, the M–F–M links are bent, and further reduction of this bond angle on compression provides an energetically low-cost path for volume reduction, leading to much lower bulk moduli than those observed for materials with the cubic ReO_3 structure, in which these same links are linear.

In contrast to most MF_3, cubic ScF_3 displays isotropic negative thermal expansion over a wide temperature range (at least 10 to 1100 K), with a linear CTE of approximately -14 ppm·K^{-1} between 60 and 110 K [35]. In an inelastic neutron scattering study, Li *et al.* determined that the thermomiotic behavior of ScF_3 has very strong contributions from low-energy phonons close to the R point, some of which involve the motion of bridging F atoms transverse to the Sc–(F)–Sc axis in a quartic potential [243]. A high-pressure X-ray and neutron diffraction study of cubic ScF_3 revealed a phase transition to rhombohedral symmetry between ∼0.5 and 0.8 GPa at ambient temperature, consistent with prior high-pressure micro-Raman work [244, 245, 246]. The critical pressure of ScF_3 was also reported to increase with temperature; for example, at 50 K, ScF_3 becomes rhombohedral at ∼0.15 GPa [35]. This relatively modest critical pressure may limit the use of ScF_3 in composites with PTE components (Chapter 5) [44]. Similar to other ReO_3-type materials, the bulk moduli for the two phases of ScF_3 were reported to be significantly different; K_0 at room temperature changed from 57(3) to 9(3) GPa between the cubic and rhombohedral phases [35, 223]. In an effort to control its CTE, solid solutions of ScF_3 with other MF_3 (M = Ti, Y, Al) are discussed in Chapters 6, 7, and 8, including the effects of cation disorder on both CTE and compressibility [238, 247, 248].

1.4 Overview of thesis

This thesis explores the thermal expansion of ReO_3-type fluorides and oxyfluorides, with particular focus on the effects of disorder and stress on thermal expansion and related properties.

An overview of instrumentation and data analysis methods is given in Chapter 2. Methods for controlling temperature and pressure in X-ray diffraction experiments are introduced. X-ray total scattering, which is used in this thesis to collect data for local structure studies using pair distribution functions (PDFs), and heat capacity measurements are described. Finally, the Rietveld method and PDF analysis are described in some detail. Chapter 3 provides a more detailed discussion of the background-reducing internal mask (BRIM), a device that allows for collection of Rietveld-quality diffraction data with precise control over temperature and pressure and reduction of parasitic scattering from the pressure vessel. The capabilities of the BRIM are demonstrated through studies of ZrW_2O_8 and $Al_2W_3O_{12}$. The BRIM is a critical tool for collecting the high-pressure data presented in Chapters 7 and 8.

The thermal expansion behaviors of two simple ReO_3-type metal trifluorides are explored in Chapter 4. Variable-temperature studies of α-AlF_3 and InF_3 are discussed. The thermal expansion of the rhombohedral and cubic phases in both materials is quantified, and the phase transition temperature is determined.

The limitations of ScF_3 (and other thermomiotic materials) in composites with large CTE mismatch are illustrated in Chapter 5. An unexpected low-temperature phase transition in ScF_3 is observed due to stresses arising from CTE mismatch with a varnish matrix. In an effort to control the thermal expansion of ScF_3, the material is doped with other metal trifluorides, and variable-temperature/pressure X-ray diffraction data are collected. The thermal expansion and pressure-related behavior of these $Sc_{1-x}M_xF_3$ solid solutions are discussed in Chapters 6 (M = Ti), 7 (M = Y), and 8 (M = Al).

The role of anion site disorder in the previously reported near-zero thermal expansion [25] of cubic ReO_3-type oxyfluoride TaO_2F is explored in Chapter 9. The local structure of TaO_2F is probed via X-ray total scattering. The average cubic model, featuring

random O and F distribution, does not adequately describe the local structure of TaO_2F. However, a supercell model featuring ordered –Ta–O–Ta–O–Ta–F– chains along <1 0 0> with different Ta–O and Ta–F distances and O/F off-axis displacements describes the local structure significantly better than does the cubic model.

Finally, overall conclusions and future directions for this work are presented in Chapter 10.

CHAPTER 2

INSTRUMENTATION AND DATA ANALYSIS

In this chapter, experimental methods are presented for both laboratory and synchrotron powder X-ray diffraction (PXRD), introduced in Section 1.1.4.1. Synchrotron *in situ* powder X-ray diffraction and methods of controlling both temperature and pressure are introduced. The background-reducing internal mask (BRIM) is described; this device is discussed in greater detail and applied in later chapters (3, 7, and 8). The theory behind total scattering and experimental methods for data collection are presented. In addition, the experimental measurement of heat capacity is introduced. Finally, data analysis methods are discussed.

2.1 Laboratory X-ray diffraction

The laboratory powder X-ray diffraction data presented herein were collected at the Georgia Institute of Technology (Atlanta, GA, USA) using a Scintag X1 diffractometer (Scintag, Inc.; Cupertino, CA, USA) equipped with a Cu $K\alpha$ tube ($\lambda \approx 1.54$ Å) and Peltier cooled solid state detector. This diffractometer (Figure 2.1a) uses the Bragg-Brentano theta-theta configuration, featuring a stationary sample around which the X-ray source and detector are rotated. Laboratory PXRD was only used herein to check sample purity and estimate ambient lattice parameters prior to synchrotron characterization.

Many of the materials characterized in this thesis are moisture-sensitive; hence, an air-tight sample holder was employed during laboratory PXRD of those materials. This sample holder, fabricated from stainless steel and Kapton film at Georgia Tech, is pictured in Figure 2.1 (b and c). The holder consists of three pieces: a sample tray, base, and top. The base contains an O-ring that allows the sample to be isolated from the ambient atmosphere by tightening outer screws. The sample tray is positioned in such a manner that the sample surface sits at the correct height required by the instrument. The top features a window made of Kapton, a polyimide film that is nearly invisible to X-rays, allowing escape of diffracted radiation from the sample. For proper isolation from moisture, the sample is

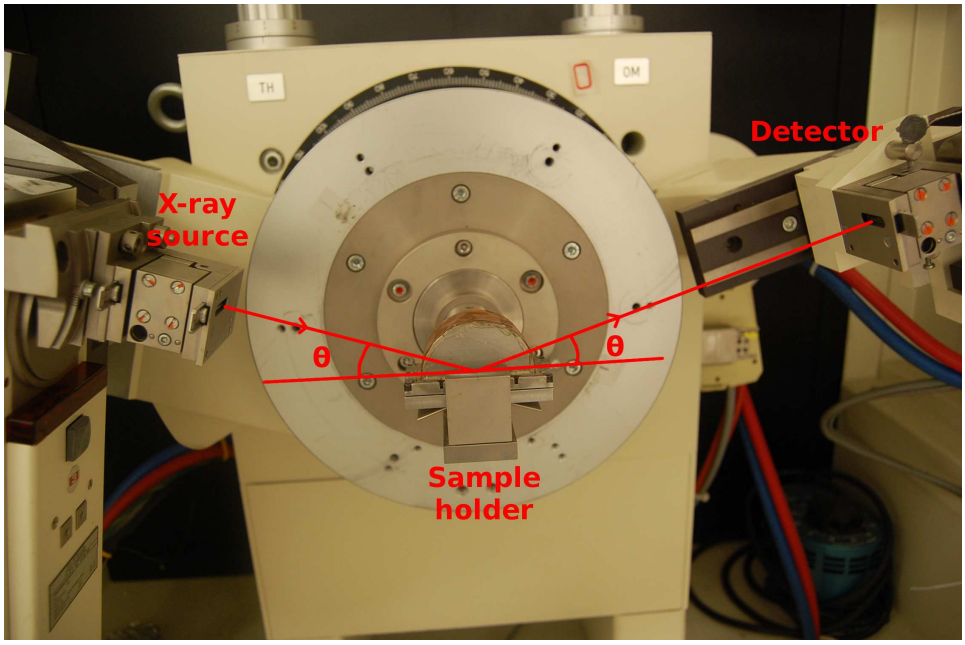

(a)

(b)

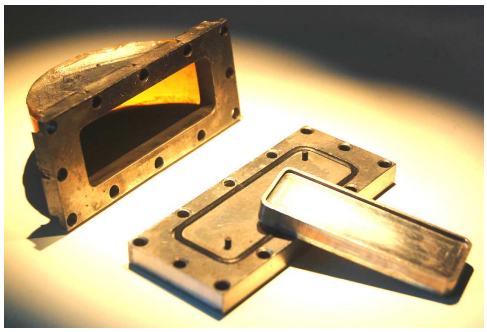

(c)

Figure 2.1: (a) Scintag X1 diffractometer at Georgia Tech, showing the Bragg-Brentano theta-theta configuration. In this configuration, the sample remains fixed while the X-ray source and detector rotate about it at identical angles. (b) Front view of the fully assembled air-tight sample holder for the diffractometer that was used for analysis of moisture-sensitive samples and (c) the three pieces of the diassembled holder (left to right: top, base, sample tray).

loaded in the holder in an inert atmosphere (glove box).

2.2 Synchrotron diffraction

Most of the X-ray diffraction data presented in this thesis were collected at the Advanced Photon Source (APS), a third-generation synchrotron at Argonne National Laboratory, near Chicago, IL, USA. Five different beamlines at the APS were used: 1-BM-C and 17-BM-B (variable-temperature PXRD with a Cryostream or wire-wound furnace), 11-ID-B (variable-pressure/temperature PXRD with the BRIM), 11-BM-B (low-temperature PXRD with a helium cryostat), and 1-ID-C (variable-temperature total scattering).

A synchrotron such as the APS operates under the principle that radiation is emitted when the path of a circulating electron changes. The synchrotron consists of electrons circulating at relativistic speeds (near the speed of light) around an evacuated ring. Devices such as bending magnets (BM), wigglers, and undulators are used to change the path of the electrons, releasing radiation that is then guided through beamlines to experimental stations called hutches.

Synchrotron X-rays are preferred over those available from a laboratory tube source for many structural investigations. Tube sources (such as Cu, Ag, or Mo) offer a limited range of radiation energies, and the X-rays are not very intense. However, the X-rays produced at synchrotrons have very high intensities, and their energies can be tuned over a wide range [249]. The high X-ray energies available at the APS were required for high-pressure studies using a thick titanium pressure vessel. Furthermore, because it has a well-defined time structure, synchrotron radiation can be used for kinetics and other time-related studies. The high intensities of synchrotron X-rays allow for rapid collection of diffraction data; measurements that require hours or days with a laboratory X-ray source can be accomplished in minutes or even seconds at a synchrotron. Therefore, diffraction data may be collected *in situ* while varying temperature or pressure on a reasonable time scale. In this section, methods for controlling temperature and pressure in synchrotron diffraction experiments are discussed.

2.2.1 Variable-temperature synchrotron diffraction

Variable-temperature, ambient-pressure PXRD measurements were conducted at beamlines 1-BM-C, 17-BM-B, and 11-BM-B of the APS.

2.2.1.1 Cryostream and wire-wound furnace

Variable-temperature, ambient-pressure PXRD experiments (100-1200 K) at 1-BM-C and 17-BM-B are summarized in Table 2.1; the results of these measurements are discussed in Chapters 4, 6, 7, and 8. These experiments used either ∼20 (1-BM-C) or ∼17 keV (17-BM-B) X-rays that were selected using a Si (111) double-crystal monochromator. Data were recorded on a PerkinElmer (Waltham, MA, USA) amorphous silicon-based area detector (2048 × 2048, 200 μm pixels). Two methods were used for temperature control: an Oxford Cryosystems Cryostream (Oxford, UK) and a wire-wound furnace. In both methods, the sample is mounted in a flowcell body developed by Chupas *et al.* [250] that is described below.

For measurements between 100 and 500 K, an Oxford Cryosystems Cryostream was used to control temperature. The setup for these experiments, all of which were performed at beamline 1-BM-C, is shown in Figure 2.2. In this setup, the powdered sample is held in a Kapton capillary in the flowcell body without heat shields, furnace elements, or gas flow through the sample. The Cryostream cools or heats the area of the sample in contact with the X-ray beam; for the most accurate temperatures, the Cryostream tip must be ∼5 mm from the sample position. The nitrogen gas temperature is measured by a platinum resistance thermometer located in the gas exchanger portion of the probe, prior to entering the Cryostream nozzle for release onto the sample; the temperature output to the controller is a mapped temperature for the sample position [251]. For each measurement, the sample is packed in a Kapton capillary with outer diameter of 0.86 mm that is sealed with epoxy; for mechanical rigidity, each of these small capillaries is held with glass wool in a Kapton capillary with outer diameter 1.02 mm. For all Cryostream experiments, the following schedule was used, with a rate of 180 K·h^{-1} for temperature ramps: cooling from ambient temperature to 100 K, holding for 15 min, heating to 500 K, holding for 15 min, cooling to

Table 2.1: Summary of variable-temperature, ambient-pressure powder X-ray diffraction experiments at 1-BM-C and 17-BM-B of the Advanced Photon Source. C = Cryostream; F = Furnace.

#	Beamline	λ (Å)	Material	Method	Chapter(s)
1.1	1-BM-C	0.60665	$Sc_{0.90}Y_{0.10}F_3$	C	7
			$Sc_{0.75}Y_{0.25}F_3$	C	7
1.2	1-BM-C	0.60665	ScF_3	C	7
			$Sc_{0.95}Y_{0.05}F_3$	C	7
			$Sc_{0.90}Y_{0.10}F_3$	F	7
2	1-BM-C	0.60650	$Sc_{0.80}Y_{0.20}F_3$	C	7
			$Sc_{0.90}Al_{0.10}F_3$	C	8
3	1-BM-C	0.60570	$Sc_{0.95}Al_{0.05}F_3$	C	8
			$Sc_{0.85}Al_{0.15}F_3$	C	8
			$Sc_{0.80}Al_{0.20}F_3$	C	8
			$Sc_{0.75}Al_{0.25}F_3$	C	8
			$Sc_{0.70}Al_{0.30}F_3$	C	8
			$Sc_{0.60}Al_{0.40}F_3$	C	8
			$Sc_{0.50}Al_{0.50}F_3$	C	8
			$Sc_{0.70}Ti_{0.30}F_3$	C	6
			$Sc_{0.50}Ti_{0.50}F_3$	C	6
			$Sc_{0.30}Ti_{0.70}F_3$	C	6
			$Sc_{0.95}Y_{0.05}F_3$	F	7
			$Sc_{0.80}Y_{0.20}F_3$	F	7
			$Sc_{0.75}Y_{0.25}F_3$	F	7
4	1-BM-C	0.61072	$Sc_{0.90}Ti_{0.10}F_3$	C	6
			$Sc_{0.60}Ti_{0.40}F_3$	C	6
			$Sc_{0.40}Ti_{0.60}F_3$	C	6
			$Sc_{0.15}Ti_{0.85}F_3$	C	6
			TiF_3	C	6
5	1-BM-C	0.61610	ScF_3	C	6, 8
			ScF_3	F	8
			$Sc_{0.85}Al_{0.15}F_3$	F	8
			$Sc_{0.70}Al_{0.30}F_3$	F	8
			$Sc_{0.60}Al_{0.40}F_3$	F	8
6	17-BM-B	0.72910	$Sc_{0.90}Al_{0.10}F_3$	F	8
			$Sc_{0.75}Al_{0.25}F_3$	F	8
			$Sc_{0.50}Al_{0.50}F_3$	F	8
			InF_3	F	4
7	17-BM-B	0.7270	α-AlF_3	F	4

100 K, holding for 15 min, and finally heating to ambient temperature (Figure 2.2b).

High-temperature (>323 K) data were collected at 1-BM-C and 17-BM-B using a wire-wound furnace (Figure 2.3). The Chupas flowcell body was used with two heating elements attached and a thermocouple placed close to the X-ray beam position; each heating element was made from Kanthal A-1 resistive wire wound around a ceramic tube, and sample temperature was monitored by a sheathed K-type thermocouple (Omega Engineering, Stamford, Connecticut, USA) [250]. Heat shields were placed on the flowcell body to both protect the detector and keep heat close to the sample. The samples were held in fused quartz capillaries under slowly flowing He. Figure 2.3a shows an assembled flowcell with heating elements and thermocouple attached, and Figure 2.3b shows the furnace experimental setup with heat shields in place and gas input/output lines attached. During furnace experiments, temperature was increased at 180 $K \cdot h^{-1}$ without cooling.

2.2.1.2 Helium cryostat

Low-temperature high-resolution synchrotron powder diffraction data were collected for ScF_3 (Chapter 5) using beamline 11-BM-B at the APS, with an average wavelength of 0.413 Å [252, 253]. A mixture of NIST standard reference materials Si (SRM 640c) and Al_2O_3 (SRM 676) was used to calibrate the instrument, in which the Si lattice constant determined the wavelength for each detector.

An Oxford Instruments closed-flow helium cryostat (OptistatCF with exchange gas) was used as a sample environment. The sample stick for this device is pictured in Figure 2.4. In this device, temperature is controlled by a combination of manual helium flow control and power dissipated in an electrical heater, both of which are regulated by a temperature controller; the temperature is monitored by a rhodium iron temperature sensor located on the heat exchanger. Data were collected at 14 K intervals when heating from the base temperature (∼6 K) to 146 K, filling in the gaps upon cooling, which resulted in data for every 7 K; data were also collected at 230 and 300 K afterwards. An equilibration time of 15 min was used for each temperature point.

An Oxford Instruments Cryostream 700 Plus N_2 gas blower was also used at 11-BM-B.

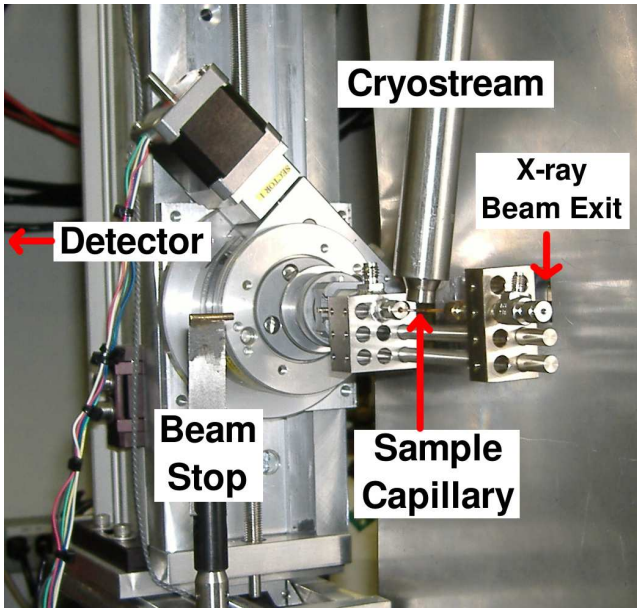

(a)

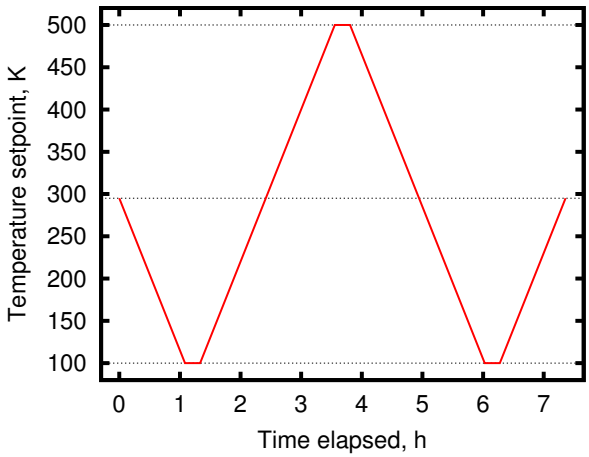

(b)

Figure 2.2: (a) Experimental setup for variable-temperature PXRD measurements with the Cryostream at beamline 1-BM-C of the Advanced Photon Source. The sample is held in a Kapton capillary that is loaded in the flowcell body (without furnace elements, heat shields, or gas flow) mounted on a goniometer. The Cryostream cools/heats the area of the sample in the X-ray beam path. X-rays enter from the right of the photo, diffract from the sample, and reach the detector, which is off-camera to the left. (b) Heating and cooling schedule used for all Cryostream experiments.

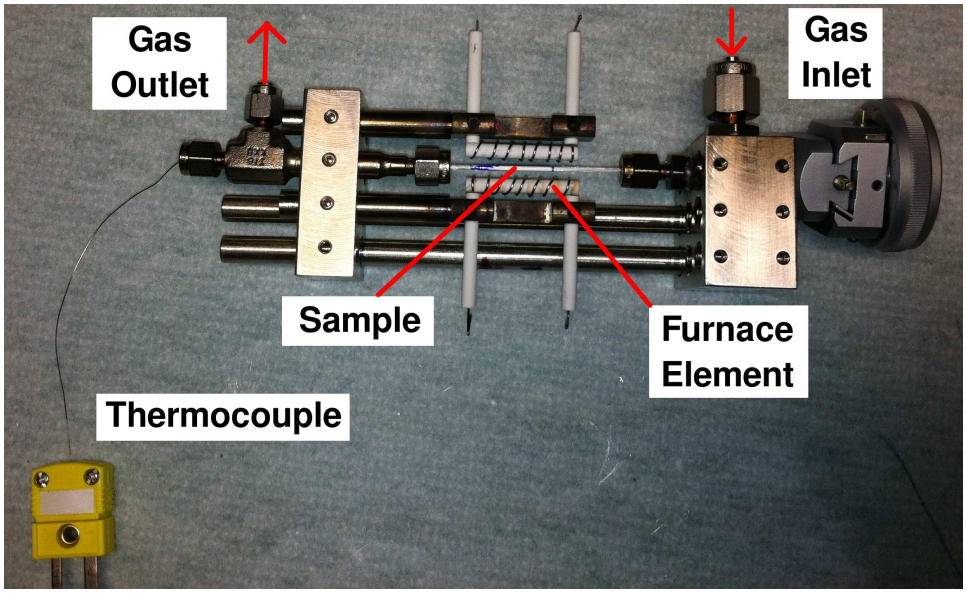

(a)

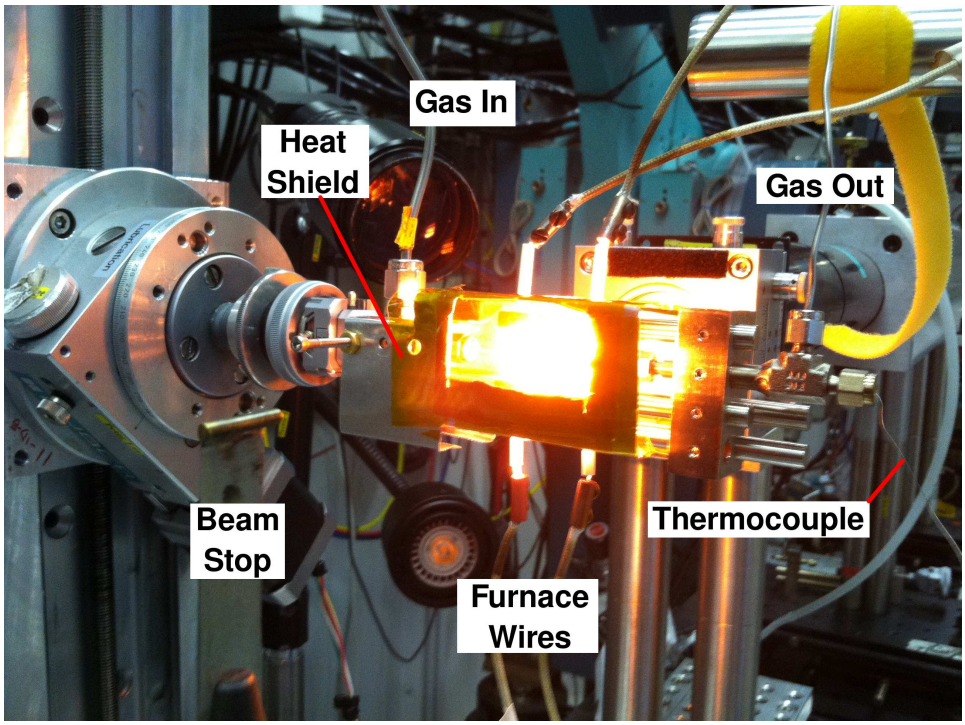

(b)

Figure 2.3: Wire-wound furnace used for high-temperature PXRD at beamlines 1-BM-C and 17-BM-B of the Advanced Photon Source. (a) Flowcell body with heating elements attached and thermocouple inserted. (b) Furnace experimental setup, photographed when heated to ∼1100 K.

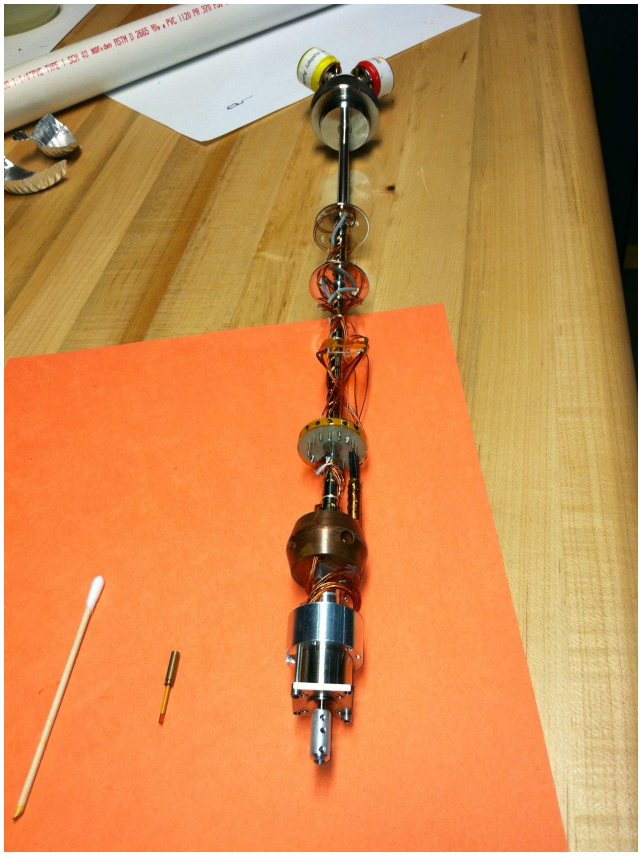

Figure 2.4: Helium cryostat sample stick used at beamline 11-BM-B of the Advanced Photon Source. The sample capillary, shown at left, is placed at the end of the stick at the bottom of the image.

Table 2.2: Specifications of the four BRIM designs. The outer diameter (OD) and inner diameter (ID) listed are those of the titanium pressure vessel. The ID of the pressure vessel is approximately equal to the OD of the BRIM itself. P_{max} is the maximum pressure limit of the setup.

BRIM	OD (mm)	ID (mm)	P_{max} (MPa)	Chapter(s)	Refs.
MK2BRIM_138	∼14.3	∼7.9	∼138	3	[254]
MK2BRIM_276	∼14.3	∼6.4	∼276	3,7	[93, 247, 254]
MK3BRIM_276	∼14.3	∼6.4	∼276	None	[93]
MK3BRIM_414	∼14.3	∼4.8	∼414	8	[95, 248]

For these measurements, data were collected while heating in 10 K intervals from 100 to 160 K and then in 20 K intervals up to 300 K.

2.2.2 Variable-pressure synchrotron diffraction[1]

The variable-pressure PXRD studies presented in this thesis make use of the background-reducing internal mask [254]. Initial evaluation of the BRIM concept is presented in Chapter 3, and the device is applied to the study of new materials in Chapters 7 and 8. In this section, the high-pressure setup and specifications of the various BRIM designs (Table 2.2) are described.

Variable-pressure/temperature PXRD measurements were conducted on beamline 11-ID-B at the Advanced Photon Source; the experiments are summarized in Table 2.3, including samples examined and BRIM designs used. High-energy X-rays (∼58 keV, $\lambda \approx 0.2127$ Å) were selected to provide adequate penetration of the sample environment (described below), dispersion of the diffraction from the sample under study, attenuation by the BRIMs, and incident intensity. Data were recorded on a PerkinElmer amorphous silicon-based area detector (2048 × 2048, 200 μm pixels). Parameters, including the position of the detector, its tilt angle relative to the beam, and its distance from the sample, were determined with the aid of a CeO_2 calibrant (Section 2.4.2.1).

[1]The work presented in this subsection has been previously published and is edited to fit the context of this thesis. Reproduced from ref. [93] with permission from the PCCP Owner Societies. Reprinted with permission from L. C. Gallington *et al. J. Appl. Phys.*, 115(5):053512, 2014 (ref. [95]). Copyright 2014, AIP Publishing LLC. Reproduced from ref. [254] with permission of the International Union of Crystallography.

Table 2.3: Summary of variable-pressure/temperature PXRD experiments at 11-ID-B of the Advanced Photon Source.

#	λ (Å)	Material	BRIM	Chapter(s)
B1	0.21270	ZrW_2O_8	MK2BRIM_138	3
		$Al_2W_3O_{12}$	MK2BRIM_276	3
B2	0.21280	ScF_3	MK2BRIM_276	7, 8
		$Sc_{0.90}Y_{0.10}F_3$	MK2BRIM_276	7
B3	0.21280	$Sc_{0.95}Y_{0.05}F_3$	MK2BRIM_276	7
		$Sc_{0.80}Y_{0.20}F_3$	MK2BRIM_276	7
		$Sc_{0.75}Y_{0.25}F_3$	MK2BRIM_276	7
B4	0.21270	$Sc_{0.95}Al_{0.05}F_3$	MK3BRIM_414	8
		$Sc_{0.90}Al_{0.10}F_3$	MK3BRIM_414	8
		$Sc_{0.85}Al_{0.15}F_3$	MK3BRIM_414	8
		$Sc_{0.80}Al_{0.20}F_3$	MK3BRIM_414	8
		$Sc_{0.70}Al_{0.30}F_3$	MK3BRIM_414	8
		$Sc_{0.60}Al_{0.40}F_3$	MK3BRIM_414	8

2.2.2.1 High-pressure sample environment

Figure 2.5 shows the general arrangement of the pressure vessel and heater block that was used for BRIM experiments. The samples were contained inside a vertically mounted Grade 5 titanium pressure tube, purchased from the High-Pressure Equipment Company (HiP), Erie, Pennsylvania, USA. Threaded and coned tubes ("pipe nipples") of various dimensions were used (Table 2.2), and the ends of these tubes were capped using Grade 5 Ti fittings from HiP. The system was pressurized using a silicone oil medium and a hand-driven syringe pump. Care was taken to rigidly restrain the pressure vessel and minimize strain from the plumbing so that the vessel position did not move during a sequence of measurements, as such movement would lead to changes in the sample-to-detector distance that would be significant (tens of micrometers) when trying to determine precise bulk moduli. An aluminum heater block, equipped with four 50 W, 110 V cartridge heaters, was clamped around the pressure vessel, and temperature was monitored by two K-type thermocouples sheathed in Kapton whose junctions were placed in holes in the heater block. A temperature calibration curve for the apparatus was created by comparing the controller set point with that measured by a thermocouple secured within a Kapton tube at the sample position; the temperature at the sample position varied from that of the heater block by only a few

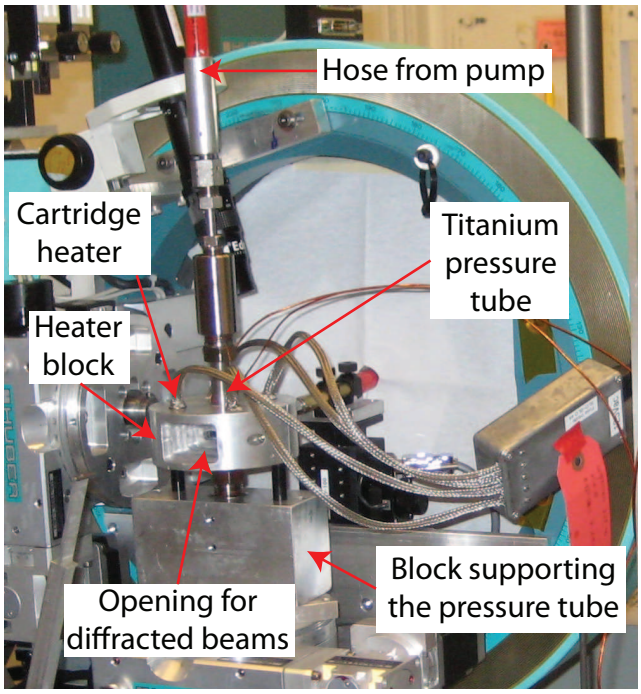

Figure 2.5: General arrangement of the titanium pressure vessel and heater block for BRIM experiments. Reproduced with permission of the International Union of Crystallography from ref. [254].

Kelvin, even at the maximum experimental temperature of ~540 K [93, 95].

2.2.2.2 Background-reducing internal mask (BRIM)

Four different BRIM designs have been manufactured, three of which are used in this thesis; the four are summarized in Table 2.2 and shown in Figure 2.6. All BRIM bodies were made from a machinable tungsten alloy using electrode discharge machining (EDM) to cut the required slots. The blade that serves as a beam stop was cut by EDM from a tungsten (rhenium) sheet and then positioned in its slot on the MK2BRIM (MK3BRIM) body with the aid of a high-temperature epoxy resin.

The BRIM design concept is shown in Figure 2.7. Two versions of the MK2BRIM design were created, differing in their maximum pressures (138 MPa for MK2BRIM_138 and 276 MPa for MK2BRIM_276). In this design, the hole parallel to the BRIM axis for the sample capillary is located on-axis, and the BRIM body fits snugly inside the pressure vessel body. Scattering from the upstream wall of the pressure vessel is largely stopped by the highly absorbing tungsten BRIM body, but some is observed on the detector at

Figure 2.6: Blade-side view of the four BRIM designs, with a penny for scale. Left to right: MK2BRIM_138, MK2BRIM_276, MK3BRIM_276, MK3BRIM_414.

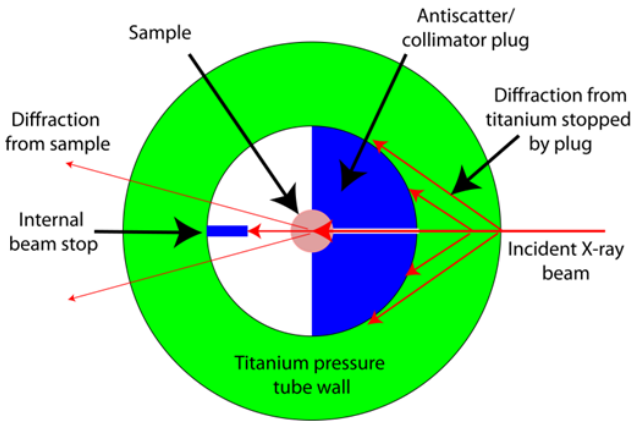

Figure 2.7: Schematic cross-section through the MK2BRIM, sample, and pressure tube at X-ray beam height. The tungsten components of the BRIM are in blue. Reproduced with permission of the International Union of Crystallography from ref. [254].

low angles (Figure 2.8a). The extent to which this scattering contaminates the recorded diffraction data depends upon the dimensions of the incident-beam slit in the BRIM and its length along the beam path. Much of this parasitic scattering could be excluded from the final one-dimensional diffraction patterns by use of a well-chosen mask during integration of the two-dimensional image using *FIT2D* [255] (Section 2.4.2.1). The beam stop blade prevents X-rays from hitting the downstream wall of the pressure vessel. However, as it is located close to the sample (∼1.25 mm), the blade also obscures some scattering from the sample at low angles. The utility of the low-angle part of a diffraction pattern is degraded by residual scattering from upstream titanium and a reduction in sample scattering due to the width of this blade combined with its position close to the sample. For both MK2BRIMs, shadowing of the sample scattering by the beam stop blade is expected to occur below $2\theta \approx 11.5°$. However, diffraction data recorded with the MK2BRIMs were found to be useful for Rietveld analyses, without correction, at lower 2θ than this supposed minimum. At Bragg angles close to the onset of shadowing, little of the sample scattering volume lies "behind" the beam stop blade. In the case of the MK2BRIM_138, with a 0.5-mm-wide by 1.9-mm-deep beam stop blade and an ∼0.3-mm-wide by ∼3.2-mm-long incident-beam slit, the diffraction data above $2\theta \approx 8°$ ($d < 1.55$ Å) were used for Rietveld analyses, and there was no titanium scattering apparent in the patterns. In the case of the MK2BRIM_276, with a 0.5-mm-wide by 1.2-mm-deep beam stop blade and an ∼0.3-mm-wide by ∼2.4-mm-long incident-beam slit, the diffraction data above $2\theta \approx 8°$ ($d < 1.55$ Å) were similarly used for Rietveld analyses, but there was some minor residual titanium scattering in the patterns (Figure 2.8).

The MK3BRIM design (Figure 2.6) is an improvement of the MK2BRIM design. Two versions of MK3BRIM were created ($P_{max} = 276$ MPa for MK3BRIM_276 and 414 MPa for MK3BRIM_414). This design delivers much better data quality at low scattering angles by using a smaller sample tube diameter that is offset from the BRIM axis to give greater distance between the internal beam stop rhenium blade and the sample; the design also has a narrower X-ray entrance slit. Another improvement of the MK3BRIM design is coil springs that prevent the BRIM from moving in the pressure vessel after being pushed into

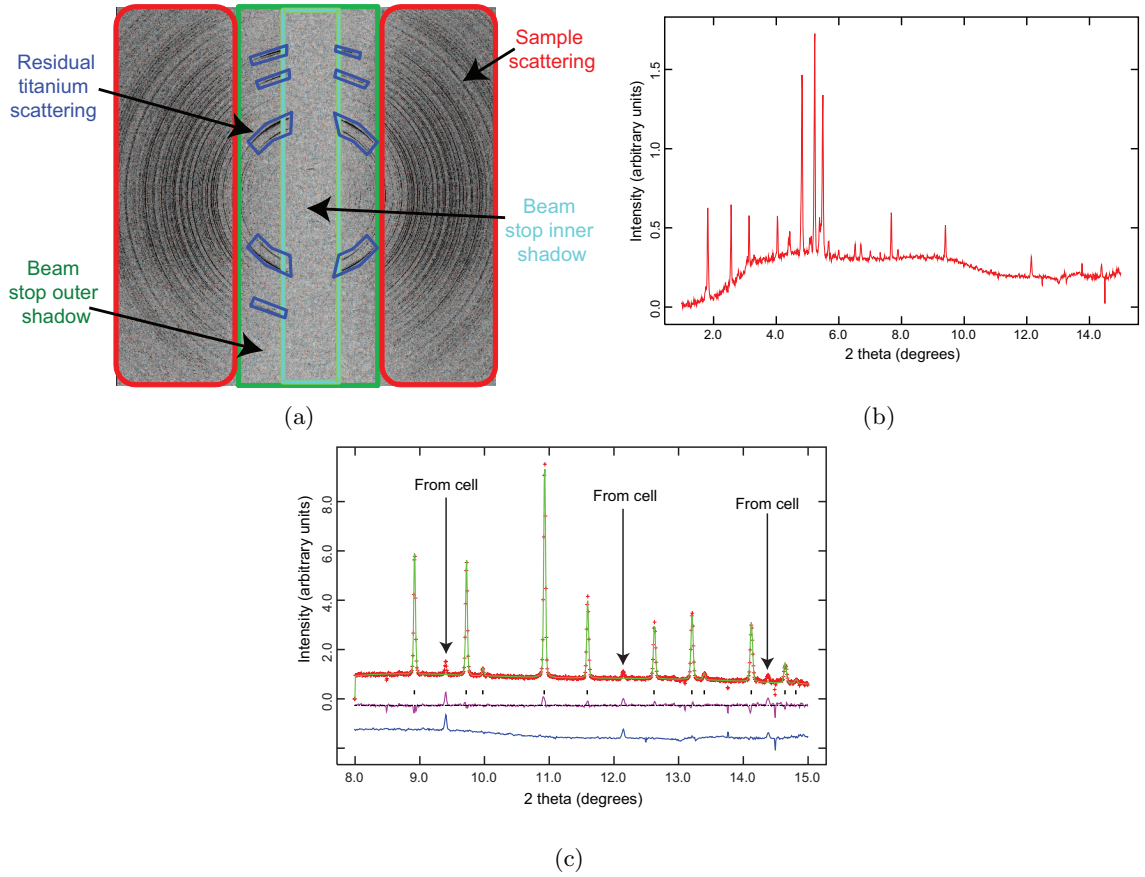

Figure 2.8: (a) Image recorded from cubic ZrW_2O_8 in the MK2BRIM_138. Some scattering from the upstream titanium vessel wall is apparent at low angles. (b) Background scattering from a silicone oil-filled pressure vessel, equipped with a MK2BRIM_276, without a sample present. (c) Rietveld fit to data from CaF_2 in an oil-filled vessel equipped with a MK2BRIM_276. Parasitic scattering from Ti is weak compared with that of the sample. The purple line is the Rietveld difference curve, and the blue line is a scaled section of the empty-cell data shown in (b). The diffraction patterns shown in (b) and (c) were integrated in *FIT2D* using the same mask. Reproduced with permission of the International Union of Crystallography from ref. [254].

place [93].

2.2.2.3 Sample preparation

A paste made from finely ground powder and silicone oil was placed in a short Kapton capillary that had been sealed at one end using a high-temperature epoxy resin. The Kapton capillary was chosen so that its size matched the inner bore of the BRIM. The capillary was centrifuged so that the powder formed a dense column and any bubbles were eliminated. If a taller column were needed, excess oil was removed, and more paste was added; the capillary was then centrifuged again.

2.2.2.4 Alignment of BRIM inside pressure vessel

For both BRIM designs, a stainless steel tube spacer was placed in the bottom of the pressure vessel to support the BRIM at the correct height. After adding silicone oil to just cover the top of the stainless steel tube, a BRIM containing the sample was slid into the pressure vessel. The BRIM was roughly aligned with a screwdriver-like device engaged in the top slot on the BRIM, so that its incident-beam slit and collimator blade lay parallel to the beam direction. The vessel was then filled with oil and sealed.

An initial X-ray alignment of the BRIM was performed with a PIN diode monitoring the transmitted beam. The bottom of the $\perp$-shaped slot was located and positioned at beam height. A combination of scans, translating the pressure vessel across the X-ray beam and rotating it around its axis, was used to center the beam stop blade approximately in the X-ray beam and align it parallel to the beam direction. The pressure vessel was then lowered so that the incident X-ray beam passed through the vertical narrow slot at the top of the $\perp$. Final adjustments to the orientation and position of the BRIM were made so that the diffraction image from the sample was clean and symmetrical, with equivalent intensities to the left and right of the beam stop blade shadow.

2.2.3 X-ray total scattering and pair distribution functions

Traditional diffraction patterns of crystalline materials feature sharp Bragg peaks that arise from long-range order. Information about the average (crystal) structure of a material can

be determined from analysis of these peaks. However, diffraction patterns also contain diffuse scattering, which is modeled as part of the background in Rietveld analyses of the data. The diffuse scattering contains information about short-range order and hence the local structure of a material. In the X-ray (or neutron) total scattering approach, Bragg and diffuse scattering are combined to calculate atomic pair distribution functions (PDFs). These functions are defined in real space (as opposed to reciprocal space) in terms of actual interatomic separations. The ability to explore short-range order makes this approach especially well-suited for materials without long-range order, such as liquids or amorphous solids [256]. Either X-rays or neutrons may be used for PDF studies; X-ray total scattering is used in Chapter 9 to examine the local structure of TaO_2F, so only X-rays are discussed here. In this subsection, the theory behind pair distribution functions and experimental methods for data collection are introduced.

2.2.3.1 Pair distribution and structure functions, $G(r)$ and $S(Q)$

The atomic pair distribution function, $G(r)$, is the Fourier transform of the total scattered X-ray intensity function, $S(Q)$, as follows:

$$G(r) = \frac{2}{\pi} \int_{Q=0}^{Q_{max}} Q[S(Q) - 1] \sin(Qr) dQ, \tag{2.1}$$

in which momentum transfer Q is related to wavelength λ and angle 2θ by:

$$Q = \frac{4\pi \sin\theta}{\lambda}. \tag{2.2}$$

The typical units for Q are Å^{-1}. The $Q[S(Q) - 1]$ part of Equation 2.1 is known as the reduced structure function, $F(Q)$.

$G(r)$ is a function of radial distance r also defined as

$$G(r) = 4\pi r[\rho(r) - \rho_0], \tag{2.3}$$

where ρ_0 is the average atomic number density and $\rho(r)$ is the atomic pair density. The PDF gives information about the number of atoms in a spherical shell of unit thickness at some distance r from a reference atom [256]. The peaks in $G(r)$ occur at real interatomic

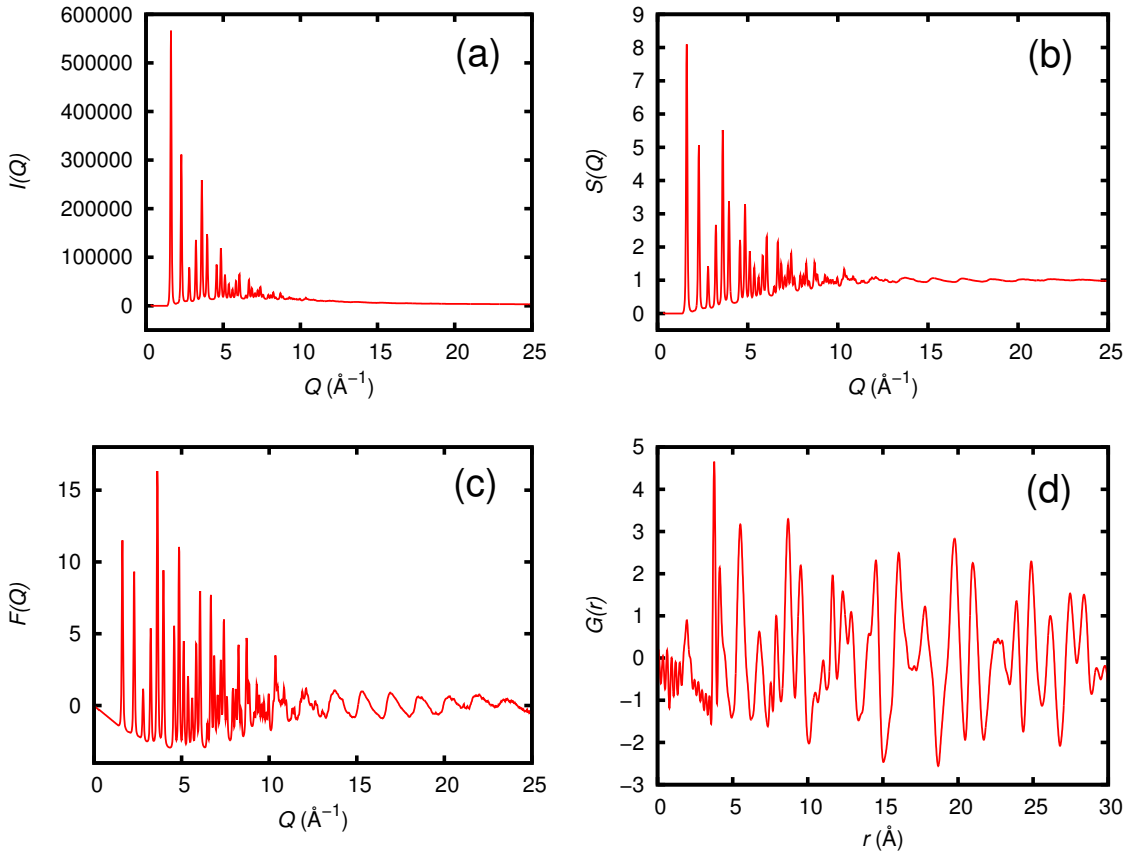

Figure 2.9: Examples of (a) $I(Q)$, (b) $S(Q)$, (c) $F(Q)$, and (d) $G(r)$. These plots are derived from total scattering data for TaO_2F at 328 K.

distances, while peak integrated intensities and widths are related to coordination number and thermal or static disorder, respectively.

The structure function, $S(Q)$, is derived from the measured coherent X-ray scattering intensity $I^{coh}(Q)$ from a sample (corrected for background and other experimental effects and normalized by the flux and number of atoms in the sample):

$$S(Q) = 1 + \frac{I^{coh}(Q) - \sum a_i |f_i(Q)|^2}{|\sum a_i f_i(Q)|^2}, \tag{2.4}$$

where a_i and f_i are the atomic concentration and X-ray atomic form factor, respectively, for atom type i.

Figure 2.9 shows example plots of $I(Q)$, $S(Q)$, $F(Q)$, and $G(r)$, derived from total scattering data for TaO_2F at 328 K.

2.2.3.2 Experimental information

One necessary experimental feature to obtain high real-space resolution in a PDF is the ability to measure to high values of Q. Ideally, Q_{max} should be greater than 30 Å^{-1}, so X-rays of at least ∼45 keV should be used for proper total scattering measurements. Although laboratory sources such as Mo and Ag can provide the proper X-ray energies, the much higher energies available at synchrotron sources are preferred for high-resolution total scattering measurements [256]. Recent growing interest in disordered materials has led to the development of dedicated high-energy beamlines (∼87 keV is possible at beamline 11-ID-B of the APS) and the means for rapid acquisition of total scattering data with a two-dimensional detector [257, 258]. With high-energy X-rays and the right detector instrumentation, a high-quality PDF may be obtained with only a few seconds of data collection; this process previously took hours, even at a synchrotron. The ability to quickly obtain total scattering data also makes possible the study of local structural changes with temperature or pressure [259].

In the study of TaO_2F presented in Chapter 9, variable-temperature (80-441 K) X-ray total scattering data were collected[2] at beamline 1-ID-C of the Advanced Photon Source (λ = 0.18505 Å) using an Oxford Cryosystems Cryostream. The sample was held in a Kapton capillary while 2D diffraction images were recorded on a General Electric amorphous silicon-based detector [260]. CeO_2 (NIST SRM 674a) was used for calibration, and scattering from an empty Kapton capillary was used for background subtraction.

Analysis of total scattering data is described in Section 2.4.3.

2.3 Heat capacity measurements

All heat capacity measurements (Chapter 7) were accomplished with a Physical Property Measurement System (PPMS) model 6000 from Quantum Design (San Diego, California, USA), a commercial relaxation calorimeter located in the laboratory of Prof. M. A. White

[2]The total scattering data were collected by G. J. Halder.

at Dalhousie University (Halifax, Nova Scotia, Canada)[3]. This calorimeter determines heat capacity at constant pressure (C_P) by measuring the heat (q) added or removed from a sample with change in temperature:

$$C_P = \left(\frac{dq}{dT}\right)_P. \tag{2.5}$$

From C_P, the heat capacity at constant volume (C_V), which is used in the Grüneisen relationship (Equation 1.11), may be calculated if the volume CTE (α_V) and isothermal bulk modulus (K_T) are known; in an isotropic system,

$$C_V = C_P - \alpha_V^2 K_T T V, \tag{2.6}$$

where T and V are temperature and volume, respectively [1]. The typical units for heat capacity are $\mathrm{J{\cdot}K^{-1}}$.

For heat capacity measurements of ScF_3 and $Sc_{1-x}Y_xF_3$, samples (∼1 mm thick) were broken into small shards (<3 mm × 3 mm) and affixed to the measurement platform with a grease that served as the thermal couplant. The heat capacities were measured from 2 to 300 K using a ^{4}He cryostat and Apiezon® N grease, from 275 to 390 K using a ^{4}He cryostat and Apiezon® H grease, and from 0.35 to 10 K using a ^{3}He cryostat and Apiezon® N grease. All reported data points met reliability criteria (≥90% thermal coupling constant between sample and platform and ≥40% sample contribution to total heat capacity). Temperature was monitored and controlled by a Cernox™ sensor (Lake Shore Cryotronics, Westerville, Ohio, USA) and thin-film resistive RuO platform heater attached directly to the bottom side of the sample platform and connected to the puck frame by eight small thermally conductive wires.

For more details concerning the proper measurement of heat capacity with a PPMS, please consult the work of Lashley *et al.* [261] and Kennedy *et al.* [262].

2.4 Data analysis

In this section, the data analysis methods that are employed in the thesis are discussed.

[3]Heat capacity data were collected by C. A. Romao and M. B. Johnson of Dalhousie University and the author.

2.4.1 Phase identification from powder diffraction data

The program *JADE* from Materials Data, Inc. (Livermore, CA, USA), with the ICDD (International Center for Diffraction Data) *PDF* database, was used for phase identification in powder samples.

2.4.2 Synchrotron diffraction data

In this subsection, methods for analyzing synchrotron powder diffraction data, including integration of two-dimensional diffraction images, correction of patterns for angular distortion, and Rietveld analysis, are discussed.

2.4.2.1 Diffraction image collection and integration

Two-dimensional synchrotron powder diffraction images were collected on an area detector (Figure 2.10a) at the Advanced Photon Source and processed using the program *QXRD*. Diffraction is observed as a collection of concentric rings (Figure 2.10b), which represent the intersection of Debye-Scherrer cones (Section 1.1.4.1) with the plane of the detector. The radii of these diffraction rings contain information about diffraction angles; integration of the intensity of a given ring yields the intensity of a particular Bragg peak at some angle. For integration, the ring center coordinates (the "beam center") on the detector must be known (represented by parameters x_C and y_C). Furthermore, this integration process is not simply integration around a circle, as the detector is not perfectly aligned perpendicular to the incident beam; therefore, the diffraction rings are slightly elliptical in shape. To describe the shape and orientation of these ellipses for integration, two parameters must be known: the angle between the principal axes of the ellipses and the coordinate axes of the image in the detector plane (the "tilt plane rotation angle", ϕ_{TPR}) and the angle between the normal of the detection plane and the direction of the incident beam (the "tilt angle", ϕ_T), which can also be viewed as the non-orthogonality of the detector plane. Finally, for integration in units of 2θ, two additional parameters must be known: the wavelength of the incident beam (λ) and the distance between the sample and detector (d_{SD}). Figure 2.11 illustrates these six parameters graphically. With the program *FIT2D* [255], samples

Table 2.4: Parameters for *FIT2D* integration of diffraction data collected on an area detector at the Advanced Photon Source: λ is the incident X-ray beam wavelength, x_C and y_C are the x- and y-coordinates (in pixels) of the beam center, respectively, d_{SD} is the sample-to-detector distance, and ϕ_{TPR} and ϕ_T are the detector tilt plane rotation angle and tilt angle, respectively. Beamtime labels (#) are defined in Tables 2.1 and 2.3, and parameters are defined in Figure 2.11.

#	**Calibrant(s)**	λ **(Å)**	x_C **(px)**	y_C **(px)**	d_{SD} **(mm)**	ϕ_{TPR} (°)	ϕ_T (°)
B1	CeO_2	0.21270	1052.292	1032.517	888.738	58.810	0.100
B2	CeO_2	0.21280	1055.647	1033.015	830.000	-113.344	-0.137
B3	CeO_2	0.21280	1056.169	1032.230	798.000	73.551	0.233
B4	CeO_2	0.21270	1056.683	1033.117	884.500	-112.391	-0.293
1.1	LaB_6	0.60665	1024.933	1018.871	249.895	32.316	-0.225
1.2	LaB_6	0.60665	1024.707	1018.831	249.880	31.365	-0.220
2	LaB_6	0.60650	1023.529	1018.118	250.040	34.530	-0.228
3	LaB_6	0.60570	1028.018	1017.790	248.551	35.145	-0.221
4	LaB_6 + CeO_2	0.61072	1035.298	1027.861	249.724	38.252	-0.187
5	LaB_6	0.61610	1032.461	1026.086	249.430	-153.073	0.175
6	LaB_6	0.72910	1024.966	1031.201	251.071	-52.519	-0.099
7	LaB_6	0.72700	1021.790	1028.938	300.691	-29.913	-0.116

of NIST standard reference materials, either LaB_6 (NIST SRM 660a) or CeO_2 (NIST SRM 674), were used to calibrate these parameters, which are listed for each beamtime in Table 2.4. After applying a custom mask to eliminate shadowing from the beam stop and other artifacts, the two-dimensional diffraction images were integrated with *FIT2D* using the appropriate parameters to produce a one-dimensional diffraction pattern (intensity *versus* angle, Figure 2.10c) and converted into an appropriate format for further analyses using *CMPR* [263].

2.4.2.2 Correction of angular distortion

Angular distortions were observed in the integrated diffraction patterns from variable-temperature, ambient-pressure experiments at 1-BM-C and 17-BM-B that were possibly associated with the oblique incidence of the X-ray beam on the relatively thick active layer of the detector. These distortions were corrected prior to Rietveld analysis (discussed below) using a calibration curve derived from the measured and expected peak positions for a standard LaB_6 sample ($2\theta_{actual}$ and $2\theta_{expected}$, respectively). Figure 2.12a shows a Rietveld fit to uncorrected LaB_6 data; the fit is poor ($R_{wp} = 0.1820$) due to shifted peak positions.

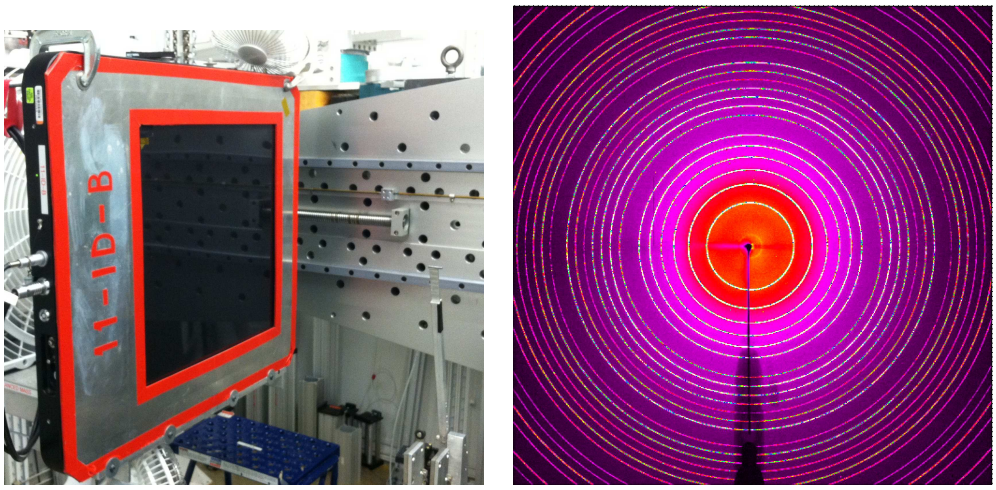

(a) (b)

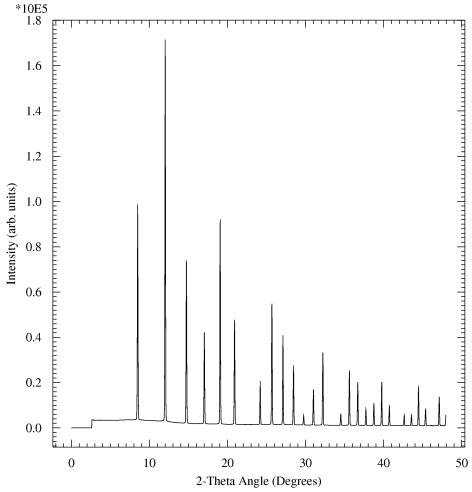

(c)

Figure 2.10: (a) Two-dimensional synchrotron diffraction images are collected on an area detector. (b) These diffraction images consist of concentric Debye-Scherrer rings. (c) With *FIT2D*, the 2D images are integrated to create a 1D diffraction pattern. The data shown here are from an LaB_6 sample (NIST SRM 660a).

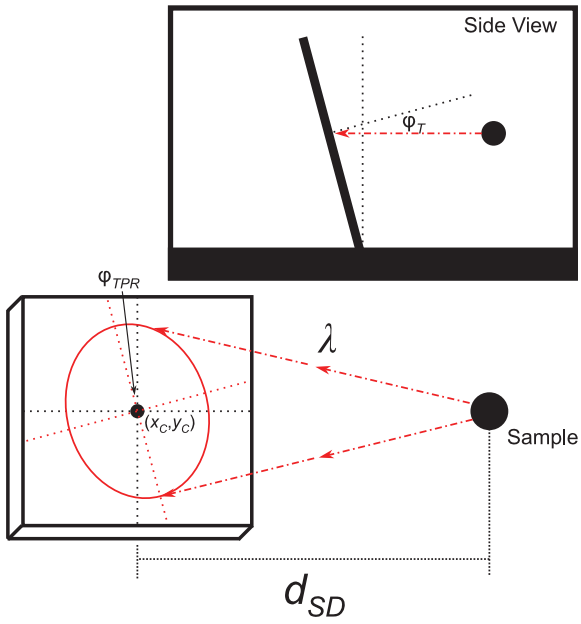

Figure 2.11: Parameters for *FIT2D* integration of diffraction data collected on an area detector. Only one diffraction ring is shown for simplicity. The figure is not to scale; some sizes, angles, and distances are exaggerated for emphasis. Parameter definitions: d_{SD} = sample-to-detector distance, λ = incident X-ray beam wavelength, (x_C,y_C) = coordinates of the beam center on the detector, ϕ_{TPR} = detector tilt plane rotation angle, ϕ_T = detector tilt angle.

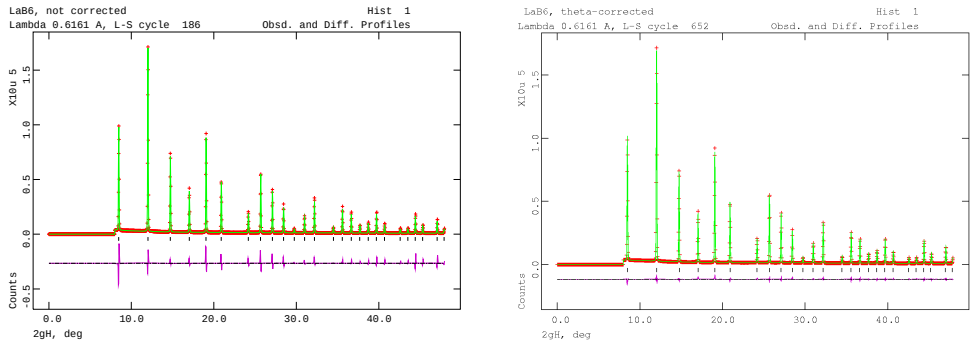

(a) (b)

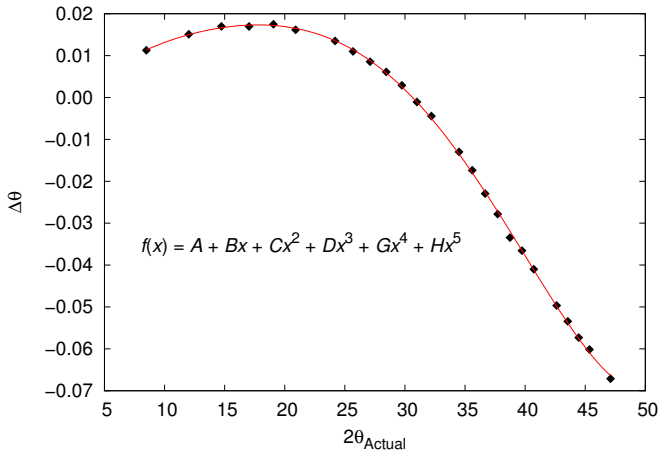

(c)

Figure 2.12: Rietveld fits to a diffraction pattern for LaB_6 (a) before and (b) after correction for angular distortion. An example $\Delta\theta$ *versus* $2\theta_{actual}$ correction curve is shown in (c).

An example of the calibration curve appears in Figure 2.12c; this curve is a fifth-order polynomial fit to $\Delta\theta$ *versus* $2\theta_{actual}$ of each LaB_6 Bragg peak, where $\Delta\theta = 2\theta_{expected} - 2\theta_{actual}$. The coefficients of this correction curve $f(x) = A + Bx + Cx^2 + Dx^3 + Gx^4 + Hx^5$ are listed in Table 2.5 for each beamtime, and an example of a Rietveld fit to corrected LaB_6 data appears in Figure 2.12b; the fit is significantly improved ($R_{wp} = 0.0340$). Furthermore, the lattice parameter calculated from corrected LaB_6 data ($a = 4.156892(18)$) is in significantly better agreement with the NIST SRM value ($a = 4.1569162(97)$) [264] than that calculated from uncorrected data ($a = 4.150856(105)$).

Table 2.5: Coefficients of the angular distortion correction curve $f(x) = A + Bx + Cx^2 + Dx^3 + Gx^4 + Hx^5$ for each beamtime. Beamtime labels (#) are defined in Tables 2.1 and 2.3.

#	A	B	C	D	G	H
1.1	-7.56864×10^{-3}	3.81208×10^{-3}	-3.27496×10^{-4}	1.63516×10^{-5}	-4.31714×10^{-7}	3.99548×10^{-9}
1.2	-5.80009×10^{-3}	3.15405×10^{-3}	-2.32607×10^{-4}	1.11411×10^{-5}	-3.13190×10^{-7}	3.03914×10^{-9}
2	-6.08687×10^{-3}	2.95287×10^{-3}	-2.42350×10^{-4}	1.20343×10^{-5}	-3.25555×10^{-7}	3.08613×10^{-9}
3	-3.45113×10^{-4}	1.67276×10^{-3}	-1.23625×10^{-4}	7.07614×10^{-6}	-2.31149×10^{-7}	2.38864×10^{-9}
4	-1.69351×10^{-2}	6.54719×10^{-3}	-6.04396×10^{-4}	2.82346×10^{-5}	-6.55759×10^{-7}	5.54399×10^{-9}
5	9.90229×10^{-3}	-8.24588×10^{-4}	1.69826×10^{-4}	-6.13737×10^{-6}	1.89587×10^{-8}	5.65221×10^{-10}
6	4.33378×10^{-3}	5.65055×10^{-4}	1.25218×10^{-4}	-9.60364×10^{-6}	2.36248×10^{-7}	-2.33966×10^{-9}
7	1.33766×10^{-2}	-1.93370×10^{-3}	2.46359×10^{-4}	-8.71641×10^{-6}	4.08488×10^{-8}	9.60579×10^{-10}

2.4.2.3 Rietveld analysis

Rietveld analysis of powder diffraction data is used to extract various structural parameters such as lattice constants and atomic displacement parameters. The method was initially developed by H. M. Rietveld in the 1960s [265]. In the Rietveld method, a powder pattern is expressed in terms of the intensity observed at a given 2θ (y_{obs}). From models for structure, experimental peak shape, and background, the calculated intensity (y_{calc}) is determined at each 2θ. A least-squares method is then employed to adjust various parameters to minimize the difference between y_{obs} and y_{calc} over the entire pattern. Refinement quality can be quantified by agreement factors, most commonly R_{wp}, the weighted profile R value:

$$R_{wp} = \left\{ \frac{\sum_i w_i [y_{i,obs} - y_{i,calc}]^2}{\sum_i w_i [y_{i,obs}]^2} \right\}^{1/2}, \tag{2.7}$$

where w_i is a weighting factor. Goodness of fit is expressed by χ^2, which compares R_{wp} to the statistically expected value R_{exp}:

$$\chi^2 = \left(\frac{R_{wp}}{R_{exp}} \right)^2 \tag{2.8}$$

where

$$R_{exp} = \left\{ \frac{n-p}{\sum_{i=1}^{n} w_i [y_{i,obs}]^2} \right\}^{1/2}; \tag{2.9}$$

n is the number of observations, and p is the number of parameters. Also, although less quantitative, refinement quality can be monitored visually by a difference curve, which can reveal specific issues with an individual fit, such as a faulty structural or peak shape model.

Perhaps the most common function for describing peak shape is the pseudo-Voigt approximation of the Voigt function, a convolution of Gaussian and Lorentzian profiles [266]. As derived by Caglioti *et al.* [267], the variation of the full width at half-maximum (FWHM) of the Gaussian contribution to peak shape with 2θ is described by

$$\mathrm{FWHM}_G^2 = G_U \tan^2\theta + G_V \tan\theta + G_W, \tag{2.10}$$

while that of the Lorentzian contribution is described by

$$\mathrm{FWHM}_L = L_X \tan\theta + \frac{L_Y}{\cos\theta}. \tag{2.11}$$

During Rietveld analysis, some or all of the parameters G_U, G_V, G_W, L_X, and L_Y are refined. The background is usually modeled by a polynomial function or linear interpolation between selected points. Structure-related parameters that are commonly refined in Rietveld analysis include lattice constants, fractional coordinates, atomic displacement parameters, and scale factor. A more detailed description of the Rietveld method is beyond the scope of this thesis but can be found elsewhere, such as ref. [268].

Several examples of Rietveld fits are shown throughout the thesis. For an example in this chapter, Figures 2.12a and 2.12b show Rietveld fits to LaB_6 ambient diffraction data before and after correction for angular distortion, respectively.

A number of programs have been developed for the Rietveld analysis of diffraction data. However, all Rietveld analyses in this thesis were accomplished with the *General Structure Analysis System* (*GSAS*) [269] and the *EXPGUI* graphical user interface [270]; for variable-temperature and -pressure experiments, in which sometimes many hundreds of patterns were collected for a given sample, *SEQGSAS*, the batch refinement mode of *GSAS*, was employed. Details of specific refinements are provided in the relevant chapters.

2.4.3 X-ray total scattering data

Raw X-ray total scattering images were integrated using *FIT2D* [255]. Pair distribution functions, $G(r)$, introduced and defined in Section 2.2.3, were computed from these data using the program *PDFgetX2* [271]. Standard corrections for background subtraction, sample absorption, oblique incidence, and Compton scattering were performed within *PDFgetX2* prior to calculation of $S(Q)$ and $G(r)$ [271]. Structural models were fit to $G(r)$ and refined using the program *PDFgui* [272].

2.4.4 Other programs

Throughout this work, the open-source program *Fityk* was an invaluable tool for curve and peak fitting [273].

CHAPTER 3

BACKGROUND REDUCTION AND PRECISE CONTROL OF PRESSURE IN VARIABLE-PRESSURE X-RAY DIFFRACTION

3.1 Introduction and motivation[1]

As discussed in Section 1.1.4.1, diffraction measurements are commonly undertaken to gain insight into the structure and behavior of a material under non-ambient and, in some cases, extreme conditions. However, parasitic scattering from the sample environment is always of concern, as it can severely degrade, or in some cases overwhelm, the scattering from the sample being studied. Such scattering is particularly problematic for studies at high pressure, where sample cell designs often place a considerable thickness of high-strength material in the beam path.

Background scattering from the sample environment can be controlled by using low- or null-scattering materials in the beam and collimation that discriminates between scattering from the sample and that from its environment. In neutron diffraction experiments, vanadium or null-scattering TiZr alloys may be used for in-beam components, and radial collimators are employed to limit the volume around the sample that the detector views [274]. In X-ray diffraction experiments, beryllium, various low-Z polymers, and boron-filled polymers can be used for in-beam components, and multichannel collimator systems have been developed [275, 276] to allow efficient angle-dispersive experiments using two-dimensional detectors without major interference from background scattering when using multi-anvil and "Paris-Edinburgh"-type pressure cells.

The construction of diffracted-beam collimators capable of eliminating nearly all scattering from the sample environment is relatively expensive and an engineering challenge,

[1]The work presented in this chapter was previously published [254] and is edited to fit the context of this thesis. Reproduced with permission of the International Union of Crystallography.

particularly when the sample volume is small. In this chapter, the performance of a lower-cost alternative to traditional diffracted-beam radial or multichannel collimators is demonstrated that is suitable for high-energy X-ray diffraction studies in fluid-pressurized large-volume cells. This design, the background-reducing internal mask (BRIM), introduced and described in Section 2.2.2, contains the powder sample at its center and fits inside the pressure vessel so that it blocks scattering from the upstream vessel wall and "stops" the straight-through X-ray beam before it hits the downstream wall.

This experimental setup offers another benefit to the study of materials that display low and negative thermal expansion: fine pressure control in a modest pressure regime. As discussed in Section 1.2.3, many thermomiotic materials have highly flexible and low-density structures that are sensitive to relatively modest pressures. Most high-pressure diffraction methods are used to achieve pressures on the order of several gigapascals, such as diamond anvil cells (DACs) or multi-anvil presses, or require large sample volumes for neutron diffraction, such as helium gas pressure cells [277]. Fine pressure control in the low-pressure regime is often not possible. In this setup, a hand-driven syringe pump with silicone oil is used to apply hydrostatic pressure to the sample with precise control over pressure; the maximum pressure depends primarily on the pressure vessel specifications but does not exceed 414 MPa.

As shown in Table 2.2, four versions of the BRIM have been constructed and used in experiments. In this chapter, the use of the two MK2BRIM designs, MK2BRIM_138 and MK2BRIM_276, which have maximum pressures of 138 and 276 MPa, respectively, is evaluated. Studies of cubic ZrW_2O_8 and $Al_2W_3O_{12}$ are presented to illustrate the potential of this device for studying the behavior of materials at low pressures and modest temperatures.

3.2 Experimental

A detailed description of the BRIM device and high-pressure setup, as well as other experimental information, can be found in Section 2.2.2.

3.3 Demonstrations of BRIM use

To verify that high-quality diffraction data could be obtained using the BRIM with sufficiently precise and reliable control of temperature and pressure, samples of cubic ZrW_2O_8 and $Al_2W_3O_{12}$ were examined. The thermomiotic material cubic ZrW_2O_8 (Section 1.2.4.1) has a relatively simple crystal structure and shows an order-disorder phase transition that has been reported to occur at 428 K and ambient pressure [21, 55] or 448 K and ambient pressure [36]. The structures of both forms of ZrW_2O_8 appear in Figure 1.6. $Al_2W_3O_{12}$ (Section 1.2.4.1) is part of a large family of tungstates and molybdates, many of which show negative thermal expansion when orthorhombic [19, 140] and undergo an orthorhombic-to-monoclinic transition on cooling or compression [96, 97, 99, 143]. The crystal structures of these phases are quite complex (Figure 1.7).

3.3.1 Order-disorder phase transition in cubic ZrW_2O_8

Powder X-ray diffraction (PXRD) data for cubic ZrW_2O_8 were collected, using an ∼0.2 mm (horizontal) by ∼0.6 mm (vertical) X-ray beam and the MK2BRIM_138 device in ∼7.9 mm ID titanium pressure tubing, at 21, 41, 62, 83, 103, and 124 MPa for each temperature (298, 324, 375, 433, 483, and 538 K). The total exposure time for each measurement, including the dark frames, was 10 min. No pressure dependence of the previously reported order-disorder phase transition temperature is observed within the relatively coarse temperature resolution of the experiment. At each pressure studied, the transition occurs between 375 and 433 K (as in, for example, Figure 3.1).

While good Rietveld fits to the ZrW_2O_8 diffraction data (from both $P2_13$ and $Pa\bar{3}$ forms) were readily obtained (Figure 3.2), the ambient-temperature bulk modulus derived from the lattice constants (∼57 GPa) is in very poor agreement with the values of 69.4 GPa and 72 GPa reported in prior neutron diffraction studies [57, 126]. This difference is attributed to changes in the sample-to-detector distance during the experiment. Improvements in the rigidity of the sample cell mounting and a rearrangement of the high-pressure plumbing to minimize any strain on the sample fixture were undertaken. After these changes, an experiment using an NaCl sample at ambient temperature (∼300 K) led to an estimated

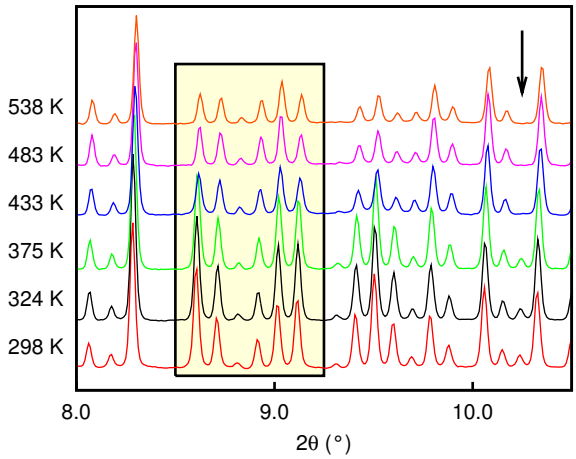

Figure 3.1: Selected diffraction data for ZrW_2O_8 collected at 62 MPa with the MK2BRIM_138. There are pronounced changes in peak intensities (see peaks in box and below arrow) between 375 and 433 K that are associated with a transition from $P2_13$ to $Pa\bar{3}$ symmetry. Redrawn from ref. [254].

isothermal bulk modulus of 23.06(3) GPa for this material, in reasonable agreement with previously reported values between 23.5 and 24 GPa [278].

Over the angular range used for Rietveld analyses, the full width at half-maximum (FWHM) of the peaks in the ZrW_2O_8 data increases from $2\theta \approx 0.03$ to 0.045°. The resolution of the data is limited by a combination of sample tube diameter, beam size, detector pixel size, and sample-to-detector distance. At a sample-to-detector distance of 850 mm and a scattering angle of $2\theta \approx 10°$, a 200 μm detector pixel spans ~0.013°, and the projection of the illuminated path through the sample (~1.6 mm) spans ~0.018°. The contribution to peak broadening from the illuminated path through the sample increases as the Bragg angle increases.

Although the data used for the Rietveld analyses are essentially free of Bragg peaks from the pressure vessel, the peak-to-background ratio in the patterns is quite low. The BRIM device, unlike a diffracted-beam multichannel collimator, is not capable of either reducing the scattering from the pressure-transmitting medium that lies in the direct beam path or discriminating against background that originates when diffracted X-rays from the sample are scattered by the pressure vessel walls.

While the crystal structure of ZrW_2O_8 is relatively simple, accurate determination of the

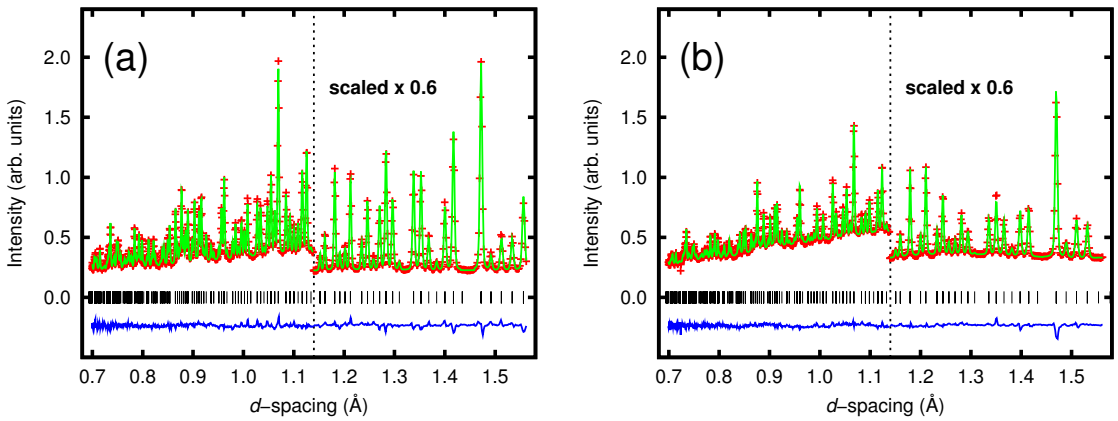

Figure 3.2: Rietveld fits using (a) $P2_13$ (ordered structure, 62 MPa, 324 K, $R_F = 0.030$) and (b) $Pa\bar{3}$ (disordered structure, 62 MPa, 483 K, $R_F = 0.054$) models for cubic ZrW_2O_8. The data were collected with the MK2BRIM_138 in an ∼7.9 mm ID pressure cell. Redrawn from ref. [254].

location of its oxygen atoms by PXRD is challenging, as most of the scattering arises from the high-Z atoms (Zr and W). The fit shown in Figure 3.2a was performed with all atomic coordinates freely varying, independent isotropic atomic displacement parameters for the four crystallographically distinct oxygen positions, and independent anisotropic displacement parameters for the three distinct metal positions, leading to chemically reasonable lengths and angles for all of the bonds, with the exception of the terminal W–O bonds, which were both unrealistically very short. Also, the anisotropy of the displacement parameter for Zr was unreasonably high. However, the isotropic and equivalent isotropic atomic displacement parameters were reasonable for all of the atoms, suggesting that shadowing from the beam-stop blade has only a modest effect on the intensities of the low-angle peaks.

Since the publication of this work, ZrW_2O_8 and its relatives $ZrMo_2O_8$ and HfW_2O_8 have been studied in greater detail with the BRIM [93, 95].

3.3.2 Orthorhombic-to-monoclinic phase transition in $Al_2W_3O_{12}$

There is a large family of materials with the orthorhombic $A_2M_3O_{12}$ structure (Section 1.2.4.3) [141], many of which show negative thermal expansion [19, 140]. Typically, though not always, these materials undergo a symmetry-lowering phase transition both on cooling and modest compression. For example, $Sc_2W_3O_{12}$ remains orthorhombic (*Pnca*) down to

the lowest temperatures studied [20] but becomes monoclinic ($P2_1/a$) when compressed to between 0.25 and 0.3 GPa; $Sc_2Mo_3O_{12}$ becomes monoclinic ($P2_1/a$) on cooling below ∼178 K [148] and monoclinic on compression to ∼0.25 GPa [99]. This orthorhombic-to-monoclinic transition is usually associated with a dramatic decrease in the bulk modulus of the material [149], and for some materials, the orthorhombic phase displays highly anisotropic compressibility. $Al_2W_3O_{12}$, which has been reported to become monoclinic on cooling to 267 K at ambient pressure [143], has previously been studied by *in situ* diffraction at high pressure using a DAC [99]. However, the onset pressure of the orthorhombic-to-monoclinic transition was so low (<0.08 GPa) compared with the uncertainty of the pressure measurement and the precision of the pressure control that is possible in a DAC that the behavior of orthorhombic $Al_2W_3O_{12}$ on compression could not be determined with a high level of confidence.

Ambient-temperature, high-pressure diffraction data for $Al_2W_3O_{12}$ were collected using an ∼0.2 mm (horizontal) by ∼0.6 mm (vertical) X-ray beam and the MK2BRIM_276 in ∼6.4 mm ID titanium pressure tubing. The maximum pressure attained for these measurements, 207 MPa, was limited by the pump used for these studies. The total exposure time at each pressure was ∼20 min.

The integrated PXRD data (Figure 3.3) show the onset of the phase transition at 83 MPa, in remarkably good agreement with prior DAC experiments [99]. The transition appears to be complete at 103 MPa, although a two-phase mixture was observed at 0.14 GPa in the DAC study.

The orthorhombic and monoclinic structures are both sufficiently complex to give a very high density of Bragg peaks in the d-spacing range available for analysis. Although the complexity of the crystal structures, combined with the limited resolution of the available data and the presence of both high- and low-Z atoms in the sample, effectively precludes the refinement of reasonable-quality crystal structures using the available data, Rietveld analyses, rather than Le Bail or similar fits, were used to obtain lattice constants. For the low-pressure data, restraints were used on the metal–oxygen bond lengths. For the high-pressure data, in which the material has a complex monoclinic structure, only the Al and

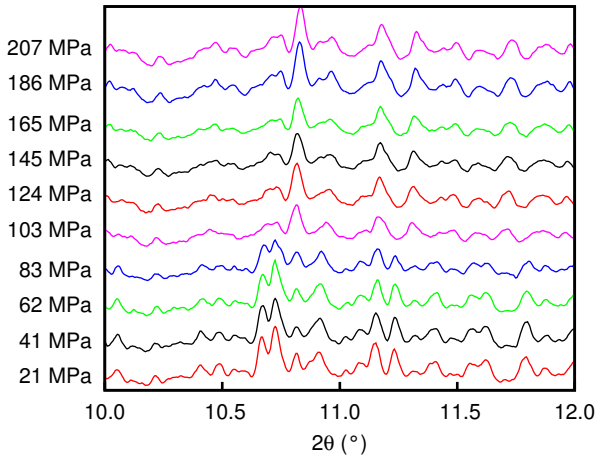

Figure 3.3: Selected diffraction data for $Al_2W_3O_{12}$ on compression, collected with the MK2BRIM_276 at ambient temperature, showing the onset of a phase transition from orthorhombic (low-pressure) to monoclinic (high-pressure) symmetry at ∼83 MPa. Redrawn from ref. [254].

W positions were refined. In these analyses, the calculated intensities from the structural model help ensure that the unit cell constants are correct, whereas the density of the Bragg peaks, combined with the limited resolution of the data, may lead to difficulties with Le Bail fitting. An example fit with the monoclinic model is shown in Figure 3.4.

The $P2_1/a$ monoclinic unit cell for $Al_2W_3O_{12}$ can be transformed to a larger (centered) cell with a monoclinic angle close to 90° and axes almost parallel to those of the original orthorhombic structure [99]. The transformed monoclinic cell dimensions are used in the following analyses and discussion.

The bulk moduli for the orthorhombic and monoclinic phases were estimated from straight-line fits to $\ln(V/V_0)$ *versus* pressure to be 41.5(9) and 20.2(6) GPa, respectively. At 83 MPa (close to the onset pressure), the reduction in volume per formula unit associated with the transition is 1.28%. This volume reduction arises entirely from compression parallel to the orthorhombic *b*- and *c*-directions; the softening of these directions is responsible for the lower bulk modulus of the monoclinic phase. The orthorhombic phase displays a near-isotropic response to pressure (Figure 3.5), but the monoclinic phase is mildly anisotropic, with linear compressibilities of $\beta_a \approx 0.97(2) \times 10^{-2}$ GPa^{-1}, $\beta_b \approx 2.20(8) \times 10^{-2}$ GPa^{-1}, and $\beta_c \approx 1.78(8) \times 10^{-2}$ GPa^{-1}.

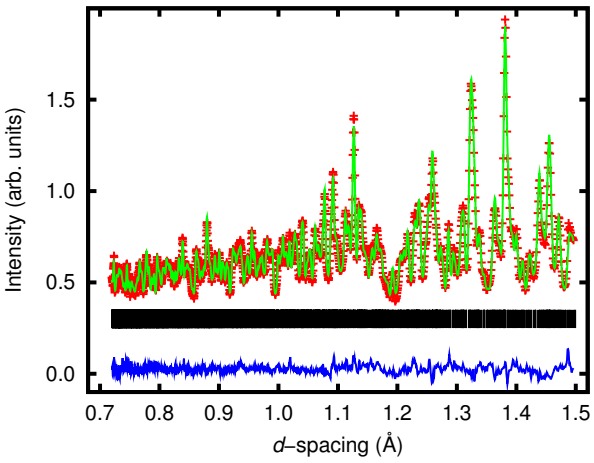

Figure 3.4: Rietveld fit with the monoclinic $Al_2W_3O_{12}$ ($P2_1/a$) model. The data were collected at 207 MPa and ambient temperature with the MK2BRIM_276 in an ∼6.4 mm ID pressure cell. Redrawn from ref. [254].

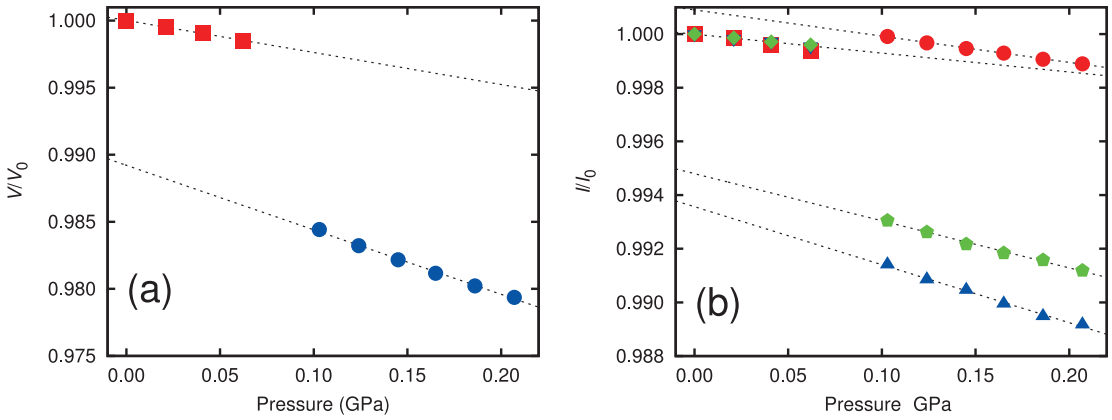

Figure 3.5: (a) Pressure dependence of the normalized unit cell volume per formula unit for $Al_2W_3O_{12}$ (orthorhombic phase, red squares; monoclinic phase, blue circles). (b) Pressure dependence of the normalized lattice constants. The points below 0.08 GPa are for the orthorhombic phase (a-axis, red squares; b-axis, blue inverted triangles; c-axis, green diamonds), and the points above this pressure are for the monoclinic phase (a-axis, red circles; b-axis, blue triangles; c-axis, green pentagons). Redrawn from ref. [254].

3.4 Conclusion

The BRIM device can be used to acquire high-quality powder diffraction data under conditions of elevated pressure and temperature where structural information or precise lattice constants are sought. The angular resolution of the diffraction patterns and their Q_{max} could be improved by changing the detector position and/or the detector itself, facilitating the examination of more complex crystal structures. The MK2BRIMs used in this chapter (and Chapter 7) are far from optimized. The parasitic scattering from the pressure vessel, present at low angles, would be reduced further by narrowing the slit through which the incident beam passes. The systematic decrease of sample Bragg peak intensity that is seen at low angle from shadowing by the beam stop could be reduced by making the beam stop blade thinner, increasing the distance between the sample and blade, reducing the sample tube diameter, and/or displacing the sample tube off the BRIM axis away from the beam stop. All of these improvements were made in the MK3BRIM design, shown in Section 2.2.2 and used in Chapter 8.

CHAPTER 4

THERMAL EXPANSION AND PHASE TRANSITION OF α-AlF_3 AND InF_3

4.1 Introduction[1]

As discussed in Section 1.3, the simple cubic ReO_3 structure (Figure 1.8), consisting of metal-centered octahedra that share anions at their corners, is of interest because of its potential for low or negative thermal expansion (NTE). This structure is related to that of perovskites, ABX_3, with a vacant A site and hence significant empty volume, and has been used to illustrate how NTE can arise from the transverse thermal motion of bridging atoms and the resulting rocking of relatively rigid units [6, 59]. Rhenium trioxide itself displays low thermal expansion at ambient conditions [32, 184, 185, 186], but members of this structural family, including fluorides and oxyfluorides, have coefficients of thermal expansion (CTE) ranging from strongly positive to strongly negative [25, 35, 205].

Many metal trifluorides (MF_3; M = Al, Cr, Fe, Ga, In, Ti, V) are only cubic at elevated temperatures, adopting a rhombohedrally distorted form of the ReO_3 structure (VF_3-type, space group $R\bar{3}c$ [279]) upon cooling [226, 227, 228, 229]. This phase transformation involves the coupled rotation of the constituent MF_6 octahedra (Figure 1.9). The thermal expansion of some ReO_3-type MF_3 has been studied but rarely quantified. The unfolding of the rhombohedral phase on heating is accompanied by strongly positive thermal expansion (PTE), while the cubic phase shows much lower or even negative thermal expansion. Notably, cubic ScF_3 displays pronounced NTE over a wide temperature range (at least 10 to 1100 K) [35]. TiF_3 is cubic above ~340 K [226, 228], and its CTE is slightly positive just above the phase transition but then becomes slightly negative above ~400 K; TiF_3 is examined in Chapter 6 in the context of ScF_3/TiF_3 solid solutions [238].

[1]The work on α-AlF_3 presented in this chapter was previously published [237] and is edited to fit the context of this thesis. Reprinted from *Journal of Solid State Chemistry*, 219, C. R. Morelock *et al.*, Thermal expansion and phase transitions of α-AlF_3, 143-147, Copyright 2014, with permission from Elsevier.

α-AlF_3 and InF_3 also have ReO_3-type connectivity; at ambient temperature, both materials are rhombohedral. α-AlF_3 becomes cubic at ~730 K [231], and the rhombohedral-to-cubic phase transition in α-AlF_3 has been studied rather extensively [227, 231, 232, 233, 234, 235]; however, the thermal expansion of α-AlF_3 has not been reported in detail. In 1984, Ravez *et al.* provided some information on the temperature dependence of unit cell volume but did not report expansion coefficients; they reported that both cubic and rhombohedral phases display positive thermal expansion [236]. In 2001, Chupas *et al.* studied α-AlF_3 in the context of γ-Al_2O_3 fluorination and catalysis. They reported that some weak reflections, potentially indicative of a residual rhombohedral distortion, persisted above the phase transition at ~739 K, and their Rietveld analyses suggested that bent Al–F–Al links persisted above the phase transition temperature [231]. A later total scattering study of α-AlF_3 revealed that the cubic phase contains local octahedral tilts [235]. The mechanism of the cubic-to-rhombohedral phase transition was studied using molecular dynamics simulations, and the authors suggested local distortions and NTE above the phase transition temperature [234]. In contrast to α-AlF_3, however, the thermal expansion of InF_3 has not been reported, although its phase transition temperature was estimated many years ago by differential scanning calorimetry (DSC; 656 ± 10 K) [227]. In this chapter, the thermal expansion behaviors of α-AlF_3 and InF_3 are examined in detail and quantified.

4.2 Materials and methods

4.2.1 Sample preparation

InF_3 (Alfa-Aesar, 99.99 %) was used as supplied without further treatment. However, anhydrous α-AlF_3 (American Elements, 99.99%) was ground thoroughly in an inert atmosphere and sealed in a nickel tube by welding. The Ni tube was then sealed in an evacuated fused quartz ampoule and heated at 1338 K for 72 h, after which it was quenched by removing from the furnace, located in a fume hood (see Chapter 6 for more information). Both samples were maintained in an inert atmosphere to avoid moisture exposure.

4.2.2 Variable-temperature synchrotron powder diffraction

Variable-temperature powder X-ray diffraction (PXRD) data were collected at beamline 17-BM-B of the Advanced Photon Source, Argonne National Laboratory, Illinois, USA, using a wire-wound furnace for temperature control (Figure 2.3) [250], heating at a rate of 180 $K{\cdot}h^{-1}$ from 323 to 1177 K for both α-AlF_3 and InF_3. No data were collected on cooling, as the sample capillary failed upon reaching the maximum temperature. The α-AlF_3 and InF_3 powder samples were packed in fused quartz capillaries under argon, and ultra-high-purity nitrogen was very slowly flowed through each capillary during data collection to avoid the ingress of any moisture. Exposure times of ∼30 s were used, with a ∼30 s wait between exposures. Section 2.2.1.1 provides more detail on the wire-wound furnace setup.

4.2.3 Data analysis

The analysis of synchrotron diffraction data is described generally in Section 2.4.2. Two-dimensional area detector images were reduced to one-dimensional patterns with *FIT2D* [255]. A calibration curve (Figure 2.12) was created from the measured and expected peak positions for a standard LaB_6 sample to correct for angular distortions in the 1D patterns that are believed to be associated with the oblique incidence of the X-ray beam on the relatively thick active layer of the detector. Finally, all Rietveld analyses were accomplished in the sequential refinement mode of *GSAS* [269, 270].

4.2.3.1 α-AlF_3

A fit to α-AlF_3 data at 323 K with a primitive rhombohedral model (space group $R\bar{3}c$) served as the starting point for sequential refinement. An isotropic atomic displacement parameter (ADP) was refined for the Al atom, while anisotropic ADPs were used for the F atoms. Unit cell volumes per formula unit were extracted during Rietveld analyses and plotted with respect to temperature; the temperature variation of the volume CTE (α_V) was estimated by differentiation of sixth-order polynomial fits to these data. For some of the analyses, the primitive rhombohedral lattice constant a_R and unit cell angle α_R extracted during Rietveld analyses were converted to hexagonal lattice constants a_H and c_H by the

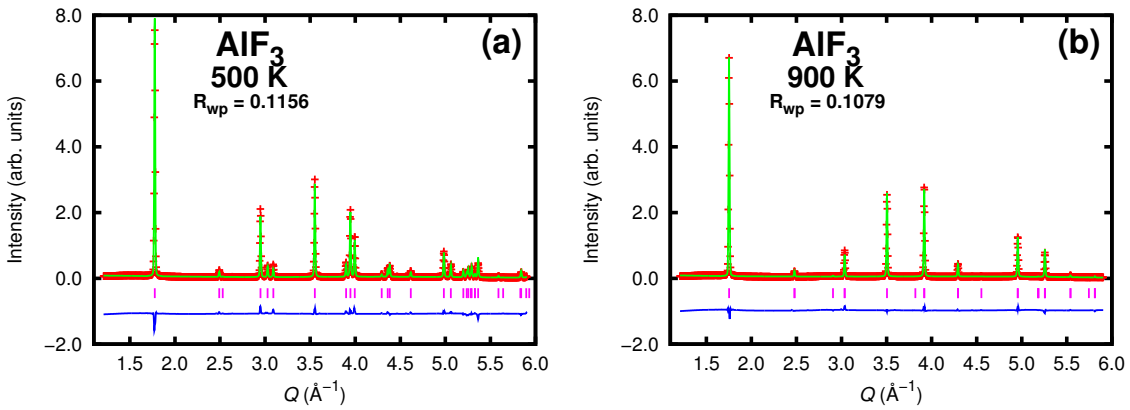

Figure 4.1: Rietveld fits (green line) to powder X-ray diffraction data (red +) using a primitive rhombohedral model for α-AlF_3: (a) 500 K; (b) 900 K. In both plots, the difference curve appears in blue, and Bragg peak positions are indicated by magenta tick marks (|).

following relationships:

$$a_H = 2a_R \sin\frac{\alpha_R}{2} \tag{4.1}$$

and

$$c_H = a_R\sqrt{3 + 6\cos\alpha_R}. \tag{4.2}$$

Example Rietveld fits are shown in Figure 4.1 for data collected below and above the phase transition temperature, 500 and 900 K, respectively.

4.2.3.2 InF_3

The coexistence of phases in the InF_3 sample somewhat complicated its analysis. The following phases exist at some temperature range in this sample: rhombohedral InF_3 (space group $R\bar{3}c$), cubic InF_3 (space group $Pm\bar{3}m$), and an InOF impurity (space group $Fddd$ [280]). The diffraction data were divided into four temperature regions (A, B, C, and D) based on the phases present (Table 4.1).

An example Rietveld fit from each region is shown in Figure 4.2. At nearly all temperatures, for both InF_3 phases, an isotropic ADP was refined for the In atom, and anisotropic ADPs were used for the F atoms. Furthermore, to better model the peak asymmetry of the InF_3 phases, profile function 4 was used in *GSAS*, which is based on the work of Stephens [281]. This function was used for the rhombohedral phase over its entire range

Table 4.1: Divisions of InF_3 variable-temperature PXRD data. R = rhombohedral; C = cubic.

Division	Temperature range	Phase(s) present
A	323-587 K	InF_3 (R)
B	587-677 K	InF_3 (R), InOF
C	677-794 K	InF_3 (R), InOF, InF_3 (C)
D	794-1170 K	InOF, InF_3 (C)

of existence and for the cubic phase in region "C". Otherwise, the pseudo-Voigt function described in Section 2.4.2.3 (profile function 3 in *GSAS*) was used.

4.3 Results and discussion

4.3.1 Sample composition and phase transition

The appearance of superlattice peaks and the splitting of other peaks at low temperatures in the variable-temperature PXRD patterns of both α-AlF_3 (Figure 4.3) and InF_3 (Figure 4.4) are evidence for the rhombohedral-to-cubic phase transition previously observed in many ReO_3-type metal trifluorides [226, 228, 229, 236]. For α-AlF_3, the phase transition appears quite clearly just above 700 K (Figure 4.3). An α-Al_2O_3 phase is also observed, an impurity likely incorporated into the sample during the annealing process; the α-Al_2O_3 peaks exist over the entire temperature range but are quite small (<1% weight fraction at 323 K). Another unidentified impurity phase appears above ~1000 K that may be a product of the reaction of α-AlF_3 and the quartz capillary. However, the α-AlF_3 peaks are much more intense than these impurity peaks.

The variable-temperature PXRD data for InF_3 (Figure 4.4) are more complex than those for α-AlF_3. This complexity is due to the existence of an InOF impurity and also a large region (>100 K) of rhombohedral/cubic InF_3 phase co-existence (Table 4.1). At 323 K, rhombohedral InF_3 exists, along with at least one unidentified impurity in trace amounts. Upon heating above 587 K, InOF peaks appear that persist to 1170 K. InOF is presumably formed by reaction with either the quartz capillary or trace moisture in the capillary. However, this InOF impurity is not present in large amounts, forming only a few weight percent of the overall sample (Figure 4.5). The cubic form of InF_3 begins to appear

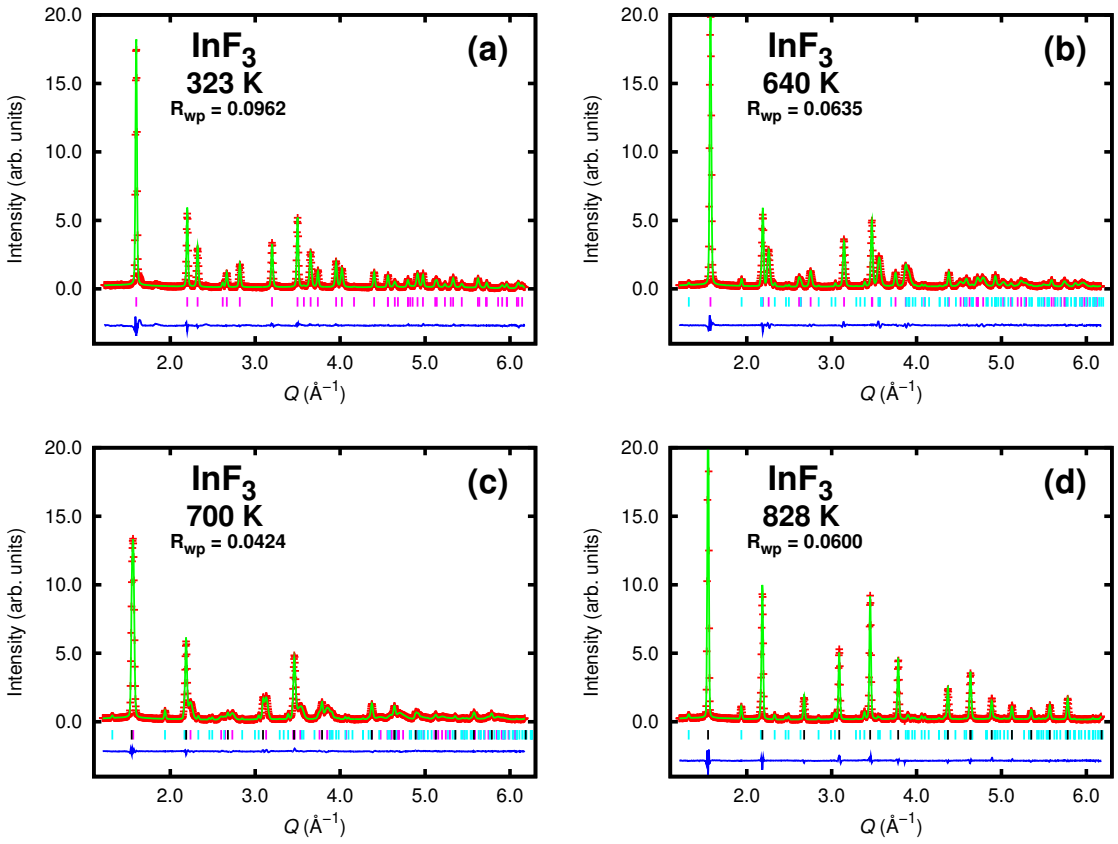

Figure 4.2: Rietveld fits (green line) to powder X-ray diffraction data (red +) for InF_3 at several temperatures: (a) 323 K; (b) 640 K; (c) 700 K; (d) 828 K. In each plot, the difference curve appears in blue, and Bragg peak positions are indicated by tick marks (|): magenta for rhombohedral InF_3, black for cubic InF_3, and cyan for InOF. The same intensity scale is used in each plot for the sake of comparison.

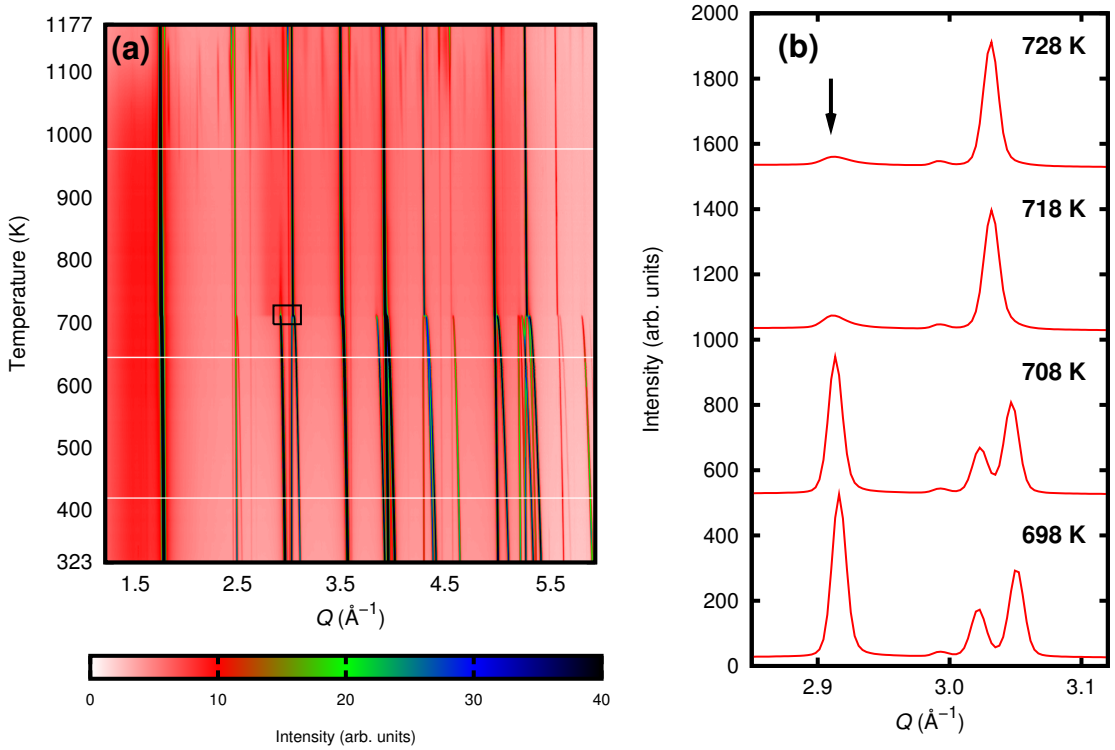

Figure 4.3: (a) Variable-temperature (323 to 1177 K) powder X-ray diffraction patterns for α-AlF_3, displayed in order of collection from bottom to top. The horizontal white lines are from frames that were lost during data collection. (b) X-ray diffraction data for α-AlF_3 at selected temperatures, showing the presence of a diffuse peak (marked by an arrow) that is incommensurate with the α-AlF_3 unit cell. These data are taken from the portion of (a) enclosed by a small box. Reproduced from ref. [237].

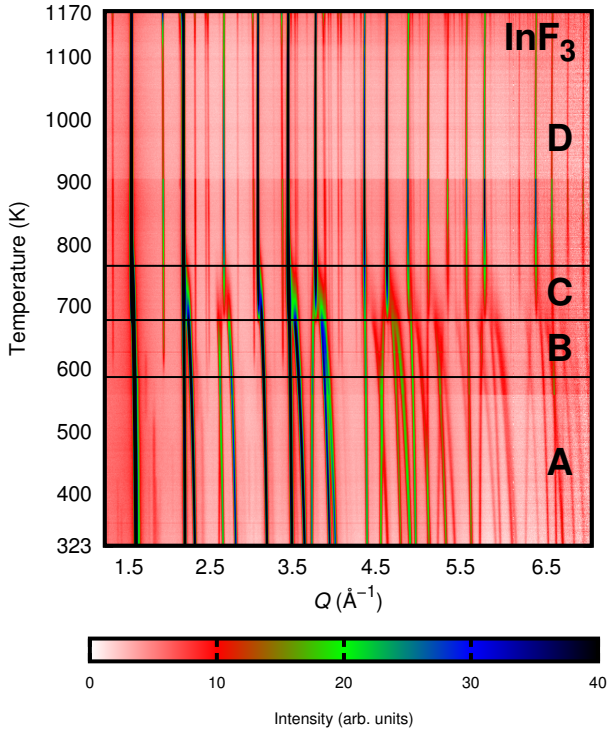

Figure 4.4: Variable-temperature (323 to 1170 K) powder X-ray diffraction patterns for InF_3, displayed in order of collection from bottom to top. Regions "A", "B", "C", and "D" are indicated (Table 4.1).

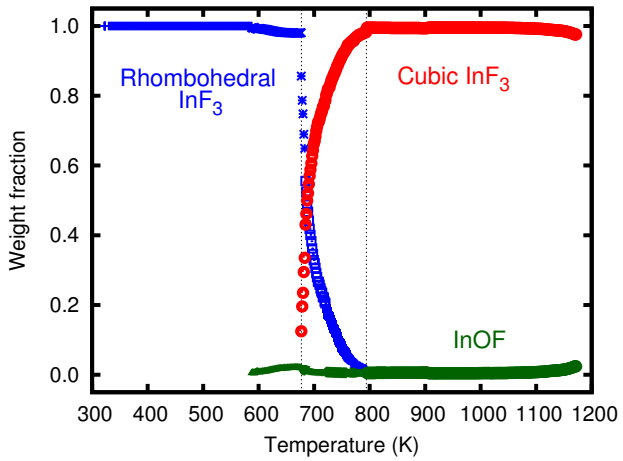

Figure 4.5: Temperature evolution of the weight fractions of phases present in the InF_3 sample, extracted from Rietveld analyses. The two dashed lines at 677 and 794 K indicate the initial appearance of cubic InF_3 and complete disappearance of rhombohedral InF_3, respectively.

at ∼677 K, and the rhombohedral form persists to ∼794 K. This ∼120 K region of phase co-existence can also be observed in the weight fractions extracted from Rietveld analyses (Figure 4.5). Cubic InF_3 survives to 1170 K; complete decomposition does not occur, as In_2O_3 peaks are not observed at any temperature.

4.3.2 Thermal expansion

4.3.2.1 α-AlF_3

The temperature dependence of both unit cell volume per formula unit (V/Z) and volume CTE (α_V) of α-AlF_3 are plotted in Figure 4.6. When heated from ambient temperature, rhombohedral α-AlF_3 exhibits strongly positive volume thermal expansion ($\alpha_V(500\text{ K}) \approx 86$ ppm·K^{-1}) as it unfolds. Above the first-order phase transition, cubic α-AlF_3 continues to expand but with a much lower CTE ($\alpha_V(900\text{ K}) \approx 25$ ppm·K^{-1}). The thermal expansion of rhombohedral α-AlF_3 is strongly anisotropic (Figure 4.7). The a-axis displays strong positive thermal expansion, while the CTE along the c-axis is close to zero. This anistropy occurs because the rhombohedral-to-cubic phase transition involves rotation of the AlF_6 octahedra around their threefold axes, which are parallel to the crystallographic c-axis. Based on the temperature dependence of c/a (Figure 4.8a), the phase transition temperature is ∼713 K, which is consistent with the temperature reported in another PXRD study (715

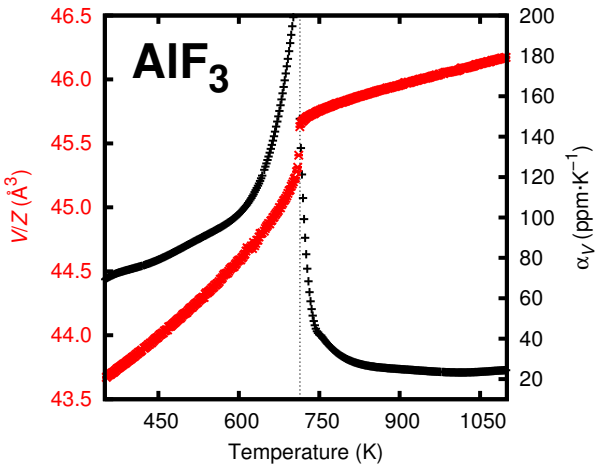

Figure 4.6: Temperature dependence of the unit cell volume per formula unit (V/Z, red $\times$) and volume CTE (α_V, black $+$) of α-AlF_3. Unit cell volumes were extracted from Rietveld analyses of PXRD data, and α_V were estimated from polynomial fits to the V/Z *versus* T data. The dashed line indicates the estimated phase transition temperature (713 K). Reproduced from ref. [237].

$\pm$ 10 K) [236] but slightly lower than that measured by DSC (725 K) [227] and PXRD (741 $\pm$ 10 K) in other studies [235].

As shown in Figure 4.3, there are some diffuse peaks at approximately the positions of the rhombohedral supercell reflections that persist to temperatures well above that of the phase transition, and the transition is accompanied by a significant increase in "background" scattering; notably, these diffuse peaks are incommensurate, in that they do not index on the α-AlF_3 unit cell. The most prominent of the diffuse peaks appears at $Q \approx 3.0$ Å^{-1} (marked by an arrow in Figure 4.3), which, prior to the phase transition, corresponds approximately to the rhombohedral (2 1 0) Bragg peak; its area drops significantly with increased temperature, and its width, which is greater than that of the Bragg peaks, increases sharply immediately above the phase transition temperature, 713 K (Figure 4.9). In addition, the peak shifts to higher angles on heating, counter to the PTE of α-AlF_3. These diffuse peaks and the jump in background due to diffuse scattering suggest the presence of short-range structural distortions in the cubic phase. Such distortions have been noted previously. Chupas *et al.* also observed weak superlattice PXRD peaks persisting

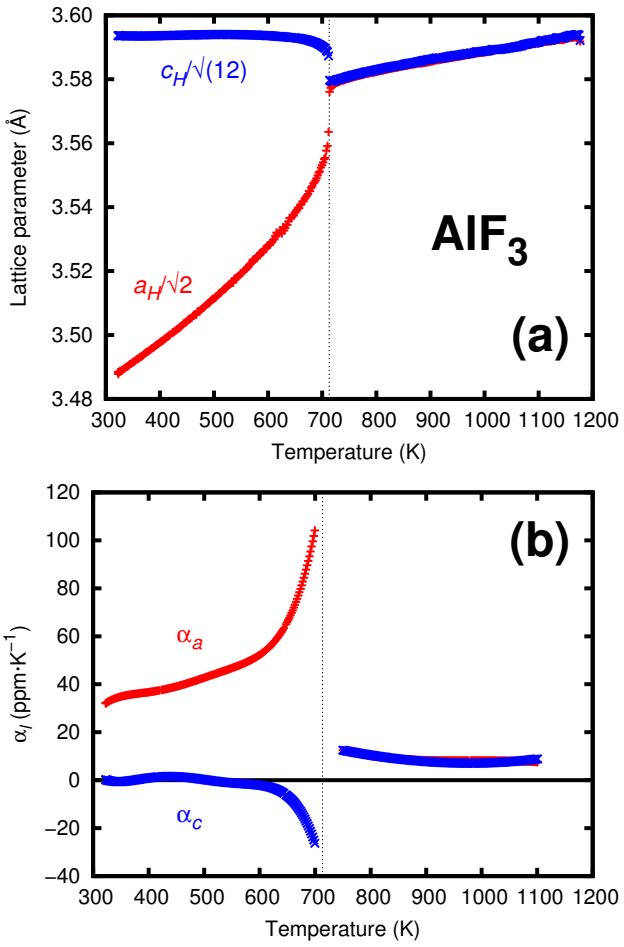

Figure 4.7: (a) Temperature dependence of the lattice parameters of α-AlF_3. Hexagonal values a_H and c_H are reduced to their cubic equivalents by the indicated factors. A rhombohedral model was used for all temperatures, even above the phase transition, where a_H and c_H refine to the same value. (b) Temperature dependence of the linear CTEs; α_a and α_c are significantly different below the phase transition temperature but equal above it. Reproduced from ref. [237].

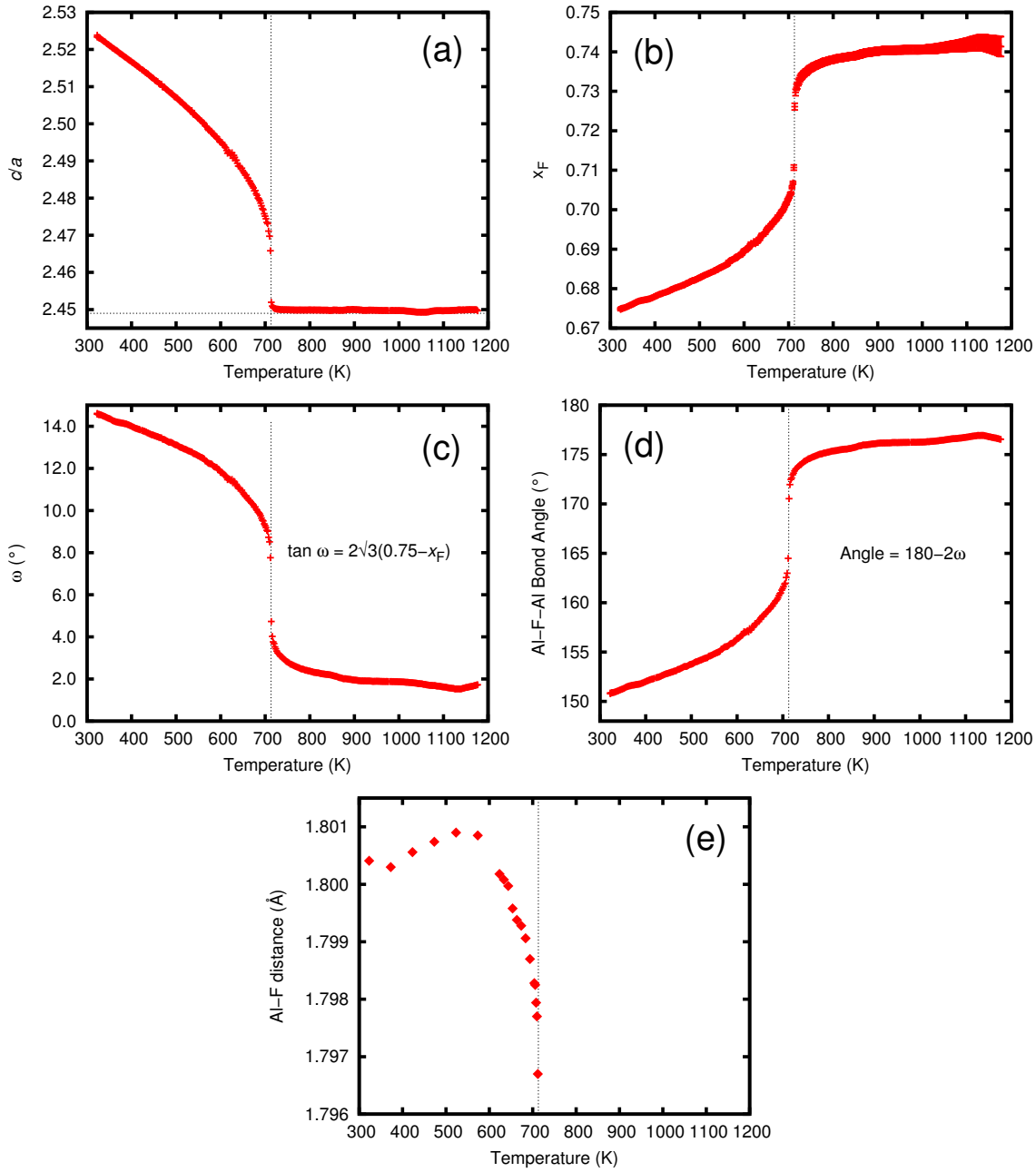

Figure 4.8: Temperature dependence of various α-AlF_3 structural parameters. (a) Ratio of lattice constants c and a (hexagonal cell), which was used to estimate the phase transition temperature of 713 K. (b) Fractional x-coordinate of F in the primitive rhombohedral cell. (c) Octahedral tilt angle ω, calculated from x_F using the equation shown. (d) Estimated Al–F–Al bond angle, related to ω by the equation shown. (e) Al–F distance. Lattice constants a and c, as well as x_F and Al–F distance, were determined by Rietveld analysis of the variable-temperature PXRD data. The expected value for c/a in the cubic phase is $\sqrt{6} = 2.449$, as indicated by the horizontal dashed line in (a). The expected value for x_F, in the absence of any disorder, in the cubic phase is 0.75, which would lead to ω and Al–F–Al bond angle values of 0 and 180°, respectively. Reproduced from ref. [237].

past the phase transition and calculated an Al–F–Al bond angle of 175.8° at 723 K, suggesting a small degree of local rhombohedral distortion [231]. Both molecular dynamics simulations [234] and pair distribution function analysis [235] confirmed the presence of bent Al–F–Al bonds and tilted octahedra in the cubic structure.

Attempts to fit a cubic model with a split F site to the data above the phase transition in the manner of Chupas *et al.* [235] yielded unrealistic values for the F position and atomic displacement parameters, perhaps because the Q range of these data is much smaller than that used by the previous authors ($Q_{max} \approx 6$ and 13 Å^{-1}, respectively). However, by using the primitive rhombohedral model at all temperatures, where the variable x_F partially accounts for disorder in the cubic phase, Al–F–Al bond angles were estimated that reasonably matched the previous observations [231, 234, 235] (Figure 4.8d). Such an approach must be treated with caution, due to the incomplete nature of the model and possible correlations involving ADPs. The apparent Al–F–Al bond angle estimated from the rhombohedral model increases steadily with temperature to at least 1100 K, which is consistent with the observation of quite strong PTE in cubic α-AlF_3. Furthermore, the Al–F distance does not vary greatly with temperature (300 to ∼600 K, Figure 4.8e), indicating the presence of rigid AlF_6 octahedra, with the positive thermal expansion principally driven by coupled rotation of these octahedra. However, beginning at ∼600 K, as the phase transition is approached, the Al–F distance appears to decrease with temperature. This behavior presumably reflects the presence of static/dynamic disorder rather than an actual decrease in the instantaneous Al–F distance. Zhao *et al.* reported similar but more pronounced behavior for the Mg–F distance in the perovskite $NaMgF_3$ [282].

Strong PTE in cubic α-AlF_3 contrasts with the behaviors of cubic InF_3 (low PTE or NTE, see below), ScF_3 (strong NTE [35]) and TiF_3 (low PTE or low NTE depending upon temperature, see Chapter 6). However, there are other examples of PTE in the cubic ReO_3 family; for example, cubic NbO_2F expands on heating between 20 and 500 K [25, 205]. The local structural study of TaO_2F presented in Chapter 9 [218] suggests that PTE in NbO_2F may arise from the presence of bent Nb–(O/F)–Nb links whose bond angles increase on heating. A similar phenomenon may be involved in the quite strong PTE of cubic α-AlF_3.

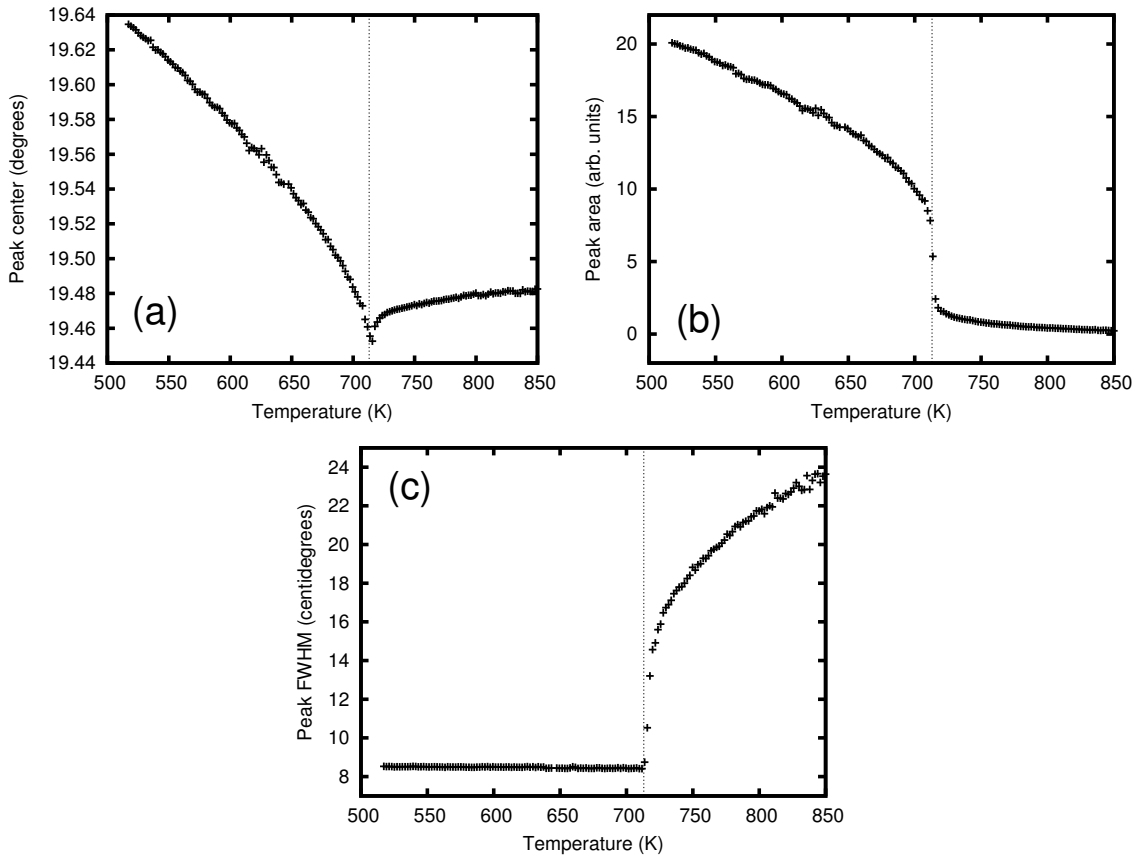

Figure 4.9: Temperature dependence of (a) center, (b) area, and (c) full width at half-maximum (FWHM) for the peak at $Q \approx 3.0$ Å^{-1}, which corresponds to the rhombohedral (2 1 0) Bragg peak before the phase transition in α-AlF_3 but is a diffuse peak that is incommensurate after the transition. The peak notably shifts to higher angles on heating above the phase transition temperature, indicative of NTE, and rapidly broadens. Reproduced from ref. [237].

4.3.2.2 InF_3

The temperature dependence of both V/Z and α_V of InF_3 (rhombohedral and cubic) are plotted in Figure 4.10 (a and b, respectively). The region of phase co-existence ("C" in Table 4.1) is indicated by dashed lines in the figure. Rhombohedral InF_3 shows strong PTE, reaching a maximum ($\alpha_V \approx 275$ ppm·K^{-1}) around 700 K, roughly coinciding with the initial appearance of the cubic phase. When formed, cubic InF_3 initially has a high positive CTE ($\alpha_V \approx 25$ ppm·K^{-1} at 794 K). From ∼850 to ∼950 K, cubic InF_3 shows zero thermal expansion; finally, the CTE is low negative above ∼950 K. Although not observed in α-AlF_3, other MF_3 exhibit low or negative thermal expansion (ScF_3 [35] and TiF_3 [228]); hence, the behavior of cubic InF_3 is not unexpected.

As in α-AlF_3, thermal expansion in rhombohedral InF_3 is strongly anisotropic (Figure 4.10c and d). Strong PTE occurs along the a-axis, with low NTE along the c-axis. The magnitude of α_a is approximately identical in both fluorides (∼35 ppm·K^{-1} at 323 K, increasing to ∼110 ppm·K^{-1} at the phase transition), while α_c is negative in InF_3 but near-zero in α-AlF_3. The temperature dependence of various rhombohedral InF_3 structural parameters is presented in Figure 4.11. A greater amount of structural distortion is evident in rhombohedral InF_3 than in α-AlF_3. Strong distortion remains even at the final disappearance of the rhombohedral phase (794 K); octahedral tilt angle ω is ∼7°, and thus, the In–F–In bond angle is ∼166°.

The appearance of cubic InF_3 at 677 K is close to the phase transition temperature measured via DSC by Daniel *et al.* (656 ± 10 K) [227]. However, the >100 K region of phase co-existence is unexpected. Three possibilities for this large region of phase co-existence are proposed below.

1. The "rhombohedral" InF_3 starting material was inhomogeneous or impure. The InF_3 sample was used as received without purification, whereas the α-AlF_3 sample was heat-treated before characterization. Although the sample appeared pure by laboratory PXRD, the synchrotron data suggest small extra peaks at the starting temperature (323 K). The sample may have contained an additional impurity and/or

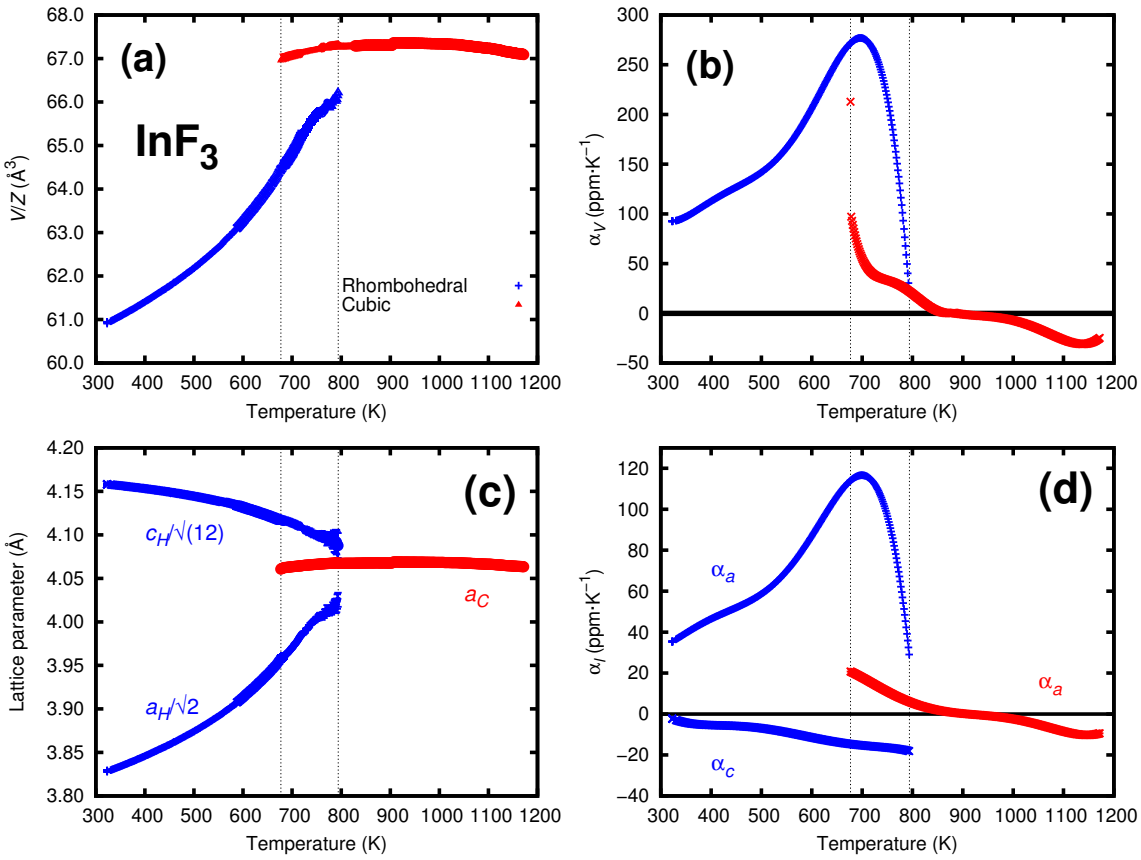

Figure 4.10: Temperature dependence of (a) the unit cell volume per formula unit (V/Z), (b) volume CTE (α_V), (c) lattice parameters, and (d) linear CTEs of InF_3. Unit cell volumes and lattice parameters were extracted from Rietveld analyses of PXRD data, and CTEs were estimated from polynomial fits to the V/Z or lattice parameter *versus* temperature data. Hexagonal values a_H and c_H are reduced to their cubic equivalents by the indicated factors. The dashed lines indicate the region of phase co-existence (677 to 794 K).

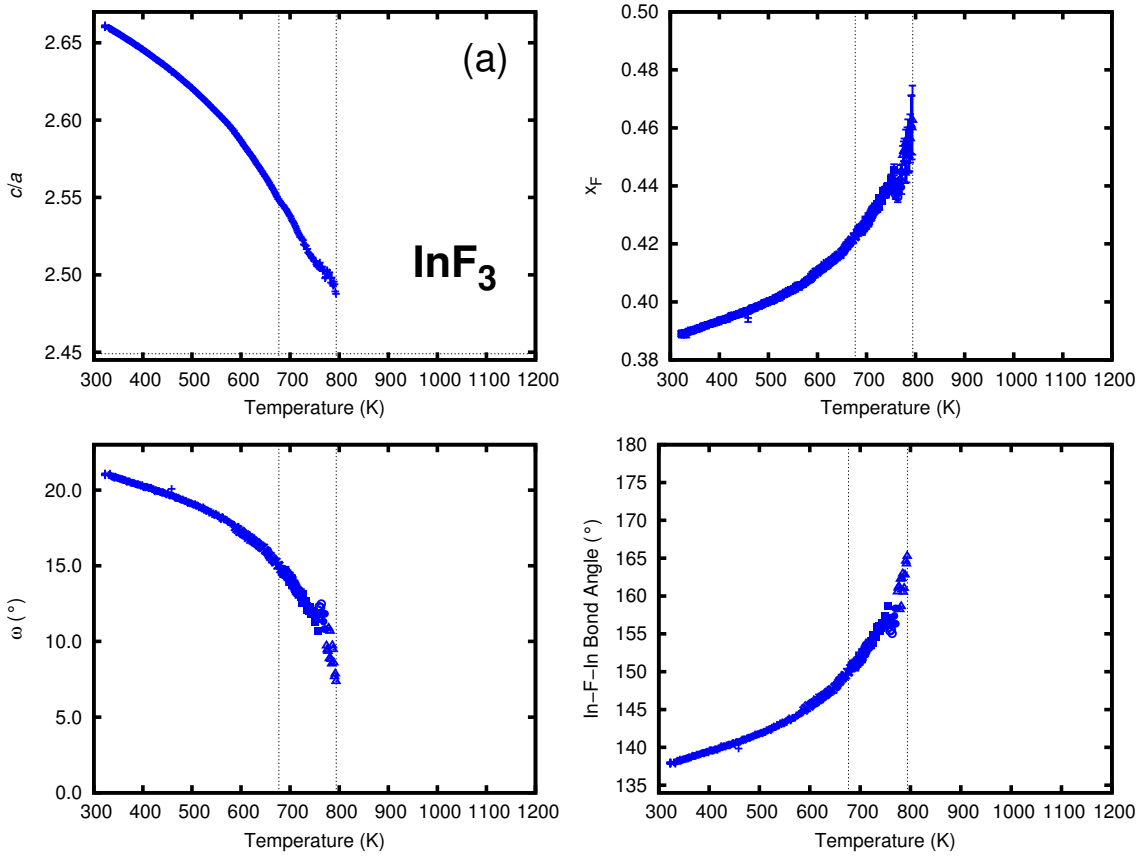

Figure 4.11: Temperature dependence of various rhombohedral InF_3 structural parameters. (a) Ratio of lattice constants c and a (hexagonal cell). (b) Fractional x-coordinate of F (primitive rhombohedral cell). (c) Octahedral tilt angle ω, calculated from x_F by the equation shown. (d) In–F–In bond angle, related to ω by the equation shown. Lattice constants a and c as well as x_F were determined by Rietveld analysis of the variable-temperature PXRD data. The expected values for c/a and ω in the cubic phase are $\sqrt{6} = 2.449$ and 0°, respectively. The dashed lines indicate the region of phase co-existence (677 to 794 K).

incorporated hydroxyl groups at the F sites (which is consistent with the formation of InOF on heating). Sample inhomogeneity may have resulted in one part of the sample undergoing the phase transition sooner than others. Heat treatment of the sample would have ensured homogeneity.

2. The kinetics for the rhombohedral-to-cubic phase transition are very sluggish. With a 180 $K \cdot h^{-1}$ heating rate, the ~120 K region of phase coexistence required ~40 min of data collection. While it is possible that the kinetics for the transition are very slow, a previous DSC study of the phase transition in InF_3, using various (non-specified) cooling and heating rates, reported a hysteresis of only 20(1) K [227].

3. The temperature in the volume illuminated by the X-ray beam was inhomogeneous. This option is possible but unlikely, as the X-ray beam was quite small (300 μm); thus, the temperature should be consistent within this small volume.

Phase co-existence of ~120 K in InF_3 may not be intrinsic to the material. An additional study with a pure (annealed) sample would provide insight into this problem.

4.4 Conclusion

Both α-AlF_3 and InF_3 have a rhombohedrally distorted (VF_3-type) ambient crystal structure that becomes cubic (ReO_3-type) on heating. This phase transition occurs at ~713 K in α-AlF_3, while in InF_3, there is a rather large temperature range with rhombohedral and cubic phase co-existence; the cubic phase first appears at ~677 K, while the rhombohedral phase disappears ~794 K. In both materials, the rhombohedral phase displays strongly positive volume thermal expansion. Cubic α-AlF_3 continues to display strong positive thermal expansion ($\alpha_V(900\ K) \approx 25\ ppm \cdot K^{-1}$), while the thermal expansion of cubic InF_3 changes from positive to zero (~850 to 950 K) to negative (above ~950 K). The positive thermal expansion of cubic α-AlF_3 may be partially due to the presence of local octahedral tilts and an associated increase in the average Al–F–Al bond angle on heating. The large region of phase co-existence in InF_3 sample is unexpected and may not be intrinsic to the material; inhomogeneity in the sample may have caused this behavior.

The discussion of ReO_3-type metal trifluorides continues in subsequent chapters: ScF_3 (Chapter 5) and ScF_3–MF_3 solid solutions (M = Ti, Y, Al; Chapters 6, 7, and 8).

CHAPTER 5

STRESS-INDUCED PHASE TRANSITION IN ScF_3 DUE TO LOW-TEMPERATURE THERMAL EXPANSION MISMATCH

5.1 Introduction[1,2]

Materials displaying negative thermal expansion (NTE) continue to attract attention due to the unusual nature of this behavior and the possibility of unique applications (Section 1.2) [4, 5, 7, 8]. Many thermomiotic materials whose contraction on heating is due to lattice vibrations have complex crystal structures. However, ScF_3, which has a simple cubic ReO_3-type structure (Figure 1.8), exhibits strong NTE at and below ambient temperature; the NTE of the material persists to ∼1100 K [35]. The prior neutron diffraction study by Greve *et al.* found that ScF_3 remains cubic down to at least 10 K, consistent with prior Raman studies in which no transition was observed down to 4 K [245]. As there is little available information on how the coefficient of thermal expansion (CTE) of ScF_3 changes from strongly negative at ∼100 K to zero at 0 K, as required by thermodynamics, a powder X-ray diffraction study of this material was undertaken using a helium flow cryostat.

During this investigation, two ScF_3 samples were prepared: one with powder packed under helium gas into an epoxy-sealed Kapton capillary and another in which the powder was embedded in GE-7031 varnish. In the latter, the role of the varnish was to provide improved thermal contact with the helium exchange gas in the cryostat. GE-7031 is a polyvinyl phenolic varnish that has been commonly used for decades in various cryogenic applications as an adhesive or sample coating due to its good thermal conductivity and mechanical strength at quite low temperatures [283, 284, 285, 286, 287, 288, 289, 290, 291]. However, as reported in this chapter, the sample embedded in GE-7031 varnish showed an unexpected symmetry-lowering phase transition at ∼50 K and yielded anomalous lattice

[1] The work presented in this chapter and Appendix A was previously published [44] and is edited to fit the context of this thesis. Reproduced with permission of the International Union of Crystallography.

[2] Supporting material for this chapter can be found in Appendix A.

constants below ∼150 K.

This chapter not only serves as a message of caution on the use of GE-7031 varnish as a sample matrix to enhance thermal equilibration at low temperatures but also demonstrates the limitations of ScF_3 (and thermomiotic materials in general) when used in composites. Based on experimental observations and quantitative estimates, the observed thermal expansion anomalies arise from stress induced by the significant thermal expansion mismatch between ScF_3 and the varnish.

5.2 Materials and methods

Scandium trifluoride (American Elements, 99.99%) was heat-treated for 72 h at 1273 K in a welded copper ampoule sealed in an evacuated fused quartz jacket; the furnace was located in a fume hood. The resulting white powder was a single phase and had a cubic crystal structure (space group $Pm\bar{3}m$), as determined by laboratory X-ray diffraction.

Variable-temperature, high-resolution synchrotron powder diffraction data were collected using beamline 11-BM-B at the Advanced Photon Source, Argonne National Laboratory, Illinois, USA, with an average wavelength of 0.413 Å [252, 253]. A helium cryostat was used for temperature control; this device and other experimental details are discussed in Section 2.2.1.2.

Two different sample preparation methods were used. In the "no varnish" method, the ground powder was packed under a helium atmosphere into an epoxy-sealed Kapton capillary; in the "varnish" method, the powder was mixed in a small amount of GE-7031 varnish (Lake Shore Cryotronics, Westerville, Ohio; diluted with 1:1 v/v toluene-ethanol mixture) under a helium atmosphere, and the resulting slurry was rolled into a ball and stuck on the end of a Kapton capillary.

Rietveld analyses of the diffraction data were accomplished using the program suite *GSAS* [269, 270]. Lattice constants and unit cell volumes extracted during Rietveld analyses at all temperatures are summarized in Table A.1 (Appendix A).

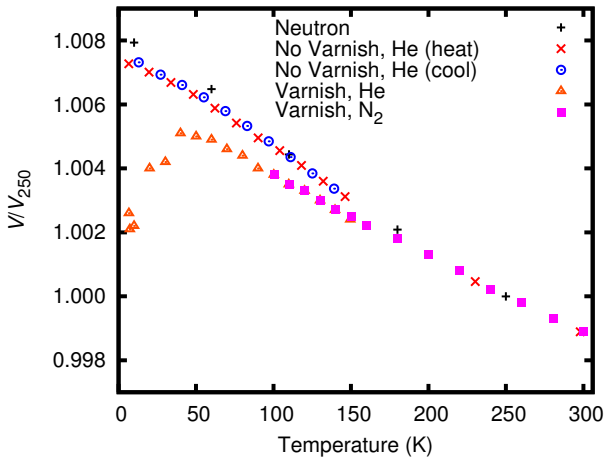

Figure 5.1: Temperature dependence of the unit cell volume for ScF_3 (normalized to 250 K), using two different sample preparation methods. Data from previously reported neutron diffraction measurements [35] are included for comparison. Reproduced with permission of the International Union of Crystallography from ref. [44].

5.3 Results and discussion

5.3.1 Low-temperature thermal expansion of ScF_3 without varnish

The initial low-temperature measurements (6-300 K) on ScF_3 did not use GE-7031 varnish as a sample matrix (*i.e.*, the "no varnish" sample described above). Rietveld analyses of these measurements yielded unit cell volumes for ScF_3 that are generally consistent with previously reported values derived from neutron powder diffraction [35], especially above 100 K, as shown in Figure 5.1 (points labeled "No Varnish, He (heat/cool)" and "Neutron"). However, the difference between the unit cell volumes derived from the X-ray measurements and those from the previous neutron experiments below 100 K raised the possibility that the true sample temperature was higher than the apparent temperature, perhaps by ∼10 K at 50 K (Figure 5.1).

To test this theory, a powder sample of $CuFeO_2$ was obtained and prepared in a way similar to the "no varnish" method described above. $CuFeO_2$ undergoes a clear (by diffraction) symmetry-lowering antiferromagnetic ordering transition at around 11 K [292]. When this "no varnish" sample was cooled to an apparent temperature of ∼6 K, as indicated by the cryostat temperature sensors, no peak splitting indicative of the known $CuFeO_2$ phase transition was observed, implying that the true sample temperature was at least 5 K higher

than that indicated. The unit cell volumes obtained on cooling and heating the "no varnish" ScF_3 sample itself also show signs of mild hysteresis that could be associated with sluggish thermal equilibration (compare the crosses and circles in Figure 5.1).

5.3.2 Low-temperature thermal expansion of ScF_3 embedded in varnish

To improve thermal contact between the sample powder and helium exchange gas, GE-7031 varnish was subsequently used as a sample matrix. Use of the varnish appeared to improve the agreement between the apparent and true sample temperatures, as peak splitting was observed at an apparent temperature of ∼6 K for $CuFeO_2$ in a varnish matrix (below the transition at ∼11 K). However, the agreement between the unit cell volumes of the "varnish" ScF_3 sample and those from the previous neutron study is worse than that observed for the "no varnish" sample (Figure 5.1). There is also considerable peak broadening in the patterns for the "varnish" sample that is not present in the absence of varnish (Figure 5.2). Large unit cell volume discrepancies observed below 150 K are dependent on the sample, not the sample environment; the "varnish" sample gives the same results when a nitrogen Cryostream is used for cooling. Most significantly, while the "no varnish" sample remains cubic down to base temperature and exhibits NTE over the entire temperature range, the "varnish" sample undergoes a cubic-to-rhombohedral phase transition at ∼50 K, accompanied by a change in the sign of the CTE from negative to positive. The reduction in unit cell volume observed for ScF_3 in varnish, compared with the previous neutron results and those for the "no varnish" samples, cannot be explained as arising from improved thermal contact with the sample environment. ScF_3 is a thermomiotic material, so improved thermal contact, which leads to a lower true sample temperature, would cause an increase in the unit cell volume, not a decrease. In the previous neutron diffraction study of ScF_3, a cubic-to-rhombohedral phase transition similar to that observed on cooling the "varnish" sample to 50 K occurred on compression to between 100 and 200 MPa [35]. These two observations strongly suggest that the anomalous behavior of the "varnish" sample arises from stress due to the thermal expansion mismatch between the varnish and ScF_3.

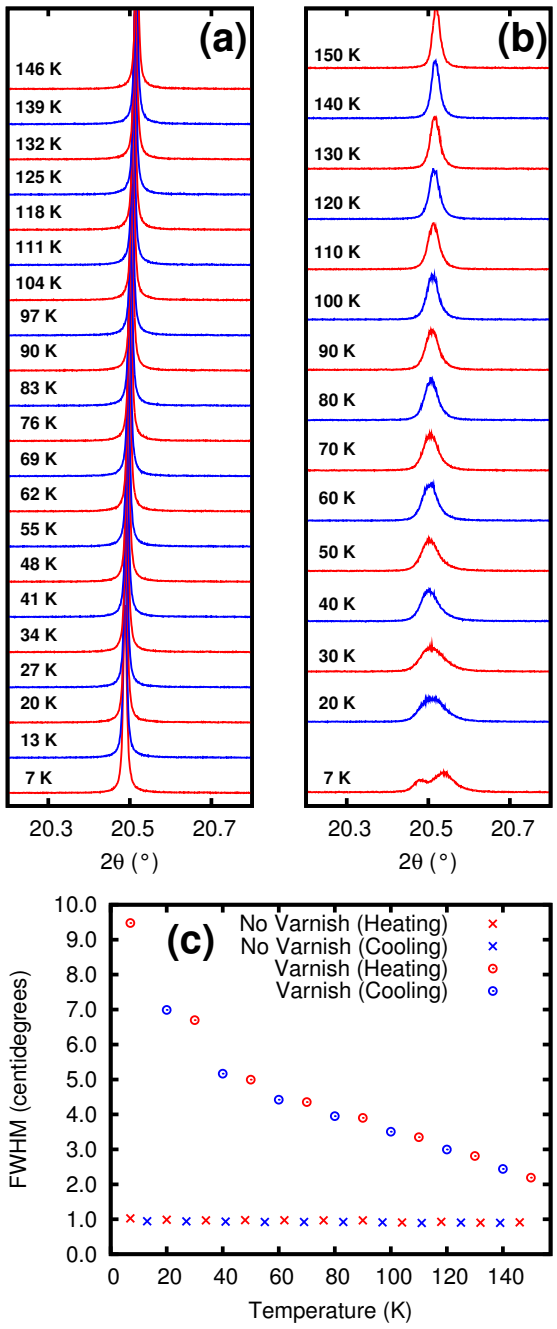

Figure 5.2: Variable-temperature X-ray diffraction data for the (2 2 2) reflection in cubic ScF_3, which splits into the (4 4 4) and (4 0 0) reflections after the cubic-to-rhombohedral phase transition. Panel (a) shows data for the "no varnish" sample, and the lack of peak splitting over this temperature range indicates the lack of a phase transition in this sample. Panel (b) shows data for the sample mixed in GE-7031 varnish; peak splitting is evident in patterns collected at the lowest temperatures. (c) Temperature dependence of the full width at half-maximum (FWHM) for the (2 2 2) reflection. Peak broadening is evident in the varnish-mixed sample, indicative of a stress distribution in the ScF_3/varnish composite. The peak width is fairly constant with temperature in the "no varnish" sample, at roughly the instrumental resolution of 0.01°. Peak widths were measured by fitting a pseudo-Voigt function to the data using *Fityk* [273]. Redrawn from ref. [44].

5.3.3 Stress in ScF_3/varnish mixture

No data on the elastic or thermal expansion properties of GE-7031 varnish were found in the literature. However, assuming that the varnish displays zero thermal expansion and is completely rigid, ScF_3 embedded within it, with an average volume CTE of ∼-30 ppm·K^{-1} and a bulk modulus of ∼60 GPa [35], would experience a stress of ∼450 MPa upon cooling from 300 to 50 K. In reality, the varnish is far from rigid, which would act to considerably reduce the stress on ScF_3 below this crude estimate, but the varnish presumably displays positive thermal expansion, which would serve to increase the stress due to the thermal expansion mismatch. Using the formula of Speight and Lobb [293] for elastic stress at a particle/matrix interface:

$$\sigma = \frac{-6E_m K_p(\alpha_p - \alpha_m)\Delta T}{2E_m + 3K_p(1+\nu_m)} \tag{5.1}$$

and assuming that the Young's modulus (E_m), Poisson's ratio (ν_m), and linear CTE (α_m) of the varnish matrix are 7 GPa, 0.37, and 50 ppm·K^{-1}, respectively, which are typical values for polymers at low temperatures [294], the estimated normal stress σ on the ScF_3 particles (K_p = 60 GPa and α_p = -10 ppm·K^{-1}) upon cooling from 300 to 50 K would be ∼145 MPa. This value is close to that expected to induce the cubic-to-rhombohedral phase transition for ScF_3 at 50 K. For a material with a bulk modulus of 60 GPa, this stress is roughly consistent with the observed difference in V/V_{250} of ∼0.001 at ∼60 K between the "no varnish" and "varnish" samples.

Finally, stresses due to differential thermal expansion would not be completely insignificant even if the filler in the varnish were not a thermomiotic material like ScF_3. Assuming the above estimates for varnish properties are reasonable, a filler with a linear CTE of 10 ppm·K^{-1}, which is not unusual for oxides, would still be expected to experience a stress of nearly 100 MPa. Stress-induced phase transitions due to differential thermal expansion have been previously observed in metal-matrix-ceramic composites where the thermomiotic material ZrW_2O_8 was used as a filler [40].

5.4 Conclusion

Although it allowed for good thermal contact, the use of GE-7031 varnish as a sample matrix for low-temperature X-ray diffraction measurements of ScF_3 resulted in anomalous behavior that is consistent with the presence of considerable stress due to the large thermal mismatch between ScF_3 and the varnish. In general, GE-7031 varnish should not be used as a sample matrix to improve thermal contact where there is likely to be significant thermal expansion mismatch between the varnish and the material under study. Furthermore, the use of ScF_3 in composites for CTE control may be limited due to the relatively modest pressures required for a phase transition and change in thermal expansion behavior. Though the use of ScF_3 in composites may be problematic, another method of CTE control, solid solution formation, is explored in the subsequent three chapters.

CHAPTER 6

THERMAL EXPANSION AND PHASE TRANSITION OF $Sc_{1-x}Ti_xF_3$ ($0 \leq x \leq 1$)

6.1 Introduction[1,2]

As discussed in Chapter 1, thermomiotic materials are of fundamental interest and have potential for application [1, 2, 3, 4, 5, 6, 7, 8]. Careful control of a material's coefficient of thermal expansion (CTE) can reduce stresses due to mismatched CTEs between different components in an assembly, and zero thermal expansion imparts both dimensional stability and good thermal shock resistance. Thermomiotic materials can in principle be used in composites to compensate for the positive thermal expansion (PTE) of other materials [40, 41, 42, 43]. However, the formation of such composites often leads to stresses from CTE mismatch between the components of the composite, which can induce deleterious phase transitions [41, 42, 43, 44]. Tuning the CTE of a monophasic material avoids such problems. Anisotropic thermal expansion even in monophasic materials can cause internal microcracking and hence mechanical failure; therefore, materials displaying isotropic thermal expansion are desirable [1, 2, 3, 4, 5, 6, 7, 8].

As shown in Section 1.2.2, several different mechanisms for negative thermal expansion (NTE) have been established, including transverse thermal motion, whereby lattice modes involving the transverse displacement of atoms or molecular fragments that bridge between coordination polyhedra have large negative Grüneisen parameters [1, 56, 59]. The transverse thermal motion mechanism is responsible for NTE in a variety of oxides, fluorides, cyanides, and MOFs (Section 1.2.4), and, in many cases, probably involves the coupled rocking of more or less rigid coordination polyhedra [56, 59]. This so-called rigid-unit mode

[1] The work presented in this chapter and Appendix B was previously published [238] and is edited to fit the context of this thesis. Reprinted with permission from C. R. Morelock *et al. Chem. Mater.*, 26(5):1936-1940, 2014. Copyright 2014, American Chemical Society.

[2] Supporting material for this chapter can be found in Appendix B.

(RUM) mechanism is perhaps most easily visualized by considering the cubic ReO_3 structure (Figures 1.5 and 1.8), which is related to that of perovskites ABX_3, with a vacant A site that creates significant empty volume [59]. ReO_3 itself displays low PTE at ambient temperature [184, 185, 186], but the isostructural ScF_3 was recently reported to display pronounced thermomiotic behavior at low temperatures ($\alpha_L \approx$ -12 ppm·K^{-1} at 100 K), with its CTE remaining negative up to ∼1100 K [35]. ScF_3 remains cubic over the entire temperature range examined by diffraction (∼10 to 1600 K) at ambient pressure [35]. The thermomiotic behavior of ScF_3 has very strong contributions from low-energy phonons close to the R point, some of which involve the motion of bridging F atoms transverse to the Sc–(F)–Sc axis in a quartic potential [243].

As discussed in Chapter 4, unlike ScF_3, many metal trifluorides MF_3 (M = Al, Cr, Fe, Ga, In, Ti, V) are rhombohedrally distorted (VF_3-type) at ambient conditions [227, 228]. Upon heating, this rhombohedral phase transforms to the cubic ReO_3-type structure via the coupled rotation of MF_6 octahedra. This transition can be visualized as rotation of octahedra about the crystallographic threefold axis (Figure 1.9). This "unfolding" is typically accompanied by significant volume expansion and hence a large positive CTE; however, the high-temperature cubic form displays much lower thermal expansion [226, 227, 228, 234, 235, 236]. TiF_3, for example, has been reported to undergo a first-order phase transition from rhombohedral to cubic symmetry just above room temperature, with strong PTE below and near-zero thermal expansion above the transition [228]. At low temperatures and relatively modest pressures (50 K and ∼150 MPa), ScF_3 undergoes a symmetry-lowering phase transition [35]. The stress required to induce this transition is relatively low; the CTE mismatch between ScF_3 and a polymer matrix is sufficient to induce it upon cooling a composite to 50 K (Chapter 5) [44].

Rare earth metal fluorides such as ScF_3 are potentially of interest for optical applications due to their transparency over a wide wavelength range. In particular, glasses based on ScF_3 are transparent from 300 nm in the ultraviolet region to 7000 nm in the infrared, typically with a classical O–H band around 3000 nm arising from hydroxyl groups trapped during

Table 6.1: Ionic radii of M^{3+} involved in $Sc_{1-x}M_xF_3$, as reported by Shannon [300]

Species	Ionic radius (Å)
Al^{3+}	0.535
Ti^{3+}	0.670
Sc^{3+}	0.745
Y^{3+}	0.900

preparation [295]. A variety of fluoroscandate systems have been explored, including ScF_3–BaF_2–YF_3 [295], ScF_3–BaF_2–ZnF_2 [296], ScF_3–BaF_2–InF_3 [296], and ScF_3–MgF_2 [297]. Crystalline ScF_3 is cubic and thus optically isotropic; a scintered and fully dense polycrystalline body with appropriately tuned thermal expansion characteristics could be of interest for some optical applications.

At least in principle, solid solution formation (introduced in Section 1.2.5) provides a means of controlling the thermal expansion of ScF_3 without forming a composite. There is very little prior work on ScF_3 solid solutions, but phase diagrams have been reported for the YbF_3–ScF_3 and LuF_3–ScF_3 systems [298, 299]; significant solid solubility was reported for both systems at high temperature. In the next three chapters (6, 7, and 8), substitution of three trivalent cations M^{3+} of various sizes into ScF_3 is systematically explored. The cations, Ti^{3+}, Y^{3+}, and Al^{3+}, were chosen because of their sizes relative to Sc^{3+}: closely matched, significantly larger, and significantly smaller, respectively (Table 6.1).

Substitution of Ti^{3+} to form $Sc_{1-x}Ti_xF_3$ ($0 \leq x \leq 1$) is first explored. The ionic radii of Sc^{3+} and Ti^{3+} are similar (0.745 and 0.670 Å, respectively [300]); hence, full solubility of TiF_3 in ScF_3 is to be expected, and there should be no major structural distortions associated with the substitution. However, TiF_3 is known to undergo a cubic-to-rhombohedral phase transition just above room temperature [228], and Ti^{3+} is Jahn-Teller active. Any structural distortion driven by this Jahn-Teller instability is likely to be small, as Ti^{3+} has a single $3d$ electron in its t_{2g} orbitals. The phase transition on cooling TiF_3 breaks the degeneracy of the t_{2g} orbitals and leaves the single d electron in an a_{1g} symmetry orbital [301]. In contrast, MnF_3 has quite significantly Jahn-Teller-distorted MnF_6 octahedra due to the high-spin d^4 Mn^{3+} ion [302].

Figure 6.1: For $Sc_{1-x}M_xF_3$ syntheses, welded nickel (or copper) ampoules were sealed in evacuated fused quartz tubes. This figure shows two reaction vessels containing Ni ampoules prior to heating in a furnace for 72 h.

In this chapter, the preparation, phase transitions, and thermal expansion characteristics of $Sc_{1-x}Ti_xF_3$ ($0 \leq x \leq 1$) between 100 and 500 K are reported.

6.2 Materials and methods

6.2.1 Syntheses and laboratory X-ray diffraction

$Sc_{1-x}Ti_xF_3$ (x = 0.00, 0.10, 0.30, 0.40, 0.50, 0.60, 0.70, 0.85, 1.00) samples were prepared from stoichiometric amounts of ScF_3 (99.99%, American Elements) and TiF_3 (99.99%, Alfa-Aesar) powders. In an inert atmosphere, the powders were thoroughly mixed and pelletized. Each pellet was enclosed in either an arc-welded Cu (for x = 0.00, 0.10, 0.30) or Ni (all other samples) ampoule. The Cu (Ni) ampoules were sealed in evacuated fused quartz tubes, heated at 1273 (1338) K for 72 h, and then quenched by removing from the furnace, which was located in a fume hood. Figure 6.1 shows two reaction vessels prior to heating: Ni tubes in evacuated fused quartz ampoules.

Sample purity and lattice parameters were examined at ambient conditions using a Scintag X1 powder X-ray diffractometer (PXRD) equipped with a Cu $K\alpha$ X-ray source and Peltier cooled solid state detector (Section 2.1). The patterns were analyzed by the Rietveld method (Section 2.4.2.3) in *GSAS* [269, 270], using either a cubic ($Pm\bar{3}m$) or rhombohedral ($R\bar{3}c$) model.

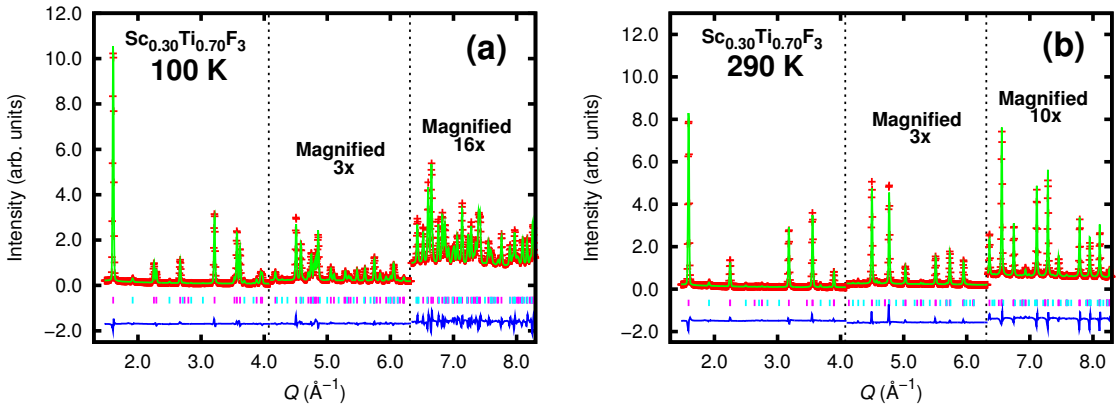

Figure 6.2: Rietveld fits (green line) using a rhombohedral model to data (red +) collected for $Sc_{0.30}Ti_{0.70}F_3$ at (a) 100 and (b) 290 K. In each plot, the difference curve appears in blue, while Bragg peak positions for the main and rutile impurity phases are indicated by magenta and cyan markers (|), respectively. Reproduced from ref. [238].

6.2.2 Variable-temperature synchrotron X-ray diffraction

Variable-temperature PXRD data (100 to 500 K) were collected at beamline 1-BM-C of the Advanced Photon Source, Argonne National Laboratory, Illinois, USA, using the Cryostream setup described in Section 2.2.1.1 and pictured in Figure 2.2.

6.2.3 Data analysis

Area detector images were integrated with *FIT2D* [255], and Rietveld analyses were accomplished using the sequential refinement mode of *GSAS* [269, 270]. General analysis of synchrotron diffraction data is described in Section 2.4.2. A fit to data collected at 100 K was used as a starting point for the sequential analyses in *GSAS*; these fits employed a rhombohedral ($x > 0.10$) or cubic ($x = 0.00$ and 0.10) model for the entire temperature range (100→500 K). The analyses for all samples, except $x = 0.00$, included a rutile-type impurity phase (space group $P4_2/mnm$), as discussed in Section 6.3.1. Representative Rietveld fits using a rhombohedral model are shown in Figure 6.2 for the $x = 0.70$ sample both before (100 K, Figure 6.2a) and after (290 K, Figure 6.2b) its phase transition. A separate set of sequential fits for all the samples was performed using a cubic model over the entire temperature range (500→100 K), with an initial fit to the 500 K data serving as a starting model.

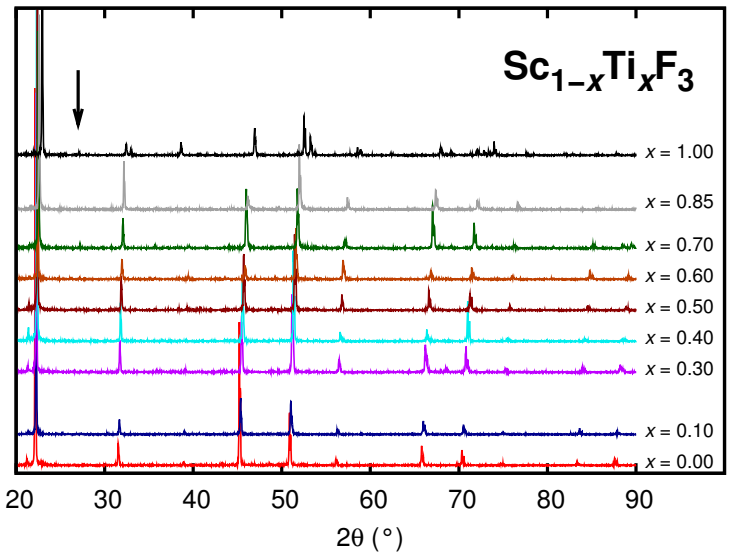

Figure 6.3: Powder X-ray diffraction data collected at ambient conditions on a laboratory diffractometer for $Sc_{1-x}Ti_xF_3$. Most patterns appear to be monophasic, with a few small extra peaks evident in the $x = 0.70$ and 1.00 patterns from a rutile-type impurity (marked with an arrow). In addition, there are small W $L\alpha$ peaks from the X-ray tube, most apparent close to $2\theta = 20°$, just to the left of the leftmost sample peak. Reproduced from ref. [238].

6.3 Results and discussion

6.3.1 Solid solution formation

Ambient laboratory PXRD data (Figure 6.3) suggest that most $Sc_{1-x}Ti_xF_3$ samples are monophasic, with some small extra peaks visible in the patterns for the $x = 0.70$ and 1.00 samples. The much higher signal-to-noise ratio of the synchrotron data reveals small extra peaks in all samples (except $x = 0.00$). These peaks match those of the rutile structure, suggesting that trace water present during the syntheses resulted in the pyrohydrolysis of the fluorides to form TiO_2 or a TiO_2-ScOF solid solution. The variation of the unit cell volume per formula unit for the cubic samples ($x \leq 0.85$) with targeted composition rather closely follows Vegard's Law (Figure 6.4), and the phase transition temperature varies linearly with targeted composition (discussed in Section 6.3.2), indicating that the true compositions of the $Sc_{1-x}Ti_xF_3$ phase are very close to those targeted.

All samples except TiF_3 ($x = 1.00$) are cubic at ambient conditions and show no evidence of TiF_3 exsolution; the annealed TiF_3 sample is rhombohedral at ambient temperature as

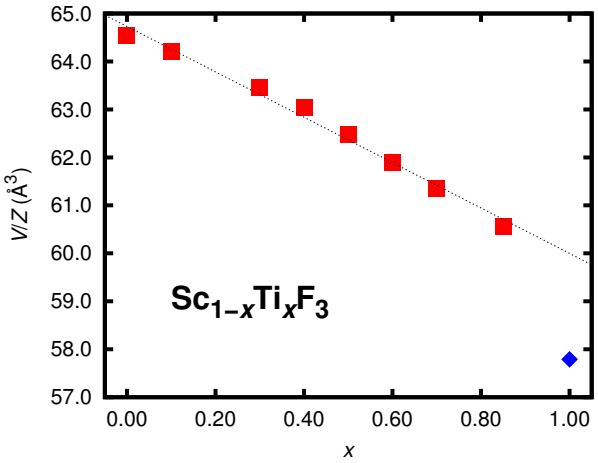

Figure 6.4: Ambient unit cell volumes per formula unit of $Sc_{1-x}Ti_xF_3$ as a function of composition. The dashed line was fit to the data $x \leq 0.90$ (red squares) as a guide to the eye. In this plot, error bars are smaller than the symbols. All samples are cubic at ambient conditions, except for TiF_3 ($x = 1.00$), which is rhombohedral (blue diamond); thus, it does not fit the Vegard's Law linear trend of the others. Reproduced from ref. [238].

expected [228]. The observed complete solid solubility at the synthesis temperature of 1338 K is consistent with the small ionic radius difference between Sc^{3+} and Ti^{3+} (∼10%). Solubility in LnF_3–ScF_3 systems with small lanthanides (Ln) is known to be low at room temperature and strongly dependent on synthesis temperature, as reported for YbF_3–ScF_3 [298] and LuF_3–ScF_3 [299].

6.3.2 Cubic-to-rhombohedral phase transition

Inspection of the synchrotron PXRD data (Figures 6.5, B.1, B.2, and B.3) reveals peak splitting and the appearance of superlattice peaks upon cooling for some samples. These results are indicative of a cubic-to-rhombohedral phase transition, analogous to that observed in several other ReO_3-type fluorides, such as α-AlF_3 [237, 234], InF_3 (Chapter 4), and TiF_3 [226, 228]. The phase transition is not observed for $x < 0.30$ between 100 and 500 K. The effects of the phase transition become more evident as x increases. Figure 6.5 compares variable-temperature PXRD data for the $x = 0.10$ and 0.70 samples to illustrate the changes associated with the phase transition; the effects are visible for $x = 0.70$ (bottom panels) but not for $x = 0.10$ (top panels).

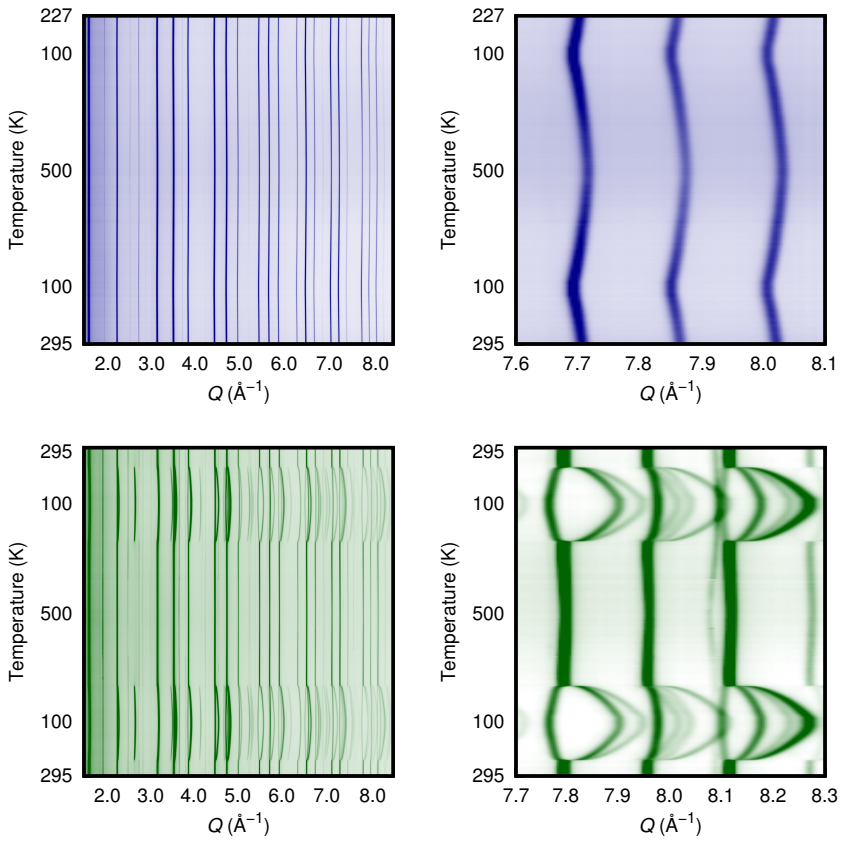

Figure 6.5: Variable-temperature (100 to 500 K) synchrotron PXRD data for $Sc_{0.90}Ti_{0.10}F_3$ (top panels) and $Sc_{0.30}Ti_{0.70}F_3$ (bottom panels). The plots in the left column show the full angular range used for Rietveld analyses, while those on the right show a high-angle portion in which the splittings associated with the phase transition are most apparent. Within each plot, the diffraction patterns are arranged in order of collection from bottom to top, which followed the temperature ramp in Figure 2.2b. Reproduced from ref. [238].

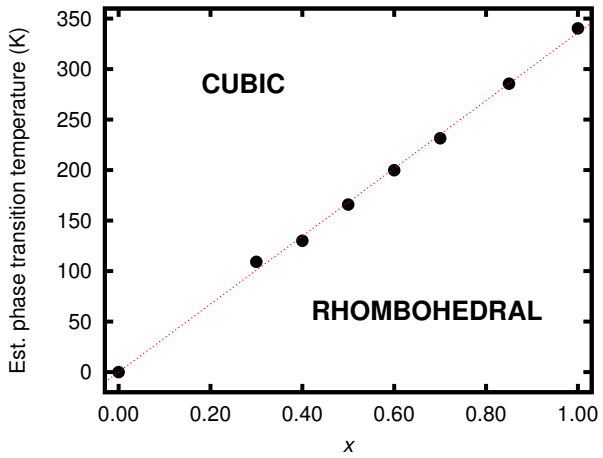

Figure 6.6: Composition-temperature phase diagram for $Sc_{1-x}Ti_xF_3$. The black circles are the experimentally determined transition temperatures, and the red dashed line is a guide to the eye. The transition temperature for ScF_3 is assumed to be 0 K, as it remains cubic down to at least 0.35 K (Chapter 7). Reproduced from ref. [238].

The phase transition temperature for each sample was estimated by following the appearance/disappearance of a supercell peak, which is only present in the low-temperature phase, upon cooling/heating (Figure B.4, Appendix B). These estimates were used to construct a composition-temperature phase diagram for $Sc_{1-x}Ti_xF_3$ (Figure 6.6). For $x \geq 0.30$, the transition temperature increases linearly with titanium content. This behavior is typical for solid solutions in the temperature range where quantum effects are not important [303]. Extrapolation of the linear trend observed for $Sc_{1-x}Ti_xF_3$ to $x = 0.00$ suggests a phase transition temperature of $\sim$0 K for ScF_3, consistent with the observation that ScF_3 does not undergo a phase transition above 10 K [35] as well as the heat capacity measurements in Chapter 7, which do not suggest a phase transition above 0.35 K. Furthermore, the estimated transition temperature for TiF_3 (340 K) is in excellent agreement with that previously measured by calorimetry (340 K) [226] and somewhat close to that reported in a prior synchrotron diffraction study (370 K) [228].

The thermally induced cubic-to-rhombohedral phase transition observed in ReO_3-type MF_3 is typically first-order, with a sharp volume discontinuity at the phase transition temperature [228]. Ti^{3+} is quite closely size-matched to Sc^{3+}, and the phase transition in $Sc_{1-x}Ti_xF_3$ is clearly first-order for large values of x; the unit cell volume changes abruptly

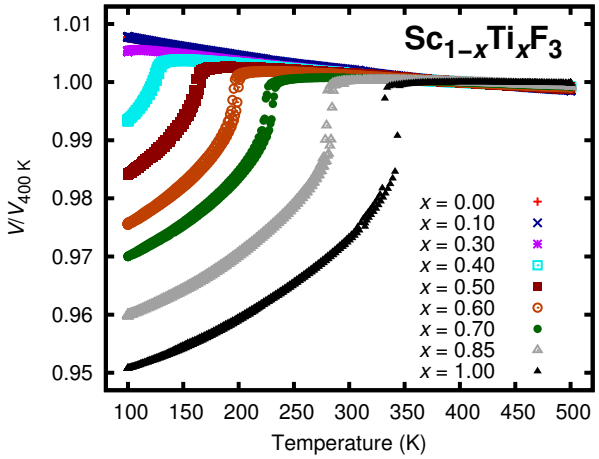

Figure 6.7: Normalized unit cell volumes for $Sc_{1-x}Ti_xF_3$ plotted with respect to temperature. The Rietveld-derived unit cell volumes V were divided by the experiment-averaged volume at 400 K (V_{400K}). Reproduced from ref. [238].

at the phase transition (Figure 6.7).

6.3.3 Thermal expansion

The temperature dependence of V/V_{400K} for each sample is shown in Figure 6.7. The unit cell volumes per formula unit (V/Z) were determined from Rietveld analyses (Figure B.5, Appendix B) and normalized by the value at 400 K (V_{400K}). The temperature dependence of the volume CTE, α_V, for each sample is shown in Figure 6.8; these CTEs were estimated by fitting polynomials to the V/Z *versus* T curves. Figure 6.8b expands the region of 6.8a between 350 and 470 K, and the average CTE for each composition over that temperature range is shown in the inset.

In the temperature range over which the materials are rhombohedral, their volume CTEs are strongly positive and their thermal expansion highly anisotropic (Figure B.6). On cooling, the quite rigid MF_6 octahedra rotate around the crystallographic threefold axis (Figure 1.9), leading to a reduction in the unit cell constant a_H while c_H expands; thus, c_H/a_H increases rapidly (Figure 6.9).

On heating to temperatures near the phase transition, the volume CTE increases quite rapidly. Immediately after the transition, the CTE becomes small and positive but then negative on further heating. Consistent with a previous diffraction study [228], cubic TiF_3

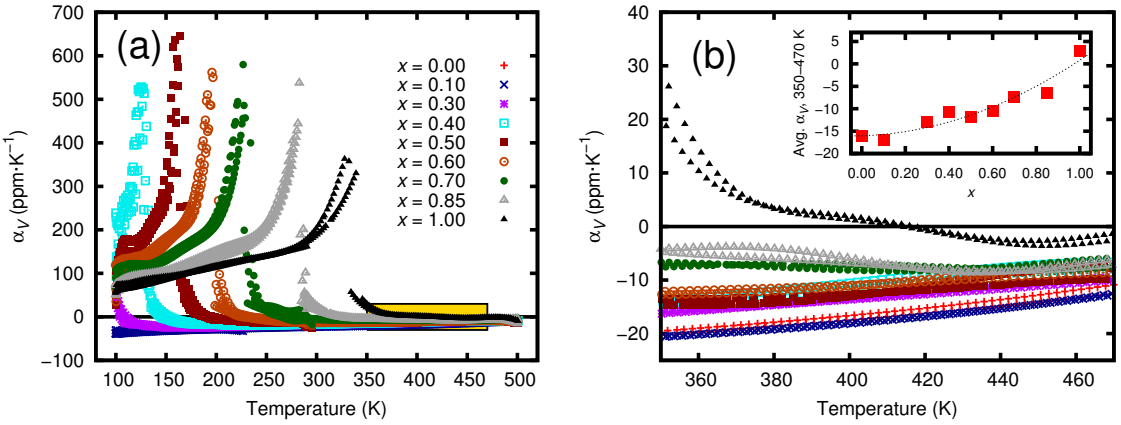

Figure 6.8: (a) Temperature dependence of the volume CTE (α_V) for each $Sc_{1-x}Ti_xF_3$ sample, estimated by fitting polynomials to the V/Z *versus* T data. (b) Expansion of the highlighted portion of panel (a). In the inset of (b), showing the average CTE of each sample from 350 to 470 K, the dashed curve is a guide to the eye. Reproduced from ref. [238].

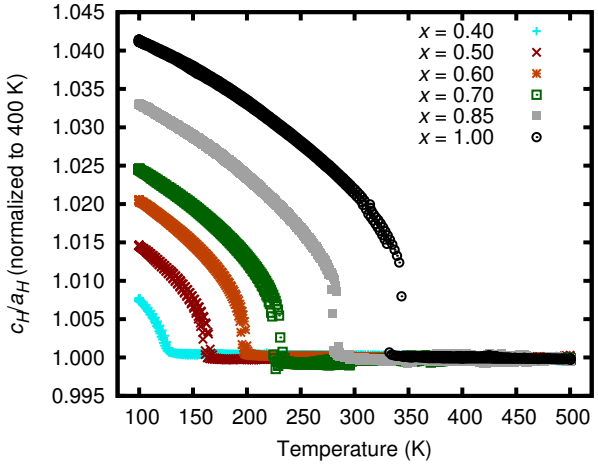

Figure 6.9: Temperature dependence of the ratio of hexagonal lattice constants c_H/a_H for several $Sc_{1-x}Ti_xF_3$, normalized to the value at 400 K. Reproduced from ref. [238].

exhibits low PTE at temperatures just above the phase transition and then low NTE at higher temperatures.

As shown in Figure 6.8b, the formation of $Sc_{1-x}Ti_xF_3$ enables some control of thermal expansion, but the occurrence of the cubic-to-rhombohedral phase transition limits the temperature range over which useful tuning might be achieved. The average CTE between 350 and 470 K generally increases with Ti composition; this temperature range is just above the phase transition for TiF_3, which hence has the most variation in CTE over this temperature range (positive to low negative). A similar trend to that in the inset results when using a different temperature range to calculate the average, such as 420 to 470 K, but with a much lower (low negative) value for TiF_3. The small amount of scatter in the inset may partly arise from minor variations in the position of the Cryostream from experiment to experiment, affecting the accuracy of sample temperature estimation and thus the estimated CTE.

6.4 Conclusion

As TiF_3 is fully soluble in ScF_3, the negative thermal expansion of $Sc_{1-x}Ti_xF_3$ is tunable at high temperatures between the behaviors of the end members. However, the temperature range over which controllable NTE can be achieved is limited by the cubic-to-rhombohedral ferroelastic phase transition that is observed in this system. The transition temperature varies in a linear fashion with composition, as commonly observed for solid solutions.

The study of $Sc_{1-x}M_xF_3$ solid solutions continues in Chapters 7 and 8 using MF_3 that are not fully soluble in ScF_3.

CHAPTER 7

THERMAL EXPANSION, COMPRESSIBILITY, AND HEAT CAPACITY OF $Sc_{1-x}Y_xF_3$ ($x \leq 0.25$)

7.1 Introduction[1,2]

As discussed in previous chapters, cubic ScF_3 displays pronounced isotropic negative thermal expansion (NTE) at low temperatures ($\alpha_L \approx -14$ ppm·K^{-1}, 60-110 K), with NTE persisting to ∼1100 K [35]. The simple structure of ScF_3 allows for relatively easy examination of the underlying phenomena leading to NTE, and the material is amenable to chemical substitution. In Chapter 5, the possible limitations of ScF_3 in composites for controlled thermal expansion were discussed. The possibility of CTE control through solid solution formation with TiF_3 was demonstrated in Chapter 6 [238]. However, the temperature range over which controllable NTE can be achieved in $Sc_{1-x}Ti_xF_3$ is limited by a cubic-to-rhombohedral ferroelastic phase transition.

The study of ScF_3 solid solutions continues in this chapter, in which Y^{3+} substitution is used to form $Sc_{1-x}Y_xF_3$. The solubility limit of YF_3 in ScF_3 is restricted by the significant difference in ionic radius between Sc^{3+} and Y^{3+} (0.745 and 0.900 Å, respectively [300]). The relatively large difference in ionic radius (21%) between Sc^{3+} and Y^{3+} provides an opportunity to examine how the structural distortions that must be associated with this size mismatch affect physical properties. In this chapter, the thermal expansion behavior from 100 to 800 K, effects of pressure on thermal expansion, and heat capacities of $Sc_{1-x}Y_xF_3$ ($x \leq 0.25$) are reported.

[1]The work presented in this chapter and Appendix C was previously published [247] or is part of an upcoming publication [304] and is edited to fit the context of this thesis. Reprinted with permission from C. R. Morelock *et al. J. Appl. Phys.*, 114(21):213501, 2013. Copyright 2013, AIP Publishing LLC.

[2]Supporting material for this chapter can be found in Appendix C.

7.2 Materials and methods

7.2.1 Synthesis and initial characterization

For non-ambient synchrotron powder X-ray diffraction (PXRD), $Sc_{1-x}Y_xF_3$ ($x = 0.00$, 0.05, 0.10, 0.20, 0.25, 0.30, 0.40) samples were prepared via the solid-state stoichiometric reaction of ScF_3 and YF_3 powders (both American Elements, 99.99%) in a similar process to that described in Section 6.2.1. In an argon-filled glove box, the powders were thoroughly mixed and pelletized; each pellet was enclosed in a Cu ampoule made by crushing the ends of a ∼5 cm length of oxygen-free Cu tube [305]. The Cu ampoules were then sealed in an evacuated fused quartz tube, along with a small amount of Ti sponge that served as a gettering agent. The tubes were heated at 1283 K for 72 h and then quenched by removing from the furnace, which was located in a fume hood.

$Sc_{1-x}Y_xF_3$ ($x = 0.05$, 0.10, 0.20, 0.25) samples for heat capacity measurements were prepared similarly. However, arc-welded Ni ampoules were used instead of crimped Cu, no gettering agent was used, and the tubes were heated at 1338 K for 72 h. After laboratory powder X-ray diffraction, the solid solution samples as well as a sample of ScF_3 were then pressed (2.0 GPa) and scintered at 1338 K in vacuum.

Ambient laboratory PXRD patterns were analyzed with the Rietveld method using *GSAS* [269, 270]. A cubic structural model (space group $Pm\bar{3}m$) was used for the analyses of all ambient data. In the $x = 0.30$ and 0.40 samples, several extra peaks were present that matched those of orthorhombic YF_3 ($Pnma$). The Rietveld analyses for these samples included YF_3 as a second phase.

7.2.2 Non-ambient synchrotron powder X-ray diffraction

Variable-temperature PXRD data (100 to 800 K) were collected at beamline 1-BM-C of the Advanced Photon Source (APS), Argonne National Laboratory, Illinois, USA, using the Cryostream (Figure 2.2) and wire-wound furnace (Figure 2.3) setups described in Section 2.2.1.1.

High-pressure/temperature data were collected using beamline 11-ID-B at the APS.

These measurements used the MK2BRIM discussed in Section 2.2.2 and Chapter 3. Measurements were performed at 0.034, 0.069, 0.103, 0.138, 0.172, 0.207, 0.241, and 0.276 GPa for each of the following temperatures: 298, 343, 388, 433, 478, and 523 K. However, the highest pressure (0.276 GPa) was not used for the two highest temperatures.

7.2.3 Analysis of non-ambient data

As discussed in Section 2.4.2, all 2D detector images were integrated with the program *FIT2D* [255]. Rietveld analyses were accomplished using *GSAS* [269, 270]. *SEQGSAS*, the batch analysis mode of *GSAS*, was used to analyze the variable-temperature diffraction patterns.

A fit of a rhombohedral ($R\bar{3}c$) structural model to data collected at 100 K was used as the starting point for *SEQGSAS* analyses. As each Cryostream measurement included two heating and two cooling ramps, there were a total of four *SEQGSAS* analyses for each measurement. A representative Rietveld fit to the ambient-pressure, variable-temperature data is shown in Figure 7.1a. A separate set of *SEQGSAS* runs was also performed using a cubic ($Pm\bar{3}m$) model. These analyses employed a fit to the 500 K data as a starting point. In each Rietveld fit of Cryostream data, the lattice parameters, isotropic atomic displacement parameters for Sc and Y (constrained to be identical), anisotropic atomic displacement parameters for F, scale factor, and a pseudo-Voigt profile function with three terms were refined; the background was modeled using a shifted Chebyschev function. For the $x = 0.25$ sample only, Rietveld refinements with anisotropic atomic displacement parameters for F were unstable above roughly the phase transition temperature, so its atomic displacement parameter was constrained to be isotropic at high temperatures.

All samples were cubic over the entire temperature range of the furnace experiments (>323 K); thus, a fit to data collected at 323 K using the $Pm\bar{3}m$ model was used as the starting point for their batch analyses.

During the analyses of high-pressure data acquired in the MK2BRIM, some regions of the diffraction patterns were excluded from the fits due to shadowing by the beam stop and residual scattering from the Ti pressure vessel. A cubic structural model was used

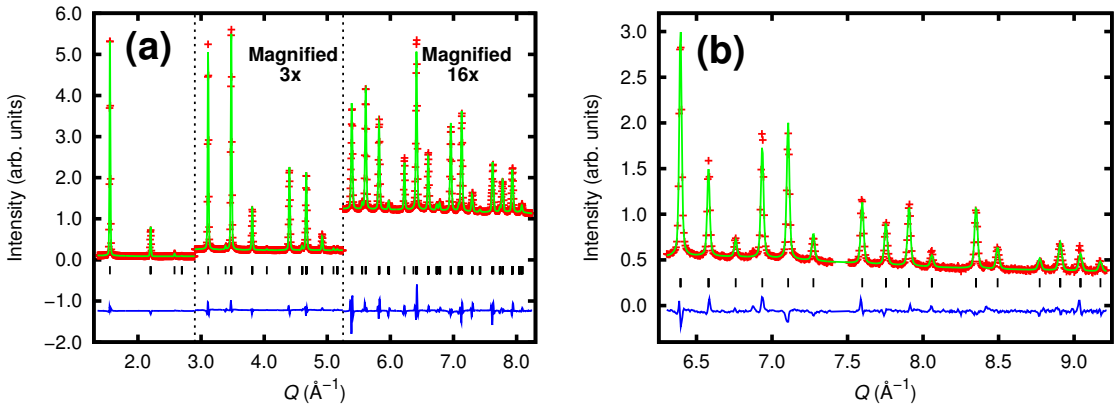

Figure 7.1: (a) Rietveld fit (green line) to data (red +) collected for $Sc_{0.90}Y_{0.10}F_3$ at 100 K and ambient pressure in the Cryostream setup, using a rhombohedral model. (b) Rietveld fit (green line) to diffraction data (red +) for $Sc_{0.80}Y_{0.20}F_3$ under ambient conditions in the high-pressure sample environment, using a cubic model. The data around $Q = 7.4$ Å^{-1} were excluded from the analysis due to scattering from the Ti pressure cell. In both plots, the residual curve appears in blue, and the reflection markers (black |) indicate Bragg peak positions. Reproduced from ref. [247].

exclusively for these analyses, as the diffraction patterns showed no supercell reflections or peak splittings within experimental resolution. Figure 7.1b shows an example fit to the data recorded in the high-pressure sample environment. In the Rietveld analyses of high-pressure data, the cubic lattice constant, isotropic atomic displacement parameters for Sc and Y (constrained to be identical), anisotropic atomic displacement parameters for F, scale factor, and three parameters of a pseudo-Voigt profile function were refined; the background was modeled using a shifted Chebyschev function. As the high-pressure measurements were performed over two blocks of beam time with somewhat different calibrations, the unit cell volume data for the solid solutions were placed on the same scale using diffraction patterns for a CaF_2 sample that was examined during both beam times.

7.2.4 Heat capacity measurements

Experimental information for the heat capacity measurements of $Sc_{1-x}Y_xF_3$ are given in Section 2.3.

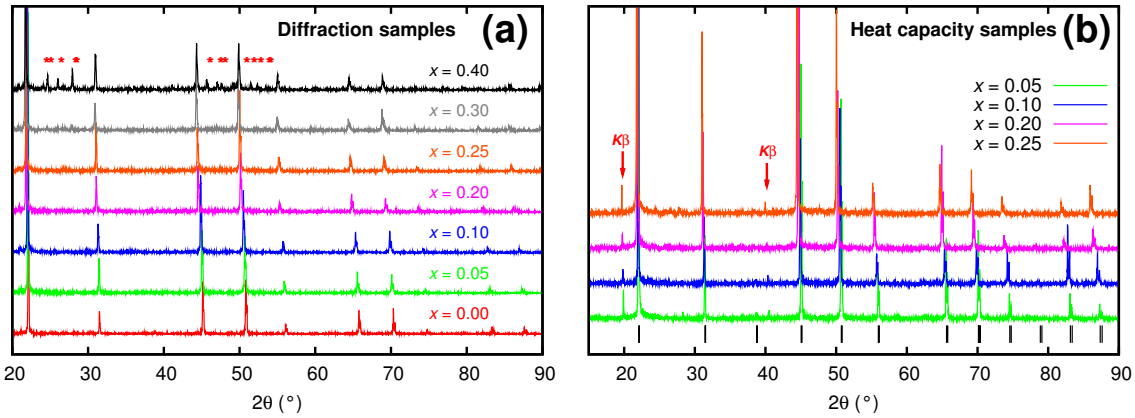

Figure 7.2: Powder X-ray diffraction (PXRD) data collected at ambient conditions on a laboratory diffractometer (Cu Kα radiation) for several $Sc_{1-x}Y_xF_3$: (a) samples used for synchrotron diffraction and (b) heat capacity measurements. In (a), reflections from insoluble YF_3 are indicated by red $*$, while in (b), K_β peaks from the X-ray tube are marked by red arrows. Reproduced from ref. [247, 304].

7.3 Results and discussion

7.3.1 Solubility of YF_3 in ScF_3

Ambient laboratory diffraction data (Figure 7.2) suggest that all $Sc_{1-x}Y_xF_3$ with $x \leq 0.25$ consist of a single cubic phase ($Pm\bar{3}m$). The patterns for $x = 0.30$ and 0.40 show several extra peaks matching those of orthorhombic YF_3 ($Pnma$), indicating a solubility limit of 25-30% at a reaction temperature of 1283 K. The ambient cubic lattice constants obtained by Rietveld analysis vary linearly with composition for $x \leq 0.25$, in agreement with Vegard's Law (Figure 7.3). Above $x \approx 0.25$, the lattice constant is no longer sensitive to YF_3 content; the values for the $x = 0.30$ and 0.40 samples are consistent with a solubility limit of $x \approx 0.28$. Estimated lattice constants for the heat capacity samples (Figure 7.3) are lower than those of the other samples for all compositions, suggesting possible differences in actual yttrium content between two samples with the same nominal content. Alternatively, the difference in quenching temperature between the two sets of reactions (1273 and 1338 K) may actually produce samples with the same yttrium content but slightly different lattice constants.

The solubility limit of YF_3 in ScF_3 is similar to that observed by Fedorov *et al.* in the YbF_3–ScF_3 system (25-30% at 1273 K), although Yb^{3+} is slightly smaller than Y^{3+} [300].

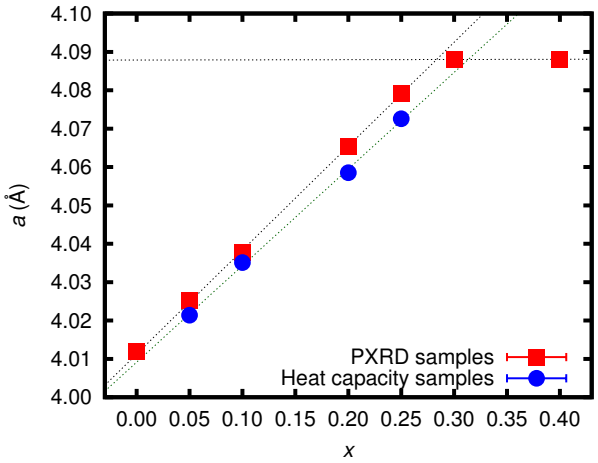

Figure 7.3: Ambient cubic lattice constant a of $Sc_{1-x}Y_xF_3$ samples used for synchrotron PXRD (red boxes) and heat capacity measurements (blue circles). The dashed lines are linear fits to the data; the intersection of the black lines is an estimate of the solubility limit of YF_3 in ScF_3 for the samples quenched from 1283 K. In this plot, error bars are smaller than the point size. Redrawn from ref. [247].

In the YbF_3–ScF_3 system, however, solubility was strongly temperature-dependent, ranging from a few percent at low temperature to ~44% at 1338 K [298]. The solubility of LuF_3 in ScF_3 has been reported to reach a maximum of 45% and to be less temperature-dependent [299]. The high-temperature diffraction data in Figure C.1 (Appendix C) show that, for some samples, YF_3 comes out of solution on heating to >800 K, which is consistent with a strong temperature dependence for the solid solubility of YF_3 in ScF_3.

The large size difference between Sc^{3+} and Y^{3+} (21%) is responsible for the relatively low solubility of YF_3. Furthermore, the difference in structure type between ScF_3 and YF_3 precludes full solubility. From the slope of the a *versus* x plot (Figure 7.3), the lattice constant of the hypothetical ReO_3-type YF_3 is estimated to be $a = 4.281$ Å. Assuming that all Y–F–Y links in the hypothetical material are linear, this value suggests an effective ionic radius for Y^{3+} of 0.880 Å, somewhat smaller than the value given by Shannon (0.900 Å) [300]. This discrepancy may be due to errors in the radius estimates, compressed Y–F bond lengths, or structural buckling (nonlinear M–F–Y links) in the solid solutions.

The relatively low solubility of YF_3 in ScF_3 contrasts with the full solubility of TiF_3 at a similar reaction temperature (Figure 6.4), which is again due to the sizes of Y^{3+} and

Ti^{3+} relative to that of Sc^{3+}.

7.3.2 Cubic-to-rhombohedral phase transition on cooling

The variable-temperature diffraction data (Figures C.2 and C.3) show peak splittings and the appearance of superlattice peaks at low temperature, indicative of a symmetry-lowering phase transition. The high signal-to-noise ratio of the synchrotron data also reveals some small extra peaks. The nature of the impurities could not be identified, but the presence of YF_3, Y_2O_3, Sc_2O_3, YOF, and ScOF was excluded.

Initial Rietveld analyses confirmed that the cubic ($Pm\bar{3}m$) materials become rhombohedral ($R\bar{3}c$) on cooling, as previously reported for several other MF_3 with ReO_3 structures [227, 228], as well as $Sc_{1-x}Ti_xF_3$ (Chapter 6), but unlike ScF_3, which does not show a phase transition at ambient pressure between 0.4 and 1600 K [35, 304]. This cubic-to-rhombohedral transition involves the cooperative rotation of the constituent MF_6 octahedra [306] ($a^-a^-a^-$ type in Glazer notation [307]). The phase transition temperature for each solid solution was estimated from peak broadening at low temperatures (Figure C.4).

A composition-temperature phase diagram is shown in Figure 7.4. The transition temperature increases rapidly on initial doping and plateaus at below ∼200 K. The transition temperature is lower than the volume maximum in the volume *versus* temperature curve for each sample (Figure 7.5), which may be associated with changes in the local structure prior to the onset of long-range cooperative MF_6 tilting at the phase transition temperature. Unlike the symmetry-lowering phase transitions observed in many ReO_3-type MF_3 on cooling, including $Sc_{1-x}Ti_xF_3$ (Chapter 6), the transition in $Sc_{1-x}Y_xF_3$ is clearly not first-order. The distortion associated with the phase transition evolves quite slowly with temperature and is small even well below the transition temperature; at 100 K, the rhombohedral unit cell angle, α, for the $x = 0.25$ sample is only ∼59.75°, corresponding to a rotation of the octahedra around ⟨111⟩, ω, of ∼6° (Figure C.5). It has been argued that the cubic-to-rhombohedral phase transition in ReO_3-type MF_3 occurs in part because the displacement of F away from its ideal position in the cubic structure leads to a set of energetically favorable dipole-dipole interactions [308]. In $Sc_{1-x}Y_xF_3$, the size mismatch between Y^{3+} and

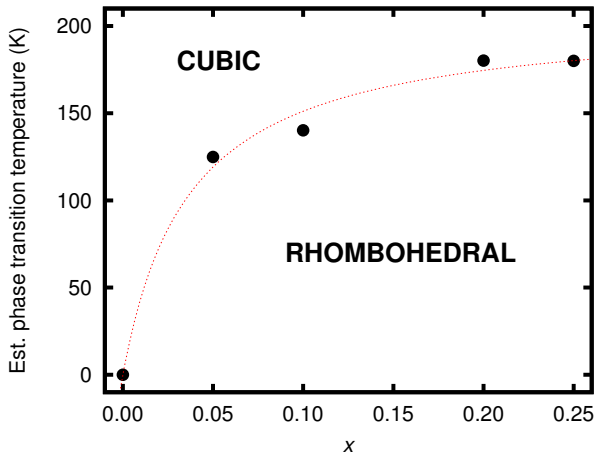

Figure 7.4: Composition-temperature phase diagram for $Sc_{1-x}Y_xF_3$. The red dashed curve is a guide to the eye. The black circles are the experimentally estimated transition temperatures. The transition temperature for ScF_3 is assumed to be 0 K, as it is known to remain cubic down to at least 0.35 K (Figure 7.11). Reproduced from ref. [247].

Sc^{3+} may well be accommodated by local structural distortions that lead to a disordered arrangement of fluoride displacements. The existence of quite large off M–(F)–M axis static displacements for the fluoride ions is supported by an examination of the atomic displacement parameters (ADPs) as a function of temperature (Figure C.6); an extrapolation of the transverse component of the ADP (U_{22}) for fluoride in the cubic phase to 0 K yields quite large values, suggesting considerable static displacements in the solid solutions. This displacement of fluoride in the solid solutions may contribute to the occurrence of the phase transition even at very low doping levels. The disorder associated with accommodating Y^{3+} in a ScF_3 matrix may also be responsible for the very small rhombohedral strains below the phase transition temperature, as they could interfere with the cooperative tilting of MF_6 octahedra.

7.3.3 Thermal expansion at ambient pressure

The unit cell volume per formula unit (V/Z), normalized by the value at 400 K (V_{400K}) and averaged across all heating/cooling cycles, is plotted with respect to temperature for each sample in Figure 7.5. The temperature dependence of the volume CTE for each sample, estimated by fitting sixth-order polynomials to the V/Z *versus* T curves, is shown in Figure

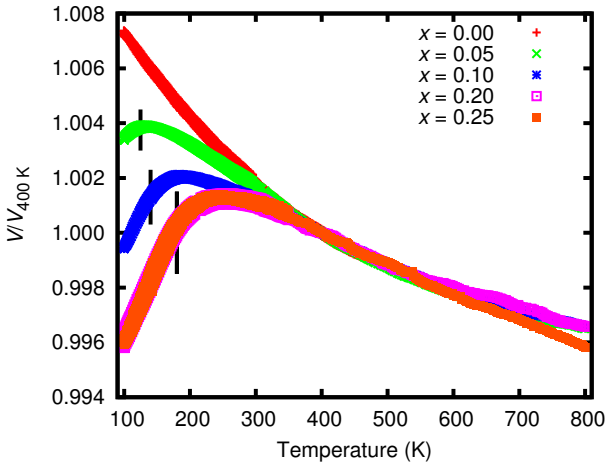

Figure 7.5: Normalized unit cell volumes for $Sc_{1-x}Y_xF_3$ plotted with respect to temperature. The Rietveld-derived unit cell volumes V were divided by the experiment-averaged volume at 400 K (V_{400K}). Reproduced from ref. [247].

7.6.

At low temperatures, the volume CTE, α_V, changes rapidly with temperature and depends strongly on composition due to the cubic-to-rhombohedral phase transition. Below the phase transition temperature, the expansion of the samples is quite strongly anisotropic (Figure C.5). The anisotropy was evaluated by converting the primitive rhombohedral cell constants, a_R and α_R, to the equivalent hexagonal values, a_H and c_H, by Equations 4.1 and 4.2. Lattice parameter a_H contracts quite strongly on cooling below the phase transition temperature, as expected for coupled rotation of quite rigid MF_6 octahedra around the crystallographic threefold axis, while c_H expands.

While CTE is significantly dependent on composition at temperatures immediately above the phase transition, α_V is largely independent of x above ~400 K and slowly increases with temperature for all x up to at least 800 K while remaining negative. This near-independence of CTE and composition is unexpected. The thermal expansion of a material is intimately related to its phonon density of states (PDOS) and the volume dependence of phonon frequencies [9, 10]. The occurrence of a cubic-to-rhombohedral phase transition on cooling, which is presumably associated with a mode softening, and the local strains and distortions associated with substituting the large Y^{3+} into ScF_3 are all suggestive of changes in the PDOS when solid solutions are formed.

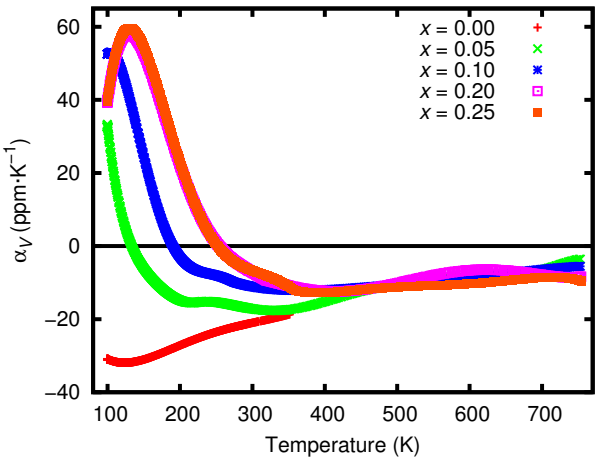

Figure 7.6: Temperature dependence of volume CTE (α_V) for each $Sc_{1-x}Y_xF_3$ sample. Reproduced from ref. [247].

7.3.4 Effect of composition on the isothermal bulk modulus and thermal expansion under pressure

All diffraction patterns acquired at high pressure for $Sc_{1-x}Y_xF_3$ are shown in Appendix C (Figures C.8, C.9, C.10, C.11, and C.12). These data were analyzed using a cubic model, as there are no noticeable peak splittings or superlattice peaks that might indicate a transformation to lower symmetry. Unit cell volumes were determined by Rietveld analysis. The variation of $\ln V$ with respect to both pressure and temperature was plotted, and straight-line fits to these plots were used to estimate average isothermal bulk moduli and volume CTEs. Isotherm and isobar plots for pure ScF_3 ($x = 0.00$) are presented in Figures 7.7a and 7.8a, respectively, and the corresponding plots for $Sc_{0.75}Y_{0.25}F_3$ are shown in Figures 7.7b and 7.8b for comparison. Isotherm and isobar plots for the other compositions are included in Appendix C (Figures C.13 and C.14, respectively).

The average values of isothermal bulk modulus (K_T) for each composition are plotted with respect to temperature in Figure 7.9, and the average α_V values (298-523 K) of each sample are plotted with respect to pressure in Figure 7.10. In the temperature and pressure ranges studied, the bulk modulus and CTE of undoped ScF_3 are almost invariant with temperature and pressure, respectively (Figures 7.9 and 7.10). However, this independence is changed by insertion of Y^{3+} into the ScF_3 framework. The average isothermal bulk moduli

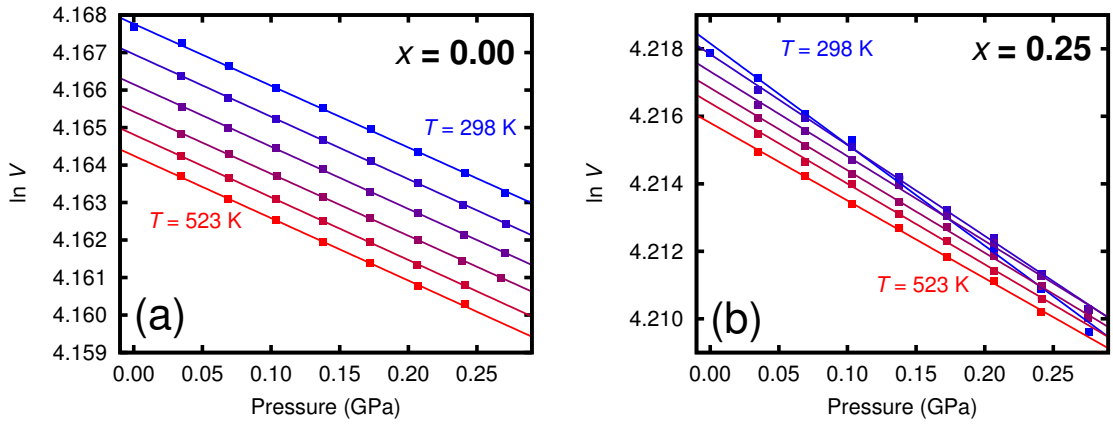

Figure 7.7: Natural logarithm of unit cell volume ($\ln V$; units of V are Å^3) plotted with respect to pressure at various temperatures (298, 343, 388, 433, 478, and 523 K) for (a) undoped ScF_3 ($x = 0.00$) and (b) $Sc_{0.75}Y_{0.25}F_3$. Linear fits to the data are included in the plots. For each sample, the lowest temperature points are in blue, and the highest temperature points are in red. In both plots, the error bars are smaller than the point size. Reproduced from ref. [247].

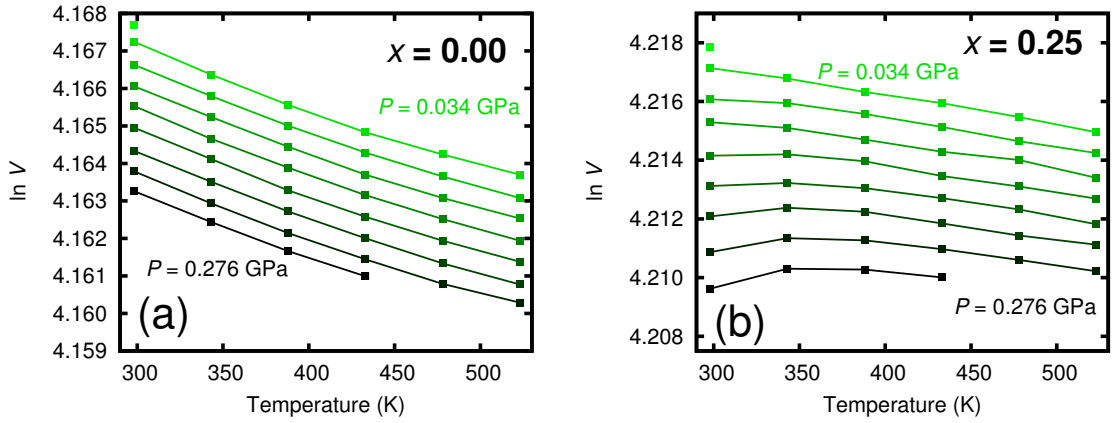

Figure 7.8: Natural logarithm of unit cell volume ($\ln V$; units of V are Å^3) plotted with respect to temperature at various pressures (0.034, 0.069, 0.103, 0.138, 0.172, 0.207, 0.241, and 0.276 GPa) for (a) undoped ScF_3 ($x = 0.00$) and (b) $Sc_{0.75}Y_{0.25}F_3$. The data points are connected with line segments as a guide to the eye. For each sample, the lowest pressure points are in green and have the highest volumes; conversely, the highest pressure points are in black and have the lowest volumes. The single unconnected point at 300 K was measured at $P = 0$. In both plots, error bars are smaller than the point size. Reproduced from ref. [247].

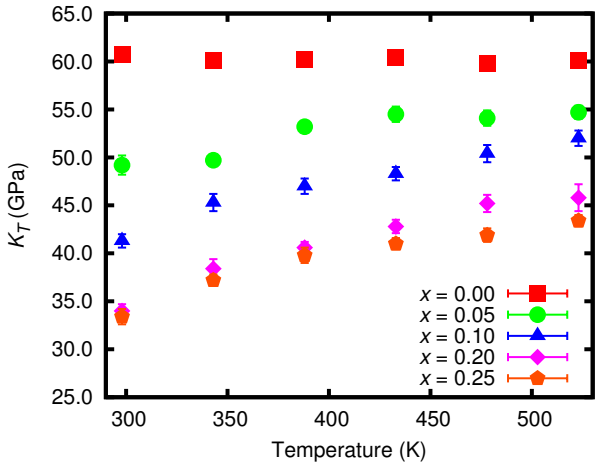

Figure 7.9: Average isothermal bulk moduli (K_T) of $Sc_{1-x}Y_xF_3$ plotted with respect to temperature. Reproduced from ref. [247].

increase on heating, and the CTEs become more positive on compression. At ambient temperature, the bulk modulus for pure ScF_3 is ~60 GPa, in good agreement with prior reports [35]. Fang and Dove have recently reported that many thermomiotic materials are likely to become softer on compression [107]. However, the absence of obvious downward curvature in the $\ln V$ *versus* P plot (Figure 7.7a) indicates that ScF_3 does not show pressure-induced softening within the accuracy of the measurements.

Yttrium substitution leads to a reduction in bulk modulus regardless of temperature; in the $x = 0.25$ sample, K_T is reduced by ~25% relative to ScF_3 at 523 K. The plots of $\ln V$ *versus* T for $x = 0.20$ and 0.25 (Figures C.14c and 7.8b, respectively) go through maxima on cooling at high pressure, similar to that observed at ambient pressure and cryogenic temperatures. The slight volume reduction on cooling after going through the maxima is presumably associated with local structural changes that are a precursor to a phase transition at lower temperatures or higher pressures. As the temperature for the cubic-to-rhombohedral phase transition is expected to increase on compression, these transition precursor effects are observed near ambient temperature, rather than cryogenic temperatures, when the samples are compressed. In addition, the relationship of $\ln V$ and P is not highly linear for higher x, especially at low T ($x = 0.25$, Figure 7.7b); the shapes of these isotherm curves appear somewhat concave-down, indicating pressure-induced softening, consistent

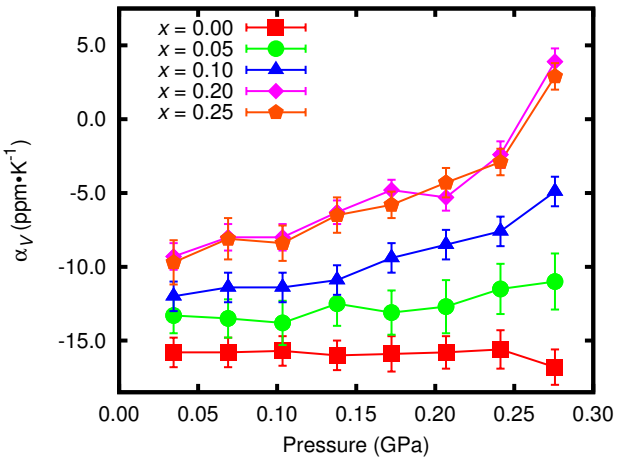

Figure 7.10: Average volume coefficients of thermal expansion (α_V) of $Sc_{1-x}Y_xF_3$ plotted with respect to pressure. The average α_V were calculated over a temperature range of 298-523 K, except for those at the highest pressure (298–433 K). The data points are connected with line segments as a guide to the eye. Reproduced from ref. [247].

with the behavior reported for $Zn(CN)_2$ and various thermomiotic zeolites [107, 108, 109].

A recent high-pressure X-ray and neutron diffraction study of cubic ScF_3 revealed a phase transition to rhombohedral symmetry between ∼0.5 and 0.8 GPa at ambient temperature, consistent with prior high-pressure micro-Raman work [244, 245, 246]. The critical pressure of ScF_3 was also reported to increase with temperature [35]. Similar to other ReO_3-type materials, the bulk moduli for the two phases of ScF_3 were reported to be significantly different; K_0 at room temperature changed from 57(3) to 9(3) GPa between the cubic and rhombohedral phases [35, 223]. Consistent with these observations, a phase transition is not observed in undoped ScF_3 in the pressure and temperature range studied (below 0.276 GPa, 298-523 K).

Materials with the VF_3-type structure are typically highly compressible but do not undergo phase transitions on modest compression [239, 240, 241, 242]. In this structure, the M–F–M links are bent, and further reduction of this bond angle on compression provides an energetically low-cost path for volume reduction, leading to much lower bulk moduli than those observed for materials with the cubic ReO_3-type structure, in which these same links are linear. In $Sc_{1-x}Y_xF_3$, insertion of the relatively large Y^{3+} into the ScF_3 matrix presumably locally distorts the ideal cubic structure. Local bending of M–F–M may be responsible

for the observed reduction in bulk moduli on yttrium substitution (Figure 7.9), as changes in already bent M–F–M bond angles on compression could provide a relatively low-energy path for volume reduction. The temperature dependence of the bulk moduli for the solid solutions could be a reflection of thermally induced changes in local structure, as suggested above in the discussion of the maxima in the $\ln V$ *versus* T plots for $x = 0.20$ and 0.25 (Figures C.14c and 7.8b). The pronounced stiffening on heating exhibited by $Sc_{1-x}Y_xF_3$ has not been observed in other thermomiotic materials. A pressure dependence to the CTE for $Zn(CN)_2$ has been reported, implying a modest temperature dependence to the bulk modulus [106]. The expansion coefficients for the thermomiotic material $Zr_2(WO_4)(PO_4)_2$ were found to be largely independent of pressure [309].

7.3.5 Heat capacities of ScF_3 and $Sc_{1-x}Y_xF_3$

The temperature dependence of the experimentally measured molar heat capacity at constant pressure (C_P) of ScF_3 is plotted in Figure 7.11. With Equation 2.6, C_P can be converted to C_V (the molar heat capacity at constant volume); however, the difference between C_P and C_V is quite small for these samples ($\frac{C_P - C_V}{C_P} \leq 0.8\%$ for ScF_3), so only C_P is given here. There is no evidence of a phase transition at any point between 0.35 and 390 K; previous studies of ScF_3 only examined as low as 10 K (PXRD) [35] and 4 K (Raman) [245]. These experimental data will be compared with density functional theory calculations in a future publication [304].

Experimentally measured C_P of $Sc_{1-x}Y_xF_3$ are shown in Figure 7.12, while complete data tables are available in Appendix C. The molar heat capacities of the Y-substituted materials are close to that of ScF_3 in their cubic (ambient) phases; however, upon cooling, they transition between 250 and 100 K (transition temperature varies with composition) to rhombohedral phases (Figure 7.4), at which point their heat capacities begin to diverge from that of ScF_3. The low-temperature heat capacities of $Sc_{1-x}Y_xF_3$ are smaller than those of ScF_3, which correlates with the positive thermal expansion of the rhombohedral phases.

A cubic-to-rhombohedral phase transition is evident in the heat capacity data for $x =$

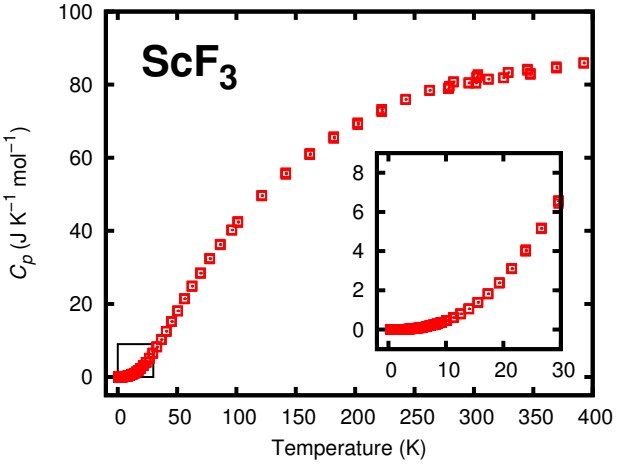

Figure 7.11: Temperature dependence of the experimentally measured molar heat capacity at constant pressure of ScF_3 (0.35 to 390 K). The inset shows the low-temperature portion of the data (0.35 to 30 K) that is enclosed by a box in the main figure. Redrawn from ref. [304].

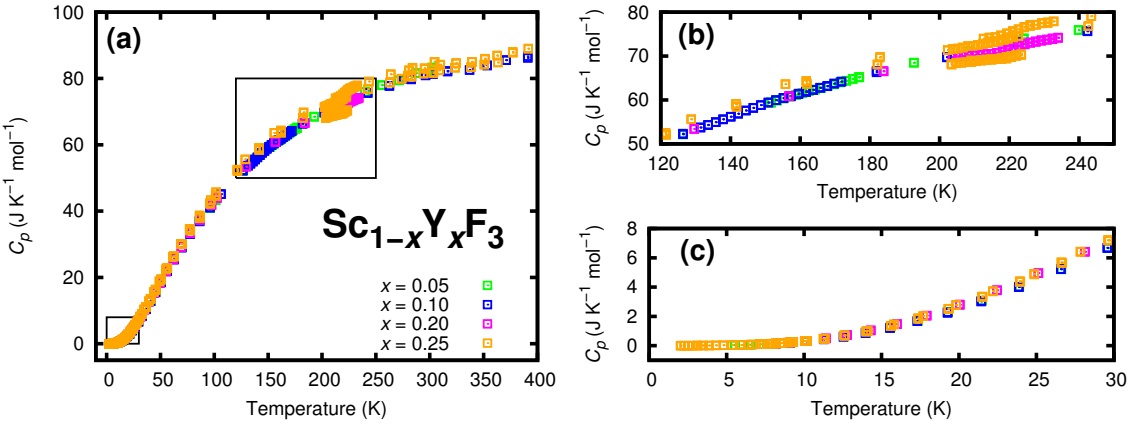

Figure 7.12: Temperature dependence of the experimentally measured molar heat capacity at constant pressure of $Sc_{1-x}Y_xF_3$: (a) 0.35 to 390 K, (b) 120 to 250 K, (c) 0.35 to 30 K. Redrawn from ref. [304].

0.20 and 0.25 at approximately 220 K and very weakly for $x = 0.10$ at 150 K. These temperatures are somewhat higher than those estimated from variable-temperature PXRD (Figure 7.4) but are close to the inflection point in the volume–temperature curves (Figure 7.5). The small anomalies in heat capacity are consistent with second-order phase transitions, as suggested by the PXRD data. A phase transition is not observed in the heat capacity data for $x = 0.05$, possibly because it was below the detection limit. A low enthalpy change is consistent with the low-temperature heat capacity results; the relatively high values for low-temperature heat capacities suggest that yttrium-substituted ScF_3 solid solutions have considerable vibrational entropy in their rhombohedral phases [310], contributing to their stability and leading to a small enthalpy of transition to the cubic phase.

7.4 Conclusion

The formation of $Sc_{1-x}Y_xF_3$ leads to a symmetry-lowering phase transition upon cooling, the temperature of which initially increases rapidly with x and then approaches a plateau at ∼200 K. Strongly composition- and temperature-dependent CTEs are observed below and immediately above the transition temperature. However, above ∼400 K, where all the samples are cubic, α_V is largely independent of x; therefore, yttrium substitution is not a useful approach to tailoring the expansion characteristics of ScF_3-based solid solutions. Yttrium substitution also significantly lowers the bulk moduli of the solid solutions. Distortions in the local structure that are needed to accommodate the large yttrium cation likely provide a low-energy path for volume reduction on compression. The bulk moduli of the solid solutions increase with temperature over the entire temperature range examined, contrary to the behavior of most materials. The strongly temperature-dependent bulk moduli and stress-dependent CTEs of the solid solutions may limit their use in composites or other applications. In contrast, however, the thermal expansion and bulk modulus of pure ScF_3 are independent of pressure and temperature, respectively. Based on heat capacity measurements between 0.35 and 390 K, no evidence of a phase transition is observed for ScF_3, while a subtle, second-order phase transition is observed for the $x = 0.10$, 0.20, and 0.25 samples. The low-temperature heat capacities of the rhombohedral phases of these

solid solutions do not share the behavior of ScF_3.

The behavior of $Sc_{1-x}Y_xF_3$ differs greatly from that of $Sc_{1-x}Ti_xF_3$, where solid solubility is not limited, and the phase transition temperature varies linearly with composition. The unusual independence of CTE in cubic $Sc_{1-x}Y_xF_3$ is not observed in cubic $Sc_{1-x}Ti_xF_3$, in which CTE is tunable over a limited temperature range between those of the end members.

The discussion of ScF_3-based solid solutions concludes in Chapter 8.

CHAPTER 8

THERMAL EXPANSION AND COMPRESSIBILITY OF $Sc_{1-x}Al_xF_3$ ($x \leq 0.50$)

8.1 Introduction[1,2]

In the preceding two chapters, thermal expansion control in ScF_3 has been explored through solid solution formation with TiF_3 (Chapter 6) and YF_3 (Chapter 7). These species were chosen based on the size of the trivalent cation relative to that of Sc^{3+}; Y^{3+} is significantly larger, while Ti^{3+} is a relatively close size match [300]. In this chapter, the study of ScF_3 solid solutions concludes with α-AlF_3 substitution. Unlike Y^{3+} or Ti^{3+}, Al^{3+} is significantly smaller than Sc^{3+} (ionic radii, 0.535 and 0.745 Å, respectively) [300]. The difference in ionic radius (33%) between Al^{3+} and Sc^{3+} is larger than that between Y^{3+} and Sc^{3+}. The structural distortions resulting from substitution of a small ion (Al^{3+}) in the ScF_3 matrix are possibly different than those arising from substitution of a large ion (Y^{3+}). Herein, the solid solubility, phase transitions, and thermal expansion behavior of $Sc_{1-x}Al_xF_3$ ($x \leq 0.50$) between 100 and 900 K as well as the effects of composition on bulk modulus and thermal expansion upon compression ($\leq$0.414 GPa) are reported.

8.2 Materials and methods

8.2.1 Synthesis and ambient characterization

Powder samples of $(1-x)ScF_3$:$xAlF_3$ (x = 0.05, 0.10, 0.15, 0.20, 0.25, 0.30, 0.40, 0.50, 0.55, 0.60, 0.70, 0.80, 0.90) were prepared by the solid state reaction of stoichiometric amounts of ScF_3 (American Elements, 99.99%) and α-AlF_3 (Alfa-Aesar, 99.99%) in a similar manner to that described in Sections 6.2.1 and 7.2.1. The powders were thoroughly mixed and pelletized in an inert atmosphere and then sealed in a Cu ($x \leq 0.20$) or Ni ampoule by

[1]The work presented in this chapter and Appendix D is edited from an upcoming publication [248] to fit the context of this thesis.

[2]Supporting material for this chapter can be found in Appendix D.

arc-welding. The Cu (Ni) ampoules were sealed inside evacuated fused quartz tubes, which were then heated at 1273 (1338) K for 72 h and quenched by removing from the furnace, which was located in a fume hood.

Ambient laboratory powder X-ray diffraction (PXRD) patterns were analyzed by the Rietveld method with *GSAS* [269, 270], using either a cubic ($Pm\bar{3}m$) or rhombohedral ($R\bar{3}c$) structural model.

8.2.2 Non-ambient synchrotron X-ray diffraction

Variable-temperature (ambient-pressure) PXRD data were collected at beamlines 1-BM-C ($\lambda \approx 0.61$ Å) and 17-BM-B ($\lambda \approx 0.7291$ Å) of the Advanced Photon Source (APS), Argonne National Laboratory, Illinois, USA, using the Cryostream (100 to 500 K, Figure 2.2) and wire-wound furnace (300 to ∼1200 K, Figure 2.3) setups described in Section 2.2.1.1.

Variable-pressure/temperature PXRD data were collected at beamline 11-ID-B of the APS. The samples (x = 0.05, 0.10, 0.15, 0.20, and 0.40) were slurried in silicone oil and loaded in Kapton capillaries that were sealed at one end with a high-temperature epoxy resin. The capillaries were loaded in the MK3BRIM_414 device introduced in Section 2.2.2 and positioned in a Grade 5 Ti pressure vessel.

Measurements were performed at pressures of 0.017, 0.052, 0.103, 0.155, 0.207, 0.259, 0.310, 0.362, and 0.414 GPa and the following temperatures: 298, 343, 388, 433, 478, and 523 K. At the highest two temperatures, the highest two pressures were not accessed. Data for the x = 0.10 sample above 310 MPa are not presented, as the apparatus did not hold pressure during attempted measurements.

The unit cell volumes obtained from five out of the 234 variable-pressure/temperature diffraction measurements (pressure ∼259 MPa with x = 0.05, 298 K; x = 0.20, 298 K; x = 0.40, 298 K; x = 0.40, 388 K; and x = 0.40, 433 K) were not used for the determination of bulk moduli and expansion coefficients, as they did not follow the trends displayed by the other data, apparently due to problems with accurate pressure determination.

8.2.3 Data analysis

As discussed in Section 2.4.2, all area detector images were integrated with *FIT2D* [255], and Rietveld analyses were accomplished with *GSAS* [269, 270]. The sequential refinement mode of *GSAS* was utilized to analyze the variable-temperature data. Representative Rietveld fits are shown in Figure 8.1. To account for differences between conditions in synchrotron measurements, the ambient-pressure unit cell volumes were scaled using the values obtained from laboratory PXRD data. Herein, only Cryostream data between 100 and 350 K are used for analysis (in samples for which both types of data were collected), while only furnace data above 350 K are used.

8.3 Results and discussion

8.3.1 Solid solubility

In the ambient laboratory PXRD patterns for the $(1-x)ScF_3$:$xAlF_3$ products (Figure 8.2), a $Sc_{1-x}Al_xF_3$ phase is observed for all x but is the only phase for $x \leq 0.50$; additional peaks corresponding to either α-AlF_3 or α-AlF_3 substituted by small amounts of ScF_3 are evident for $x > 0.50$, the intensities of which increase with x. The unit cell volumes and weight fractions for each of these phases (where applicable) were determined by Rietveld analyses of the laboratory PXRD data (Figure 8.3a, c). The volumes follow Vegard's Law below $x \approx 0.50$, suggesting that the solubility limit of α-AlF_3 in ScF_3 is between 50 and 55% at reaction temperature (1338 K). Notably, an extrapolation of a straight-line fit to the unit cell volumes for $Sc_{1-x}Al_xF_3$ at 800 K (Figure 8.3b), where all of the samples are cubic, agrees well with the volume for pure AlF_3 at this temperature, which indicates that the effective size of Al^{3+} in the solid solutions is the same as that in AlF_3, even though the large size mismatch between Al^{3+} and Sc^{3+} must lead to considerable structural distortions in the solid solution. Samples with $x > 0.50$ contain an α-AlF_3-type second phase, the amount of which increases linearly with x. The unit cell volume for this phase appears invariant with overall sample composition, indicating a solid solubility for ScF_3 in AlF_3 of <10%. The asymmetry in solid solubility (∼50% AlF_3 in ScF_3 but <10% ScF_3 in AlF_3) suggests that cation size mismatches are more readily accommodated in ReO_3-type MF_3

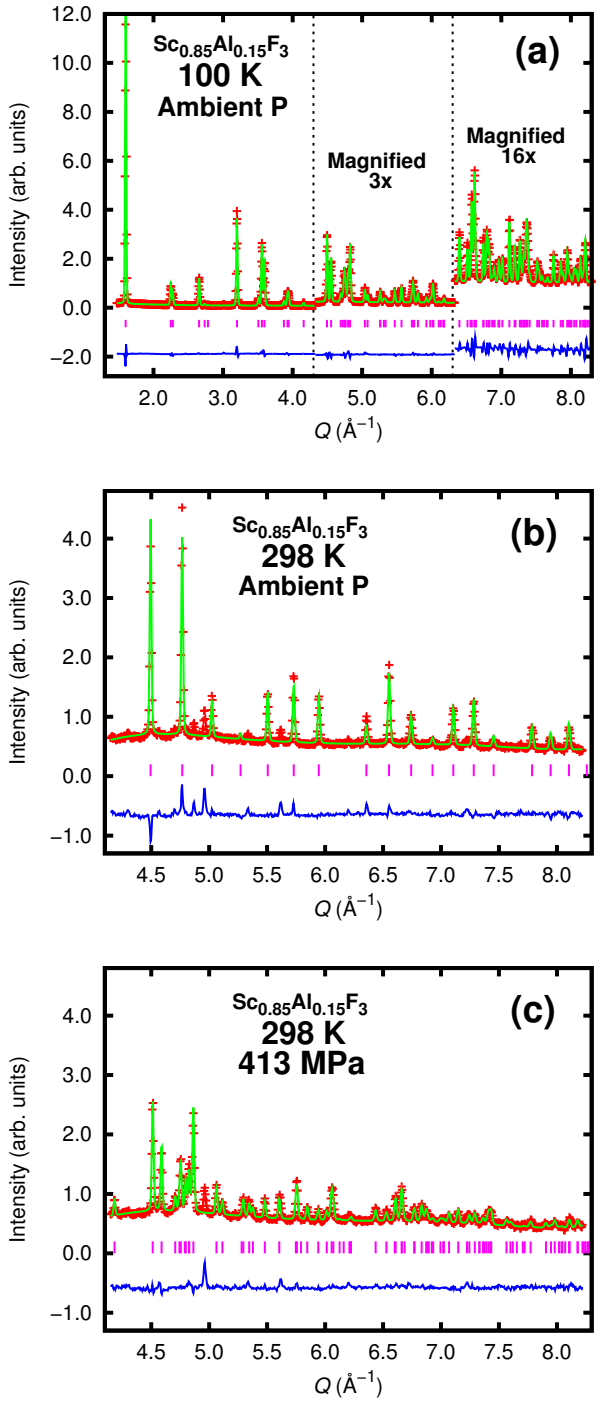

Figure 8.1: Rietveld fits (green line) to data (red +) collected for $Sc_{0.85}Al_{0.15}F_3$ at (a) 100 K and ambient pressure, (b) ambient temperature and pressure, and (c) ambient temperature and 413 MPa. A rhombohedral model was used in panels (a) and (c), while a cubic model was used in (b). In these plots, the difference curve appears in blue, and Bragg peak positions are marked by magenta tick marks (|). The data in panel (a) were collected in the Cryostream setup, while panels (b) and (c) were collected in the high-pressure setup; extra peaks in the latter two are residual scattering from the tungsten BRIM body and rhenium beam stop blade. Reproduced from ref. [248].

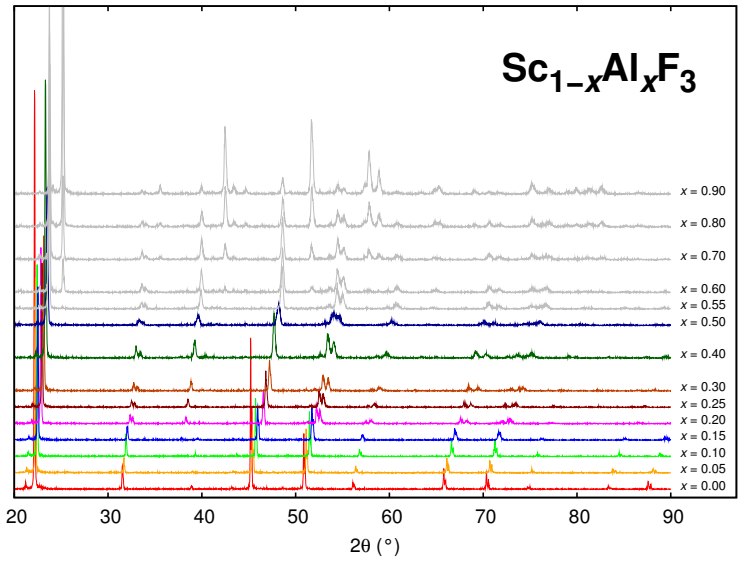

Figure 8.2: Powder X-ray diffraction data collected at ambient conditions on a laboratory diffractometer for $(1-x)ScF_3$:$xAlF_3$. With the signal-to-noise ratio of the lab diffractometer, samples with $x \leq 0.50$ appear to be a single phase ($Sc_{1-x}Al_xF_3$). Patterns for samples containing a second α-AlF_3-rich phase ($x > 0.50$) are colored grey. The pattern for ScF_3 ($x = 0.00$) also appears in Figure 6.3. Reproduced from ref. [248].

solid solutions when the substituting cation is smaller than the matrix cation.

The solubility limit for α-AlF_3 in ScF_3 (50%) at 1338 K is much higher than the ~25% limit observed for YF_3 in ScF_3 at 1273 K (Chapter 7), even though the size mismatch between Y^{3+} and Sc^{3+} is less than that between Al^{3+} and Sc^{3+} (21 and 33%, respectively). Insertion of a relatively small cation (such as Al^{3+}) into the ScF_3 matrix is apparently easier than insertion of a large cation (such as Y^{3+}). In contrast to $Sc_{1-x}Y_xF_3$ and $Sc_{1-x}Al_xF_3$, however, full solubility is observed in $Sc_{1-x}Ti_xF_3$ at 1338 K due to the similar ionic radii of Sc^{3+} and Ti^{3+} (Chapter 6). Previous reports of LnF_3–ScF_3 (Ln = Yb [298], Lu [299]) systems suggest that solubility in these solid solutions is probably strongly dependent on reaction temperature.

8.3.2 Phase transition and thermal expansion at ambient pressure

Variable-temperature, ambient-pressure synchrotron PXRD data for all $Sc_{1-x}Al_xF_3$ are shown in Appendix D (Cryostream: Figures D.1, D.2, D.3; Furnace: Figures D.4, D.5, D.6). In the furnace data, the solid solutions decompose at some point above 900 K;

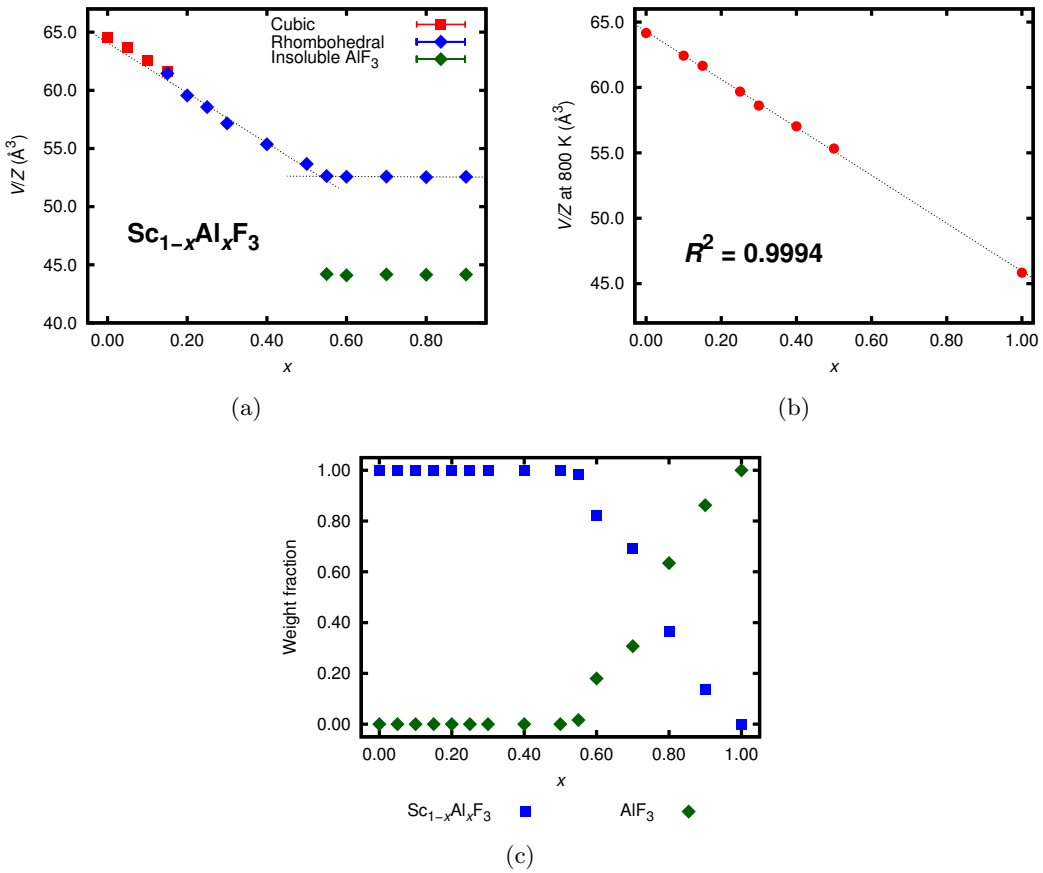

Figure 8.3: (a) Ambient unit cell volumes per formula unit of $Sc_{1-x}Al_xF_3$ extracted from Rietveld analyses of laboratory PXRD data using either a cubic (red squares) or rhombohedral (blue diamonds) model. V/Z of the extra α-AlF_3 phase (rhombohedral) are indicated by green diamonds. The dashed lines are linear fits to the data; their intersection is an indicator of the solubility limit of α-AlF_3 in ScF_3. The V/Z for ScF_3 ($x = 0.00$) also appears in Figure 6.4. (b) Unit cell volumes per formula unit of $Sc_{1-x}Al_xF_3$ at 800 K, extracted from Rietveld analyses of synchrotron PXRD data. The dashed line is a linear fit to the data ($R^2 = 0.9994$). The volume for pure α-AlF_3 is from Figure 4.6. In (a) and (b), error bars are smaller than the symbols. (c) Weight fractions of $Sc_{1-x}Al_xF_3$ (cubic or rhombohedral, blue squares) and α-AlF_3 (green diamonds) in each sample, extracted from Rietveld analyses. Reproduced from ref. [248].

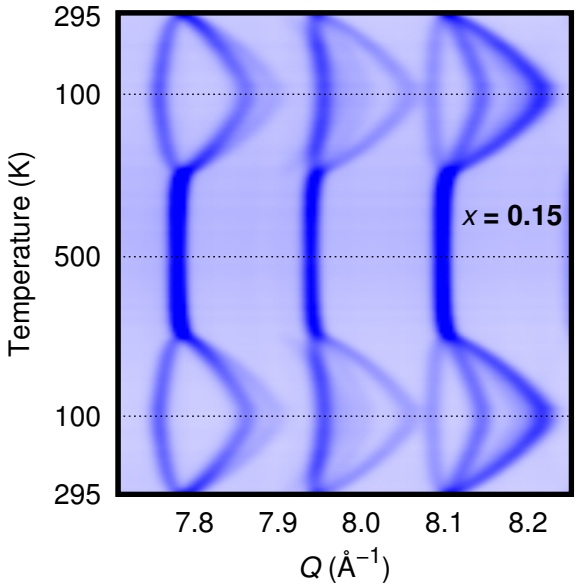

Figure 8.4: Variable-temperature (Cryostream, 100-500 K) PXRD data collected for $Sc_{0.85}Al_{0.15}F_3$. Only the high-angle portion of the patterns is shown to demonstrate the peak splitting indicative of a symmetry-lowering phase transition. Patterns are arranged in order of collection from bottom to top, which followed the temperature ramp in Figure 2.2b. Reproduced from ref. [248].

hereafter, only data collected below 900 K are discussed.

An example of Cryostream variable-temperature PXRD data ($x = 0.15$) is shown in Figure 8.4. From peak splitting and the appearance of supercell peaks in the PXRD data at low temperatures, a symmetry-lowering phase transition is evident in all samples between 100 and 500 K ($x \geq 0.05$). As demonstrated in previous chapters, the same cubic-to-rhombohedral transition occurs in other ReO_3-type MF_3 [237, 227, 228], as well as $Sc_{1-x}Ti_xF_3$ (Chapter 6) and $Sc_{1-x}Y_xF_3$ (Chapter 7), but not ScF_3, which remains cubic down to 0.35 K, according to the heat capacity measurements in Chapter 7. In some cases ($x > 0.15$), this transition is evident above ambient temperature, which is not the case in any $Sc_{1-x}Y_xF_3$ compositions or $Sc_{1-x}Ti_xF_3$ with $x \leq 0.80$.

The phase transition temperature of each sample was estimated from the temperature dependence of supercell peak intensity (Figure D.7). A composition-temperature phase diagram (at ambient pressure) for $Sc_{1-x}Al_xF_3$ is shown in Figure 8.5. Phase transition temperature increases smoothly with composition and plateaus at ∼500 K as the solubility

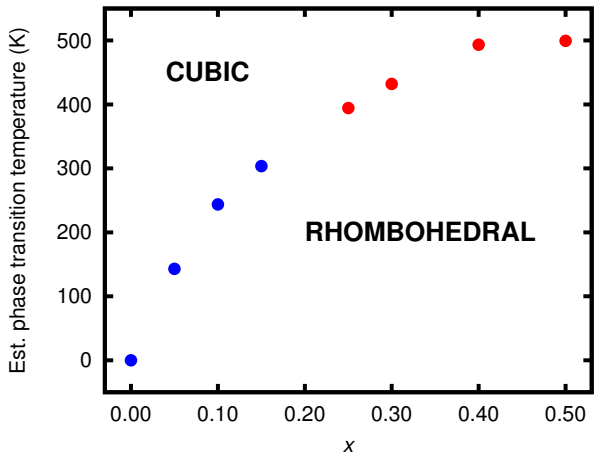

Figure 8.5: Composition-temperature phase diagram for $Sc_{1-x}Al_xF_3$ at ambient pressure. Blue circles are experimental transition temperatures from Cryostream measurements, while red circles are those from furnace measurements. ScF_3 remains cubic down to at least 0.35 K (Chapter 7), so its transition temperature is given here as 0 K. Reproduced from ref. [248].

limit is reached, similar to $Sc_{1-x}Y_xF_3$ (Figure 7.4). While ScF_3 is not known to become rhombohedral above 0.35 K at ambient pressure (Chapter 7), the first-order phase transition in pure α-AlF_3 occurs at ∼713 K (Chapter 4), well above the transition temperature of any $Sc_{1-x}Al_xF_3$.

The cubic-to-rhombohedral phase transformation of the ReO_3 structure occurs due to the coupled rotation of octahedra when cooled (Figure 1.9). In the case of $Sc_{1-x}Al_xF_3$, octahedral rotation around <1 1 1> is large, reaching ∼14° at 100 K for the most Al-rich solid solutions, which corresponds to a M–F–M bond angle of ∼156° (Figure D.8). As in $Sc_{1-x}Y_xF_3$, the significant size mismatch between Sc^{3+} and Al^{3+} apparently leads to local structural distortions that create a disordered arrangement of fluoride displacements away from their crystallographic average positions. This disorder is reflected in the atomic displacement parameters (ADPs) for fluorine (Figure D.9). In particular, as the aluminum content increases, the value for the transverse component of the ADP for F (U_{22}) extrapolated to 0 K increases significantly.

The unit cell volumes per formula unit (V/Z) of $Sc_{1-x}Al_xF_3$ were extracted during Rietveld analyses and are plotted with respect to temperature in Figure 8.6a. Unlike the phase transition observed in α-AlF_3 (Chapter 4) and TiF_3 (Chapter 6), but similar to that

in $Sc_{1-x}Y_xF_3$ (Chapter 7), the transition in these solid solutions is not first-order.

The volume CTE (α_V) for each $Sc_{1-x}Al_xF_3$ composition was estimated by fitting polynomials to V/Z *versus* T data; the temperature dependence of α_V is plotted in Figure 8.6b. As in other ReO_3-type MF_3, the CTE of rhombohedral $Sc_{1-x}Al_xF_3$ is strongly positive and changes rapidly with temperature. The CTE of the cubic form increases steadily with x, varying from negative ($x < 0.15$) to near-zero ($x = 0.15$) to positive ($x > 0.15$) above ~600 K. However, the variation of the cubic-phase CTE with x decreases as temperature increases (Figure 8.6c); CTEs for the solid solutions at several temperatures between 300 and 800 K are plotted with respect to x in Figure D.10. Although the CTE is tunable over a significant range above 600 K, the temperatures at which tuning is possible, while remaining cubic, are probably too high for most applications. The CTE of cubic $Sc_{1-x}Al_xF_3$ is much more sensitive to composition than that observed for either cubic $Sc_{1-x}Y_xF_3$, whose CTE is unexpectedly almost constant with composition (Figure 7.6), or cubic $Sc_{1-x}Ti_xF_3$, whose CTE is tunable above 350 K but over a limited, negative range (Figure 6.8). The thermal expansion behavior of highly-doped $Sc_{1-x}Al_xF_3$ ($x > 0.15$) is similar to that of pure α-AlF_3, in that the cubic form shows PTE rather than NTE (Chapter 4).

As in other ReO_3-type MF_3, including α-AlF_3, $Sc_{1-x}Ti_xF_3$, and $Sc_{1-x}Y_xF_3$ (Chapters 4, 6, and 7, respectively), thermal expansion in rhombohedral $Sc_{1-x}Al_xF_3$ is strongly anisotropic. As shown in Figure D.8, the hexagonal a-axis expands rapidly with temperature due to rotation of the rigid MF_6 octahedra about the threefold symmetry axis, while the hexagonal c-axis contracts, with overall positive volume thermal expansion (Figure 8.6).

8.3.3 Phase transitions, isothermal bulk modulus, and thermal expansion under pressure

The larger solid solubility range of $Sc_{1-x}Al_xF_3$ ($x \leq 0.50$) allows for a more thorough exploration of the effects of composition on bulk modulus than that reported for $Sc_{1-x}Y_xF_3$ ($x \leq 0.25$, Chapter 7). Based on the splitting of certain peaks and appearance of supercell peaks, either a cubic or rhombohedral model was used in Rietveld analyses of the variable-pressure/temperature PXRD data for $Sc_{1-x}Al_xF_3$ (Figures D.12 to D.16) to extract unit cell volumes (V). Figure 8.7 (a and b) shows $\ln V$ with respect to pressure and temperature,

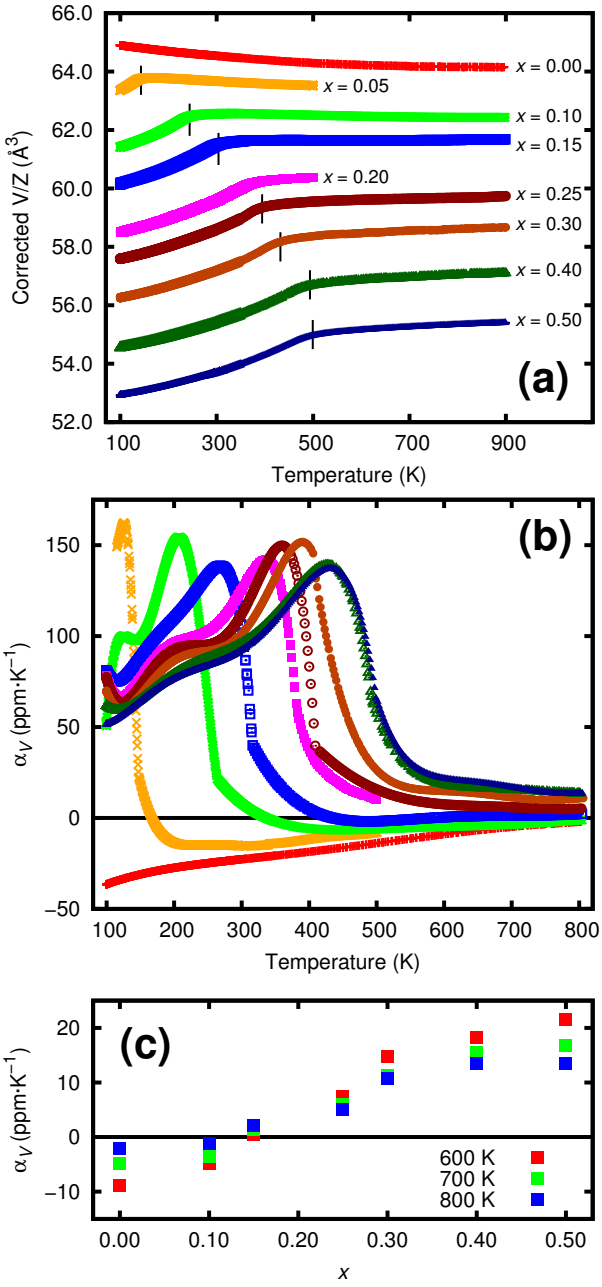

Figure 8.6: Temperature dependence of (a) unit cell volume per formula unit (V/Z) and (b) volume CTE (α_V) for $Sc_{1-x}Al_xF_3$. Volumes were extracted from Rietveld analyses of variable-temperature PXRD data and then corrected for calibration differences at different data collection times; CTE was estimated by fitting polynomials to the volume curves. In (a), estimated phase transition temperatures are indicated by black vertical lines. (c) Composition dependence of α_V at 600, 700, and 800 K. Data below 500 K for pure ScF_3 ($x = 0.00$) also appear in Figures 6.7 and 6.8. Reproduced from ref. [248].

respectively, for all samples. All lattice constants and unit cell volumes are tabulated in Appendix D.

Phase diagrams for all samples, based on the structural model used in the Rietveld analyses, appear in Appendix D (pressure-composition and pressure-temperature, Figures D.17 and D.18, respectively); however, the pressure-temperature phase diagrams for the $x = 0.15$ and 0.20 samples are shown in Figure 8.8. As expected, the samples become rhombohedral with sufficient compression (cooling) at a constant temperature (pressure). Although the $x = 0.05$ sample remains cubic upon compression to 413 MPa at all temperatures between 298 and 523 K (Figure D.18), increased Al^{3+} substitution shifts the critical temperature upward at a given pressure and the critical pressure downward at a given temperature. In contrast to these materials, all $Sc_{1-x}Y_xF_3$ ($x \leq 0.25$) remain cubic on compression to 276 MPa at all temperatures between 298 and 523 K (Chapter 7).

The slope of the pressure-temperature phase boundary for each of the solid solution compositions studied (Figures 8.8 and D.18) is 0.4-0.5 $K \cdot MPa^{-1}$, which is close to that estimated for undoped ScF_3 ($\sim$0.4 $K \cdot MPa^{-1}$) based on the low-temperature data (<300 K) in a previous study [35]. These values are much larger in magnitude than that typically found for perovskites undergoing octahedral-tilting phase transitions [311]. The principles governing displacive phase transitions in perovskites have received considerable attention due to their technological and geological importance. This work is directly applicable to $Sc_{1-x}Al_xF_3$, as the ReO_3 structure is that of a perovskite with a vacant A site. In 1975, based on an analysis of the balance between short- and long-range interactions, it was proposed that, for perovskites displaying zone-boundary phase transitions, like that in $Sc_{1-x}Al_xF_3$, the temperature-pressure phase boundary slope ($\frac{dT_c}{dP}$) should be positive, whereas zone-center transitions should show a negative slope [311]. After finding examples of perovskites displaying octahedral tilting transitions, which typically involve the softening of zone-boundary phonon modes, where the phase boundary slope was negative, such as $LaAlO_3$ [312], Angel *et al.* reanalyzed the problem [313], concluding that the slope of the phase boundary depends on the relative compressibility of the A- and B-site coordination polyhedra in the

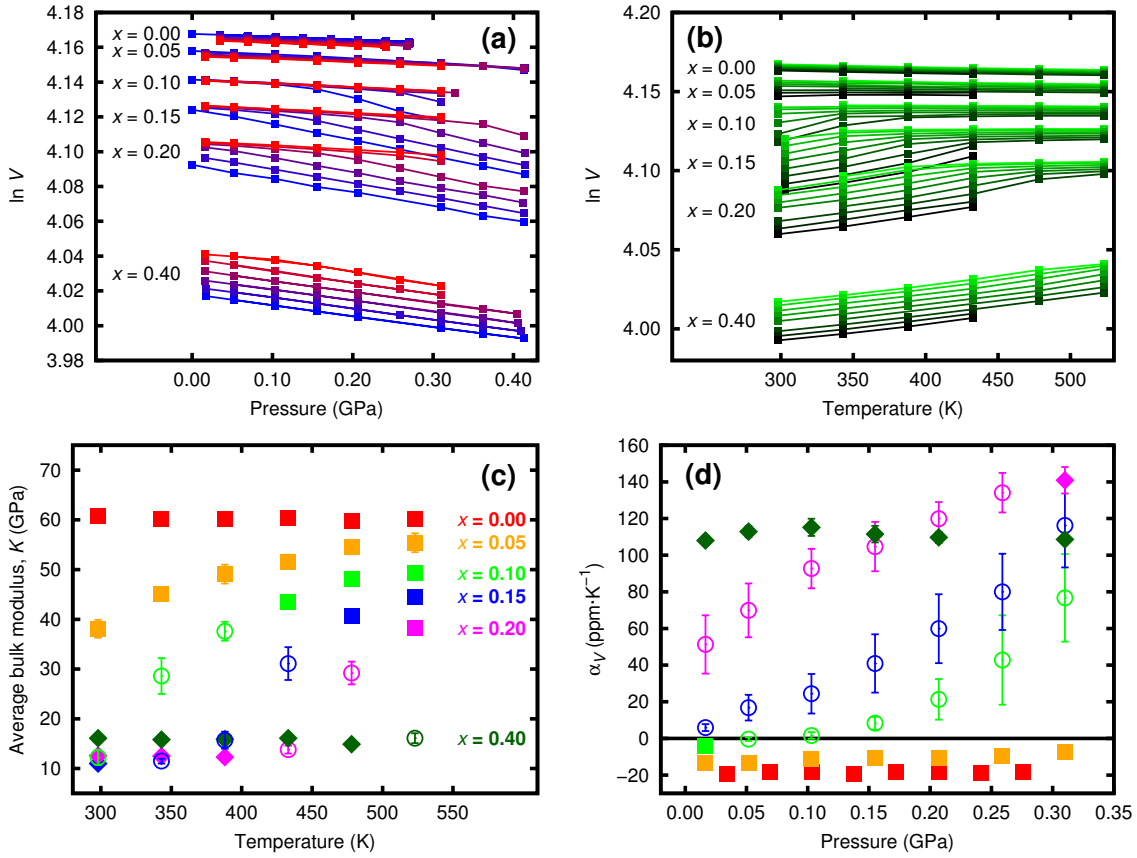

Figure 8.7: (a) Natural logarithm of unit cell volume (ln V; units of V are Å^3) with respect to pressure at various temperatures (298, 343, 388, 433, 478, and 523 K), and (b) ln V with respect to temperature at various pressures (0.017, 0.052, 0.103, 0.155, 0.207, 0.258, 0.310, 0.362, and 0.413 GPa) for $Sc_{1-x}Al_xF_3$. In both plots, data points are connected with line segments as a guide to the eye, and error bars are smaller than the point size. In (a), the lowest temperature points for each sample are blue, and the highest temperature points are red. Similarly, in (b), the lowest pressure points for each sample are green and have the highest volumes, while the highest pressure points are black and have the lowest volumes. (c) Temperature dependence of average isothermal bulk modulus (K_T) and (d) pressure dependence (<0.35 GPa) of average volume CTE (α_V, 298-523 K) for $Sc_{1-x}Al_xF_3$. In (c)/(d), squares (diamonds) indicate that the structure of the material is cubic (rhombohedral) at all pressures/temperatures at the specified temperature/pressure; open circles denote that the phase transition occurs over the pressure/temperature range used to calculate the given value. All data for pure ScF_3 ($x = 0.00$) also appear in Figures 7.7, 7.8, 7.9, and 7.10. Reproduced from ref. [248].

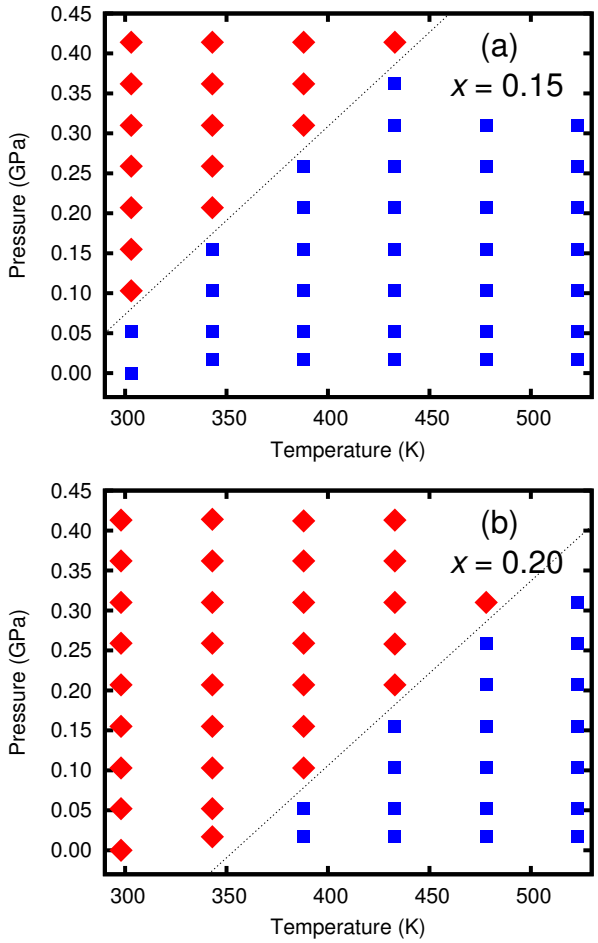

Figure 8.8: Pressure-temperature phase diagrams for (a) $Sc_{0.85}Al_{0.15}F_3$ and (b) $Sc_{0.80}Al_{0.20}F_3$. Blue squares (red diamonds) indicate that the structure of the material is cubic (rhombohedral) at the specified conditions. Dashed lines indicate estimated phase boundaries. Reproduced from ref. [248].

perovskite. In $LaAlO_3$, the LaO_{12} polyhedron is less compressible than the AlO_6 octahedron, and volume reduction on compression involves compression of the AlO_6 octahedra combined with a reduction in the octahedral tilts, leading to an unusual situation in which compression is associated with a transition that involves an increase in symmetry ($R\bar{3}c$ to $Pm\bar{3}m$) [313]. In $Sc_{1-x}Al_xF_3$, the A site is vacant, so the AF_{12} polyhedron is highly compressible relative to the BF_6 octahedron, leading to a positive phase boundary slope.

Average isothermal bulk moduli (K_T) were calculated from straight-line fits to ln V *versus* P plots and are plotted with respect to temperature in Figure 8.7c. In a similar manner, average volume CTEs were calculated from straight-line fits to ln V *versus* T plots and are plotted with respect to pressure in Figure 8.7d. These linear fits are good for cases in which the structure remains cubic or rhombohedral at all pressures/temperatures at the specified temperature/pressure; such cases are marked by solid symbols in Figures 8.7c and 8.7d. However, for cases in which the phase transition occurs over the pressure or temperature range used to calculate K_T or α_V, the linear fits are poor; these cases are denoted by open circles in Figures 8.7c and 8.7d.

Increasing Al^{3+} substitution in ScF_3 leads to a decrease in bulk modulus at each temperature between 298 and 523 K (Figure 8.7c). Unlike cubic ScF_3 in the range 300-550 K (Section 7.3.4), the bulk moduli of the cubic solid solution samples increase on heating. This thermal stiffening is atypical of most materials, although it has been observed in $Sc_{1-x}Y_xF_3$ (Chapter 7) and strongly laser-excited gold [314]. Fang *et al.* recently provided a possible theoretical basis for this behavior and indicated that thermal stiffening might occur in thermomiotic materials that are highly anharmonic [315]. The strong temperature dependence of the bulk moduli implies that the materials must also display pressure-dependent thermal expansion. These two characteristics are related by Equation 1.15. The expansion coefficients shown in Figure 8.7d are strongly temperature-dependent, but, as many of them were computed over a temperature range in which there is a phase transition, there is also a contribution from the phase transition to this behavior.

In contrast with the cubic form, rhombohedral $Sc_{1-x}Al_xF_3$ is quite soft ($K_T \approx$ 10-15 GPa), although K_0 at ambient temperature for rhombohedral ScF_3 is similar, 9(3) GPa [35,

223]. Another ReO_3-type material, NbO_2F, has a similar bulk modulus (K_0 = 9.6 GPa) when rhombohedral above 0.47 GPa [220]. This rhombohedral structure features bent M–F–M links that are easily bent further upon compression; hence, materials with this structure are more compressible than those with the cubic structure, in which these same links are linear. This relationship is best illustrated by comparing the bulk moduli of ScF_3 and $Sc_{0.60}Al_{0.40}F_3$ in Figure 8.7c. ScF_3 is cubic at all temperatures and pressures examined and thus features linear Sc–F–Sc links that are not readily compressed; however, the highly-doped solid solution is rhombohedrally distorted at nearly all temperatures and pressures examined and thus has a much lower bulk modulus at all temperatures.

Most materials stiffen upon compression; however, pressure-induced softening has been observed in several thermomiotic materials, including highly doped $Sc_{1-x}Y_xF_3$ (Chapter 7), ZrW_2O_8 [105], $ZrMo_2O_8$ [92], HfW_2O_8 [95], $Zn(CN)_2$ [106, 109], and various zeolites [107]; this phenomenon has been shown to be temperature-dependent [110]. Pressure-induced softening is not evident in ScF_3 within the accuracy of the measurements in Chapter 7 nor is the behavior observed in $Sc_{1-x}Al_xF_3$ compositions that remain cubic for all pressures at a given temperature.

8.4 Conclusion

Similar to many ReO_3-type MF_3, such as α-AlF_3, a cubic-to-rhombohedral phase transition is observed in $Sc_{1-x}Al_xF_3$, the temperature of which increases smoothly with x, approaching ~500 K at $x \approx 0.50$. The CTE of rhombohedral $Sc_{1-x}Al_xF_3$ is strongly positive, while the cubic-phase CTE (>600 K) varies from negative ($x < 0.15$) to near-zero ($x = 0.15$) to positive ($x > 0.20$), providing a greater possibility for tuning than either cubic $Sc_{1-x}Ti_xF_3$ or cubic $Sc_{1-x}Y_xF_3$. However, the $Sc_{1-x}Al_xF_3$ system does not provide for a tunable CTE in a cubic material at ambient temperature. The isothermal bulk moduli of the cubic solid solutions are lowered by Al^{3+} substitution; the unusual property of thermal stiffening is also observed, a behavior similar to that observed for $Sc_{1-x}Y_xF_3$ (Chapter 7).

CHAPTER 9

ROLE OF ANION SITE DISORDER IN THE NEAR-ZERO THERMAL EXPANSION OF TaO_2F

9.1 Introduction[1,2]

While very strong negative thermal expansion (NTE) has been observed in ScF_3 at and below room temperature that persists up to ∼1100 K [35, 243], other well-studied materials with the cubic ReO_3 structure, including several oxyfluorides, do not exhibit notable NTE (Section 1.3.2) [25, 225]. TaO_2F [204], for example, exhibits very low, nearly zero, thermal expansion [25, 206]. The lack of NTE in these materials has inspired further investigation.

As discussed in previous chapters, negative thermal expansion in ReO_3-type materials can be explained as arising from the thermally induced rocking of MX_6 octahedral rigid units, connected only at their corners via M–X–M linkages (Figure 1.5). The rocking involves transverse motion of the X anion normal to the $M \cdots M$ axis; this motion is expected to produce negative thermal expansion when the M–X–M angle is close to 180°, as displacement of X off the $M \cdots M$ axis in any direction (with comparatively minor expansion of the individual M–X bonds) leads to a reduction in the $M \cdots M$ separation. However, M–X–M angles significantly smaller than 180° are not optimal for NTE, as the displacement of X in some directions will increase the $M \cdots M$ separation [25]. The behavior of some MF_3 on cooling illustrates these points (Chapter 4); similar behavior is observed in the $Sc_{1-x}M_xF_3$ solid solutions discussed in Chapters 6, 7, and 8. These compounds have cubic ReO_3 structures at elevated temperatures and undergo a cubic-to-rhombohedral phase transition upon cooling due to the coupled rotation of the MF_6 octahedra. The rhombohedral forms, with bent M–F–M bonds, show strong positive thermal expansion,

[1] The work presented in this chapter and Appendix E was previously published [218] and is edited to fit the context of this thesis. Reprinted with permission from C. R. Morelock *et al. Chem. Mater.*, 25(9):1900-1904, 2013. Copyright 2013, American Chemical Society.

[2] Supporting material for this chapter can be found in Appendix E.

but the cubic forms, with crystallographic M–F–M bond angles of 180°, display near-zero or perhaps low negative thermal expansion [226, 228, 234, 235]. However, as shown in Chapter 4, cubic α-AlF_3 continues to show PTE, perhaps due to the presence of local octahedral tilts and an associated increase in the average Al–F–Al bond angle on heating.

Under ambient conditions, TaO_2F adopts a cubic ReO_3-type average structure, with a disordered distribution of O and F over the available anion sites. The material displays a cubic-to-rhombohedral phase transition at low pressures on compression [221] and has recently attracted attention for its potential as a mid-IR transparent window material [206]. The presence of O/F disorder in materials of this type is typical; none of the perovskites $KTiO_2F$ [207], $BaScO_2F$ [208], $BaFeO_2F$ [209], $SrFeO_2F$ [210], $PbScO_2F$ [211], or $PbFeO_2F$ [212] have been reported as anion-ordered. In TaO_2F, there is only a single crystallographic average Ta–X (X = O, F) distance, but on chemical grounds, the Ta–O and Ta–F bonds are expected to have different lengths. Using the bond valence parameters of Brese and O'Keeffe [316], the expected lengths for the Ta–O and Ta–F bonds are 1.92 and 2.14 Å, respectively. To accommodate these different lengths, the local, short-range structure of TaO_2F must deviate from the average (crystal) structure. In an electron diffraction study of closely related NbO_2F, one-dimensional ordering of the O and F atoms with unequal Nb–X (X = O, F) bond lengths was reported, with significant static displacements of Nb from the ideal cation site [213]. Furthermore, in a variable-temperature neutron diffraction study of TaO_2F, Tao and Sleight reported that the O and F atoms have large transverse atomic displacement parameters (ADPs) that persist at low temperatures. The authors suggested that these large ADPs likely arise from static tilting of the TaO_4F_2 octahedra and the possibility of non-linear Ta–(O/F)–Ta bonds [25]. In this chapter, the local structure of TaO_2F is examined using variable-temperature X-ray total scattering to better understand the role of the disordered O/F anion site in the material's thermal expansion.

9.2 Materials and methods

9.2.1 Synthesis

Based on the procedure of Frevel and Rinn [204], TaO_2F was prepared[3] by dissolving Ta_2O_5 (STREM Chemicals, 99.8%) in a Pt crucible with concentrated HF (Mallinckrodt, 48%), followed by slow evaporation to dryness. The remaining powder was transferred to a Teflon container and heated at ∼453 K for 10 h. Note that hydrofluoric acid is highly toxic and corrosive and must be handled cautiously with the proper protective equipment; contact with liquid or vapor requires immediate treatment with proper procedures [317, 318, 319, 320].

9.2.2 X-ray total scattering

Variable-temperature (80 to 441 K) X-ray total scattering data were collected[4] on beamline 1-ID-C of the Advanced Photon Source using an Oxford Cryosystems Cryostream; further experimental details are provided in Section 2.2.3.2. Analysis of total scattering data is described in Section 2.4.3, and examples of extracted[5] $G(r)$ for TaO_2F at various temperatures appear in Figure E.1.

9.3 Results and discussion

9.3.1 Simple cubic ReO_3-type model

A simple cubic ReO_3-type model ($Pm\bar{3}m$) was initially fit to the PDF data obtained at 80 K. The model provides an excellent fit at distances beyond ∼8 Å (R_W [8-40 Å] = 12.6%; Figure 9.1a); however, there are significant deficiencies in the fit at low r (R_W [1.5-8.0 Å] = 61.0%; Figure 9.1b). The deviations in the fit are principally associated with Ta$\cdots$Ta correlations between linearly bridged metal centers: Ta–(X)–Ta at ∼3.9 Å and, to a lesser extent, Ta–(X–Ta–X)–Ta at ∼7.8 Å. The simple cubic model only allows for single distinct Ta$\cdots$Ta distances of these types, but the data suggest the presence of two distinct Ta$\cdots$Ta distances in each case. Peak fitting indicates that the nearest-neighbor Ta$\cdots$Ta separations

[3]The TaO_2F sample was prepared by M. Cetinkol.

[4]The total scattering data were collected by G. J. Halder.

[5]PDFs were extracted by M. Cetinkol and K. W. Chapman and initially analyzed by B. K. Greve.

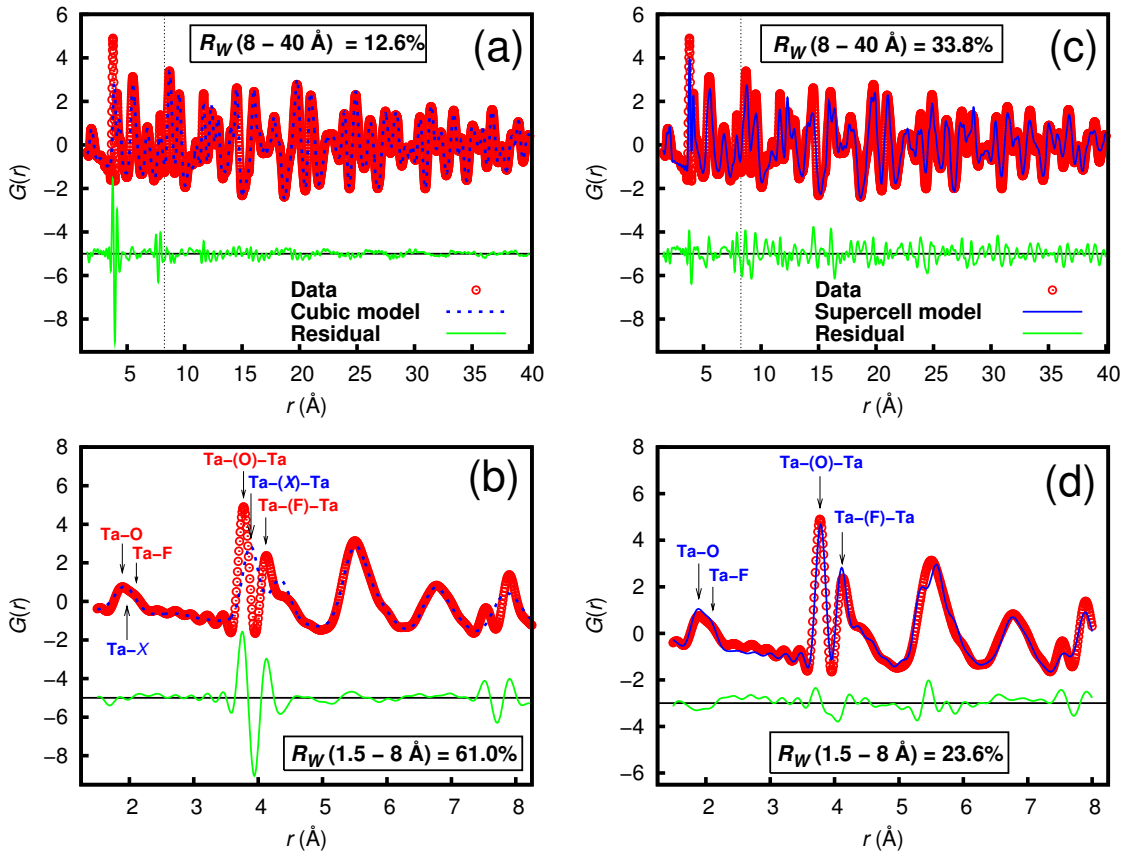

Figure 9.1: (a) Fit for a simple cubic ReO_3-type model (dashed blue line) to a PDF (red circles) obtained at 80 K for TaO_2F. The agreement is poor for $r <\sim 8$ Å but significantly better at higher r. (b) The 1.5-8.0 Å region of (a), emphasizing the poor fit of the Ta–X and Ta–(X)–Ta peaks (X = O, F). (c) $3 \times 3 \times 3$ supercell model (solid blue line) fit to the same PDF as in (a). The agreement is good for $r <\sim 8$ Å but worse at higher r. (d) The 1.5-8.0 Å region of (c), with the Ta–(O/F) and Ta–(O/F)–Ta peaks labeled. Reproduced from ref. [218].

are 3.773 and 4.118 Å, with a population ratio of approximately 2:1. Two distinct Ta–(X–Ta–X)–Ta distances are also evident at ∼7.5 and ∼7.9 Å, with a population ratio of approximately 1:2. The distinct Ta$\cdots$Ta distances and population ratios are consistent with the existence of different Ta–O and Ta–F bond lengths and bridging distances, as well as the sample stoichiometry ($d_{\text{Ta–O–Ta}} < d_{\text{Ta–F–Ta}}$ 2:1 relative abundance; sample O:F = 2:1).

9.3.2 Supercell model

As the deviations in the fit of the simple cubic model are limited to approximately two unit cell lengths, a supercell model was constructed to better describe the local structure. On the basis of diffuse scattering observed in electron diffraction patterns, Brink *et al.* proposed that O and F ordered along <1 0 0> in NbO_2F, giving rise to –Nb–O–Nb–O–Nb–F– chains [213]. This ordering pattern implies that the metal is always *cis*-coordinated by fluorine, as might be expected [217], which is consistent with the observation of two distinct Ta–(X–Ta–X)–Ta distances at ∼7.5 and ∼7.9 Å, with a population ratio of ∼1:2. A cubic $3 \times 3 \times 3$ supercell model was constructed, featuring ordered O$\cdots$O$\cdots$F along <1 0 0> and propagated displacements of Ta and the bridging anions along the Ta–X–Ta direction to give contracted Ta–(O)–Ta and expanded Ta–(F)–Ta distances of ∼3.8 and ∼4.1 Å, respectively. The F positions along each chain in the supercell were chosen randomly, yielding TaO_5F, TaO_4F_2, and TaO_3F_3 octahedra in the model used, not just TaO_4F_2. The O/F were placed midway between bridged Ta$\cdots$Ta pairs. This model gave a much improved fit to the local structure (R_W [1.5-8.0 Å] = 23.9%). The most notable deviation in the fit occurred for the directly bonded Ta–(O/F) distance, which was contracted relative to the data, suggesting that the anions are displaced from the Ta$\cdots$Ta axis.

The supercell model was modified to include <1 0 0> displacement of the anions perpendicular to the Ta$\cdots$Ta axis, and the displaced anions were disordered over four sites. The magnitude for the displacement, δ, was estimated based on geometric considerations using Ta–X distances and Ta–(X)–Ta distances determined from direct peak fitting (Table 9.1). These values were averaged over the temperature range examined (80-487 K). The Ta–X distances are in remarkably good agreement with those expected based on bond valence sum considerations. The displacements are consistent with the large transverse component of the atomic displacement parameters for O/F observed by Tao and Sleight in a low-temperature neutron diffraction study [25]. A detailed description of the supercell model and its creation is found in Appendix E.

The anion-displaced supercell model provides an excellent fit to the local structure (R_W [1.5-8.0 Å] = 23.6%; Figure 9.1d) compared to the simple ReO_3 or ordered supercell models,

Table 9.1: Temperature-averaged Ta–X–Ta (X = O, F) bond angles, Ta–X and Ta–(X)–Ta separations, and anion displacements δ_X from the Ta$\cdots$Ta axis in TaO_2F over 80-487 K. Average atomic separations were obtained by curve fitting to the variable-temperature PDFs, and angles and δ_X were calculated geometrically from the separations. Estimated standard deviations for the temperature-averaged values are given in parentheses. Note that a systematic error, which would not show up in least-squares based error estimates, of only ∼0.004 Å in the Ta–O separation estimates would be enough to imply linear rather than bent Ta–O–Ta links.

Link	**Angle (°)**	**Ta–X (Å)**	**Ta–(X)–Ta (Å)**	δ_X **(Å)**
Ta–O–Ta	172(1)	1.891(2)	3.7731(2)	0.13(2)
Ta–F–Ta	155(1)	2.109(6)	4.1181(10)	0.45(3)

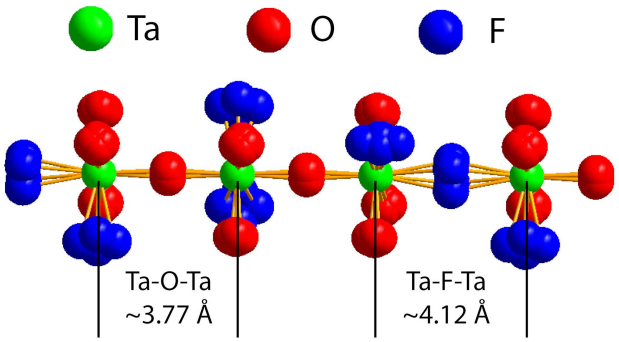

Figure 9.2: Single –Ta–O–Ta–O–Ta–F–Ta– chain from the TaO_2F anion-displaced supercell model. Reproduced from ref. [218].

supporting the observation of non-linear Ta–X–Ta geometry. Beyond ∼8 Å, the goodness of fit decreases (R_W [8-40 Å] = 33.8%; Figure 9.1c), likely reflecting the limitations of applying an inherently long-range ordered model to an intrinsically disordered system and/or strain. A single representative –Ta–O–Ta–O–Ta–F–Ta– chain is shown in Figure 9.2.

The proposal that both the Ta–F–Ta and Ta–O–Ta links are bent is initially somewhat surprising. On average, the longer Ta–F and Ta–(F)–Ta distances should be under compression, which can be accommodated by bending. By contrast, the shorter Ta–O and Ta–(O)–Ta distances may be expected to be under tension, which is in apparent conflict with the bending of the Ta–O–Ta linkages. However, the best estimate for the bending of these linkages is very small when considering the errors in these analyses and, if real, may be driven by the need to avoid unfavorable distortions of the TaX_6 octahedra.

It is reasonable to expect geometrically distinct M–X–M links, as observed in TaO_2F, in other disordered mixed-anion materials with ReO_3-type or perovskite structures, such as $ATaO_2N$ (A = Ba, Sr, Ca) [321]. However, the X-ray total scattering measurements on TaO_2F are particularly sensitive to this difference, as contributions to the PDFs from Ta$\cdots$Ta correlations are strong when compared to those from anion-anion correlations; furthermore, there are no A-site cations to add complexity to the PDFs, and the expected difference between the Ta–O and Ta–F bond lengths is large. In a neutron total scattering study of $BaTaO_2N$ [322], models with different Ta–O and Ta–N bond lengths were used, but the existence of geometrically distinct Ta–O–Ta and Ta–N–Ta links was not qualitatively obvious from the neutron PDFs. However, the existence of distinct Ta–O–Ta and Ta–F–Ta is readily apparent from the X-ray PDFs for TaO_2F. Recent work on $SrMO_2N$ (M = Nb, Ta) has shown that, in these materials, there is robust local ordering of oxide and nitride. The nitrogen atoms linking *cis*-MO_4N_2 octahedra tend to lie preferentially in two-dimensional sheets within the structure, leading to materials that appear to be almost metrically cubic at elevated temperatures but are in fact of lower symmetry [323]. As the PDFs for TaO_2F clearly show very different Ta–O–Ta and Ta–F–Ta separations, two-dimensional ordering of the Ta–F–Ta chains, analogous to that found for M–N–M in $SrMO_2N$, would lead to a pronounced deviation from cubic metric symmetry that is not observed in TaO_2F.

9.3.3 Thermal expansion of TaO_2F

As the cubic ReO_3-type model agrees with experimental PDFs at high r (Figure 9.1a), it was used to extract the temperature dependence of the lattice constants from the PDFs by fitting the PDFs from r = 13 to 40 Å. As expected, the lattice constant is equivalent to the weighted average of the Ta–(O)–Ta and Ta–(F)–Ta separations. Notably, none of the three distances varies significantly with temperature; their coefficients of thermal expansion (CTEs) all lie within the range -1 to +1 ppm·K^{-1} between 100 and 380 K.

This near-equivalent response to heating is somewhat surprising, as the local structure of TaO_2F clearly contains geometrically distinct Ta–O–Ta and Ta–F–Ta links that have different Ta$\cdots$Ta separations and average Ta–X–Ta angles (Table 9.1). As discussed

in previous chapters, heating metal trifluorides with rhombohedrally distorted ReO_3-type structures, such as α-AlF_3, leads to an increase in the crystallographic M–F–M bond angle and strong positive thermal expansion until this crystallographic bond angle approaches 180° (as in, for example, Figure 4.8), suggesting that the Ta–O–Ta and Ta–F–Ta links, with their different average bond angles, might respond differently to temperature; yet, no significant systematic change with temperature is observed for these angles (Figure 9.3a) or the anion off-axis displacements δ_X calculated from the angles (Figure 9.3b). However, in rhombohedrally distorted MF_3, the increase in the M–F–M angle on heating and the resulting positive thermal expansion occur in the context of a cooperative tilting of MF_6 octahedra. Such a cooperative tilting is not possible in TaO_2F, as it is cubic on average.

TaO_2F does not display significant NTE due to the "buckled" nature of its local structure (it contains bent Ta–X–Ta links) and the strains associated with the disordered arrangement of geometrically distinct Ta–O–Ta and Ta–F–Ta links. There is no particular reason why this type of local structure should lead to near-zero thermal expansion rather than modest positive or negative thermal expansion. However, the "bent" nature of the Ta–X–Ta links is not ideal for NTE, and the disordered nature of the local structure inhibits the complete elimination of these bent links by the cooperative tilting of octahedra, which leads to the strong positive thermal expansion observed in rhombohedral MF_3. Note that NbO_2F, which is expected to have a similar local structure, is known to display quite strong thermal expansion below room temperature [25, 205]. This proposal for TaO_2F is consistent with work on ReO_3 itself, in which the absence of strong NTE has been attributed to static displacement of the oxygen atoms transverse from the Re–O–Re bond [186], and prior work on TaO_2F by Tao and Sleight, in which the observation of large O/F transverse ADP values persisting to low temperatures was associated with the near-zero thermal expansion [25].

9.4 Conclusion

Local distortions away from the ideal ReO_3-type structure, associated with the need to accommodate the different bonding requirements of the disordered O/F anions, contribute to the occurrence of near-zero thermal expansion in TaO_2F rather than NTE. The local

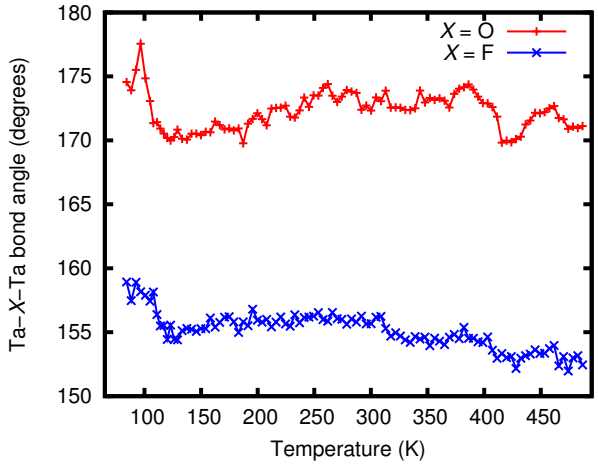

(a)

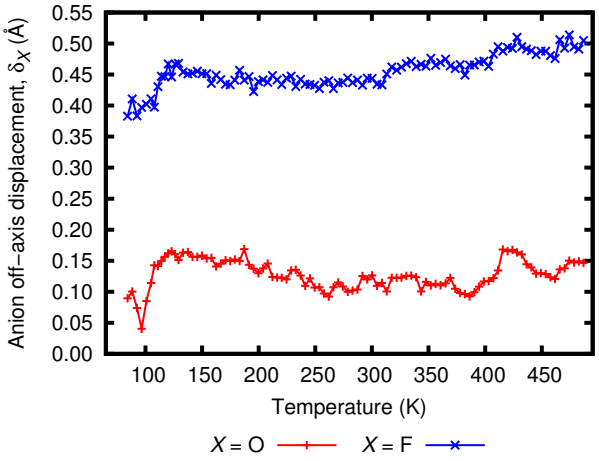

(b)

Figure 9.3: Temperature dependence of (a) Ta–X–Ta bond angle and (b) anion off-axis displacement δ_X (X = O, F) in TaO_2F, calculated from interatomic separations by geometry. Reproduced from ref. [218].

structure of TaO_2F is poorly described by an ideal cubic ReO_3-type model with O and F randomly distributed over the available anion sites, whereas a $3 \times 3 \times 3$ supercell model featuring –Ta–O–Ta–O–Ta–F– chains along <1 0 0> with different Ta–O and Ta–F distances and O/F off-axis displacements gives much better agreement with the PDFs for small separations (< 8 Å). Analyses of PDFs derived from variable-temperature measurements over different length scales indicate an average linear CTE close to zero with similar contributions from the geometrically distinct Ta–O–Ta and Ta–F–Ta links in TaO_2F.

CHAPTER 10

CONCLUSIONS AND POSSIBLE FUTURE DIRECTIONS

The thermal expansion behaviors of several materials with ReO_3-type connectivity have been explored in this thesis, with a particular focus on the effects of structural disorder and stress on thermal expansion. The cubic ReO_3 framework is a very simple structure with all of the key features required for negative thermal expansion (NTE) arising from the transverse thermal motion of bridging atoms and rotation of rigid polyhedra. In the preceding chapters, with extensive use of *in situ* variable-temperature/pressure synchrotron X-ray diffraction as well as X-ray total scattering, the effects on thermal expansion and related properties (compressibility and heat capacity) of both cation and anion substitution and the stress and disorder produced by these structural changes have been demonstrated. Despite the simplicity of the ReO_3 structure, some rather complex and unexpected phenomena are observed, especially when disorder is introduced. A variety of thermal expansion behaviors in the ReO_3 family is observed, with volume coefficients of thermal expansion (CTEs) that range from highly negative to near-zero to highly positive; in addition, CTE can be affected by modest stress. In this concluding chapter, the results of this thesis are summarized, and possible future studies are suggested.

Even the thermal expansion of simple, ordered ReO_3-type metal trifluorides is not straightforward, as demonstrated in Chapter 4. At ambient conditions, both α-AlF_3 and InF_3 have a rhombohedrally distorted form of the ReO_3 crystal structure that becomes cubic on heating. This phase transition occurs at ~713 K in α-AlF_3, while in InF_3, an unexpectedly large temperature range (between ~680 and ~795 K) is observed with rhombohedral and cubic phase co-existence. The rhombohedral phase of both α-AlF_3 and InF_3 displays strongly anisotropic and positive thermal expansion. However, while α-AlF_3 continues to display strong positive thermal expansion (volume CTE at 900 K $\approx$ 25 ppm$\cdot$K^{-1}),

the thermal expansion of cubic InF_3 changes from positive to zero (∼850 to 950 K) to negative (above ∼950 K) upon heating. The positive thermal expansion of cubic α-AlF_3 may be partially due to the presence of local octahedral tilts and an associated increase of the average Al–F–Al bond angle on heating. The phase co-existence observed in InF_3 may not be intrinsic to the compound but instead due to sample inhomogeneity.

In contrast to other ReO_3-type metal trifluorides, such as α-AlF_3 and InF_3, cubic ScF_3 displays strong isotropic NTE over a broad temperature range that is most pronounced at low temperatures [35]. At ambient pressure, ScF_3 remains cubic down to very low temperatures (∼10 K from neutron diffraction [35], 4 K from Raman spectroscopy [245], or 0.35 K from the heat capacity measurements in Chapter 7). However, when ScF_3 powder is mixed with a polyvinyl phenolic varnish (GE-7031), an unexpected cubic-to-rhombohedral phase transition in the trifluoride is observed at ∼50 K, exhibiting smaller low-temperature unit cell volumes than samples without the varnish matrix. Experimental observations and quantitative estimates suggest that these anomalies are the result of stress induced by thermal expansion mismatch between the varnish matrix (large positive CTE) and ScF_3 (quite large negative CTE). The potentially deleterious effects of thermal expansion mismatch and limitations of ScF_3 during use in CTE-controlled composites, a potential application for materials showing NTE, were demonstrated in Chapter 5.

As an alternative to composites, solid solution formation for thermal expansion control in ScF_3 was investigated; thermal expansion studies of $Sc_{1-x}M_xF_3$ (M = Ti, Y, and Al) solid solutions were the focus of Chapters 6, 7, and 8, respectively. Differently sized cations were substituted into the ScF_3 framework and, via variable-temperature/pressure synchrotron diffraction (including use of the background-reducing internal mask (BRIM) discussed and demonstrated in Chapter 3), explored the effects on both thermal expansion and compressibility. In the simplest case, $Sc_{1-x}Ti_xF_3$, Sc^{3+} and Ti^{3+} are closely size-matched, allowing full solubility of TiF_3 in ScF_3 at synthesis temperature (1338 K). The temperature for the cubic-to-rhombohedral phase transition in $Sc_{1-x}Ti_xF_3$ varies linearly with composition (above 100 K), and, at high Ti content, the transition is clearly first-order. The rhombohedral phase for each composition examined exhibits strongly positive thermal

expansion, while the expansion of the cubic phase (between 420 and 500 K) is negative or low positive for all $Sc_{1-x}Ti_xF_3$, with a small degree of CTE tunability (average volume CTE between 350 and 470 K varies from ∼-16 to ∼+4 ppm·K^{-1} with increased Ti content).

The two solid solution families featuring size-mismatched cations, however, exhibit somewhat different behaviors than $Sc_{1-x}Ti_xF_3$. Full solubility is not observed in either family at reaction temperature as a result of the size mismatch. First, insertion of the relatively large Y^{3+} ion into ScF_3 results in a subtle (clearly not first-order) cubic-to-rhombohedral phase transition upon cooling from ambient temperature to 100 K, even at low substitution levels (5%); this subtle phase transition is also observed via heat capacity measurements. The rhombohedral-phase CTE is strongly dependent on both composition and temperature; however, above 400 K, where all samples are cubic, the CTE appears to be largely independent of composition. Also, as shown in Chapters 7 and 8, the isothermal bulk modulus and CTE of ScF_3, but not those of its solid solutions, are independent of temperature and pressure, respectively. Y^{3+} substitution lowers the bulk modulus, even at temperatures where the samples are cubic; the solid solutions also stiffen upon heating. The larger solubility range of $Sc_{1-x}Al_xF_3$ (∼50%) compared to $Sc_{1-x}Y_xF_3$ (∼25%) allows for a broader exploration of the effects of composition on thermal expansion and compressibility, although insertion of the relatively small Al^{3+} ion into ScF_3 has similar effects to Y^{3+} substitution. A second-order cubic-to-rhombohedral phase transition is also observed in $Sc_{1-x}Al_xF_3$, the temperature of which increases smoothly with Al^{3+} substitution, approaching 500 K at high Al content. The rhombohedral-phase CTE is strongly positive, while that of the cubic phase above ∼600 K varies from negative ($x < 0.15$) to approximately zero ($x = 0.15$) to positive ($x > 0.20$) with Al^{3+} substitution. As in $Sc_{1-x}Y_xF_3$, cubic $Sc_{1-x}Al_xF_3$ elastically stiffen on heating, and Al^{3+} substitution causes softening at a given temperature. The slope of the pressure-temperature phase boundary (∼0.5 K·MPa^{-1}) is much steeper than that for most symmetry-lowering phase transitions in perovskites.

In addition to cation disorder, a cubic ReO_3-type material that features anion disorder, TaO_2F, was also studied. Local distortions away from the ideal cubic structure, associated with the need to accommodate the different bonding requirements of the disordered O and

F, contribute to the (previously reported [25]) occurrence of near-zero thermal expansion rather than NTE in TaO_2F. The local structure of TaO_2F is poorly described by a cubic ReO_3-type model with O and F randomly distributed over the available anion sites, but a supercell model featuring –Ta–O–Ta–O–Ta–F– chains along <1 0 0>, with different Ta–O and Ta–F distances and O/F off-axis displacements, gives much better agreement with pair distribution functions (PDFs) derived from X-ray total scattering data for small separations (<8 Å). Analyses of PDFs derived from variable-temperature X-ray total scattering measurements of TaO_2F (80 to 487 K), over different length scales, indicate an average CTE close to zero, with similar contributions from the geometrically distinct Ta–O–Ta and Ta–F–Ta links.

Based on the results presented in this thesis, the following additional studies are suggested:

1. The ∼120 K region of phase co-existence observed in InF_3 (Chapter 4) is unusual and should be further examined. Unlike α-AlF_3, the InF_3 sample used in Chapter 4 was not annealed prior to characterization and may not have been adequately homogeneous; thus, the observed phase co-existence may not be intrinsic to InF_3. An additional high-temperature PXRD study of InF_3 with an annealed sample may provide insight into this question.

2. The thermal expansion behavior of additional ReO_3-type MF_3 should be characterized. The thermal expansion of InF_3 is reported and that of α-AlF_3 quantified for the first time, but the CTEs of several other MF_3 (for example, M = Fe, Ga, and V) have not been reported to date. A high-temperature PXRD study of FeF_3 was attempted (not reported) but failed due to decomposition of the sample before any phase transition was observed. With the proper samples and experimental setup, the CTEs of these simple, ordered materials could be measured over a wide temperature range, providing benchmarks for studies of solid solutions or other related disordered materials.

3. Solid solutions of ScF_3 with other MF_3 (besides M = Al, Ti, and Y) could be explored,

one of which may offer a wider range of thermal expansion control than M = Al, Ti, and Y at near-ambient temperatures. In addition, the synthesis of these solid solutions used in this work, especially reaction temperature, could be optimized. Solid solubility in ScF_3 solid solutions is known to be strongly temperature-dependent, so higher solubility limits than 25 and 50% may be possible in $Sc_{1-x}Y_xF_3$ and $Sc_{1-x}Al_xF_3$, respectively, at higher reaction temperatures than those used herein (1273 and 1338 K).

4. One particular result from the solid solution studies that requires further exploration is the independence of volume CTE with composition above ~400 K in $Sc_{1-x}Y_xF_3$ (Figure 7.6). Knowledge of the entire phonon density of states for $Sc_{1-x}Y_xF_3$ and the volume dependence of its phonon frequencies is needed. From the lattice dynamics of $Sc_{1-x}Y_xF_3$, perhaps explored with variable-temperature/pressure inelastic neutron scattering, the mode Grüneisen parameters of the solid solutions could be calculated. If possible, density functional theory calculations for these disordered systems would also provide some insight into lattice dynamics. The effort required for such studies, however, may not be worth the outcome.

5. This study of $Sc_{1-x}M_xF_3$ demonstrates the contribution of local-scale structural distortions (those of the size-mismatched cations) to thermal expansion. In the examples discussed in this thesis, lowering temperature results in long-range rhombohedral distortion (*i.e.*, a symmetry-lowering phase transition) that contributes to the existence of positive thermal expansion. However, a structure featuring non-ordered, local-scale structural distortions could provide the desired control over CTE but suppress the phase transition. One such possibility based on this work is the introduction of some amount of *both* Al^{3+} and Y^{3+} into the ScF_3 framework (assuming cation-site disorder).

6. TaO_2F displays near-zero thermal expansion rather than NTE probably due to local distortions introduced by the different bonding requirements of O and F. The closely related cubic ReO_3-type material NbO_2F displays strong positive thermal expansion between 20 and 300 K [25]. A closer examination of the local structure of NbO_2F with

X-ray total scattering (similar to the study discussed in Chapter 9) would be useful to explain the difference in thermal expansion behaviors of the two oxyfluorides.

APPENDIX A

CHAPTER 5 SUPPORTING MATERIAL

Table A.1: Cubic lattice constants, unit cell volumes, and volumes normalized to 250 K, at various temperatures, of ScF_3. The lattice constants (a) were extracted during Rietveld analysis of powder diffraction data. For the "No Varnish, He" sets, V_{250} was linearly extrapolated from surrounding values (64.771); the same is true for both "Varnish" sets (64.748 was used for both). The V/V_{250} are plotted in Figure 5.1. The "Neutron" lattice constants are from ref. [35].

T (K)	a (Å)	V (Å^3)	V/V_{250}	Data set
10	4.02398	65.158	1.0079	Neutron
60	4.02204	65.064	1.0065	Neutron
110	4.01932	64.932	1.0044	Neutron
180	4.01618	64.780	1.0021	Neutron
250	4.01339	64.645	1.0000	Neutron
6.6	4.025686(5)	65.241	1.0073	No Varnish, He (heat)
19.7	4.025338(5)	65.224	1.0070	No Varnish, He (heat)
33.75	4.024906(4)	65.203	1.0067	No Varnish, He (heat)
48.25	4.023837(4)	65.179	1.0063	No Varnish, He (heat)
62.15	4.023215(4)	65.151	1.0059	No Varnish, He (heat)
76.05	4.023215(4)	65.121	1.0054	No Varnish, He (heat)
90.1	4.022593(4)	65.091	1.0050	No Varnish, He (heat)
104	4.022058(4)	65.065	1.0046	No Varnish, He (heat)
118.05	4.021441(4)	65.035	1.0041	No Varnish, He (heat)
132.1	4.020798(4)	65.003	1.0036	No Varnish, He (heat)

Table A.1: *Continued on next page*

Table A.1: *Continued from previous page*

T (K)	a (Å)	V (Å^3)	V/V_{250}	Data set
146.2	4.020154(4)	64.972	1.0031	No Varnish, He (heat)
230.2	4.016597(4)	64.800	1.0005	No Varnish, He (heat)
298	4.014483(7)	64.698	0.9989	No Varnish, He (heat)
13	4.025749(5)	65.244	1.0073	No Varnish, He (cool)
27.1	4.025237(5)	65.219	1.0069	No Varnish, He (cool)
40.95	4.024803(5)	65.198	1.0066	No Varnish, He (cool)
55	4.024294(4)	65.173	1.0062	No Varnish, He (cool)
68.95	4.023705(4)	65.145	1.0058	No Varnish, He (cool)
82.95	4.023090(4)	65.115	1.0053	No Varnish, He (cool)
96.9	4.022463(4)	65.084	1.0048	No Varnish, He (cool)
111.05	4.021793(4)	65.052	1.0044	No Varnish, He (cool)
125.05	4.021125(4)	65.019	1.0038	No Varnish, He (cool)
139.1	4.020469(4)	64.988	1.0034	No Varnish, He (cool)
6.65	4.019261(23)	64.929	1.0026	Varnish, He
7.3	4.018627(25)	64.898	1.0021	Varnish, He
10	4.018734(24)	64.903	1.0022	Varnish, He
20	4.021092(22)	65.018	1.0040	Varnish, He
30.2	4.021388(22)	65.032	1.0042	Varnish, He
39.95	4.022528(17)	65.087	1.0051	Varnish, He
50.05	4.022403(15)	65.081	1.0050	Varnish, He
59.95	4.022300(11)	65.076	1.0049	Varnish, He
69.9	4.021892(10)	65.057	1.0046	Varnish, He
80	4.021618(8)	65.043	1.0044	Varnish, He
90	4.021167(8)	65.021	1.0040	Varnish, He
100.15	4.020867(8)	65.007	1.0038	Varnish, He
109.85	4.020480(7)	64.988	1.0035	Varnish, He

Table A.1: *Continued on next page*

Table A.1: *Continued from previous page*

T **(K)**	a **(Å)**	V **(Å^3)**	V/V_{250}	**Data set**
120	4.020113(7)	64.970	1.0033	Varnish, He
130	4.019731(6)	64.952	1.0030	Varnish, He
139.7	4.019424(6)	64.937	1.0027	Varnish, He
149.55	4.019009(6)	64.917	1.0024	Varnish, He
100.4	4.020846(8)	65.006	1.0038	Varnish, N_2
110.15	4.020504(7)	64.989	1.0035	Varnish, N_2
120.05	4.020102(7)	64.970	1.0033	Varnish, N_2
130.1	4.019750(6)	64.953	1.0030	Varnish, N_2
140.25	4.019399(6)	64.936	1.0027	Varnish, N_2
150.1	4.019059(5)	64.919	1.0025	Varnish, N_2
160.1	4.018699(5)	64.902	1.0022	Varnish, N_2
180.15	4.018130(4)	64.874	1.0018	Varnish, N_2
200.15	4.017473(4)	64.842	1.0013	Varnish, N_2
220.1	4.016796(4)	64.810	1.0008	Varnish, N_2
240.15	4.016085(4)	64.775	1.0002	Varnish, N_2
260.1	4.015450(4)	64.744	0.9998	Varnish, N_2
280.4	4.014883(4)	64.717	0.9993	Varnish, N_2
300.1	4.014321(4)	64.690	0.9989	Varnish, N_2

APPENDIX B

CHAPTER 6 SUPPORTING MATERIAL

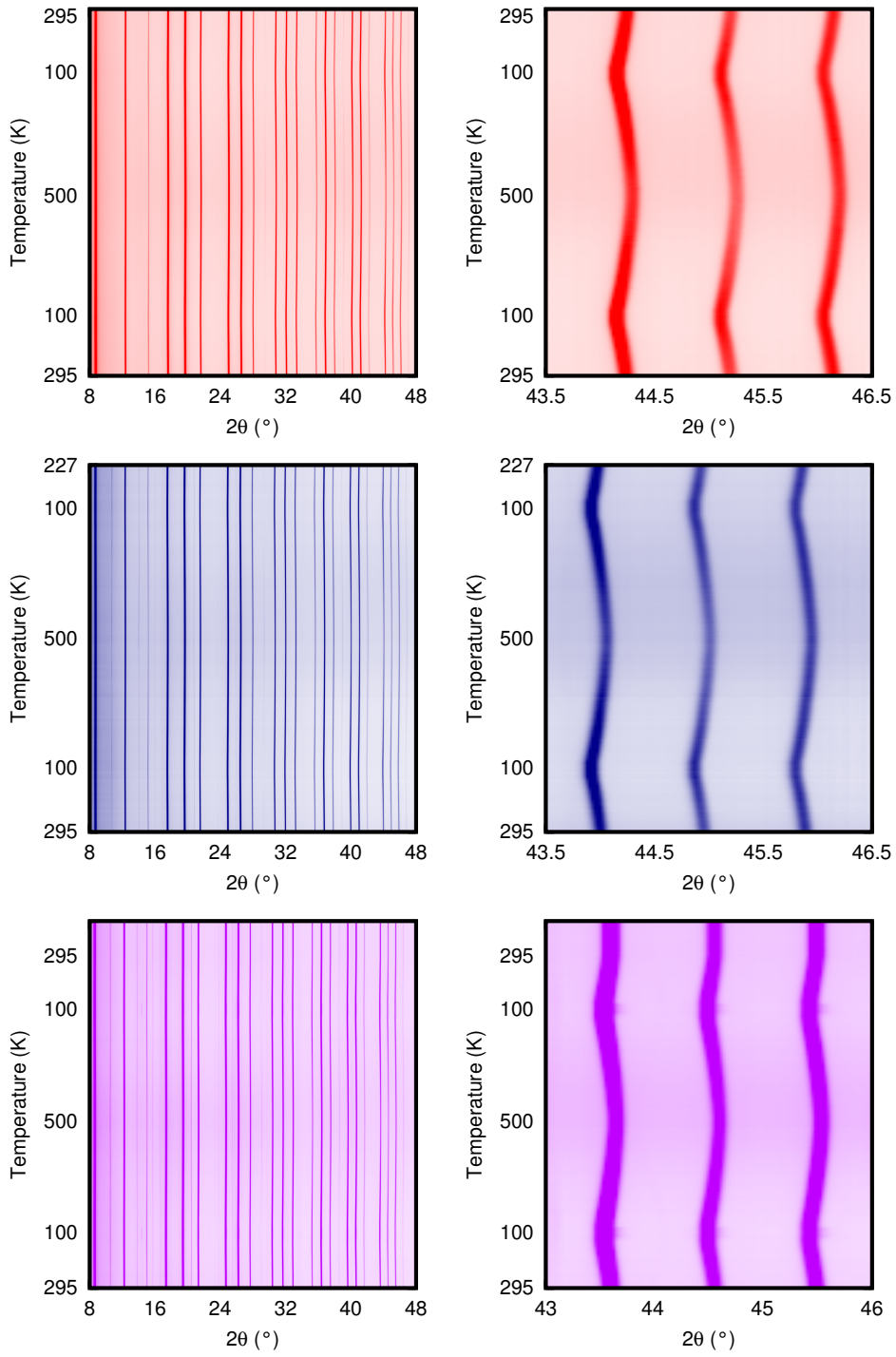

Figure B.1: Variable-temperature (100-500 K) powder X-ray diffraction (PXRD) data collected for $Sc_{1-x}Ti_xF_3$ in which $x = 0.00$ (top), 0.10 (middle), and 0.30 (bottom). The plots in the left column show the full angular range used for Rietveld analyses, while those on the right show a high-angle portion in which the splittings associated with the phase transition are most apparent (where applicable). Within each plot, diffraction patterns are arranged in order of collection from bottom to top, which followed the temperature ramp in Figure 2.2b. Reproduced from ref. [238].

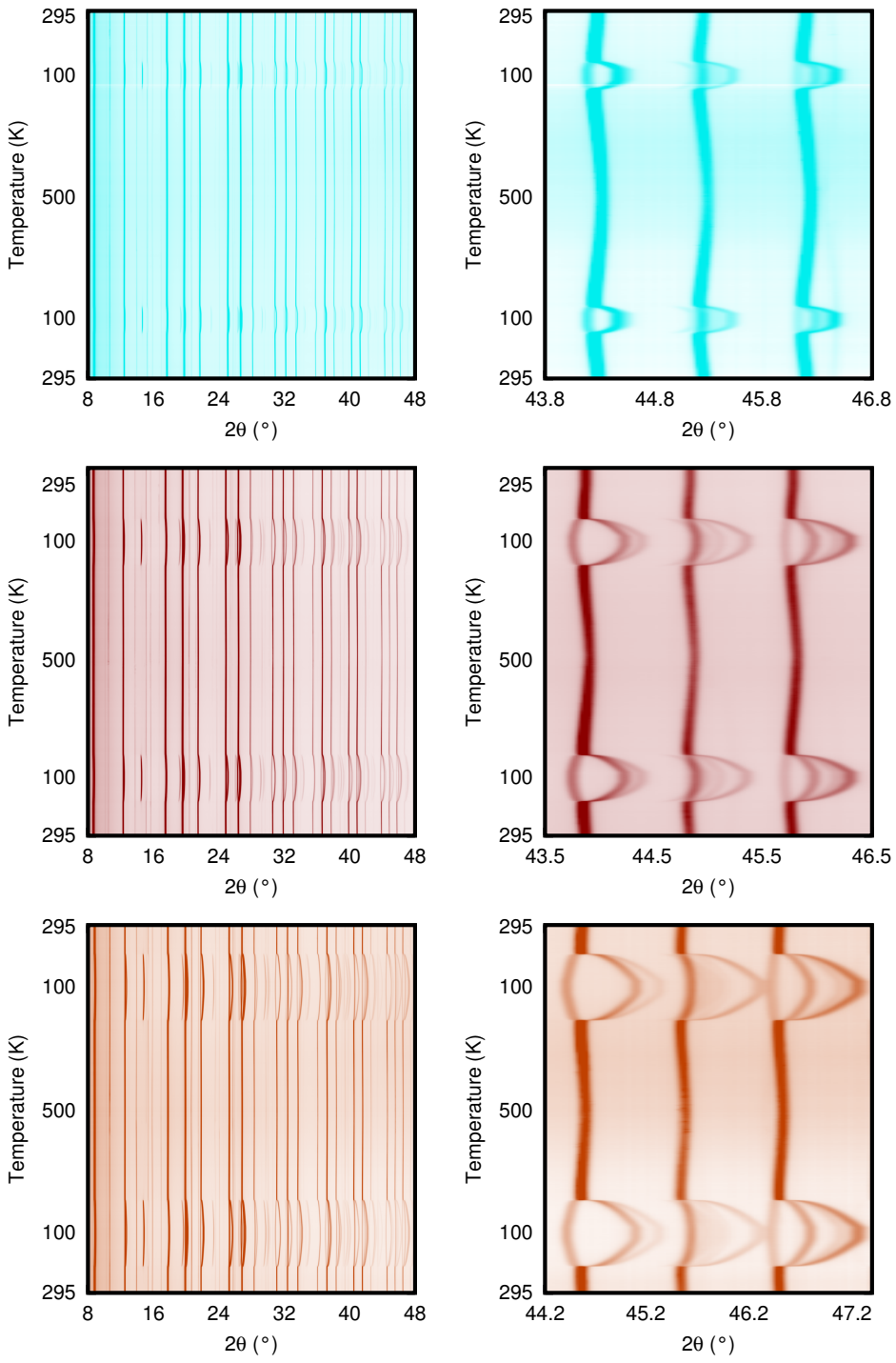

Figure B.2: Variable-temperature (100-500 K) PXRD data collected for $Sc_{1-x}Ti_xF_3$ in which $x = 0.40$ (top), 0.50 (middle), and 0.60 (bottom). The plots in the left column show the full angular range used for Rietveld analyses, while those on the right show a high-angle portion in which the splittings associated with the phase transition are most apparent. Within each plot, diffraction patterns are arranged in order of collection from bottom to top, which followed the temperature ramp in Figure 2.2b. Reproduced from ref. [238].

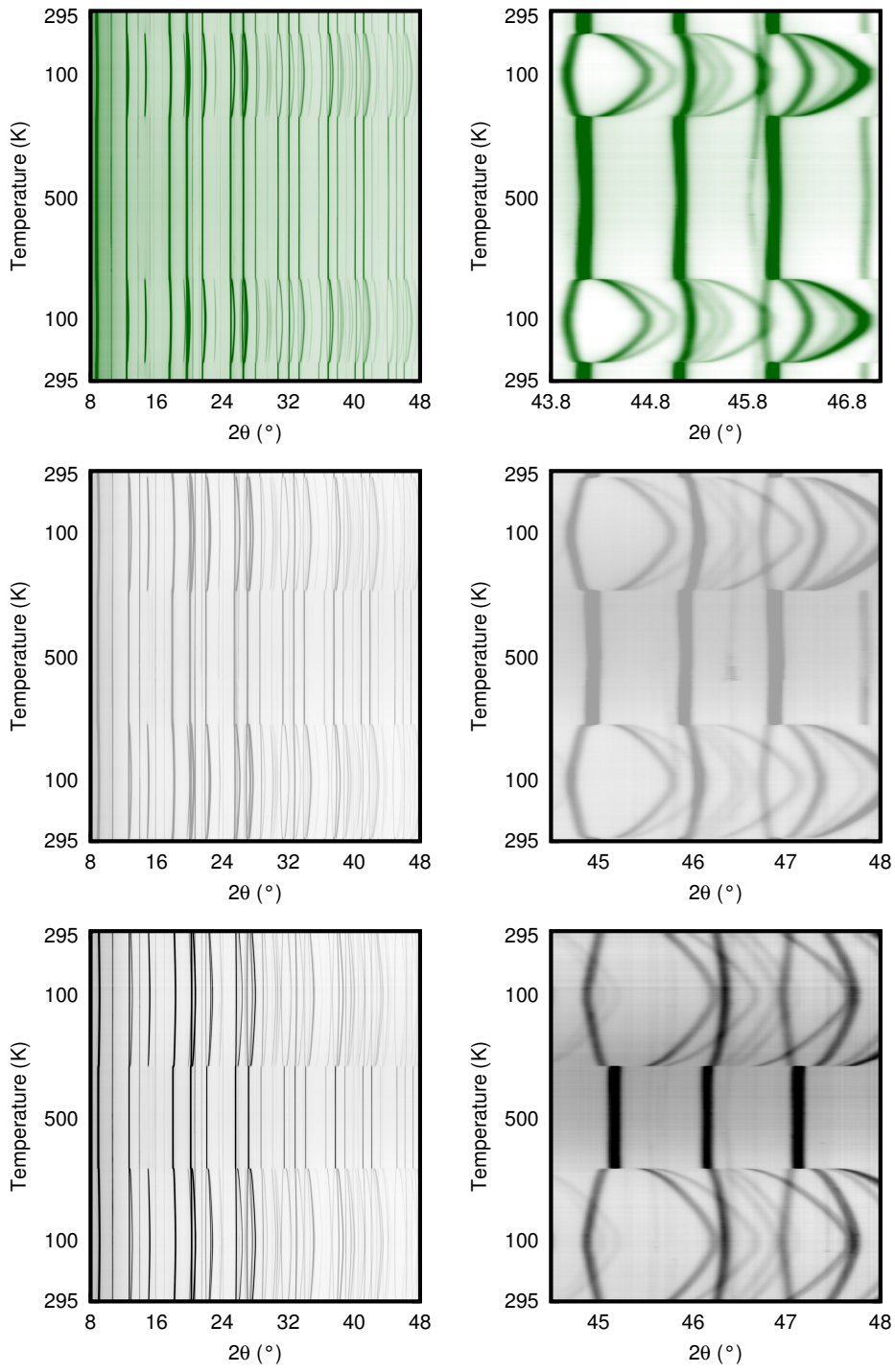

Figure B.3: Variable-temperature (100-500 K) PXRD data collected for $Sc_{1-x}Ti_xF_3$ in which $x = 0.70$ (top), 0.85 (middle), and 1.00 (bottom). The plots in the left column show the full angular range used for Rietveld analyses, while those on the right show a high-angle portion in which the splittings associated with the phase transition are most apparent. Within each plot, diffraction patterns are arranged in order of collection from bottom to top, which followed the temperature ramp in Figure 2.2b. Reproduced from ref. [238].

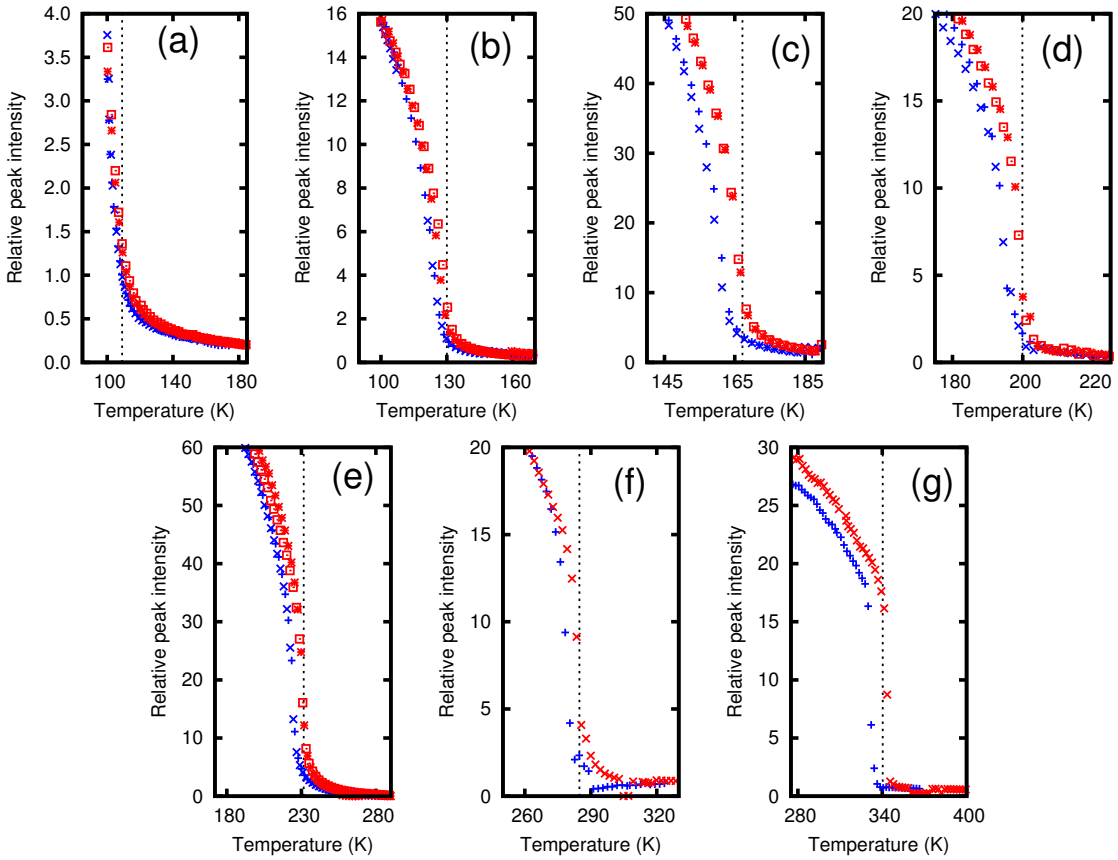

Figure B.4: The cubic-to-rhombohedral phase transition temperature for each $Sc_{1-x}Ti_xF_3$ sample was estimated by monitoring the intensity of the rhombohedral (2 1 0) Bragg reflection ($d \approx 2.3$-2.4 Å), which is only present in the rhombohedral structure (low temperatures). A pseudo-Voigt profile with linear background was fit to the synchrotron PXRD data using the program *Fityk* [273]. Straight lines were fit to the peak intensity *versus* temperature curves (shown here) at both high temperatures (where there was some residual intensity, perhaps associated with diffuse scattering) and low temperatures (just before the phase transition); the intersection of these lines was considered the transition temperature. The values estimated for heating and cooling curves differed somewhat, so the average is reported here. In this figure, the phase transition temperature of each sample is indicated by a black dashed vertical line: (a) $x = 0.30$, (b) $x = 0.40$, (c) $x = 0.50$, (d) $x = 0.60$, (e) $x = 0.70$, (f) $x = 0.85$, (g) $x = 1.00$. Data for $x = 0.00$ and 0.10 are not included, as these samples remain cubic between 100 and 500 K. In each plot, red points indicate data collected on heating, while blue points indicate data collected on cooling. Reproduced from ref. [238].

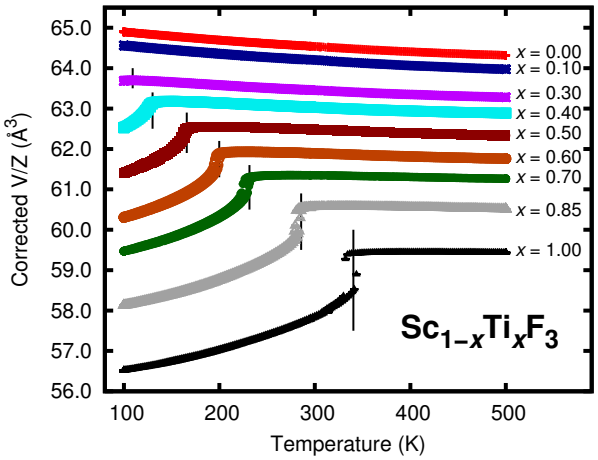

Figure B.5: Temperature dependence of V/Z for $Sc_{1-x}Ti_xF_3$. These volumes were extracted in Rietveld analyses of the variable-temperature PXRD data and then corrected to account for calibration differences between experiments conducted during different beam times. Phase transition temperature estimates (see Figure B.4) are indicated by black vertical lines. Reproduced from ref. [238].

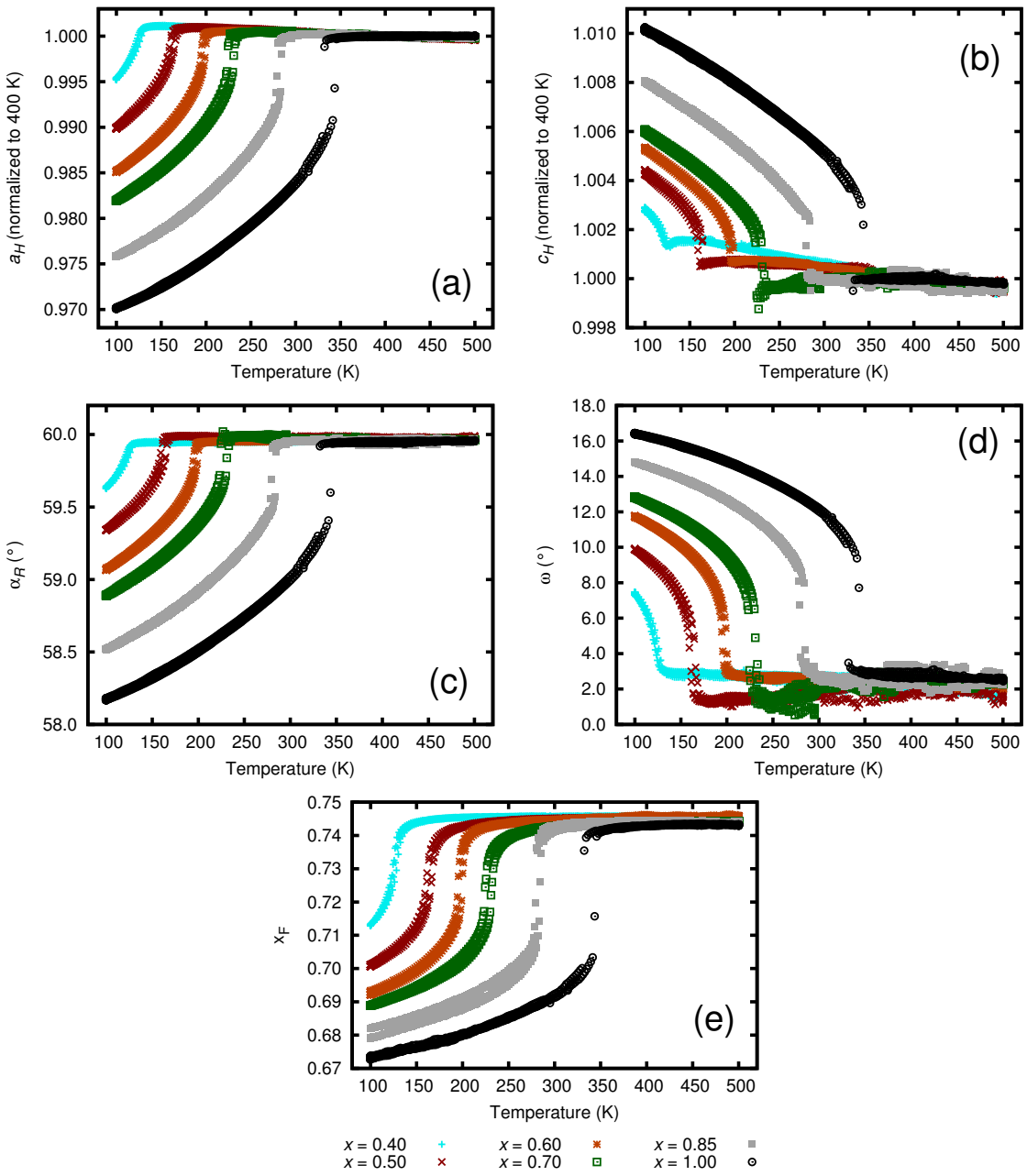

Figure B.6: Temperature dependence of unit cell parameters for $Sc_{1-x}Ti_xF_3$: (a), (b) hexagonal lattice constants a_H and c_H, both normalized to 400 K, (c) primitive rhombohedral unit cell angle α_R, (d) octahedral tilt angle ω, and (e) fractional x-coordinate of F (rhombohedral cell). Primitive rhombohedral cell constants a_R and α_R were determined by Rietveld analysis of the variable-temperature PXRD data and converted to hexagonal constants using Equations 4.1 and 4.2. Octahedral tilt angle was computed using $\cos\omega = \frac{a_H}{c_H}\sqrt{6}$. The expected values for α_R and ω in the cubic phase are 60 and 0°, respectively. The rhombohedral model used in the Rietveld analyses is over-parameterized, which in combination with imperfections in the data, leads to small discrepancies between the observed and expected values of α_R and ω. Samples that are cubic between 100 and 500 K ($x = 0.00$ and 0.10) are not shown here, and $x = 0.30$ is excluded because its phase transition occurs just above 100 K. Reproduced from ref. [238].

APPENDIX C

CHAPTER 7 SUPPORTING MATERIAL

Table C.1: Lattice constants and unit cell volumes of ScF_3 at various temperatures and pressures. These values were determined by Rietveld analyses of high-pressure, high-temperature data and are presented here without scaling.

T (K)	P (GPa)	a (Å)	esd(a)	V (Å^3)	esd(V)
298	0.000	4.011752	0.000031	64.566	0.001
298	0.069	4.010346	0.000030	64.498	0.001
298	0.138	4.008869	0.000032	64.427	0.002
298	0.207	4.007273	0.000031	64.350	0.001
298	0.270	4.005854	0.000033	64.281	0.002
298	0.242	4.006557	0.000032	64.315	0.002
298	0.173	4.008102	0.000032	64.390	0.002
298	0.104	4.009581	0.000032	64.461	0.002
298	0.035	4.011175	0.000030	64.538	0.001
343	0.069	4.009232	0.000032	64.444	0.002
343	0.138	4.007714	0.000032	64.371	0.002
343	0.207	4.006182	0.000034	64.297	0.002
343	0.271	4.004741	0.000039	64.228	0.002
343	0.240	4.005401	0.000040	64.260	0.002
343	0.173	4.006985	0.000040	64.336	0.002
343	0.103	4.008482	0.000038	64.408	0.002
343	0.035	4.010003	0.000036	64.481	0.002
388	0.069	4.008175	0.000037	64.393	0.002

Table C.1: *Continued on next page*

Table C.1: *Continued from previous page*

T (K)	P (GPa)	a (Å)	esd(a)	V (Å^3)	esd(V)
388	0.138	4.006680	0.000039	64.321	0.002
388	0.207	4.005127	0.000041	64.246	0.002
388	0.270	4.003715	0.000054	64.178	0.003
388	0.240	4.004346	0.000053	64.209	0.003
388	0.172	4.005871	0.000049	64.282	0.002
388	0.104	4.007429	0.000043	64.357	0.002
388	0.035	4.008924	0.000038	64.429	0.002
433	0.069	4.007224	0.000041	64.347	0.002
433	0.138	4.005709	0.000046	64.274	0.002
433	0.207	4.004158	0.000046	64.200	0.002
433	0.268	4.002815	0.000056	64.135	0.003
433	0.239	4.003423	0.000055	64.164	0.003
433	0.172	4.004923	0.000053	64.237	0.003
433	0.104	4.006423	0.000047	64.309	0.002
433	0.035	4.007951	0.000045	64.382	0.002
478	0.069	4.006355	0.000047	64.306	0.002
478	0.138	4.004850	0.000048	64.233	0.002
478	0.207	4.003272	0.000052	64.157	0.003
478	0.241	4.002535	0.000055	64.122	0.003
478	0.172	4.004075	0.000054	64.196	0.003
478	0.103	4.005599	0.000048	64.269	0.002
478	0.034	4.007150	0.000046	64.344	0.002
523	0.069	4.005605	0.000046	64.269	0.002
523	0.138	4.004069	0.000049	64.196	0.002
523	0.207	4.002519	0.000054	64.121	0.003
523	0.241	4.001874	0.000056	64.090	0.003

Table C.1: *Continued on next page*

Table C.1: *Continued from previous page*

T (K)	P (GPa)	a (Å)	esd(a)	V (Å^3)	esd(V)
523	0.172	4.003330	0.000052	64.160	0.003
523	0.104	4.004869	0.000050	64.234	0.002
523	0.035	4.006435	0.000046	64.309	0.002

Table C.2: Lattice constants and unit cell volumes of $Sc_{0.95}Y_{0.05}F_3$ at various temperatures and pressures. These values were determined by Rietveld analyses of high-pressure, high-temperature data and are presented here without scaling.

T (K)	P (GPa)	a (Å)	esd(a)	V (Å^3)	esd(V)
298	0.000	4.011346	0.000067	64.546	0.003
298	0.069	4.009468	0.000062	64.456	0.003
298	0.138	4.007596	0.000066	64.365	0.003
298	0.207	4.005882	0.000095	64.283	0.005
298	0.276	4.003748	0.000079	64.180	0.004
298	0.241	4.004792	0.000067	64.230	0.003
298	0.172	4.006886	0.000065	64.331	0.003
298	0.103	4.008821	0.000064	64.424	0.003
298	0.035	4.010351	0.000064	64.498	0.003
343	0.069	4.008599	0.000056	64.414	0.003
343	0.138	4.006867	0.000071	64.330	0.003
343	0.207	4.004883	0.000072	64.235	0.003
343	0.276	4.003031	0.000078	64.146	0.004
343	0.241	4.003883	0.000082	64.187	0.004
343	0.172	4.005874	0.000065	64.282	0.003
343	0.103	4.007658	0.000061	64.368	0.003
343	0.035	4.009446	0.000059	64.454	0.003

Table C.2: *Continued on next page*

Table C.2: *Continued from previous page*

T (K)	P (GPa)	a (Å)	esd(a)	V (Å^3)	esd(V)
388	0.069	4.007721	0.000057	64.371	0.003
388	0.138	4.005941	0.000065	64.286	0.003
388	0.207	4.004175	0.000075	64.201	0.004
388	0.276	4.002416	0.000078	64.116	0.004
388	0.241	4.003325	0.000067	64.160	0.003
388	0.172	4.004996	0.000065	64.240	0.003
388	0.103	4.006724	0.000056	64.323	0.003
388	0.035	4.008421	0.000058	64.405	0.003
433	0.069	4.006787	0.000055	64.326	0.003
433	0.138	4.005127	0.000065	64.246	0.003
433	0.207	4.003427	0.000067	64.165	0.003
433	0.276	4.001772	0.000078	64.085	0.004
433	0.241	4.002672	0.000071	64.128	0.003
433	0.172	4.004499	0.000064	64.216	0.003
433	0.103	4.005958	0.000064	64.286	0.003
433	0.035	4.007754	0.000049	64.373	0.002
478	0.069	4.006091	0.000049	64.293	0.002
478	0.138	4.004576	0.000054	64.220	0.003
478	0.207	4.002871	0.000062	64.138	0.003
478	0.276	4.000946	0.000069	64.045	0.003
478	0.241	4.001986	0.000079	64.095	0.004
478	0.172	4.003626	0.000061	64.174	0.003
478	0.103	4.005335	0.000055	64.256	0.003
478	0.034	4.007060	0.000040	64.339	0.002
523	0.069	4.005407	0.000049	64.260	0.002
523	0.138	4.003836	0.000056	64.184	0.003

Table C.2: *Continued on next page*

Table C.2: *Continued from previous page*

T (K)	P (GPa)	a (Å)	esd(a)	V (Å^3)	esd(V)
523	0.207	4.002047	0.000066	64.098	0.003
523	0.241	4.001331	0.000067	64.064	0.003
523	0.172	4.002943	0.000059	64.141	0.003
523	0.103	4.004661	0.000052	64.224	0.003
523	0.035	4.006356	0.000047	64.306	0.002

Table C.3: Lattice constants and unit cell volumes of $Sc_{0.90}Y_{0.10}F_3$ at various temperatures and pressures. These values were determined by Rietveld analyses of high-pressure, high-temperature data and are presented here without scaling.

T (K)	P (GPa)	a (Å)	esd(a)	V (Å^3)	esd(V)
298	0.000	4.038371	0.000044	65.860	0.002
298	0.069	4.036293	0.000037	65.758	0.002
298	0.138	4.034289	0.000045	65.660	0.002
298	0.207	4.031917	0.000039	65.544	0.002
298	0.275	4.029396	0.000037	65.421	0.002
298	0.241	4.030705	0.000032	65.485	0.002
298	0.173	4.032951	0.000031	65.595	0.002
298	0.104	4.035282	0.000034	65.709	0.002
298	0.035	4.037446	0.000036	65.814	0.002
343	0.069	4.035586	0.000035	65.723	0.002
343	0.138	4.033648	0.000037	65.629	0.002
343	0.207	4.031591	0.000034	65.528	0.002
343	0.275	4.029279	0.000035	65.416	0.002
343	0.241	4.030679	0.000034	65.484	0.002
343	0.172	4.032490	0.000034	65.572	0.002

Table C.3: *Continued on next page*

Table C.3: *Continued from previous page*

T (K)	P (GPa)	a (Å)	esd(a)	V (Å^3)	esd(V)
343	0.103	4.034559	0.000038	65.673	0.002
343	0.035	4.036598	0.000035	65.773	0.002
388	0.069	4.034975	0.000037	65.694	0.002
388	0.138	4.033135	0.000040	65.604	0.002
388	0.206	4.031110	0.000041	65.505	0.002
388	0.275	4.028932	0.000034	65.399	0.002
388	0.241	4.030127	0.000034	65.457	0.002
388	0.173	4.032149	0.000039	65.556	0.002
388	0.104	4.034086	0.000037	65.650	0.002
388	0.035	4.035872	0.000037	65.737	0.002
433	0.069	4.034262	0.000036	65.659	0.002
433	0.138	4.032314	0.000039	65.564	0.002
433	0.207	4.030336	0.000035	65.467	0.002
433	0.275	4.028502	0.000035	65.378	0.002
433	0.241	4.029333	0.000040	65.418	0.002
433	0.172	4.031507	0.000038	65.524	0.002
433	0.104	4.033264	0.000041	65.610	0.002
433	0.035	4.035086	0.000036	65.699	0.002
478	0.069	4.033381	0.000040	65.616	0.002
478	0.138	4.031559	0.000040	65.527	0.002
478	0.207	4.029757	0.000041	65.439	0.002
478	0.242	4.028748	0.000038	65.390	0.002
478	0.172	4.030767	0.000043	65.488	0.002
478	0.104	4.032623	0.000037	65.579	0.002
478	0.035	4.034295	0.000039	65.660	0.002
523	0.069	4.032836	0.000041	65.589	0.002

Table C.3: *Continued on next page*

Table C.3: *Continued from previous page*

T (K)	P (GPa)	a (Å)	esd(a)	V (Å^3)	esd(V)
523	0.138	4.030993	0.000039	65.499	0.002
523	0.207	4.029324	0.000038	65.418	0.002
523	0.241	4.028403	0.000040	65.373	0.002
523	0.172	4.030113	0.000038	65.456	0.002
523	0.104	4.031859	0.000040	65.541	0.002
523	0.035	4.033791	0.000041	65.636	0.002

Table C.4: Lattice constants and unit cell volumes of $Sc_{0.80}Y_{0.20}F_3$ at various temperatures and pressures. These values were determined by Rietveld analyses of high-pressure, high-temperature data and are presented here without scaling.

T (K)	P (GPa)	a (Å)	esd(a)	V (Å^3)	esd(V)
298	0.000	4.051765	0.000039	66.516	0.002
298	0.069	4.049467	0.000029	66.404	0.001
298	0.138	4.046966	0.000037	66.281	0.002
298	0.207	4.044309	0.000040	66.150	0.002
298	0.276	4.040680	0.000039	65.973	0.002
298	0.241	4.042571	0.000023	66.065	0.001
298	0.172	4.045513	0.000026	66.210	0.001
298	0.104	4.048393	0.000038	66.351	0.002
298	0.035	4.050605	0.000033	66.460	0.002
343	0.069	4.048948	0.000050	66.378	0.002
343	0.138	4.046877	0.000036	66.277	0.002
343	0.207	4.044380	0.000039	66.154	0.002
343	0.276	4.041732	0.000040	66.024	0.002
343	0.241	4.042823	0.000031	66.078	0.002

Table C.4: *Continued on next page*

Table C.4: *Continued from previous page*

T (K)	P (GPa)	a (Å)	esd(a)	V (Å^3)	esd(V)
343	0.172	4.045508	0.000031	66.209	0.002
343	0.104	4.048109	0.000046	66.337	0.002
343	0.035	4.050087	0.000040	66.434	0.002
388	0.069	4.048696	0.000032	66.366	0.002
388	0.138	4.046429	0.000045	66.255	0.002
388	0.207	4.044262	0.000044	66.148	0.002
388	0.276	4.041673	0.000038	66.021	0.002
388	0.241	4.043019	0.000047	66.087	0.002
388	0.172	4.045338	0.000033	66.201	0.002
388	0.103	4.047669	0.000033	66.316	0.002
388	0.035	4.049731	0.000042	66.417	0.002
433	0.069	4.048097	0.000039	66.337	0.002
433	0.138	4.045856	0.000035	66.226	0.002
433	0.207	4.043851	0.000043	66.128	0.002
433	0.276	4.041388	0.000039	66.007	0.002
433	0.241	4.042775	0.000037	66.075	0.002
433	0.172	4.044714	0.000033	66.170	0.002
433	0.104	4.047087	0.000032	66.287	0.002
433	0.035	4.049067	0.000037	66.384	0.002
478	0.069	4.047474	0.000039	66.306	0.002
478	0.138	4.045438	0.000029	66.206	0.001
478	0.207	4.043234	0.000035	66.098	0.002
478	0.241	4.042330	0.000036	66.053	0.002
478	0.172	4.044425	0.000040	66.156	0.002
478	0.103	4.046603	0.000037	66.263	0.002
478	0.035	4.048363	0.000041	66.350	0.002

Table C.4: *Continued on next page*

Table C.4: *Continued from previous page*

T (K)	P (GPa)	a (Å)	esd(a)	V (Å^3)	esd(V)
523	0.069	4.047033	0.000039	66.284	0.002
523	0.138	4.045047	0.000038	66.187	0.002
523	0.207	4.042686	0.000042	66.071	0.002
523	0.241	4.041837	0.000041	66.029	0.002
523	0.172	4.044052	0.000044	66.138	0.002
523	0.104	4.045967	0.000036	66.232	0.002
523	0.035	4.047770	0.000045	66.320	0.002

Table C.5: Lattice constants and unit cell volumes of $Sc_{0.75}Y_{0.25}F_3$ at various temperatures and pressures. These values were determined by Rietveld analyses of high-pressure, high-temperature data and are presented here without scaling.

T (K)	P (GPa)	a (Å)	esd(a)	V (Å^3)	esd(V)
298	0.000	4.065204	0.000039	67.181	0.002
298	0.069	4.062762	0.000040	67.060	0.002
298	0.138	4.060169	0.000040	66.932	0.002
298	0.207	4.057369	0.000040	66.793	0.002
298	0.276	4.054030	0.000042	66.629	0.002
298	0.241	4.055717	0.000039	66.712	0.002
298	0.172	4.058764	0.000039	66.862	0.002
298	0.103	4.061700	0.000044	67.008	0.002
298	0.035	4.064203	0.000044	67.131	0.002
343	0.069	4.062583	0.000046	67.051	0.002
343	0.138	4.060236	0.000046	66.935	0.002
343	0.207	4.057759	0.000048	66.813	0.002
343	0.276	4.054961	0.000047	66.675	0.002

Table C.5: *Continued on next page*

Table C.5: *Continued from previous page*

T (K)	P (GPa)	a (Å)	esd(a)	V (Å^3)	esd(V)
343	0.241	4.056363	0.000042	66.744	0.002
343	0.172	4.058910	0.000040	66.870	0.002
343	0.103	4.061455	0.000042	66.995	0.002
343	0.035	4.063722	0.000053	67.108	0.003
388	0.069	4.062094	0.000055	67.027	0.003
388	0.138	4.059903	0.000046	66.919	0.002
388	0.207	4.057589	0.000041	66.804	0.002
388	0.276	4.054913	0.000040	66.672	0.002
388	0.241	4.056258	0.000039	66.739	0.002
388	0.172	4.058672	0.000047	66.858	0.002
388	0.103	4.060901	0.000047	66.968	0.002
388	0.035	4.063115	0.000059	67.078	0.003
433	0.069	4.061485	0.000064	66.997	0.003
433	0.138	4.059230	0.000053	66.885	0.003
433	0.207	4.057035	0.000045	66.777	0.002
433	0.276	4.054567	0.000042	66.655	0.002
433	0.241	4.055865	0.000044	66.719	0.002
433	0.172	4.058198	0.000045	66.834	0.002
433	0.103	4.060357	0.000055	66.941	0.003
433	0.035	4.062582	0.000066	67.051	0.003
478	0.069	4.060823	0.000076	66.964	0.004
478	0.138	4.058753	0.000053	66.862	0.003
478	0.207	4.056478	0.000044	66.749	0.002
478	0.241	4.055362	0.000044	66.694	0.002
478	0.172	4.057676	0.000047	66.809	0.002
478	0.103	4.059966	0.000061	66.922	0.003

Table C.5: *Continued on next page*

Table C.5: *Continued from previous page*

T (K)	P (GPa)	a (Å)	esd(a)	V (Å^3)	esd(V)
478	0.035	4.061946	0.000072	67.020	0.004
523	0.069	4.060289	0.000083	66.938	0.004
523	0.138	4.058182	0.000060	66.834	0.003
523	0.207	4.056064	0.000052	66.729	0.003
523	0.241	4.054840	0.000046	66.669	0.002
523	0.172	4.057005	0.000049	66.775	0.002
523	0.103	4.059142	0.000060	66.881	0.003
523	0.035	4.061242	0.000080	66.985	0.004

Table C.6: Experimental heat capacity data for ScF_3, listed in order of collection (columns wrap across multiple pages). Sample mass was 15.46 mg. Only data points that met two reliability criteria (≥90% thermal coupling constant between sample and platform and ≥40% sample contribution to the total heat capacity) are included. Units of C_P are J·K^{-1}·mol^{-1}.

T (K)	C_P	T (K)	C_P	T (K)	C_P	T (K)	C_P
303.35	82.806	86.29	36.246	23.91	4.082	6.62	0.155
302.98	82.421	86.28	36.288	23.89	4.036	6.61	0.154
303.01	82.417	86.28	36.264	23.89	4.025	6.61	0.155
282.68	80.628	77.57	32.478	21.47	3.129	5.94	0.113
282.84	80.853	77.56	32.517	21.47	3.106	5.94	0.113
282.84	80.804	77.56	32.481	21.46	3.119	5.95	0.113
262.59	78.323	69.70	28.524	19.30	2.395	5.33	0.085
262.70	78.490	69.69	28.506	19.28	2.389	5.33	0.084
262.70	78.512	69.69	28.494	19.28	2.393	5.33	0.084
242.43	75.863	62.61	24.941	17.34	1.836	4.79	0.063
242.52	76.080	62.60	24.908	17.32	1.825	4.79	0.063

Table C.6: *Continued on next page*

Table C.6: *Continued from previous page*

T (K)	C_P	T (K)	C_P	T (K)	C_P	T (K)	C_P
242.51	75.941	62.60	24.899	17.32	1.825	4.79	0.062
222.29	73.158	56.26	21.481	15.58	1.401	4.30	0.046
222.37	73.276	56.25	21.448	15.57	1.393	4.30	0.045
222.36	73.235	56.25	21.445	15.57	1.394	4.30	0.046
202.13	69.510	50.54	18.150	14.01	1.066	3.86	0.034
202.18	69.563	50.53	18.119	13.99	1.063	3.86	0.032
202.18	69.506	50.53	18.111	13.99	1.060	3.86	0.033
181.94	65.727	45.41	15.237	12.58	0.811	3.47	0.024
181.98	65.753	45.40	15.210	12.57	0.806	3.47	0.024
181.98	65.660	45.40	15.194	12.57	0.808	3.47	0.024
161.75	61.112	40.81	12.563	11.30	0.616	3.12	0.017
161.76	61.098	40.80	12.535	11.30	0.613	3.11	0.017
161.76	61.205	40.80	12.534	11.29	0.614	3.11	0.017
141.55	55.828	36.67	10.269	10.15	0.469	2.80	0.012
141.55	55.868	36.66	10.247	10.15	0.467	2.80	0.012
141.55	55.869	36.66	10.244	10.15	0.466	2.80	0.012
121.36	49.661	32.95	8.282	9.11	0.354	2.52	0.008
121.35	49.699	32.93	8.262	9.11	0.353	2.51	0.008
121.35	49.735	32.94	8.259	9.11	0.354	2.51	0.008
101.18	42.518	29.61	6.577	8.19	0.270	2.26	0.006
101.17	42.577	29.59	6.569	8.19	0.269	2.26	0.006
101.16	42.454	29.59	6.574	8.19	0.269	2.26	0.006
96.13	40.190	26.60	5.168	7.35	0.202	2.03	0.004
96.12	40.191	26.59	5.183	7.35	0.202	2.03	0.004
96.12	40.187	26.59	5.180	7.35	0.201	2.03	0.004

Table C.7: Experimental heat capacity data for ScF_3, listed in order of collection (columns wrap across multiple pages). Sample mass was 6.41 mg. Only data points that met two reliability criteria (≥90% thermal coupling constant between sample and platform and ≥40% sample contribution to the total heat capacity) are included. Units of C_P are $J{\cdot}K^{-1}{\cdot}mol^{-1}$.

T (K)	C_P	T (K)	C_P	T (K)	C_P	T (K)	C_P
222.34	72.616	62.61	24.828	19.27	2.374	5.93	0.108
222.42	72.614	62.58	24.799	19.26	2.369	5.93	0.106
222.42	72.737	62.59	24.775	19.26	2.368	5.93	0.105
202.16	69.073	56.25	21.377	17.32	1.817	5.33	0.079
202.21	69.047	56.23	21.361	17.31	1.811	5.32	0.079
202.21	69.145	56.23	21.361	17.31	1.811	5.33	0.080
181.97	65.322	50.53	18.067	15.57	1.382	4.79	0.059
182.00	65.313	50.51	18.037	15.56	1.380	4.78	0.060
181.99	65.368	50.51	18.028	15.56	1.379	4.79	0.059
161.78	60.781	45.40	15.165	13.99	1.048	4.30	0.043
161.79	60.867	45.38	15.131	13.98	1.046	4.30	0.043
161.78	60.866	45.38	15.138	13.98	1.046	4.30	0.043
141.60	55.407	40.79	12.500	12.57	0.795	3.86	0.031
141.57	55.583	40.77	12.477	12.56	0.793	3.86	0.031
141.57	55.543	40.77	12.480	12.56	0.793	3.86	0.031
121.41	49.547	36.65	10.192	11.28	0.601	3.47	0.023
121.36	49.538	36.63	10.202	11.28	0.599	3.47	0.022
121.35	49.535	36.64	10.186	11.28	0.600	3.47	0.022
101.22	42.322	32.93	8.199	10.13	0.453	3.12	0.016
101.16	42.272	32.91	8.223	10.13	0.450	3.11	0.016
101.16	42.357	32.91	8.220	10.13	0.451	3.11	0.017
96.09	40.258	29.59	6.426	9.10	0.344	2.80	0.012

Table C.7: *Continued on next page*

Table C.7: *Continued from previous page*

T (K)	C_P	T (K)	C_P	T (K)	C_P	T (K)	C_P
96.10	40.232	29.56	6.536	9.10	0.341	2.79	0.012
96.10	40.252	29.57	6.537	9.10	0.341	2.80	0.012
86.31	36.143	26.59	5.170	8.18	0.259	2.52	0.008
86.27	36.187	26.57	5.134	8.17	0.257	2.51	0.008
86.27	36.383	26.57	5.143	8.18	0.257	2.51	0.008
77.58	32.333	23.88	4.019	7.35	0.193	2.26	0.006
77.55	32.277	23.87	3.981	7.34	0.192	2.26	0.006
77.56	32.324	23.87	4.016	7.35	0.193	2.26	0.006
69.70	28.384	21.46	3.101	6.61	0.146	2.03	0.004
69.68	28.365	21.44	3.099	6.60	0.146	2.03	0.004
69.68	28.384	21.45	3.089	6.60	0.146	2.03	0.004

Table C.8: Experimental heat capacity data for ScF_3, listed in order of collection (columns wrap across multiple pages). Sample mass was 10.30 mg. Only data points that met two reliability criteria ($\geq$90% thermal coupling constant between sample and platform and $\geq$40% sample contribution to the total heat capacity) are included. Units of C_P are $mJ{\cdot}K^{-1}{\cdot}mol^{-1}$.

T (K)	C_P	T (K)	C_P	T (K)	C_P	T (K)	C_P
10.09	455.91	4.28	44.05	1.81	2.53	0.78	0.23
10.07	453.95	4.28	43.84	1.81	2.52	0.78	0.23
10.07	454.43	4.27	43.92	1.81	2.50	0.78	0.22
9.26	363.59	3.93	34.10	1.67	1.92	0.72	0.19
9.25	363.04	3.93	34.00	1.67	1.90	0.72	0.19
9.24	363.49	3.93	33.94	1.67	1.91	0.71	0.19
8.50	292.81	3.60	25.81	1.53	1.44	0.66	0.17
8.49	291.46	3.60	25.70	1.53	1.43	0.66	0.17

Table C.8: *Continued on next page*

Table C.8: *Continued from previous page*

T (K)	C_P	T (K)	C_P	T (K)	C_P	T (K)	C_P
8.49	292.65	3.60	25.73	1.53	1.42	0.66	0.17
7.79	234.36	3.31	19.82	1.41	1.09	0.60	0.15
7.78	234.06	3.31	19.79	1.41	1.07	0.60	0.14
7.79	234.38	3.31	19.67	1.41	1.08	0.60	0.15
7.14	187.07	3.04	15.02	1.29	0.83	0.56	0.14
7.14	186.66	3.04	14.92	1.29	0.83	0.56	0.14
7.14	186.92	3.04	14.86	1.29	0.82	0.56	0.13
6.57	148.49	2.79	11.22	1.19	0.64	0.51	0.12
6.56	148.03	2.79	11.18	1.19	0.64	0.51	0.11
6.56	147.87	2.79	11.19	1.19	0.64	0.51	0.12
6.03	118.06	2.56	8.27	1.09	0.50	0.47	0.11
6.02	117.94	2.56	8.17	1.09	0.50	0.47	0.11
6.02	118.05	2.56	8.20	1.09	0.50	0.47	0.11
5.53	92.94	2.35	6.25	1.00	0.40	0.44	0.10
5.53	92.74	2.35	6.18	1.00	0.40	0.44	0.09
5.53	93.03	2.35	6.26	1.00	0.40	0.44	0.10
5.08	73.16	2.14	4.61	0.92	0.33	0.41	0.08
5.07	72.78	2.15	4.62	0.92	0.32	0.41	0.09
5.07	72.66	2.15	4.64	0.92	0.33	0.41	0.09
4.66	56.83	1.97	3.36	0.85	0.26	0.38	0.09
4.66	56.57	1.97	3.39	0.85	0.27	0.38	0.09
4.66	56.65	1.97	3.41	0.85	0.27	0.38	0.09

Table C.9: Experimental heat capacity data for ScF_3, listed in order of collection (columns wrap across multiple pages). Sample mass was 8.136 mg. Only data points that met two reliability criteria (≥90% thermal coupling constant between sample and platform and ≥40% sample contribution to the total heat capacity) are included. Units of C_P are $mJ \cdot K^{-1} \cdot mol^{-1}$.

T (K)	C_P	T (K)	C_P	T (K)	C_P	T (K)	C_P
302.20	82013.24	4.67	56.51	1.97	3.23	0.85	0.28
302.27	82053.52	4.66	56.33	1.97	3.23	0.85	0.27
302.30	81869.41	4.66	56.35	1.97	3.24	0.85	0.30
10.09	457.63	4.28	43.49	1.81	2.41	0.78	0.24
10.07	456.60	4.28	43.43	1.81	2.40	0.78	0.24
10.07	455.81	4.28	43.33	1.81	2.41	0.78	0.25
9.26	364.64	3.93	33.68	1.67	1.84	0.72	0.20
9.24	364.43	3.93	33.45	1.67	1.83	0.72	0.22
9.24	364.03	3.93	33.44	1.67	1.78	0.66	0.18
8.49	292.56	3.59	25.13	1.53	1.38	0.66	0.17
8.48	292.18	3.59	25.11	1.53	1.37	0.66	0.18
8.48	291.81	3.60	25.14	1.53	1.34	0.60	0.16
7.80	234.27	3.32	19.42	1.41	1.05	0.60	0.13
7.78	234.42	3.31	19.23	1.41	1.04	0.60	0.15
7.78	234.42	3.31	19.20	1.41	1.06	0.56	0.17
7.15	187.64	3.04	14.56	1.29	0.80	0.56	0.16
7.14	187.25	3.04	14.46	1.29	0.87	0.51	0.14
7.14	187.67	3.04	14.45	1.29	0.81	0.51	0.13
6.57	148.21	2.79	10.85	1.19	0.69	0.51	0.14
6.56	147.65	2.79	10.74	1.19	0.62	0.47	0.12
6.55	147.69	2.79	10.80	1.19	0.60	0.47	0.11
6.55	147.96	2.56	7.91	1.09	0.54	0.47	0.12

Table C.9: *Continued on next page*

Table C.9: *Continued from previous page*

T (K)	C_P	T (K)	C_P	T (K)	C_P	T (K)	C_P
6.56	147.99	2.56	7.86	1.09	0.52	0.44	0.10
6.56	148.24	2.56	7.84	1.09	0.49	0.44	0.11
5.54	92.34	2.35	5.97	1.00	0.41	0.40	0.08
5.52	92.24	2.35	5.93	1.00	0.42	0.40	0.09
5.52	92.29	2.35	5.96	1.00	0.42	0.40	0.10
5.08	72.69	2.15	4.43	0.92	0.35	0.38	0.10
5.08	72.61	2.15	4.39	0.92	0.34	0.38	0.10
5.08	72.46	2.15	4.38	0.92	0.35	0.38	0.10

Table C.10: Experimental heat capacity data for ScF_3, listed in order of collection. Sample mass was 8.62 mg. Only data points that met two reliability criteria ($\geq$90% thermal coupling constant between sample and platform and $\geq$40% sample contribution to the total heat capacity) are included.

T (K)	C_P ($J \cdot K^{-1} \cdot mol^{-1}$)
279.29	79.616
279.00	79.456
279.01	79.398
295.61	80.640
295.63	80.431
295.62	80.384
312.14	81.615
312.16	81.436
312.15	81.415
329.06	83.359
328.62	83.311

Table C.10: *Continued on next page*

Table C.10: *Continued from previous page*

T (K)	C_P ($J \cdot K^{-1} \cdot mol^{-1}$)
328.65	83.262
345.04	84.306
345.04	84.099
345.04	83.862

Table C.11: Experimental heat capacity data for ScF_3, listed in order of collection. Sample mass was 12.78 mg. Only data points that met two reliability criteria ($\geq$90% thermal coupling constant between sample and platform and $\geq$40% sample contribution to the total heat capacity) are included.

T (K)	C_P ($J \cdot K^{-1} \cdot mol^{-1}$)
278.75	79.087
278.38	78.936
278.39	78.859
301.62	80.588
301.65	80.457
301.64	80.326
324.89	81.951
324.91	81.842
324.90	81.837
347.49	83.120
347.52	82.730
347.51	82.982
369.34	84.964
369.48	84.476
369.45	84.613

Table C.11: *Continued on next page*

Table C.11: *Continued from previous page*

T (K)	C_P ($J{\cdot}K^{-1}{\cdot}mol^{-1}$)
392.44	86.112
392.47	85.806
392.43	85.849

Table C.12: Experimental heat capacity data for $Sc_{0.95}Y_{0.05}F_3$, listed in order of collection (columns wrap across multiple pages). Sample mass was 13.86 mg. Only data points that met two reliability criteria ($\geq$90% thermal coupling constant between sample and platform and $\geq$40% sample contribution to the total heat capacity) are included. Units of C_P are $J{\cdot}K^{-1}{\cdot}mol^{-1}$.

T (K)	C_P	T (K)	C_P	T (K)	C_P	T (K)	C_P
303.32	82.437	171.45	64.013	151.69	59.394	36.69	10.457
302.87	82.314	171.48	63.982	151.63	59.476	36.67	10.441
302.88	82.399	171.48	64.034	151.64	59.429	36.67	10.437
287.00	81.564	169.64	63.524	126.39	52.131	32.96	8.408
287.14	81.647	169.68	63.546	126.40	52.189	32.95	8.386
287.14	81.620	169.67	63.608	126.40	52.145	32.94	8.387
271.30	79.389	167.84	63.151	101.18	43.317	29.62	6.675
271.41	79.453	167.86	63.201	101.17	43.253	29.61	6.653
271.42	79.427	167.87	63.191	101.16	43.308	29.61	6.649
255.57	77.936	166.03	62.752	96.13	41.000	26.62	5.214
255.67	78.049	166.06	62.822	96.13	41.027	26.60	5.208
255.67	77.949	166.07	62.742	96.13	41.080	26.61	5.206
239.82	75.915	164.23	62.333	86.33	37.006	23.90	4.024
239.92	75.973	164.26	62.385	86.31	36.962	23.90	4.000
239.91	75.902	164.25	62.397	86.31	36.972	23.90	4.004

Table C.12: *Continued on next page*

Table C.12: *Continued from previous page*

T (K)	C_P	T (K)	C_P	T (K)	C_P	T (K)	C_P
224.11	73.919	162.43	61.977	77.60	33.194	21.48	3.086
224.19	74.064	162.46	61.976	77.57	33.237	21.46	3.056
224.19	74.014	162.45	62.019	77.57	33.227	21.48	3.055
208.38	70.984	160.63	61.487	69.74	29.159	19.30	2.299
208.44	71.038	160.65	61.535	69.71	29.139	19.29	2.292
208.44	71.117	160.65	61.564	69.71	29.140	19.28	2.285
192.62	68.426	158.82	61.160	62.64	25.482	17.34	1.701
192.67	68.483	158.85	61.100	62.61	25.454	17.33	1.696
192.66	68.555	158.85	61.120	62.61	25.462	17.33	1.695
176.85	65.084	157.02	60.775	56.30	21.857	15.58	1.247
176.89	65.186	157.05	60.771	56.26	21.879	15.57	1.243
176.89	65.168	157.04	60.812	56.26	21.886	15.57	1.242
176.98	65.216	155.21	60.365	50.59	18.503	14.00	0.904
176.89	65.156	155.24	60.375	50.55	18.515	13.99	0.900
176.88	65.219	155.24	60.300	50.55	18.518	13.99	0.901
175.05	64.733	153.42	59.835	45.45	15.500	12.58	0.649
175.08	64.848	153.44	59.869	45.42	15.489	12.58	0.647
175.09	64.856	153.44	59.909	45.42	15.499	12.58	0.646
173.25	64.398	151.61	59.372	40.84	12.797	11.30	0.460
173.29	64.367	151.64	59.452	40.81	12.774	11.30	0.458
173.28	64.409	151.64	59.416	40.81	12.781	11.30	0.458

Table C.13: Experimental heat capacity data for $Sc_{0.95}Y_{0.05}F_3$, listed in order of collection. Sample mass was 8.58 mg. Only data points that met two reliability criteria (≥90% thermal coupling constant between sample and platform and ≥40% sample contribution to the total heat capacity) are included. Units of C_P are $mJ \cdot K^{-1} \cdot mol^{-1}$.

T (K)	C_P	T (K)	C_P	T (K)	C_P
301.83	82900.71	8.49	173.64	6.56	71.71
302.02	83182.42	8.47	173.22	6.55	70.76
302.02	83369.99	8.47	172.66	6.54	70.44
10.09	312.34	7.78	129.76	6.01	52.86
10.07	311.16	7.77	128.96	6.00	52.50
10.06	311.04	7.77	128.68	6.00	52.49
9.25	233.24	7.14	97.07	5.54	40.17
9.23	231.75	7.13	96.30	5.53	39.40
9.23	231.42	7.13	96.53	5.52	39.08

Table C.14: Experimental heat capacity data for $Sc_{0.90}Y_{0.10}F_3$, listed in order of collection (columns wrap across multiple pages). Sample mass was 9.58 mg. Only data points that met two reliability criteria (≥90% thermal coupling constant between sample and platform and ≥40% sample contribution to the total heat capacity) are included. Units of C_P are $J \cdot K^{-1} \cdot mol^{-1}$.

T (K)	C_P	T (K)	C_P	T (K)	C_P	T (K)	C_P
303.23	81.350	150.89	59.427	77.54	33.083	17.31	1.678
302.90	81.410	148.71	58.788	77.54	33.134	17.31	1.672
302.91	81.421	148.73	58.823	69.68	29.068	17.31	1.670
283.06	80.583	148.73	58.836	69.69	29.001	15.55	1.216
282.74	79.854	146.55	58.154	69.69	29.002	15.55	1.212

Table C.14: *Continued on next page*

Table C.14: *Continued from previous page*

T (K)	C_P	T (K)	C_P	T (K)	C_P	T (K)	C_P
282.74	79.706	146.57	58.233	62.58	25.448	15.55	1.210
262.51	77.692	146.56	58.184	62.59	25.393	13.97	0.869
262.60	77.850	144.38	57.652	62.59	25.400	13.97	0.868
262.60	77.851	144.41	57.551	56.24	21.875	13.97	0.866
242.37	75.674	144.40	57.597	56.24	21.842	12.55	0.616
242.43	75.714	142.22	56.845	56.23	21.849	12.55	0.613
242.43	75.604	142.24	56.867	50.53	18.535	12.55	0.613
222.26	73.051	142.24	56.895	50.53	18.511	11.28	0.431
222.29	73.262	140.05	56.170	50.53	18.501	11.28	0.429
222.29	73.172	140.08	56.206	45.40	15.534	11.28	0.429
202.11	69.658	140.07	56.196	45.40	15.495	10.14	0.297
202.10	69.800	137.89	55.549	45.39	15.494	10.13	0.295
202.10	69.741	137.91	55.638	40.78	12.845	10.14	0.294
181.94	66.264	137.91	55.564	40.79	12.795	9.10	0.204
181.91	66.410	135.78	54.987	40.78	12.796	9.10	0.203
181.91	66.639	135.75	54.912	36.64	10.486	9.10	0.203
161.75	61.848	135.76	54.944	36.65	10.462	8.18	0.139
161.71	61.897	133.57	54.256	36.65	10.453	8.18	0.139
161.71	61.845	133.59	54.337	32.92	8.427	8.18	0.139
161.75	61.988	133.58	54.349	32.92	8.404	303.24	81.739
161.70	61.915	131.40	53.772	32.92	8.404	171.88	64.182
161.70	61.884	131.42	53.730	29.58	6.694	171.82	64.226
159.52	61.294	131.41	53.681	29.58	6.667	171.82	64.134
159.54	61.424	126.41	52.191	29.58	6.666	169.79	63.758
159.53	61.477	126.36	52.360	26.57	5.236	169.81	63.760
157.36	60.931	126.37	52.208	26.57	5.224	169.81	63.732

Table C.14: *Continued on next page*

Table C.14: *Continued from previous page*

T (K)	C_P	T (K)	C_P	T (K)	C_P	T (K)	C_P
157.38	60.894	106.14	45.128	26.58	5.219	167.77	63.119
157.38	60.792	106.17	45.116	23.85	4.014	167.79	63.240
155.19	60.373	106.16	45.126	23.87	3.996	167.78	63.109
155.22	60.495	95.90	41.762	23.87	4.012	165.75	62.810
155.22	60.500	96.08	41.086	21.43	3.009	165.76	62.792
153.04	59.964	96.09	40.982	21.44	3.047	165.76	62.767
153.05	59.939	86.25	36.979	21.45	3.051	163.72	62.302
153.05	59.943	86.28	36.871	19.27	2.276	163.74	62.332
150.87	59.387	86.27	36.954	19.27	2.230	163.74	62.301
150.89	59.419	77.52	33.165	19.25	2.269		

Table C.15: Experimental heat capacity data for $Sc_{0.95}Y_{0.10}F_3$, listed in order of collection. Sample mass was 15.05 mg. Only data points that met two reliability criteria ($\geq$90% thermal coupling constant between sample and platform and $\geq$40% sample contribution to the total heat capacity) are included. Units of C_P are $J{\cdot}K^{-1}{\cdot}mol^{-1}$.

T (K)	C_P	T (K)	C_P	T (K)	C_P
276.06	79.917	316.52	82.052	370.94	85.545
275.75	79.846	316.51	82.294	370.96	85.500
275.76	79.783	336.92	82.601	390.85	86.711
296.09	81.214	336.91	82.513	390.99	86.166
296.13	80.986	353.35	83.845	390.97	86.308
296.12	80.884	353.34	84.032		
316.48	82.316	370.77	85.550		

Table C.16: Experimental heat capacity data for $Sc_{0.80}Y_{0.20}F_3$, listed in order of collection (columns wrap across multiple pages). Sample mass was 7.72 mg. Only data points that met two reliability criteria (≥90% thermal coupling constant between sample and platform and ≥40% sample contribution to the total heat capacity) are included. Units of C_P are $J{\cdot}K^{-1}{\cdot}mol^{-1}$.

T (K)	C_P	T (K)	C_P	T (K)	C_P	T (K)	C_P
234.06	74.240	216.47	70.676	102.48	43.909	28.13	6.418
233.98	74.087	214.86	70.507	97.38	41.782	28.13	6.409
233.97	74.188	214.88	70.561	97.40	41.781	25.13	4.954
232.36	74.079	214.88	70.466	97.40	41.780	25.13	4.943
232.39	73.914	213.26	70.497	86.95	37.358	25.13	4.950
232.39	73.796	213.29	70.410	86.92	37.364	22.46	3.779
230.77	73.656	213.29	70.395	86.92	37.350	22.45	3.792
230.80	73.754	211.68	70.207	77.71	33.317	22.46	3.769
230.79	73.805	211.70	70.299	77.68	33.366	20.05	2.769
229.18	73.642	211.69	70.310	77.68	33.377	20.05	2.807
229.21	73.582	210.08	70.199	69.42	29.154	20.06	2.807
229.20	73.437	210.11	70.182	69.40	29.151	17.91	2.053
227.58	73.403	210.10	70.199	69.40	29.141	17.91	2.049
227.62	73.309	208.49	70.026	61.99	25.439	17.92	2.051
227.61	73.188	208.51	70.072	61.97	25.427	16.00	1.479
225.99	72.975	208.51	70.175	61.97	25.423	16.00	1.475
226.02	73.189	206.90	69.939	55.37	21.803	16.01	1.475
226.02	73.004	206.92	70.093	55.36	21.772	14.31	1.046
224.40	72.811	206.92	69.975	55.36	21.764	14.30	1.041
224.43	72.626	205.31	69.770	49.46	18.298	14.30	1.043
224.42	72.715	205.33	69.961	49.45	18.265	12.78	0.724

Table C.16: *Continued on next page*

Table C.16: *Continued from previous page*

T (K)	C_P	T (K)	C_P	T (K)	C_P	T (K)	C_P
222.81	72.286	205.33	69.937	49.45	18.262	12.77	0.722
222.84	72.279	203.72	69.781	44.18	15.311	12.77	0.723
222.83	72.393	203.74	69.735	44.18	15.274	11.42	0.495
221.21	71.919	203.73	69.818	44.18	15.264	11.41	0.494
221.24	71.845	184.00	66.492	39.47	12.705	11.41	0.494
221.24	71.982	183.90	66.621	39.46	12.670	10.17	0.324
219.63	71.377	183.90	66.530	39.46	12.674	10.18	0.326
219.65	71.592	156.75	60.869	35.24	10.274	10.18	0.327
219.65	71.378	156.77	60.884	35.24	10.264	9.10	0.220
218.04	71.058	156.76	60.853	35.25	10.260	9.09	0.218
218.06	70.979	129.62	53.381	31.48	8.183	9.09	0.219
218.06	71.115	129.62	53.410	31.48	8.177		
216.45	70.782	129.62	53.455	31.49	8.174		
216.48	70.673	102.52	43.959	28.13	6.422		

Table C.17: Experimental heat capacity data for $Sc_{0.75}Y_{0.25}F_3$, listed in order of collection (columns wrap across multiple pages). Sample mass was 5.40 mg. Only data points that met two reliability criteria ($\geq$90% thermal coupling constant between sample and platform and $\geq$40% sample contribution to the total heat capacity) are included. Units of C_P are $J{\cdot}K^{-1}{\cdot}mol^{-1}$.

T (K)	C_P	T (K)	C_P	T (K)	C_P	T (K)	C_P
161.78	64.123	69.81	30.080	32.97	9.031	15.59	1.349
161.76	64.274	69.74	30.152	32.96	8.998	15.58	1.344
161.75	64.381	69.74	30.157	32.96	9.011	15.59	1.343
141.63	58.962	62.70	26.385	29.63	7.207	14.02	0.966

Table C.17: *Continued on next page*

Table C.17: *Continued from previous page*

T (K)	C_P	T (K)	C_P	T (K)	C_P	T (K)	C_P
141.57	59.084	62.64	26.421	29.62	7.193	14.00	0.961
141.57	59.134	62.63	26.453	29.62	7.190	14.01	0.961
121.43	52.454	56.34	22.846	26.61	5.707	12.60	0.683
121.37	52.466	56.29	22.847	26.61	5.648	12.59	0.678
121.36	52.548	56.28	22.852	26.62	5.654	12.59	0.679
101.25	44.781	50.60	19.431	23.93	4.419	11.32	0.474
101.22	44.751	50.58	19.429	23.92	4.356	11.31	0.472
101.21	44.741	50.58	19.433	23.91	4.364	11.32	0.471
96.17	42.448	45.46	16.379	21.48	3.350	10.17	0.326
96.17	42.435	45.45	16.348	21.49	3.340	10.17	0.322
96.18	42.530	45.44	16.340	21.48	3.323	10.17	0.323
86.39	38.169	40.84	13.600	19.32	2.511	9.14	0.223
86.34	38.060	40.84	13.561	19.31	2.505	9.13	0.222
86.34	38.263	40.83	13.562	19.31	2.504	9.13	0.221
77.68	34.175	36.69	11.167	17.35	1.855	8.21	0.151
77.59	34.332	36.69	11.139	17.34	1.847	8.20	0.151
77.60	34.421	36.69	11.139	17.34	1.846	8.21	0.150

Table C.18: Experimental heat capacity data for $Sc_{0.75}Y_{0.25}F_3$, listed in order of collection (columns wrap across multiple pages). Sample mass was 10.60 mg. Only data points that met two reliability criteria ($\geq$90% thermal coupling constant between sample and platform and $\geq$40% sample contribution to the total heat capacity) are included. Units of C_P are $J{\cdot}K^{-1}{\cdot}mol^{-1}$.

T (K)	C_P	T (K)	C_P	T (K)	C_P	T (K)	C_P
303.62	81.879	202.34	71.346	23.96	4.374	2.81	0.004

Table C.18: *Continued on next page*

Table C.18: *Continued from previous page*

T (K)	C_P	T (K)	C_P	T (K)	C_P	T (K)	C_P
303.25	81.557	202.35	71.357	21.53	3.363	2.81	0.004
303.26	81.658	182.25	68.131	21.52	3.340	2.81	0.004
282.91	80.514	182.14	68.089	21.52	3.348	2.52	0.003
283.08	80.631	182.14	68.071	19.34	2.527	2.52	0.003
283.07	80.531	161.89	63.645	19.34	2.516	2.52	0.003
262.76	78.746	161.93	63.631	19.34	2.512	2.27	0.002
262.91	78.768	161.92	63.703	17.37	1.867	2.26	0.002
262.89	78.783	141.72	58.440	17.37	1.859	2.26	0.002
242.59	76.776	141.73	58.476	17.38	1.847	2.03	0.002
242.72	76.865	141.73	58.443	15.61	1.359	2.03	0.002
242.71	76.801	121.53	52.091	15.60	1.353	2.03	0.002
222.45	74.552	121.52	52.039	15.61	1.354	203.53	68.002
222.55	74.531	121.52	52.074	14.04	0.976	203.35	68.167
222.54	74.622	101.36	44.607	14.03	0.971	203.35	68.221
222.69	74.563	101.34	44.505	14.03	0.971	204.73	68.476
222.54	74.523	101.33	44.534	12.62	0.691	204.81	68.350
222.54	74.508	96.29	42.220	12.61	0.688	204.81	68.327
221.05	74.270	96.30	42.138	12.61	0.688	206.17	68.605
221.10	74.270	96.29	42.152	11.33	0.481	206.25	68.474
221.09	74.199	86.46	38.029	11.33	0.478	206.25	68.435
219.60	73.910	86.46	37.879	11.33	0.479	207.61	68.698
219.66	74.037	86.45	37.912	10.18	0.330	207.69	68.629
219.66	73.924	77.72	34.209	10.17	0.329	207.69	68.573
218.16	73.655	77.70	34.147	10.18	0.329	209.02	69.043
218.22	73.675	77.70	34.121	9.14	0.227	209.10	68.981
218.21	73.665	69.86	30.016	9.13	0.225	209.11	68.624

Table C.18: *Continued on next page*

Table C.18: *Continued from previous page*

T (K)	C_P	T (K)	C_P	T (K)	C_P	T (K)	C_P
216.73	73.386	69.83	29.996	9.14	0.226	210.44	68.917
216.77	73.403	69.83	30.002	8.21	0.155	210.49	68.861
216.77	73.359	62.76	26.329	8.21	0.153	210.50	68.829
215.28	73.154	62.72	26.312	8.21	0.154	211.86	69.123
215.34	73.130	62.73	26.309	7.38	0.105	211.95	68.983
215.33	73.167	56.40	22.756	7.37	0.104	211.94	68.982
213.84	73.038	56.37	22.732	7.37	0.104	213.39	69.236
213.90	72.876	56.37	22.732	6.65	0.073	213.47	69.093
213.88	72.986	50.69	19.338	6.63	0.073	213.46	69.072
212.40	72.780	50.65	19.352	6.63	0.073	214.83	69.348
212.45	72.712	50.65	19.342	5.96	0.049	214.91	69.184
212.44	72.762	45.55	16.259	5.95	0.049	214.90	69.209
210.96	72.510	45.50	16.285	5.95	0.049	216.30	69.294
211.01	72.515	45.51	16.291	5.35	0.034	216.33	69.385
211.00	72.544	40.93	13.512	5.35	0.034	216.35	69.368
209.51	72.349	40.89	13.513	5.35	0.034	217.77	69.313
209.57	72.344	40.89	13.515	4.80	0.024	217.75	69.650
209.56	72.359	36.77	11.128	4.80	0.024	217.80	69.581
208.07	72.229	36.75	11.111	4.80	0.024	219.24	69.362
208.12	72.315	36.75	11.114	4.31	0.017	219.18	69.858
208.12	72.225	33.04	9.016	4.31	0.017	219.23	69.812
206.64	71.942	33.02	8.997	4.31	0.017	220.60	69.689
206.68	72.013	33.02	8.997	3.87	0.012	220.55	70.059
206.67	71.879	29.69	7.201	3.87	0.012	220.60	70.003
205.19	71.743	29.67	7.184	3.87	0.012	222.04	69.961
205.23	71.691	29.67	7.180	3.48	0.008	222.00	70.305

Table C.18: *Continued on next page*

Table C.18: *Continued from previous page*

T (K)	C_P	T (K)	C_P	T (K)	C_P	T (K)	C_P
205.23	71.713	26.68	5.672	3.48	0.008	222.04	70.226
203.75	71.571	26.66	5.662	3.48	0.008	223.48	70.196
203.79	71.660	26.67	5.660	3.13	0.006	223.44	70.481
203.79	71.609	23.97	4.376	3.12	0.006	223.48	70.465
202.30	71.373	23.95	4.371	3.12	0.006		

Table C.19: Experimental heat capacity data for $Sc_{0.75}Y_{0.25}F_3$, listed in order of collection (columns wrap across multiple pages). Sample mass was 9.37 mg. Only data points that met two reliability criteria ($\geq$90% thermal coupling constant between sample and platform and $\geq$40% sample contribution to the total heat capacity) are included. Units of C_P are $J{\cdot}K^{-1}{\cdot}mol^{-1}$.

T (K)	C_P	T (K)	C_P	T (K)	C_P	T (K)	C_P
304.68	85.048	220.98	75.720	77.08	34.616	19.82	2.793
304.30	85.073	219.29	75.168	77.08	34.571	19.81	2.771
304.32	84.885	219.31	75.189	68.83	30.148	19.82	2.772
283.86	83.064	219.30	75.156	68.84	30.116	17.70	2.028
284.04	83.269	217.62	74.727	68.84	30.106	17.69	2.017
284.04	83.152	217.64	74.688	61.46	26.260	17.70	2.019
263.68	81.240	217.63	74.719	61.45	26.251	15.80	1.452
263.83	81.236	215.94	74.342	61.45	26.251	15.80	1.447
263.82	81.336	215.97	74.303	54.89	22.443	15.80	1.445
243.45	79.106	215.96	74.309	54.88	22.396	14.11	1.022
243.57	79.064	214.27	74.136	54.88	22.400	14.11	1.017
243.56	79.058	214.30	74.180	49.01	18.855	14.11	1.018
232.79	77.909	214.29	74.272	49.02	18.808	12.60	0.708

Table C.19: *Continued on next page*

Table C.19: *Continued from previous page*

T (K)	C_P	T (K)	C_P	T (K)	C_P	T (K)	C_P
232.68	77.899	212.60	73.905	49.01	18.801	12.60	0.707
232.68	77.878	212.62	74.023	43.77	15.666	12.60	0.705
230.98	77.707	212.62	73.967	43.77	15.621	11.25	0.484
231.01	77.691	182.96	69.868	43.76	15.628	11.25	0.480
231.01	77.482	182.82	69.666	39.09	12.822	11.25	0.481
229.32	77.550	182.82	69.655	39.09	12.786	10.04	0.321
229.35	77.532	155.77	63.587	39.08	12.788	10.03	0.320
229.34	77.426	155.79	63.600	34.91	10.368	10.04	0.320
227.64	77.105	155.78	63.576	34.90	10.327	8.96	0.217
227.67	77.188	128.78	55.578	34.90	10.327	8.95	0.216
227.67	77.164	128.76	55.614	31.16	8.251	8.96	0.217
225.98	76.860	128.76	55.598	31.17	8.210	8.00	0.143
226.00	77.138	101.79	45.645	31.17	8.204	8.00	0.142
226.00	76.838	101.76	45.698	27.85	6.433	8.00	0.143
224.30	76.477	101.76	45.705	27.84	6.419	7.17	0.097
224.33	76.677	96.69	43.291	27.84	6.400	7.16	0.096
224.33	76.673	96.71	43.242	24.87	4.859	7.16	0.095
222.63	76.162	96.70	43.309	24.85	4.916	6.39	0.066
222.66	76.077	86.30	38.637	24.86	4.916	6.38	0.066
222.65	76.056	86.29	38.662	22.20	3.699	6.39	0.064
220.96	75.464	86.29	38.740	22.19	3.731		
220.98	75.694	77.08	34.680	22.20	3.731		

Table C.20: Experimental heat capacity data for $Sc_{0.75}Y_{0.25}F_3$, listed in order of collection. Sample mass was 8.98 mg. Only data points that met two reliability criteria (≥90% thermal coupling constant between sample and platform and ≥40% sample contribution to the total heat capacity) are included.

T (K)	C_P ($J{\cdot}K^{-1}{\cdot}mol^{-1}$)
274.06	79.969
273.77	79.827
273.77	79.872

Table C.21: Experimental heat capacity data for $Sc_{0.75}Y_{0.25}F_3$, listed in order of collection. Sample mass was 9.37 mg. Only data points that met two reliability criteria (≥90% thermal coupling constant between sample and platform and ≥40% sample contribution to the total heat capacity) are included. Units of C_P are $J{\cdot}K^{-1}{\cdot}mol^{-1}$.

T (K)	C_P	T (K)	C_P	T (K)	C_P
280.88	82.540	324.49	84.696	362.57	86.964
280.55	82.426	324.49	84.526	362.67	86.842
280.56	82.387	324.48	84.674	362.65	86.911
295.17	83.105	339.14	85.070	376.95	88.064
295.18	83.118	339.15	84.988	377.07	87.704
295.18	82.875	339.15	85.002	377.07	87.918
309.82	84.079	351.22	85.786	391.37	89.069
309.83	84.152	351.22	85.970	391.43	88.888
309.83	84.221	351.23	85.987		

Table C.22: Experimental heat capacity data for $Sc_{0.75}Y_{0.25}F_3$, listed in order of collection. Sample mass was 11.05 mg. Only data points that met two reliability criteria (≥90% thermal coupling constant between sample and platform and ≥40% sample contribution to the total heat capacity) are included. Units of C_P are $J{\cdot}K^{-1}{\cdot}mol^{-1}$.

T (K)	C_P	T (K)	C_P	T (K)	C_P
280.05	80.991	308.86	82.449	338.11	83.367
279.67	80.727	308.86	82.436	350.70	84.133
279.67	80.813	323.49	83.258	350.69	84.193
294.27	81.446	323.47	83.258	350.69	84.216
294.26	81.517	323.48	83.279	363.28	84.858
294.26	81.469	338.14	83.382	363.28	84.778
308.88	82.492	338.11	83.360		

Table C.23: Experimental heat capacity data for $Sc_{0.75}Y_{0.25}F_3$, listed in order of collection. Sample mass was 6.28 mg. Only data points that met two reliability criteria (≥90% thermal coupling constant between sample and platform and ≥40% sample contribution to the total heat capacity) are included. Units of C_P are $J{\cdot}K^{-1}{\cdot}mol^{-1}$.

T (K)	C_P	T (K)	C_P	T (K)	C_P
10.09	0.319	9.27	0.236	7.85	0.130
10.07	0.317	8.55	0.176	7.85	0.130
10.07	0.317	8.53	0.175	7.23	0.097
9.29	0.236	8.53	0.175	7.22	0.097
9.27	0.236	7.87	0.130	7.22	0.096

Table C.24: Experimental heat capacity data for $Sc_{0.75}Y_{0.25}F_3$, listed in order of collection. Sample mass was 4.44 mg. Only data points that met two reliability criteria ($\geq$90% thermal coupling constant between sample and platform and $\geq$40% sample contribution to the total heat capacity) are included. Units of C_P are $J{\cdot}K^{-1}{\cdot}mol^{-1}$.

T (K)	C_P	T (K)	C_P	T (K)	C_P
10.11	0.316	9.29	0.233	9.29	0.235
10.10	0.315	10.11	0.317	9.28	0.235
10.09	0.315	10.09	0.318	8.56	0.175
9.31	0.233	10.09	0.317	8.55	0.175
9.29	0.234	9.30	0.235	8.54	0.175

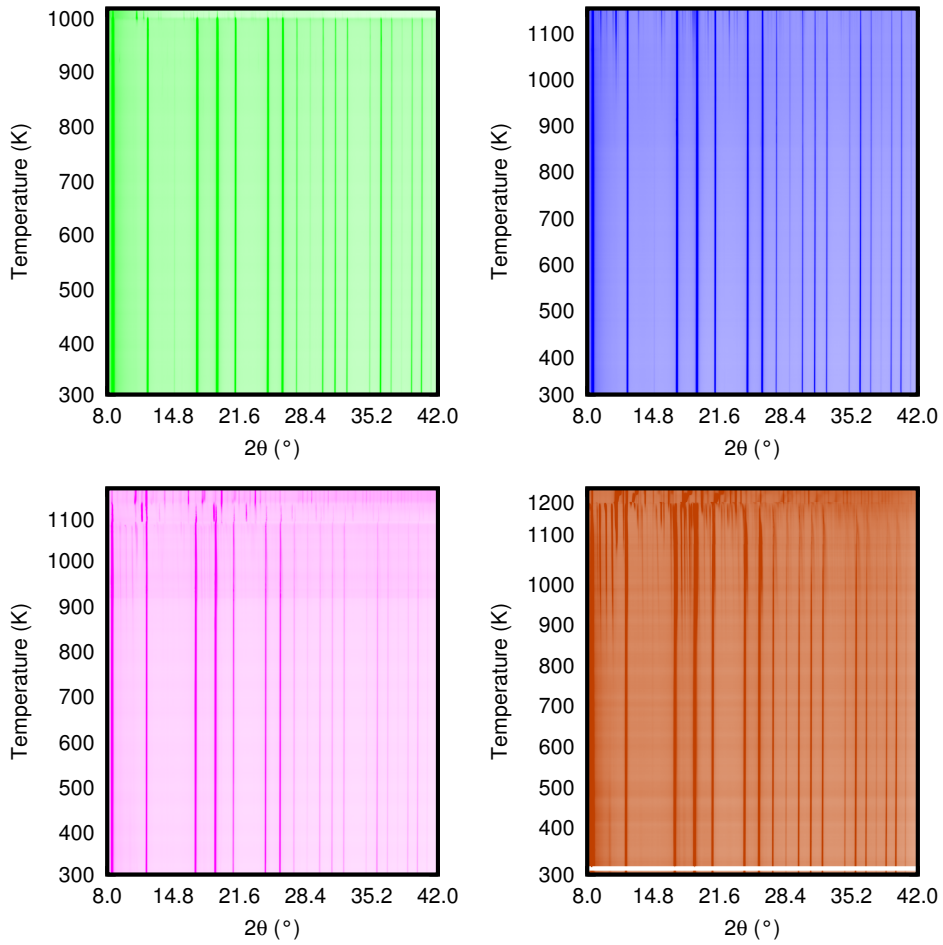

Figure C.1: Stackplots of variable-temperature (furnace, >300 K) PXRD patterns collected for $Sc_{1-x}Y_xF_3$ in which $x = 0.05$ (top left), 0.10 (top right), 0.20 (bottom left), and 0.25 (bottom right). Within each stackplot, the patterns are arranged in the order of collection from bottom to top. Reproduced from ref. [247].

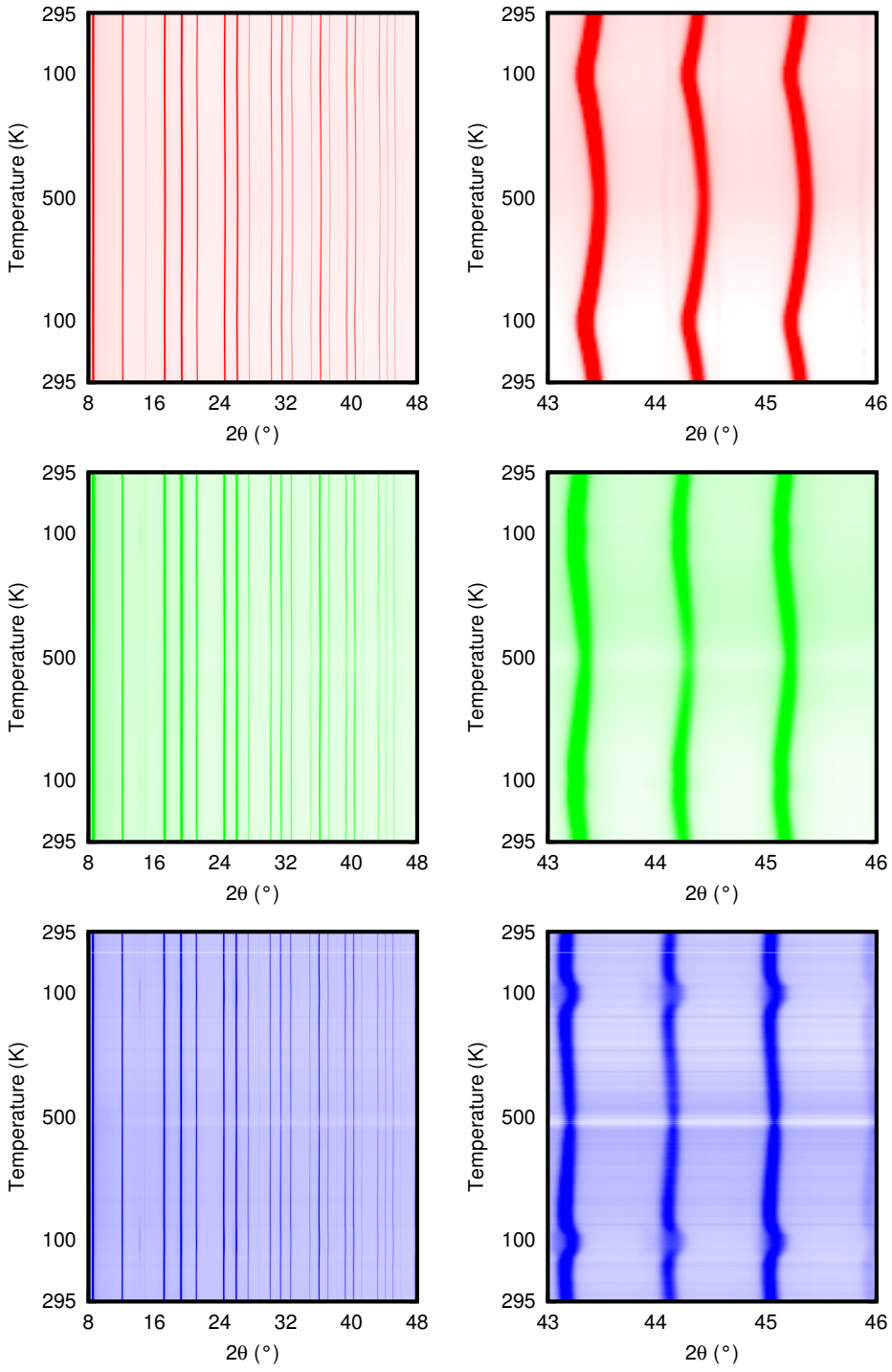

Figure C.2: Stackplots of variable-temperature (Cryostream, 100-500 K) PXRD patterns collected for $Sc_{1-x}Y_xF_3$ in which $x = 0.00$ (top), 0.05 (middle), and 0.10 (bottom). The stackplots in the left column show the full 2θ range used in Rietveld analyses of the data, while those in the right column show a portion of the full pattern. Within a stackplot, the patterns are arranged in the order of collection from bottom to top, which followed the temperature ramp in Figure 2.2b. Reproduced from ref. [247].

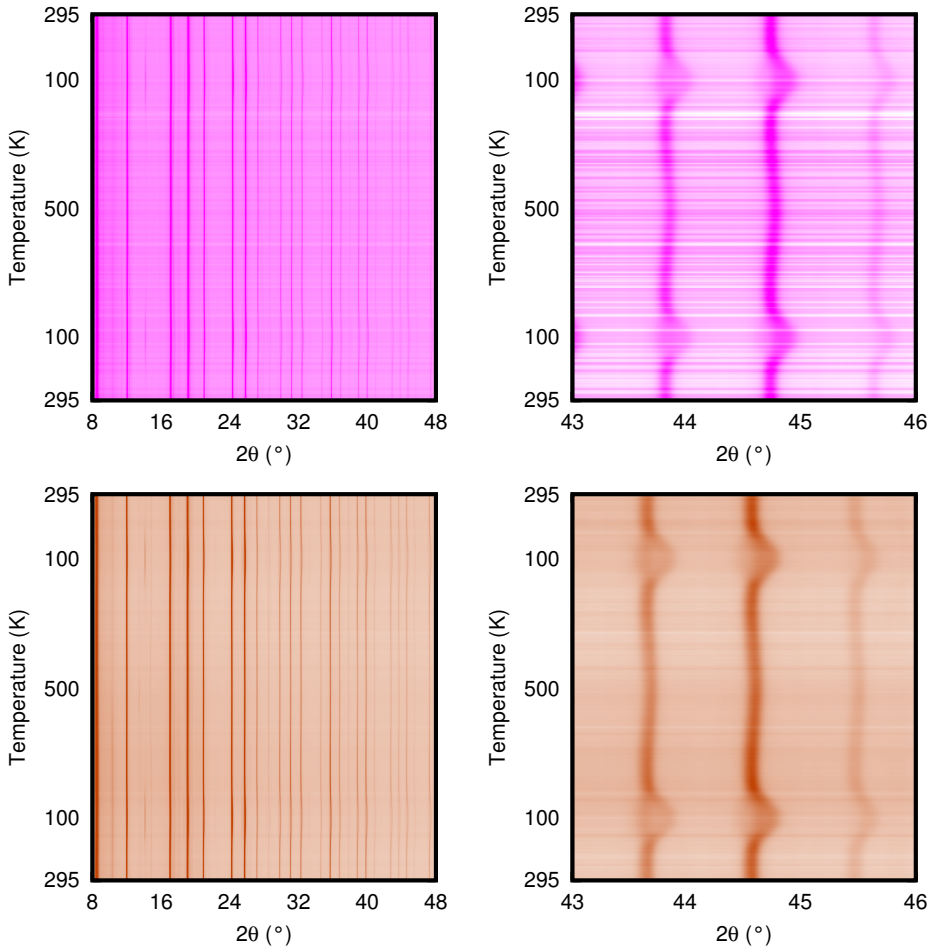

Figure C.3: Stackplots of variable-temperature (Cryostream, 100-500 K) PXRD patterns collected for $Sc_{1-x}Y_xF_3$ in which $x = 0.20$ (top) and 0.25 (bottom). The stackplots in the left column show the full 2θ range used in Rietveld analyses of the data, while those in the right column show a portion of the full pattern. Within a stackplot, the patterns are arranged in the order of collection from bottom to top, which followed the temperature ramp in Figure 2.2b. Reproduced from ref. [247].

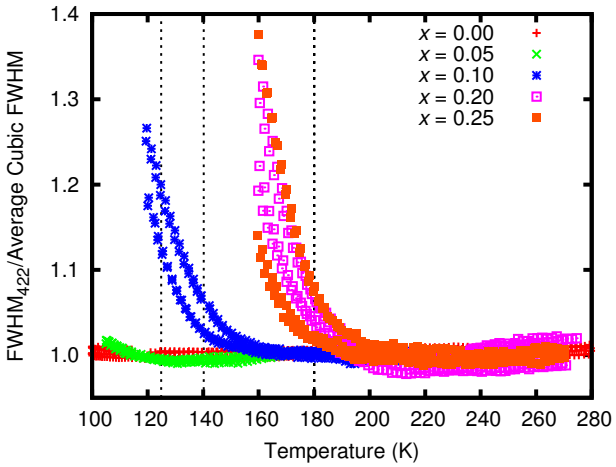

Figure C.4: The cubic-to-rhombohedral phase transition temperature for each of the solid solution samples was estimated by monitoring the full width at half-maximum (FWHM) of the cubic (4 2 2) Bragg reflection ($d \approx 0.83$ Å), which splits into the primitive rhombohedral (6 2 0) and (4 6 6) Bragg reflections at low temperatures. Its width was estimated by fitting a pseudo-Voigt function, along with a linear background, using the program *Fityk* [273]. The intersection of straight-line fits to the FWHM *versus* temperature curve at both high and low temperatures was taken to be the transition temperature. As the values estimated from the heating and cooling curves were somewhat different, their average is reported. Phase transition temperatures estimated by examining the temperature dependence of rhombohedral angle α were in good agreement with those determined using the above line-broadening approach (Figure C.5). This figure presents the temperature dependence of the FWHM of the cubic (4 2 2) Bragg reflection of $Sc_{1-x}Y_xF_3$, normalized by the average FWHM over the cubic region, which was used to estimate the phase transition temperatures (indicated by vertical dashed lines). Reproduced from ref. [247].

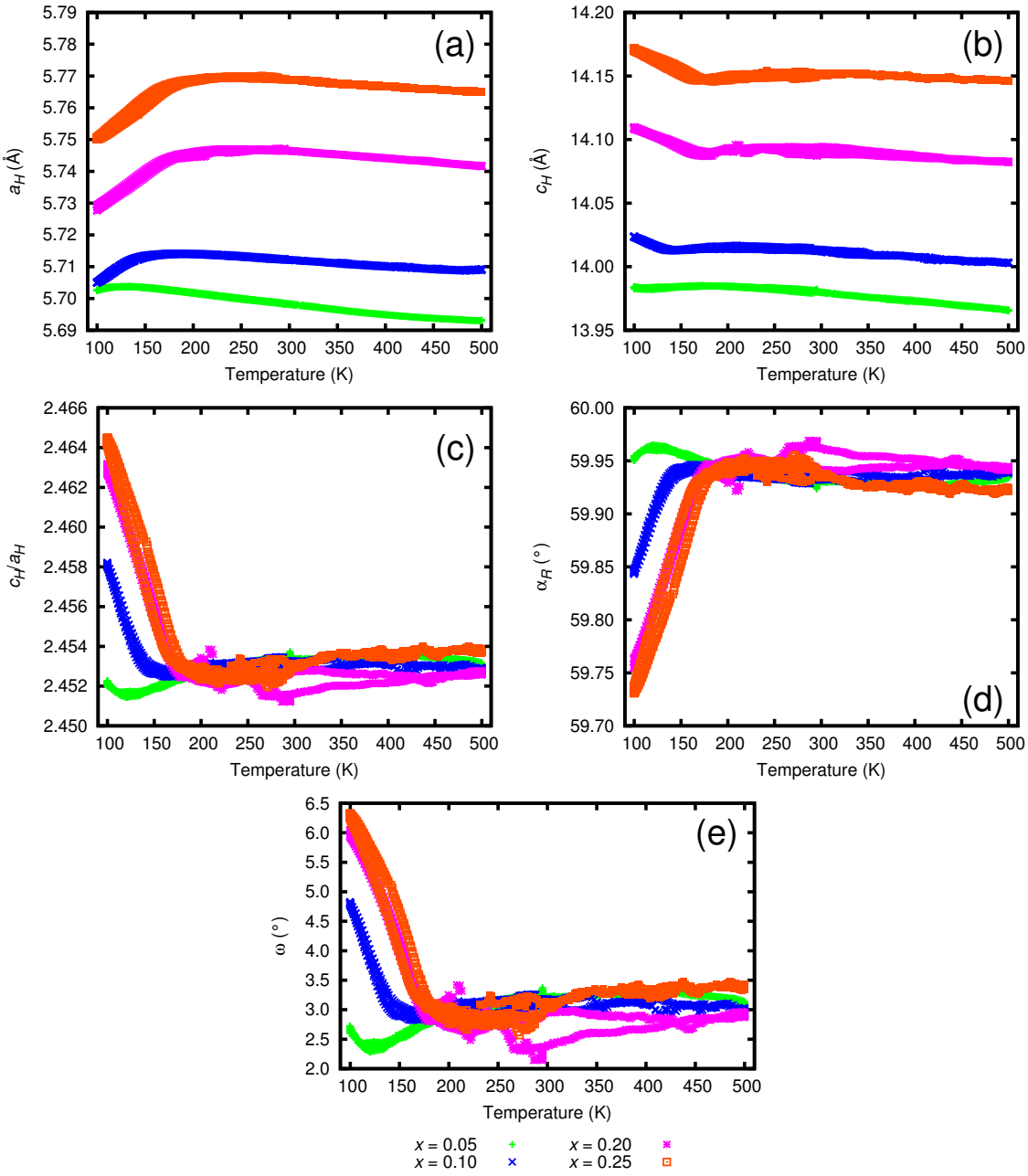

Figure C.5: Temperature dependence of various unit cell parameters: (a),(b),(c) hexagonal unit cell lengths a_H and c_H and their ratio c_H/a_H; (d) rhombohedral unit cell angle α_R; (e) octahedral tilt angle ω. The lattice constants and angle are derived from Rietveld analysis, while octahedral tilt angle is defined as $\cos\omega = \sqrt{6}[c_H/a_H]^{-1}$. The latter three parameters converge to similar values for all x, but this convergence is at a slightly unexpected value. The c_H/a_H ratio of a cubic cell is expected to be $\sqrt{6} = 2.449$, while α_R and ω should be 60 and 0°, respectively. The slight discrepancy between the observed and expected values of these parameters is due to the inadequacy of the rhombohedral model used in Rietveld refinement to fit cubic data; the fit is over-parameterized in such cases. Reproduced from ref. [247].

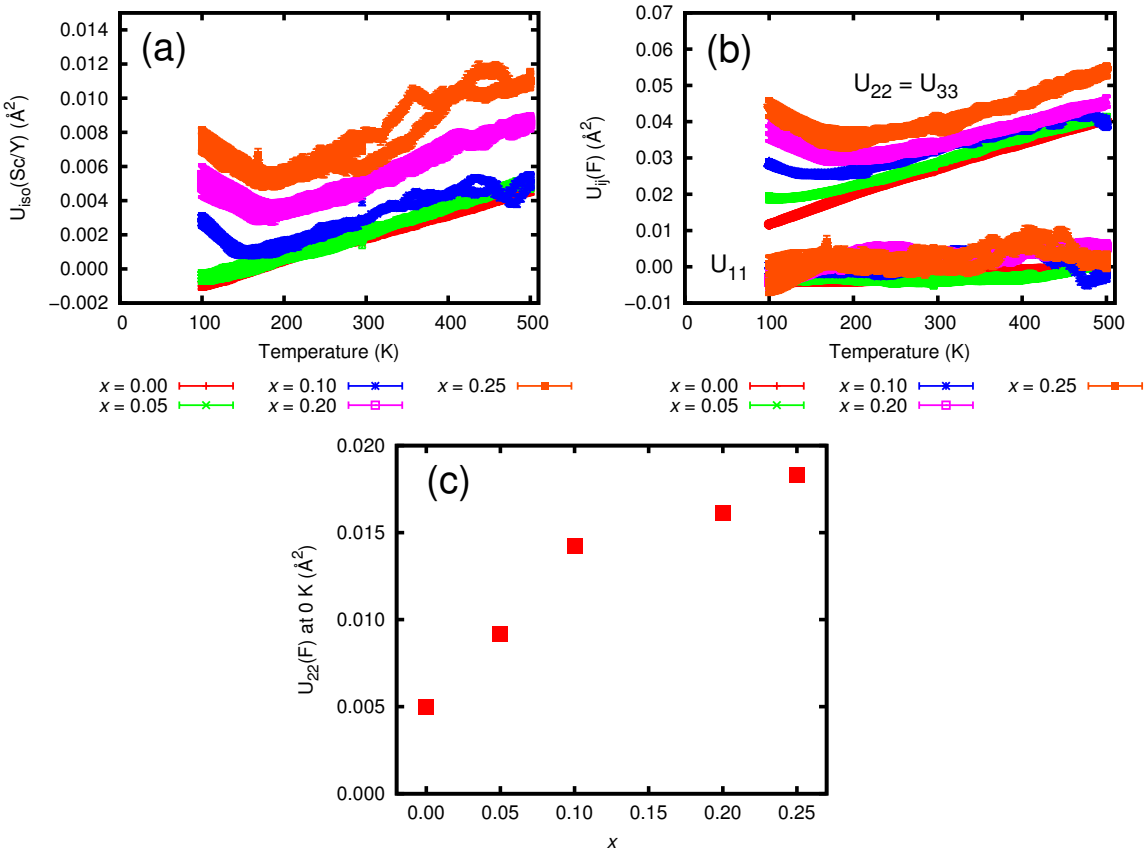

Figure C.6: Atomic displacement parameters for $Sc_{1-x}Y_xF_3$, determined by Rietveld analyses of the variable temperature (Cryostream, 100-500 K) PXRD data using a cubic structural model: (a) U_{iso} of Sc and Y, constrained to be equal; (b) U_{11} and $U_{22}(= U_{33})$ of F; (c) estimated value of U_{22} of F at 0 K, extrapolated from plot (b), for different values of x. In (c), error bars, derived from least-squares fits, are smaller than the point size. The scatter in U_{iso} in (a), especially for $x = 0.25$, is a result of the inadequacy of the data. Furthermore, the scatter in (a) is prominent because of the scale on which the data are plotted. None of the data were corrected for absorption, potentially resulting in U values that are lower than expected, which explains the slightly negative values of U_{iso} and U_{11} in (a) and (b). While the absolute values are in error, the trends with temperature and composition should be valid. Reproduced from ref. [247].

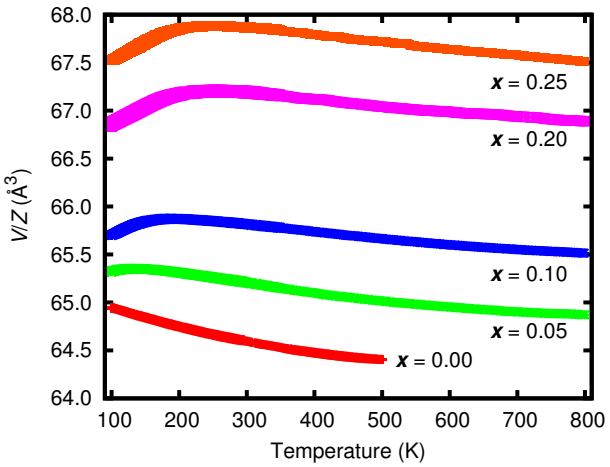

Figure C.7: Temperature dependence of V/Z for $Sc_{1-x}Y_xF_3$. These volumes were extracted from Rietveld analyses of the variable-temperature PXRD data. However, as the complete set of variable-temperature measurements was conducted over several different blocks of beam time using two different sample environments, each with different calibrations, the furnace and Cryostream results for each sample were scaled to one another. Heating and cooling curves overlap quite well on this scale. Reproduced from ref. [247].

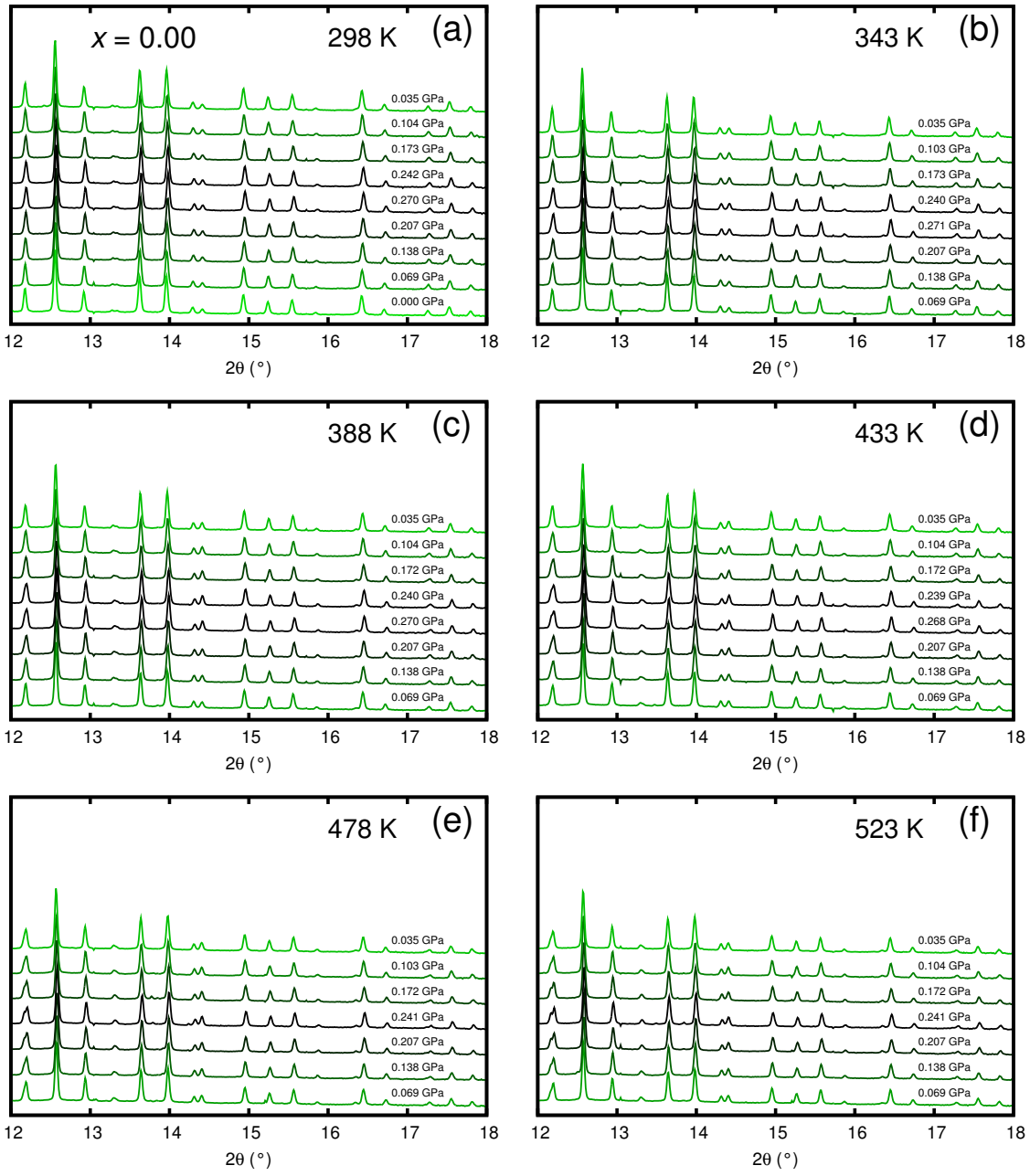

Figure C.8: Stackplots of variable-pressure/temperature PXRD patterns collected for ScF_3. Each panel represents a particular temperature, and the patterns within each panel were collected at different pressures, arranged in order of collection from bottom to top. Extra peaks (not sample-related) in the patterns are from the titanium pressure vessel. Reproduced from ref. [247].

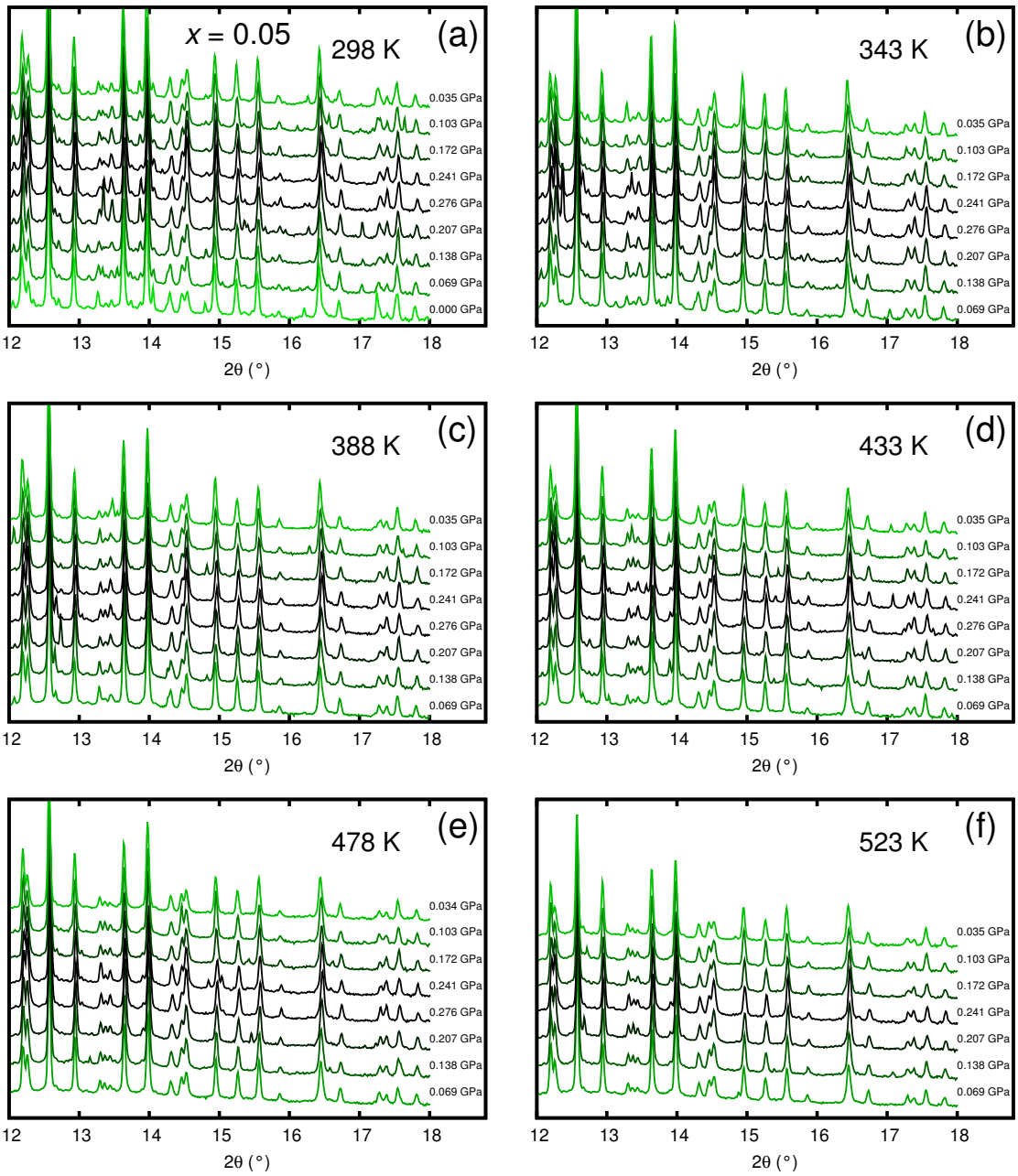

Figure C.9: Stackplots of variable-pressure/temperature PXRD patterns collected for $Sc_{0.95}Y_{0.05}F_3$. Each panel represents a particular temperature, and the patterns within each panel were collected at different pressures, arranged in order of collection from bottom to top. Extra peaks (not sample-related) in the patterns are from the titanium pressure vessel. An experimental error (improper BRIM alignment) was likely the cause of the greater number of extra peaks for this sample relative to the others. Reproduced from ref. [247].

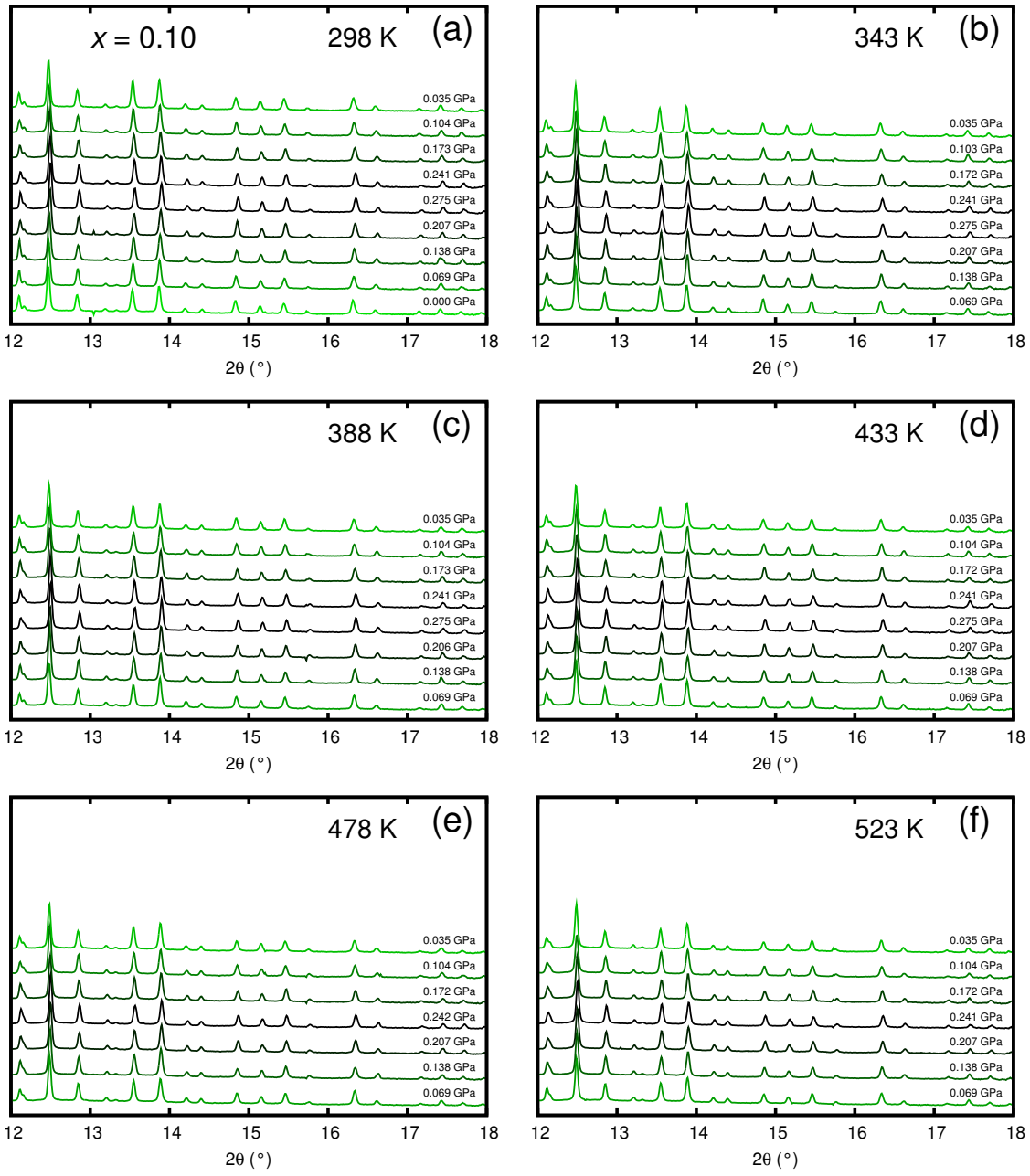

Figure C.10: Stackplots of variable-pressure/temperature PXRD patterns collected for $Sc_{0.90}Y_{0.10}F_3$. Each panel represents a particular temperature, and the patterns within each panel were collected at different pressures, arranged in order of collection from bottom to top. Extra peaks (not sample-related) in the patterns are from the titanium pressure vessel. Reproduced from ref. [247].

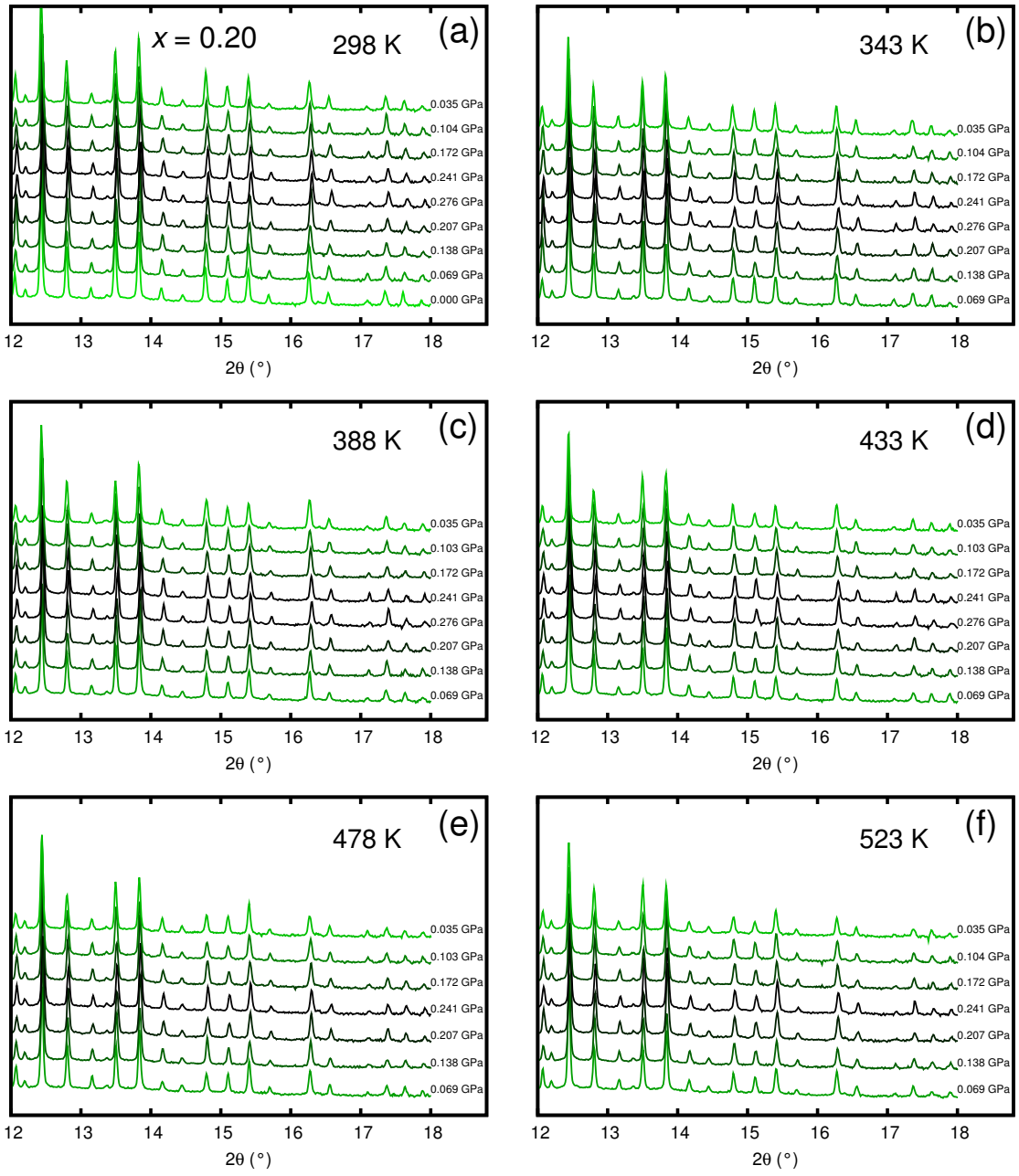

Figure C.11: Stackplots of variable-pressure/temperature PXRD patterns collected for $Sc_{0.80}Y_{0.20}F_3$. Each panel represents a particular temperature, and the patterns within each panel were collected at different pressures, arranged in order of collection from bottom to top. Extra peaks (not sample-related) in the patterns are from the titanium pressure vessel. Reproduced from ref. [247].

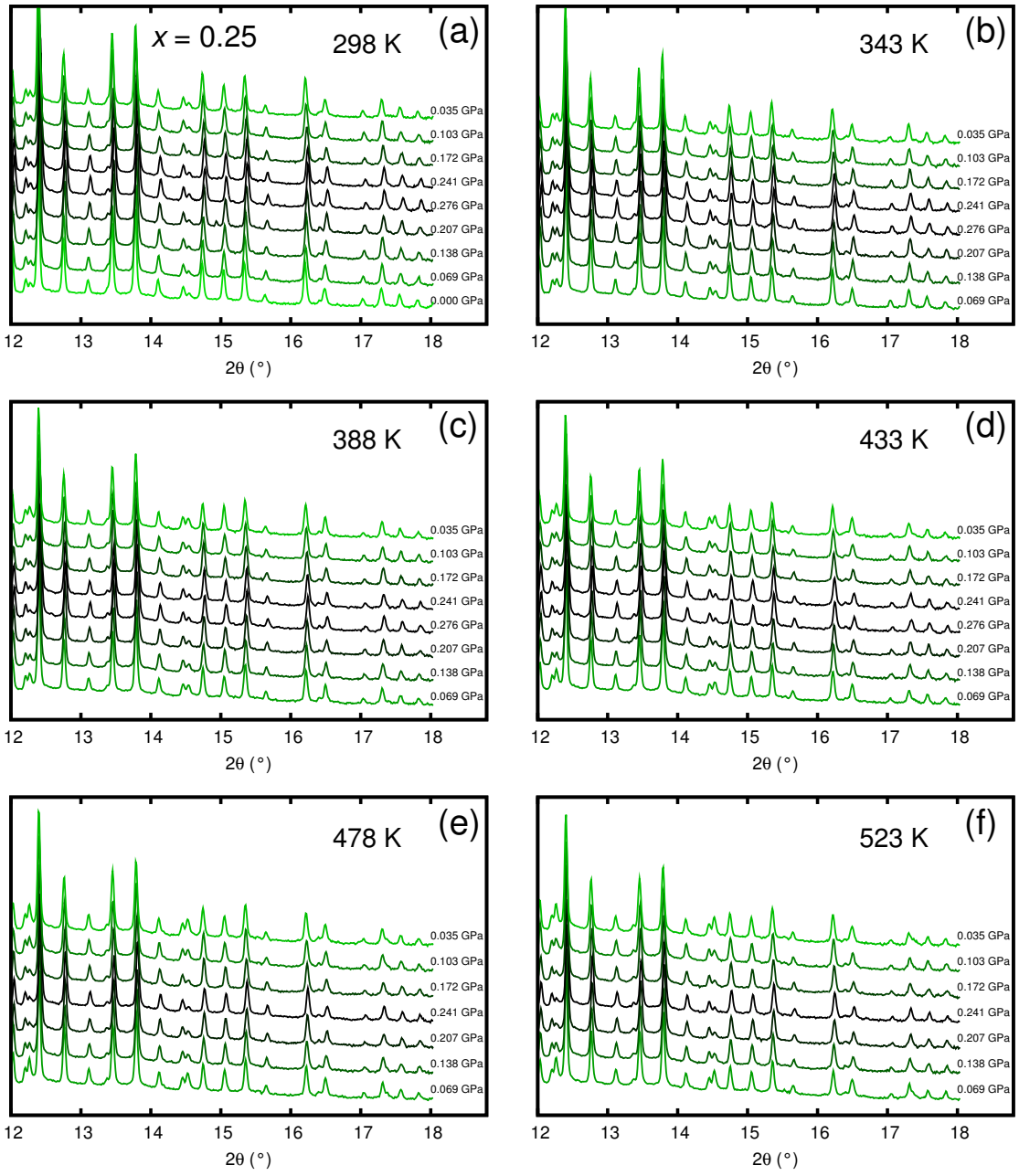

Figure C.12: Stackplots of variable-pressure/temperature PXRD patterns collected for $Sc_{0.75}Y_{0.25}F_3$. Each panel represents a particular temperature, and the patterns within each panel were collected at different pressures, arranged in order of collection from bottom to top. Extra peaks (not sample-related) in the patterns are from the titanium pressure vessel. Reproduced from ref. [247].

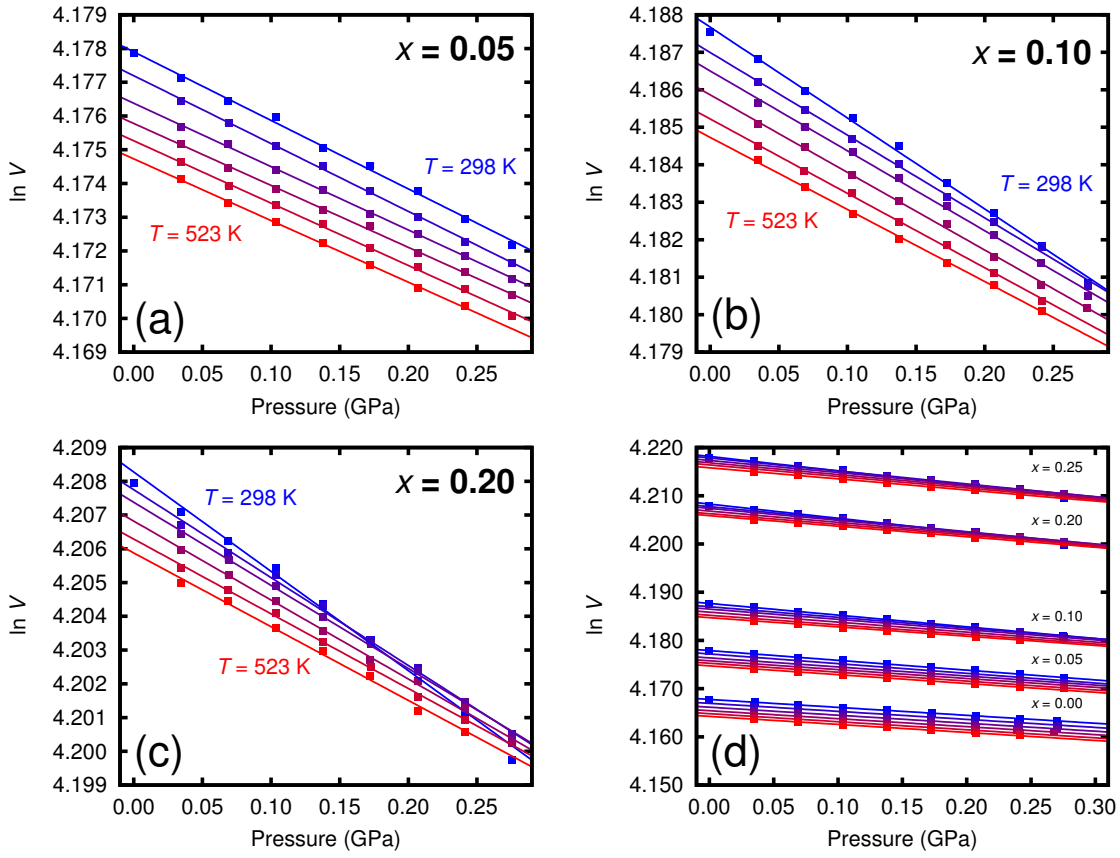

Figure C.13: Natural logarithm of unit cell volume ($\ln V$; units of V are Å^3) plotted with respect to pressure at various temperatures (298, 343, 388, 433, 478, and 523 K) for (a) $Sc_{0.95}Y_{0.05}F_3$, (b) $Sc_{0.90}Y_{0.10}F_3$, and (c) $Sc_{0.80}Y_{0.20}F_3$. Panel (d) shows the data from the other panels, as well as those for $x = 0.00$ and 0.25, plotted on the same scale. Linear fits to the data are included in the plots. For each sample, the lowest temperature points are in blue and have the generally highest volumes; conversely, the highest temperature points are in red and have the generally lowest volumes. In all plots, error bars are smaller than the point size. Reproduced from ref. [247].

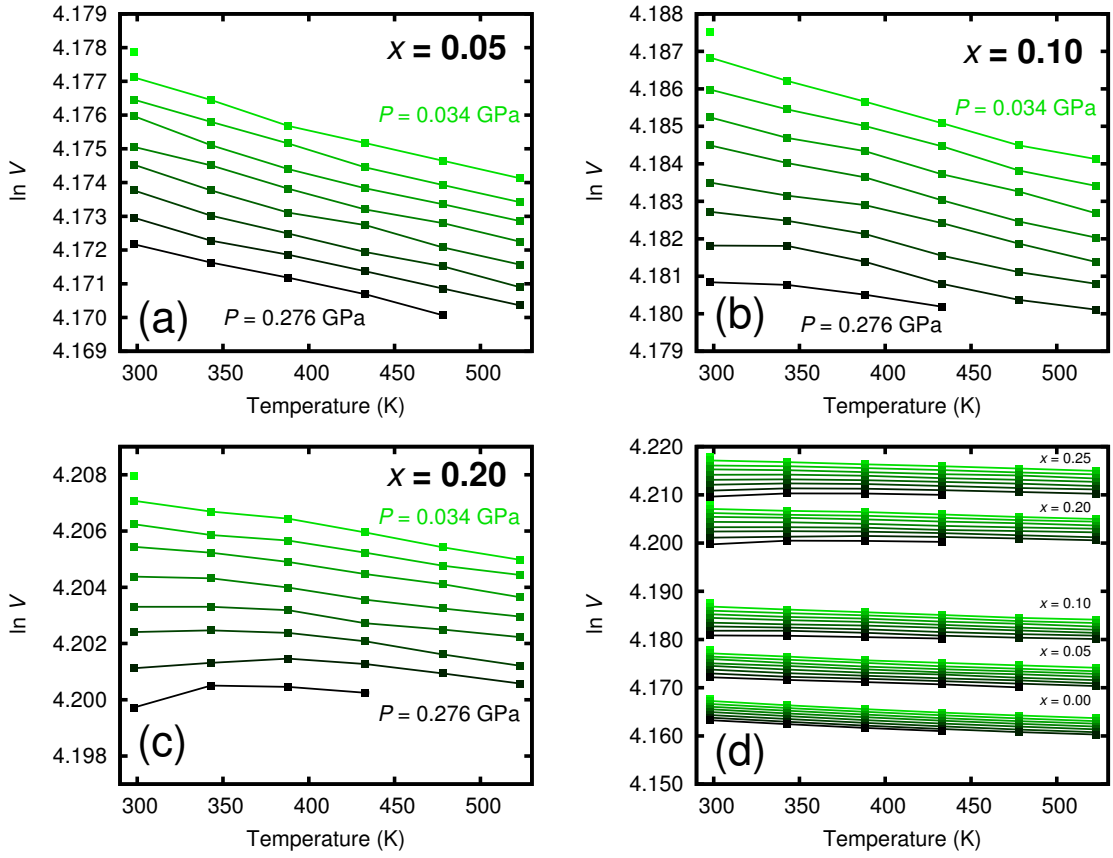

Figure C.14: Natural logarithm of unit cell volume ($\ln V$; units of V are Å^3) plotted with respect to temperature at various pressures (0.034, 0.069, 0.103, 0.138, 0.172, 0.207, 0.241, and 0.276 GPa) for (a) $Sc_{0.95}Y_{0.05}F_3$, (b) $Sc_{0.90}Y_{0.10}F_3$, and (c) $Sc_{0.80}Y_{0.20}F_3$. Panel (d) shows the data from the other panels, as well as those for $x = 0.00$ and 0.25, plotted on the same scale. The data points are connected with line segments as a guide to the eye. For each sample, the lowest pressure points are in green and have the highest volumes; conversely, the highest pressure points are in black and have the lowest volumes. In each plot, the single unconnected point at 300 K was measured at $P = 0$. In all plots, error bars are smaller than the point size. Reproduced from ref. [247].

APPENDIX D

CHAPTER 8 SUPPORTING MATERIAL

Table D.1: Lattice constants and unit cell volumes of $Sc_{0.95}Al_{0.05}F_3$ at various temperatures and pressures. These values were determined by Rietveld analyses of high-pressure, high-temperature PXRD data and are presented here without scaling. Italicized data were omitted from Analysis (see Section 8.2.3). Numbers in parentheses are estimated standard deviations from least-squares fits during Rietveld analyses.

T (K)	P (GPa)	Structure	a (Å)	α_R (°)	V/Z (Å^3)
298	0.000	Cubic	3.99869(7)	–	63.937(4)
298	0.103	Cubic	3.99596(8)	–	63.806(4)
298	0.207	Cubic	3.9928(1)	–	63.655(5)
298	0.310	Cubic	3.9892(1)	–	63.484(5)
298	0.413	Cubic	3.98408(7)	–	63.239(3)
298	0.362	Cubic	3.98709(7)	–	63.383(3)
298	*0.258*	*Cubic*	*3.98704(7)*	–	*63.380(3)*
298	0.155	Cubic	3.99453(7)	–	63.738(3)
298	0.052	Cubic	3.99731(7)	–	63.871(3)
343	0.017	Cubic	3.99742(9)	–	63.877(4)
343	0.103	Cubic	3.99490(8)	–	63.756(4)
343	0.207	Cubic	3.99226(8)	–	63.629(4)
343	0.310	Cubic	3.98936(8)	–	63.491(4)
343	0.414	Cubic	3.98545(7)	–	63.304(3)
343	0.362	Cubic	3.98741(8)	–	63.398(4)
343	0.259	Cubic	3.99082(7)	–	63.560(3)

Table D.1: *Continued on next page*

Table D.1: *Continued from previous page*

T (K)	P (GPa)	Structure	a (Å)	α_R (°)	V/Z (Å^3)
343	0.155	Cubic	3.99362(7)	–	63.695(3)
343	0.052	Cubic	3.99649(8)	–	63.832(4)
388	0.017	Cubic	3.99629(9)	–	63.822(4)
388	0.103	Cubic	3.9949(1)	–	63.757(5)
388	0.207	Cubic	3.99191(8)	–	63.613(4)
388	0.310	Cubic	3.98854(8)	–	63.452(4)
388	0.413	Cubic	3.98542(7)	–	63.303(4)
388	0.362	Cubic	3.98706(7)	–	63.381(3)
388	0.258	Cubic	3.99027(8)	–	63.534(4)
388	0.155	Cubic	3.99258(6)	–	63.645(3)
388	0.052	Cubic	3.99512(8)	–	63.766(4)
433	0.017	Cubic	3.99548(9)	–	63.783(4)
433	0.103	Cubic	3.99362(9)	–	63.694(4)
433	0.207	Cubic	3.99076(9)	–	63.558(4)
433	0.310	Cubic	3.98817(8)	–	63.434(4)
433	0.414	Cubic	3.98499(9)	–	63.282(4)
433	0.362	Cubic	3.98720(8)	–	63.388(4)
433	0.259	Cubic	3.98965(8)	–	63.505(4)
433	0.155	Cubic	3.99230(8)	–	63.631(4)
433	0.052	Cubic	3.99478(8)	–	63.750(4)
478	0.016	Cubic	3.99496(1)	–	63.758(5)
478	0.103	Cubic	3.99281(9)	–	63.656(4)
478	0.207	Cubic	3.99045(9)	–	63.543(4)
478	0.310	Cubic	3.98777(9)	–	63.415(4)
478	0.259	Cubic	3.98894(9)	–	63.471(4)
478	0.155	Cubic	3.99188(9)	–	63.611(4)

Table D.1: *Continued on next page*

Table D.1: *Continued from previous page*

T (K)	P (GPa)	Structure	a (Å)	α_R (°)	V/Z (Å^3)
478	0.052	Cubic	3.99405(9)	–	63.715(4)
523	0.017	Cubic	3.9941(1)	–	63.721(6)
523	0.103	Cubic	3.99258(9)	–	63.645(4)
523	0.207	Cubic	3.9897(1)	–	63.508(5)
523	0.310	Cubic	3.98728(9)	–	63.392(4)
523	0.258	Cubic	3.98866(1)	–	63.457(5)
523	0.155	Cubic	3.99127(9)	–	63.582(4)
523	0.052	Cubic	3.9934(1)	–	63.683(5)

Table D.2: Lattice constants and unit cell volumes of $Sc_{0.90}Al_{0.10}F_3$ at various temperatures and pressures. These values were determined by Rietveld analyses of high-pressure, high-temperature PXRD data and are presented here without scaling. Numbers in parentheses are estimated standard deviations from least-squares fits during Rietveld analyses.

T (K)	P (GPa)	Structure	a (Å)	α_R (°)	V/Z (Å^3)
298	0.000	Cubic	3.97677(6)	–	62.892(3)
298	0.103	Cubic	3.97323(5)	–	62.724(2)
298	0.207	Rhombohedral	5.6134(2)	59.764(2)	62.200(5)
298	0.310	Rhombohedral	5.6066(2)	59.394(2)	61.451(5)
298	0.259	Rhombohedral	5.6096(2)	59.537(2)	61.754(3)
298	0.155	Cubic	3.96959(6)	–	62.552(3)
298	0.052	Cubic	3.97498(6)	–	62.806(3)
343	0.017	Cubic	3.97663(6)	–	62.885(3)
343	0.104	Cubic	3.97395(5)	–	62.758(2)
343	0.207	Cubic	3.96966(6)	–	62.555(3)
343	0.310	Rhombohedral	5.6084(2)	59.799(3)	62.086(4)

Table D.2: *Continued on next page*

Table D.2: *Continued from previous page*

T (K)	P (GPa)	Structure	a (Å)	α_R (°)	V/Z (Å^3)
343	0.259	Cubic	3.96710(5)	–	62.434(2)
343	0.155	Cubic	3.97166(7)	–	62.649(3)
343	0.052	Cubic	3.97544(5)	–	62.828(2)
388	0.017	Cubic	3.97646(6)	–	62.877(3)
388	0.103	Cubic	3.97427(0)	–	62.773(3)
388	0.207	Cubic	3.97067(6)	–	62.602(3)
388	0.310	Cubic	3.96649(6)	–	62.405(3)
388	0.259	Cubic	3.96770(7)	–	62.462(3)
388	0.155	Cubic	3.97227(5)	–	62.678(3)
388	0.052	Cubic	3.97549(7)	–	62.831(3)
433	0.017	Cubic	3.97618(7)	–	62.864(3)
433	0.103	Cubic	3.97403(6)	–	62.761(3)
433	0.207	Cubic	3.97070(7)	–	62.604(3)
433	0.310	Cubic	3.96737(7)	–	62.447(3)
433	0.327	Cubic	3.96682(7)	–	62.421(3)
433	0.259	Cubic	3.96908(7)	–	62.527(3)
433	0.155	Cubic	3.97255(7)	–	62.692(3)
433	0.052	Cubic	3.97524(7)	–	62.819(3)
478	0.017	Cubic	3.97510(7)	–	62.855(3)
478	0.104	Cubic	3.97376(8)	–	62.749(4)
478	0.207	Cubic	3.97090(8)	–	62.614(4)
478	0.310	Cubic	3.96784(8)	–	62.469(4)
478	0.259	Cubic	3.96945(9)	–	62.545(4)
478	0.155	Cubic	3.97264(8)	–	62.696(4)
478	0.052	Cubic	3.97505(8)	–	62.810(4)
523	0.017	Cubic	3.9757(1)	–	62.839(5)

Table D.2: *Continued on next page*

Table D.2: *Continued from previous page*

T (K)	P (GPa)	Structure	a (Å)	α_R (°)	V/Z (Å^3)
523	0.103	Cubic	3.97358(9)	–	62.740(4)
523	0.207	Cubic	3.97091(9)	–	62.614(4)
523	0.310	Cubic	3.9679(1)	–	62.473(5)
523	0.259	Cubic	3.9694(1)	–	62.545(5)
523	0.155	Cubic	3.97215(9)	–	62.672(4)
523	0.052	Cubic	3.97515(9)	–	62.815(4)

Table D.3: Lattice constants and unit cell volumes of $Sc_{0.85}Al_{0.15}F_3$ at various temperatures and pressures. These values were determined by Rietveld analyses of high-pressure, high-temperature PXRD data and are presented here without scaling. Numbers in parentheses are estimated standard deviations from least-squares fits during Rietveld analyses.

T (K)	P (GPa)	Structure	a (Å)	α_R (°)	V/Z (Å^3)
303	0.000	Cubic	3.95390(7)	–	61.813(3)
303	0.103	Rhombohedral	5.5894(2)	59.683(2)	61.293(5)
303	0.207	Rhombohedral	5.5837(2)	59.405(2)	60.717(3)
303	0.310	Rhombohedral	5.5770(2)	59.145(2)	60.131(5)
303	0.414	Rhombohedral	5.5704(2)	58.885(2)	59.556(5)
303	0.362	Rhombohedral	5.5736(2)	59.015(2)	59.840(5)
303	0.259	Rhombohedral	5.5804(2)	59.270(2)	60.416(5)
303	0.155	Rhombohedral	5.5866(2)	59.536(2)	60.994(3)
303	0.052	Cubic	3.94886(9)	–	61.576(4)
343	0.017	Cubic	3.95520(6)	–	61.874(3)
343	0.103	Cubic	3.95088(6)	–	61.671(3)
343	0.207	Rhombohedral	5.5847(2)	59.659(2)	61.105(5)
343	0.310	Rhombohedral	5.5793(2)	59.340(2)	60.482(5)

Table D.3: *Continued on next page*

Table D.3: *Continued from previous page*

T (K)	P (GPa)	Structure	a (Å)	α_R (°)	V/Z (Å^3)
343	0.414	Rhombohedral	5.5725(2)	59.063(2)	59.874(5)
343	0.362	Rhombohedral	5.5758(2)	59.197(2)	60.167(5)
343	0.259	Rhombohedral	5.5824(2)	59.485(2)	60.786(3)
343	0.155	Cubic	3.94560(9)	–	61.424(4)
343	0.052	Cubic	3.95376(5)	–	61.806(3)
388	0.017	Cubic	3.95622(5)	–	61.922(2)
388	0.103	Cubic	3.95297(5)	–	61.769(2)
388	0.207	Cubic	3.94839(6)	–	61.554(3)
388	0.310	Rhombohedral	5.5804(2)	59.674(2)	60.984(5)
388	0.414	Rhombohedral	5.5752(2)	59.300(2)	60.291(5)
388	0.362	Rhombohedral	5.5785(2)	59.465(2)	60.631(3)
388	0.259	Cubic	3.94432(7)	–	61.364(3)
388	0.155	Cubic	3.95084(5)	–	61.669(2)
388	0.052	Cubic	3.95507(5)	–	61.867(2)
433	0.017	Cubic	3.95651(7)	–	61.935(3)
433	0.104	Cubic	3.95387(5)	–	61.811(2)
433	0.207	Cubic	3.95044(5)	–	61.651(2)
433	0.310	Cubic	3.94581(5)	–	61.434(2)
433	0.414	Rhombohedral	5.5760(2)	59.713(2)	60.894(4)
433	0.362	Cubic	3.94275(6)	–	61.291(3)
433	0.259	Cubic	3.94817(5)	–	61.544(2)
433	0.155	Cubic	3.95221(5)	–	61.733(2)
478	0.052	Cubic	3.95553(5)	–	61.889(2)
478	0.017	Cubic	3.95684(6)	–	61.951(3)
478	0.104	Cubic	3.95420(5)	–	61.827(2)
478	0.207	Cubic	3.95082(5)	–	61.668(2)

Table D.3: *Continued on next page*

Table D.3: *Continued from previous page*

T (K)	P (GPa)	Structure	a (Å)	α_R (°)	V/Z (Å^3)
478	0.310	Cubic	3.94730(5)	–	61.503(3)
478	0.259	Cubic	3.94926(5)	–	61.595(2)
478	0.155	Cubic	3.95279(5)	–	61.761(2)
478	0.052	Cubic	3.95591(5)	–	61.907(2)
523	0.017	Cubic	3.95682(6)	–	61.950(3)
523	0.103	Cubic	3.95439(6)	–	61.835(3)
523	0.207	Cubic	3.95136(5)	–	61.693(2)
523	0.310	Cubic	3.94824(6)	–	61.547(3)
523	0.259	Cubic	3.94974(5)	–	61.618(2)
523	0.155	Cubic	3.95304(5)	–	61.772(2)
523	0.052	Cubic	3.95589(6)	–	61.906(3)

Table D.4: Lattice constants and unit cell volumes of $Sc_{0.80}Al_{0.20}F_3$ at various temperatures and pressures. These values were determined by Rietveld analyses of high-pressure, high-temperature PXRD data and are presented here without scaling. Italicized data were omitted from Analysis (see Section 8.2.3). Numbers in parentheses are estimated standard deviations from least-squares fits during Rietveld analyses.

T (K)	P (GPa)	Structure	a (Å)	α_R (°)	V/Z (Å^3)
298	0.000	Rhombohedral	5.5541(2)	59.501(2)	59.889(3)
298	0.103	Rhombohedral	5.5484(2)	59.287(2)	59.409(5)
298	0.207	Rhombohedral	5.5425(2)	59.081(3)	58.939(5)
298	0.310	Rhombohedral	5.5361(3)	58.869(4)	58.441(5)
298	0.413	Rhombohedral	5.5313(3)	58.631(4)	57.963(5)
298	0.362	Rhombohedral	5.5335(3)	58.725(4)	58.161(5)
298	*0.259*	*Rhombohedral*	*5.5334(4)*	*58.733(5)*	*58.170(5)*

Table D.4: *Continued on next page*

Table D.4: *Continued from previous page*

T (K)	P (GPa)	Structure	a (Å)	α_R (°)	V/Z (Å^3)
298	0.155	Rhombohedral	5.5459(3)	59.146(4)	59.135(5)
298	0.052	Rhombohedral	5.5512(4)	59.363(5)	59.605(5)
343	0.017	Rhombohedral	5.5539(2)	59.675(2)	60.123(4)
343	0.103	Rhombohedral	5.5501(2)	59.474(2)	59.723(3)
343	0.207	Rhombohedral	5.5448(2)	59.241(2)	59.233(5)
343	0.310	Rhombohedral	5.5389(2)	59.028(2)	58.751(3)
343	0.414	Rhombohedral	5.5331(2)	58.793(3)	58.243(3)
343	0.362	Rhombohedral	5.5359(2)	58.911(3)	58.494(3)
343	0.259	Rhombohedral	5.5420(2)	59.133(2)	58.992(3)
343	0.155	Rhombohedral	5.5478(2)	59.352(3)	59.480(5)
343	0.052	Rhombohedral	5.5527(2)	59.591(3)	59.968(4)
388	0.017	Cubic	3.9254(1)	–	60.487(4)
388	0.103	Rhombohedral	5.5499(3)	59.769(3)	60.124(5)
388	0.207	Rhombohedral	5.5467(3)	59.467(3)	59.604(5)
388	0.310	Rhombohedral	5.5414(2)	59.210(2)	59.078(3)
388	0.412	Rhombohedral	5.5355(3)	58.998(3)	58.599(4)
388	0.362	Rhombohedral	5.5386(2)	59.111(3)	58.856(4)
388	0.259	Rhombohedral	5.5442(3)	59.317(4)	59.318(5)
388	0.155	Rhombohedral	5.5485(3)	59.607(3)	59.856(5)
388	0.052	Cubic	3.9229(1)	–	60.370(5)
433	0.017	Cubic	3.9279(1)	–	60.603(5)
433	0.103	Cubic	3.9242(1)	–	60.432(5)
433	0.207	Rhombohedral	5.5455(5)	59.833(6)	60.066(7)
433	0.310	Rhombohedral	5.5430(4)	59.453(4)	59.465(5)
433	0.413	Rhombohedral	5.5385(3)	59.202(3)	58.977(5)
433	0.362	Rhombohedral	5.5408(3)	59.291(4)	59.171(5)

Table D.4: *Continued on next page*

Table D.4: *Continued from previous page*

T (K)	P (GPa)	Structure	a (Å)	α_R (°)	V/Z (Å^3)
433	0.258	Rhombohedral	5.5450(4)	59.628(5)	59.770(7)
433	0.155	Cubic	3.9211(1)	–	60.291(5)
433	0.052	Cubic	3.9267(1)	–	60.547(5)
478	0.017	Cubic	3.9289(1)	–	60.651(6)
478	0.103	Cubic	3.9260(1)	–	60.513(4)
478	0.207	Cubic	3.9218(1)	–	60.322(3)
478	0.310	Rhombohedral	5.538(1)	59.973(8)	60.010(0)
478	0.259	Cubic	3.9192(1)	–	60.204(4)
478	0.155	Cubic	3.9240(1)	–	60.421(4)
478	0.052	Cubic	3.9278(1)	–	60.598(4)
523	0.017	Cubic	3.9295(1)	–	60.676(6)
523	0.103	Cubic	3.9270(1)	–	60.563(4)
523	0.207	Cubic	3.9235(1)	–	60.398(4)
523	0.310	Cubic	3.9194(1)	–	60.212(5)
523	0.259	Cubic	3.9217(1)	–	60.316(5)
523	0.155	Cubic	3.9253(1)	–	60.481(5)
523	0.052	Cubic	3.9285(1)	–	60.633(5)

Table D.5: Lattice constants and unit cell volumes of $Sc_{0.60}Al_{0.40}F_3$ at various temperatures and pressures. These values were determined by Rietveld analyses of high-pressure, high-temperature PXRD data and are presented here without scaling. Italicized data were omitted from Analysis (see Section 8.2.3). Numbers in parentheses are estimated standard deviations from least-squares fits during Rietveld analyses.

T (K)	P (GPa)	Structure	a (Å)	α_R (°)	V/Z (Å^3)
298	0.017	Rhombohedral	5.4339(2)	59.078(2)	55.538(3)

Table D.5: *Continued on next page*

Table D.5: *Continued from previous page*

T (K)	P (GPa)	Structure	a (Å)	α_R (°)	V/Z (Å^3)
298	0.104	Rhombohedral	5.4294(2)	58.948(3)	55.230(3)
298	0.207	Rhombohedral	5.4249(2)	58.774(3)	54.866(3)
298	0.310	Rhombohedral	5.4205(2)	58.607(3)	54.516(3)
298	0.413	Rhombohedral	5.4161(3)	58.464(3)	54.200(5)
298	0.362	Rhombohedral	5.4183(2)	58.531(3)	54.351(3)
298	*0.259*	*Rhombohedral*	*5.4206(2)*	*58.609(3)*	*54.523(3)*
298	0.155	Rhombohedral	5.4272(2)	58.863(3)	55.052(3)
298	0.052	Rhombohedral	5.4320(2)	59.028(3)	55.414(5)
343	0.017	Rhombohedral	5.4360(2)	59.211(3)	55.773(3)
343	0.104	Rhombohedral	5.4318(2)	59.088(3)	55.484(3)
343	0.207	Rhombohedral	5.4270(2)	58.913(3)	55.112(3)
343	0.310	Rhombohedral	5.4226(2)	58.737(3)	55.748(3)
343	0.410	Rhombohedral	5.4187(2)	58.576(3)	55.422(3)
343	0.362	Rhombohedral	5.4208(2)	58.648(3)	54.579(3)
343	0.259	Rhombohedral	5.4251(2)	58.820(3)	54.932(3)
343	0.155	Rhombohedral	5.4296(2)	59.000(3)	55.303(3)
343	0.052	Rhombohedral	5.4348(2)	59.155(3)	55.665(3)
388	0.017	Rhombohedral	5.4381(2)	59.359(3)	56.030(5)
388	0.103	Rhombohedral	5.4344(2)	59.222(3)	55.740(3)
388	0.207	Rhombohedral	5.4295(2)	59.057(3)	55.375(5)
388	0.310	Rhombohedral	5.4249(2)	58.877(3)	55.001(3)
388	0.405	Rhombohedral	5.4214(2)	58.709(3)	54.677(3)
388	0.362	Rhombohedral	5.4235(2)	58.793(3)	54.847(3)
388	*0.259*	*Rhombohedral*	*5.4242(2)*	*58.821(3)*	*54.906(3)*
388	0.155	Rhombohedral	5.4321(2)	59.138(3)	55.557(3)
388	0.052	Rhombohedral	5.4370(2)	59.286(3)	55.904(3)

Table D.5: *Continued on next page*

Table D.5: *Continued from previous page*

T (K)	P (GPa)	Structure	a (Å)	α_R (°)	V/Z (Å^3)
433	0.017	Rhombohedral	5.4392(3)	59.563(3)	56.329(5)
433	0.103	Rhombohedral	5.4361(3)	59.386(3)	55.005(4)
433	0.207	Rhombohedral	5.4321(2)	59.207(3)	55.648(5)
433	0.310	Rhombohedral	5.4276(2)	59.027(3)	55.277(5)
433	0.404	Rhombohedral	5.4243(3)	58.871(3)	55.975(5)
433	0.362	Rhombohedral	5.4257(3)	58.957(3)	55.129(5)
433	*0.259*	*Rhombohedral*	*5.4266(2)*	*58.977(3)*	*55.181(5)*
433	0.155	Rhombohedral	5.4341(2)	59.292(3)	55.822(5)
433	0.052	Rhombohedral	5.4381(3)	59.479(3)	56.188(5)
478	0.017	Cubic	3.8411(1)	–	56.672(5)
478	0.103	Rhombohedral	5.4365(3)	59.639(4)	56.346(5)
478	0.207	Rhombohedral	5.4336(3)	59.389(3)	55.930(4)
478	0.310	Rhombohedral	5.4298(2)	59.196(3)	55.564(5)
478	0.259	Rhombohedral	5.4320(2)	59.288(3)	55.749(5)
478	0.155	Rhombohedral	5.4353(3)	59.494(3)	56.120(5)
478	0.052	Cubic	3.8377(2)	–	56.525(7)
523	0.016	Cubic	3.8457(1)	–	56.879(3)
523	0.103	Cubic	3.8420(1)	–	56.712(4)
523	0.207	Rhombohedral	5.4323(4)	59.705(4)	56.300(6)
523	0.310	Rhombohedral	5.4310(2)	59.399(3)	55.862(4)
523	0.259	Rhombohedral	5.4324(3)	59.513(3)	56.055(5)
523	0.155	Cubic	3.8375(1)	–	56.517(5)
523	0.052	Cubic	3.8444(1)	–	56.819(3)

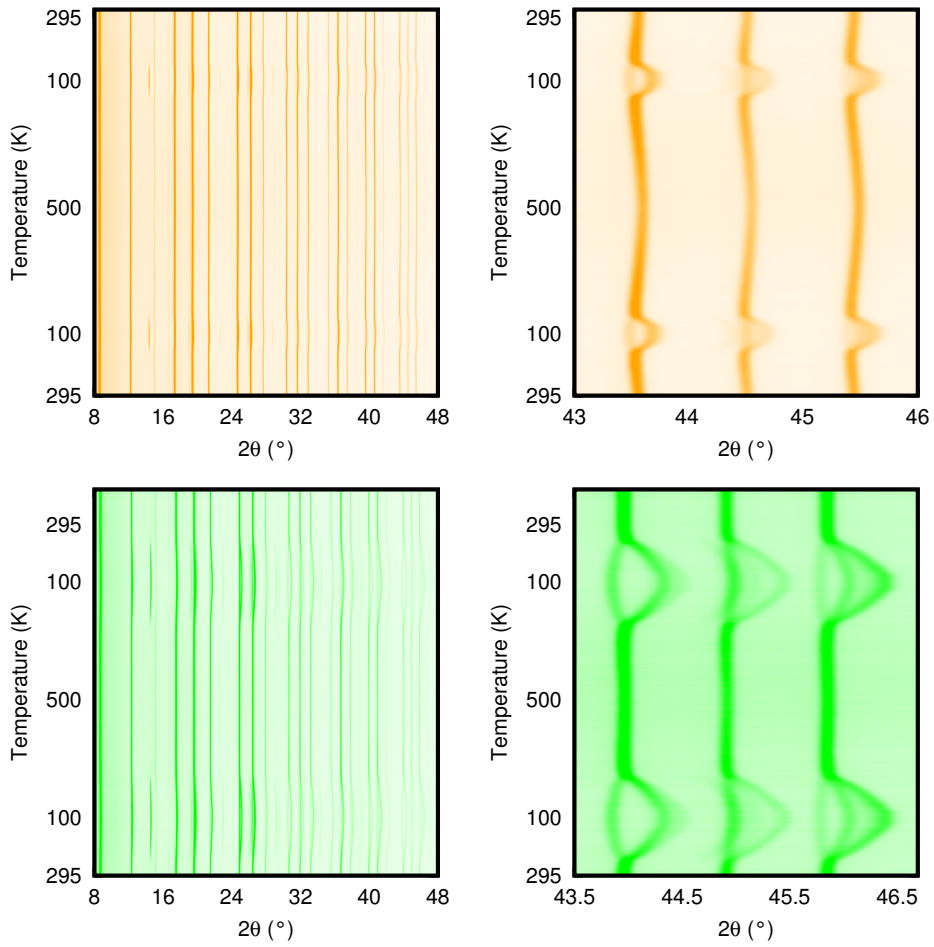

Figure D.1: Variable-temperature (Cryostream, 100-500 K) PXRD data for $Sc_{0.95}Al_{0.05}F_3$ (top) and $Sc_{0.90}Al_{0.10}F_3$ (bottom). The plots in the left column show the full angular range used for Rietveld analysis, while those on the right show a portion of the data. Within each panel, patterns are arranged in order of collection from bottom to top, which followed the temperature ramp in Figure 2.2b. Reproduced from ref. [248].

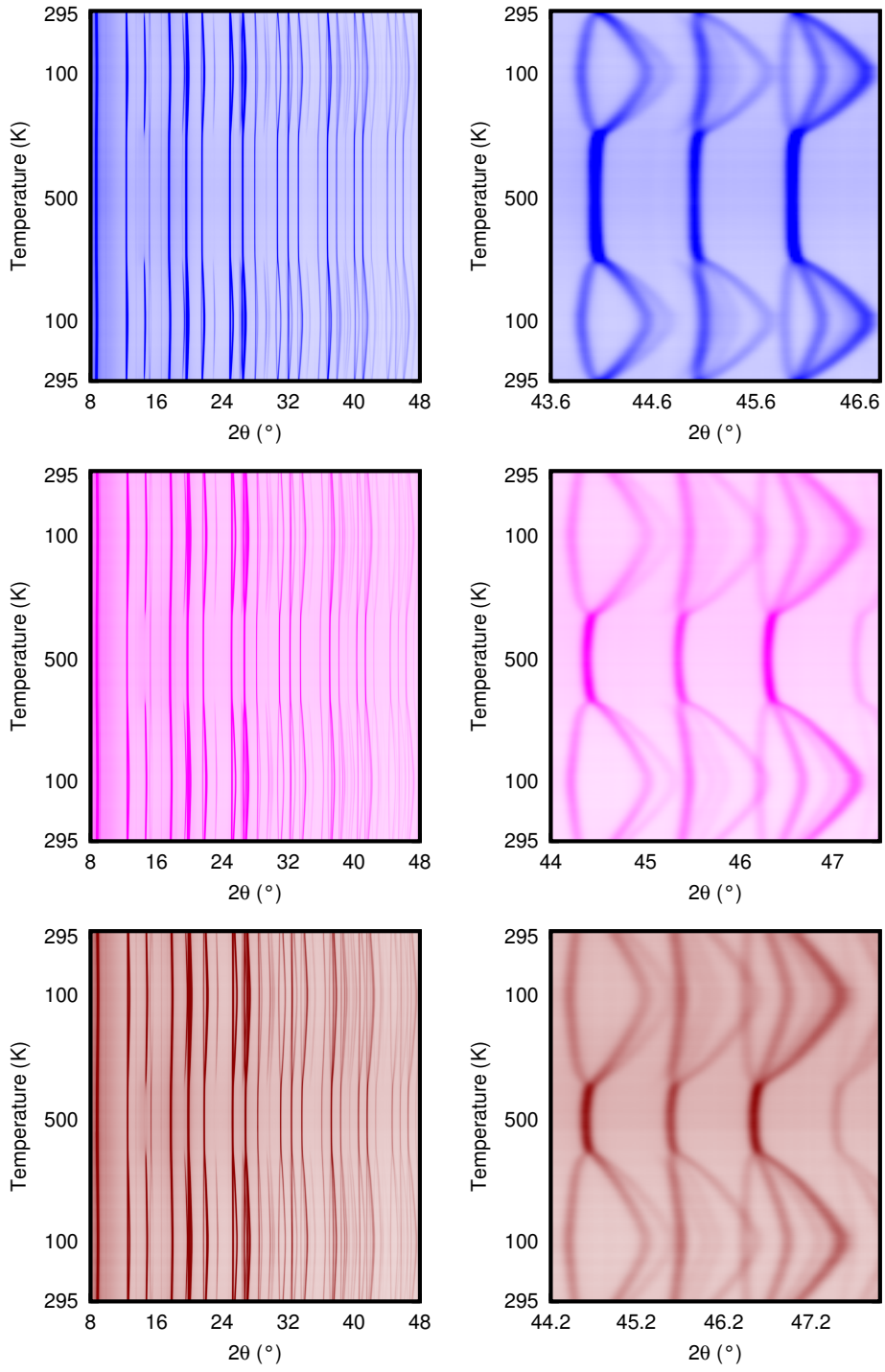

Figure D.2: Variable-temperature (Cryostream, 100-500 K) PXRD data for $Sc_{0.85}Al_{0.15}F_3$ (top), $Sc_{0.80}Al_{0.20}F_3$ (middle), and $Sc_{0.75}Al_{0.25}F_3$ (bottom). The plots in the left column show the full angular range used for Rietveld analysis, while those on the right show a portion of the data. Within each panel, patterns are arranged in order of collection from bottom to top, which followed the temperature ramp in Figure 2.2b. Reproduced from ref. [248].

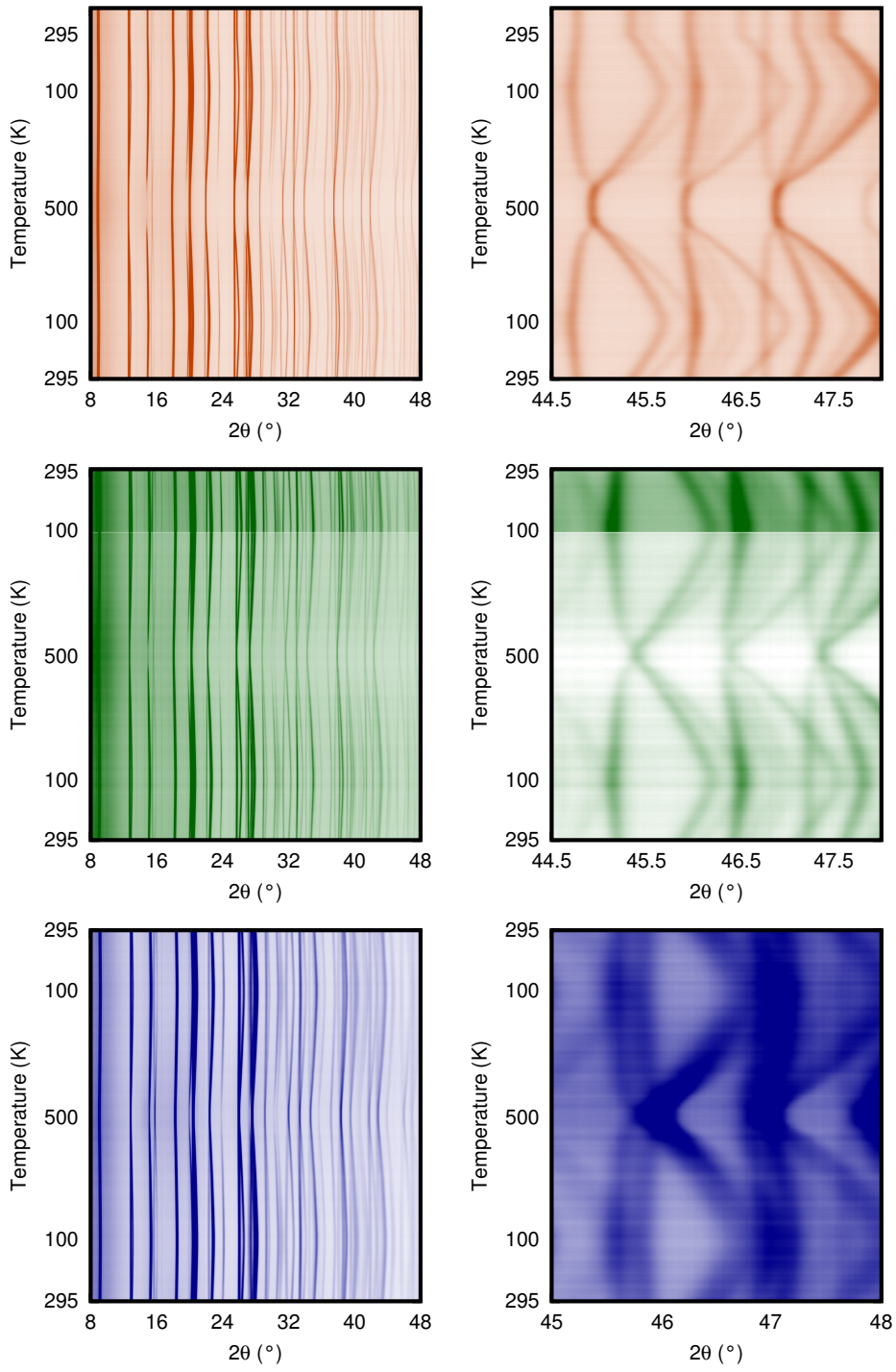

Figure D.3: Variable-temperature (Cryostream, 100-500 K) PXRD data for $Sc_{0.70}Al_{0.30}F_3$ (top), $Sc_{0.60}Al_{0.40}F_3$ (middle), and $Sc_{0.50}Al_{0.50}F_3$ (bottom). The plots in the left column show the full angular range used for Rietveld analysis, while those on the right show a portion of the data. Within each panel, patterns are arranged in order of collection from bottom to top, which followed the temperature ramp in Figure 2.2b. Reproduced from ref. [248].

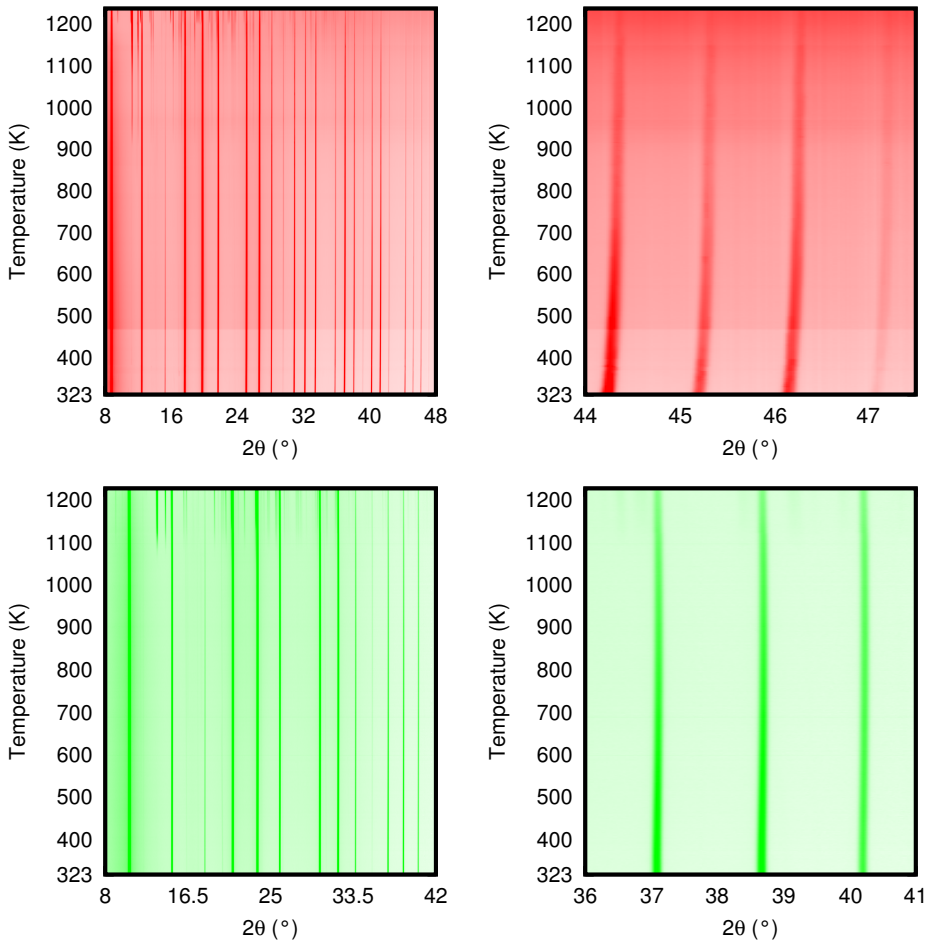

Figure D.4: Variable-temperature (furnace, 300-1200 K) PXRD data for ScF_3 (top) and $Sc_{0.90}Al_{0.10}F_3$ (bottom). The plots in the left column show the full angular range used for Rietveld analysis, while those on the right show a portion of the data. Within each panel, patterns are arranged in order of collection from bottom to top. Reproduced from ref. [248].

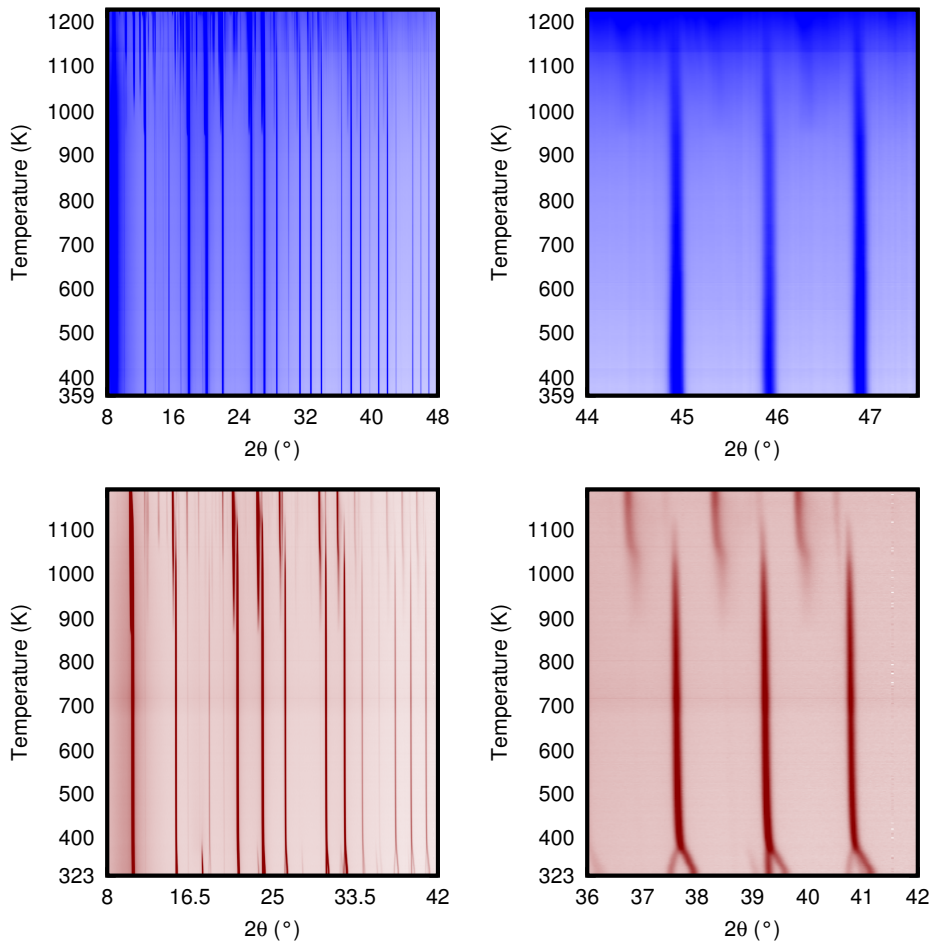

Figure D.5: Variable-temperature (furnace, 300-1200 K) PXRD data for $Sc_{0.85}Al_{0.15}F_3$ (top) and $Sc_{0.75}Al_{0.25}F_3$ (bottom). The plots in the left column show the full angular range used for Rietveld analysis, while those on the right show a portion of the data. Within each panel, patterns are arranged in order of collection from bottom to top. Reproduced from ref. [248].

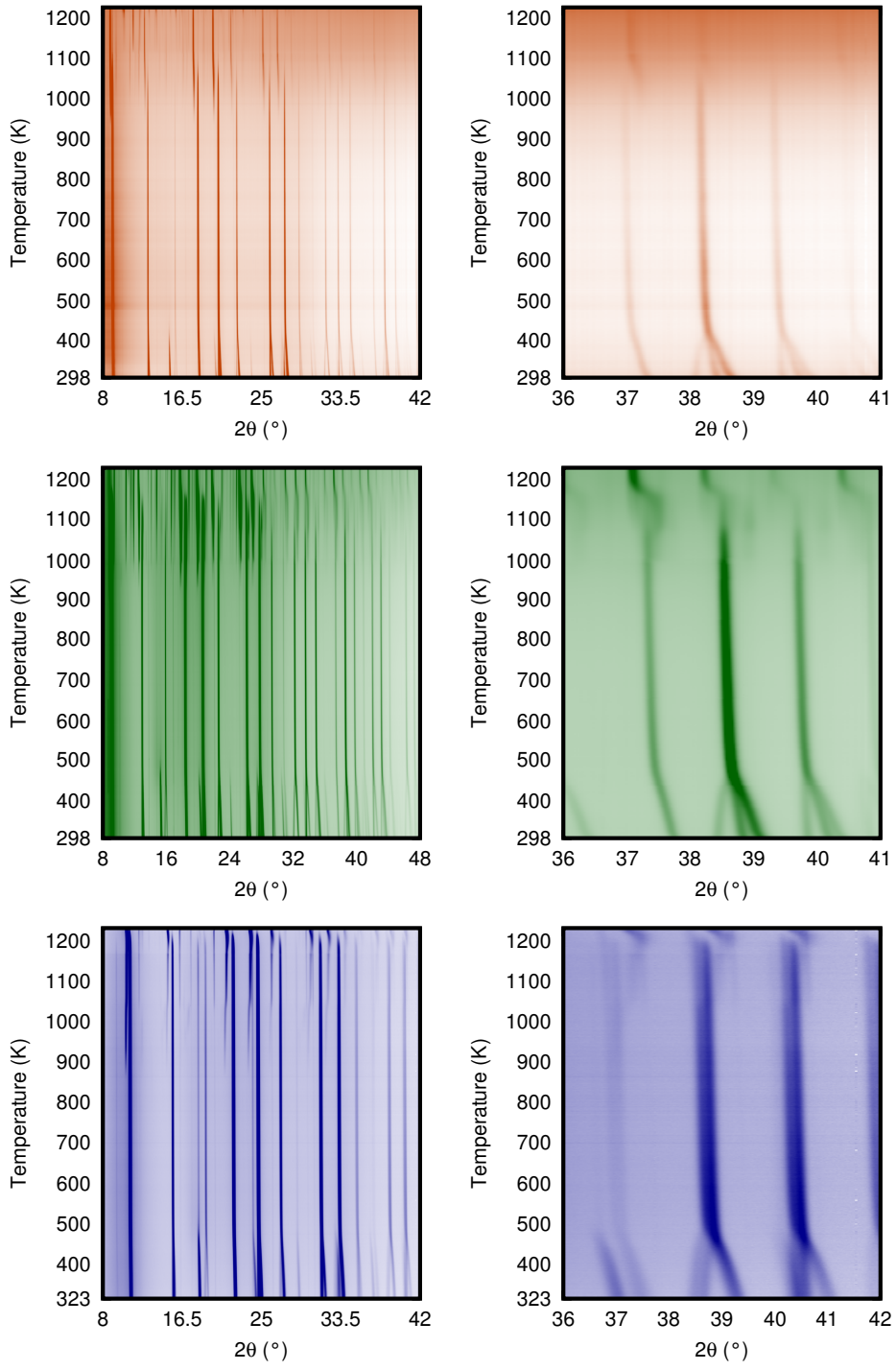

Figure D.6: Variable-temperature (furnace, 300-1200 K) PXRD data for $Sc_{0.70}Al_{0.30}F_3$ (top), $Sc_{0.60}Al_{0.40}F_3$ (middle), and $Sc_{0.50}Al_{0.50}F_3$ (bottom). The plots in the left column show the full angular range used for Rietveld analysis, while those on the right show a portion of the data. Within each panel, patterns are arranged in order of collection from bottom to top. Reproduced from ref. [248].

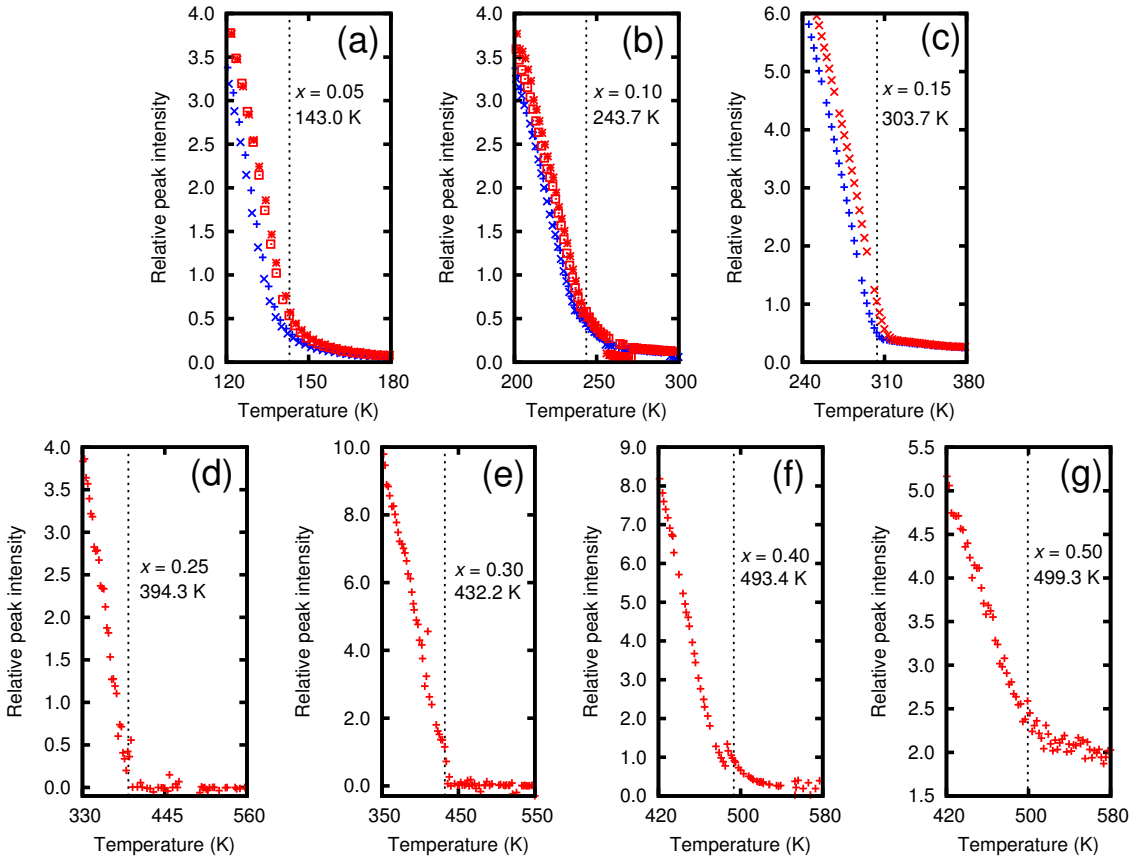

Figure D.7: Temperature dependence of rhombohedral (2 1 0) peak intensity in variable-temperature powder X-ray diffraction patterns for $Sc_{1-x}Al_xF_3$, used for estimation of phase transition temperature. The intensity in panel (g) does not drop to zero at the transition temperature, indicating the presence of residual scattering, perhaps from an impurity. Reproduced from ref. [248].

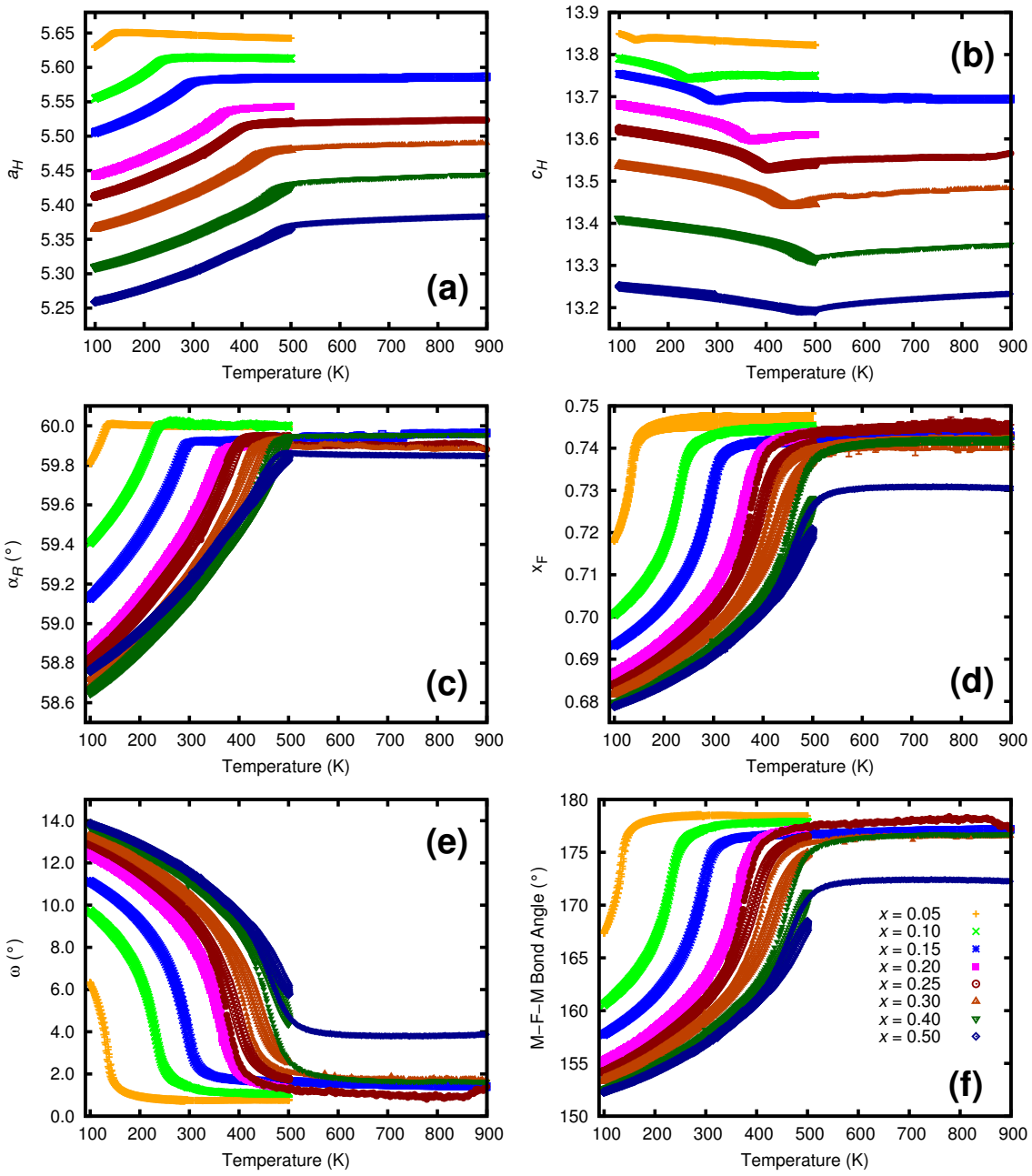

Figure D.8: Temperature dependence of various unit cell parameters for $Sc_{1-x}Al_xF_3$: hexagonal unit cell lengths (a) a_H and (b) c_H, (c) rhombohedral unit cell angle α_R, (d) fractional x-coordinate of F in the rhombohedral cell, (e) octahedral tilt angle ω, and (f) M–F–M bond angle (M = Sc, Al). Data from both furnace and Cryostream measurements are shown. The reported values come from refinements using a rhombohedral model, even at temperatures where the samples were cubic. It is unclear why the values for the x = 0.50 sample deviate significantly at high temperatures from what would be expected for a cubic structure. The non-ideal values of x_F for samples that are cubic (x_F = 0.75 is the ideal value) presumably contain a contribution from the static disorder. Reproduced from ref. [248].

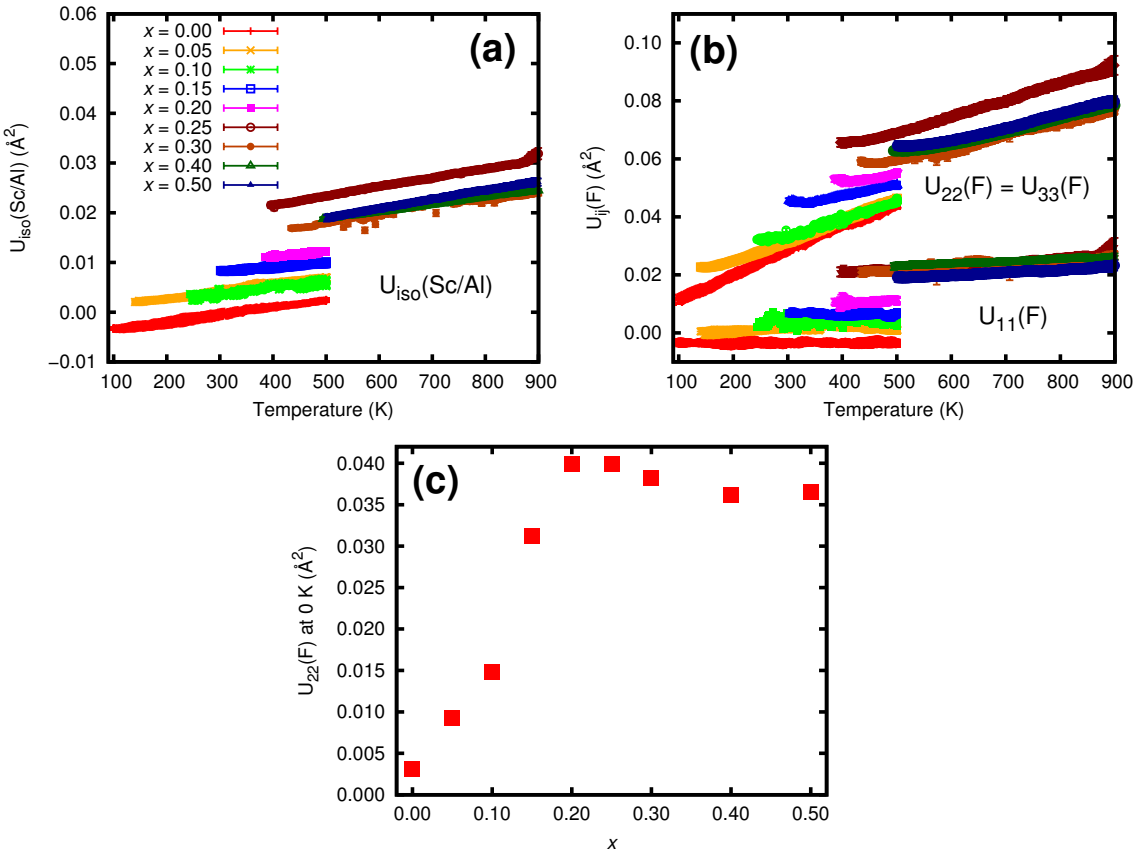

Figure D.9: Atomic displacement parameters for $Sc_{1-x}Al_xF_3$, determined by Rietveld analyses of variable-temperature PXRD data using a cubic structural model. Values are only shown for the temperature ranges where the samples are cubic. In cases where no values are shown above 500 K, the reported results come from the analysis of Cryostream data; in cases where values are shown above 500 K, the reported results come from furnace experiments. Panel (a) shows U_{iso} of Sc and Al, which were constrained to be equal, while panel (b) shows U_{ij} of F. The estimated value of U_{22} at 0 K for each sample was extrapolated from (b) and plotted in (c). The values from the Cryostream and furnace measurements are affected by absorption to differing extents, complicating a comparison of the values from these two sources. However, increasing the amount of Al^{3+} in the solid solutions leads to an initial increase in the 0 K extrapolated values of U_{22}, suggesting the presence of increasing amounts of static disorder. Reproduced from ref. [248].

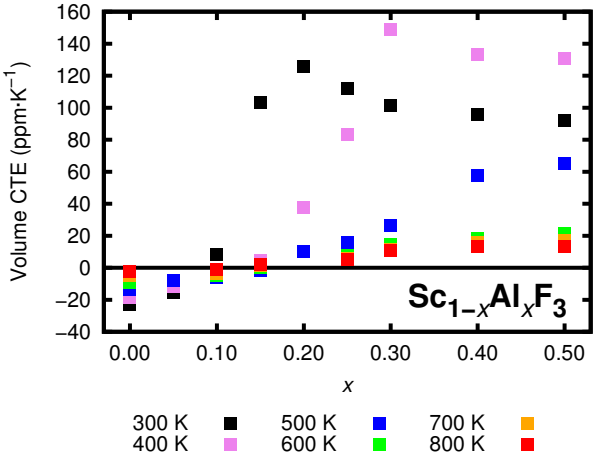

Figure D.10: Composition dependence of volume CTE for $Sc_{1-x}Al_xF_3$ at 300, 400, 500, 600, 700, and 800 K. The CTEs for pure ScF_3 ($x = 0.00$) for temperatures $\leq$500 K are also found in Figure 6.8. Reproduced from ref. [248].

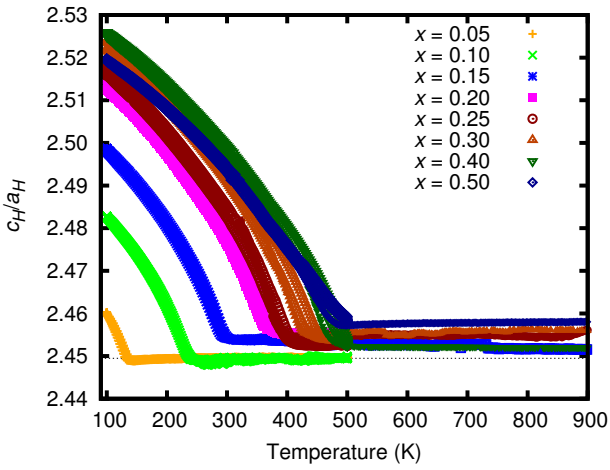

Figure D.11: Temperature dependence of the ratio of hexagonal lattice parameters c_H and a_H for each $Sc_{1-x}Al_xF_3$ sample, each of which was extracted from Rietveld analyses of variable-temperature PXRD data. The expected value of c_H/a_H above the rhombohedral-to-cubic phase transition is $\sqrt{6} = 2.449$. Reproduced from ref. [248].

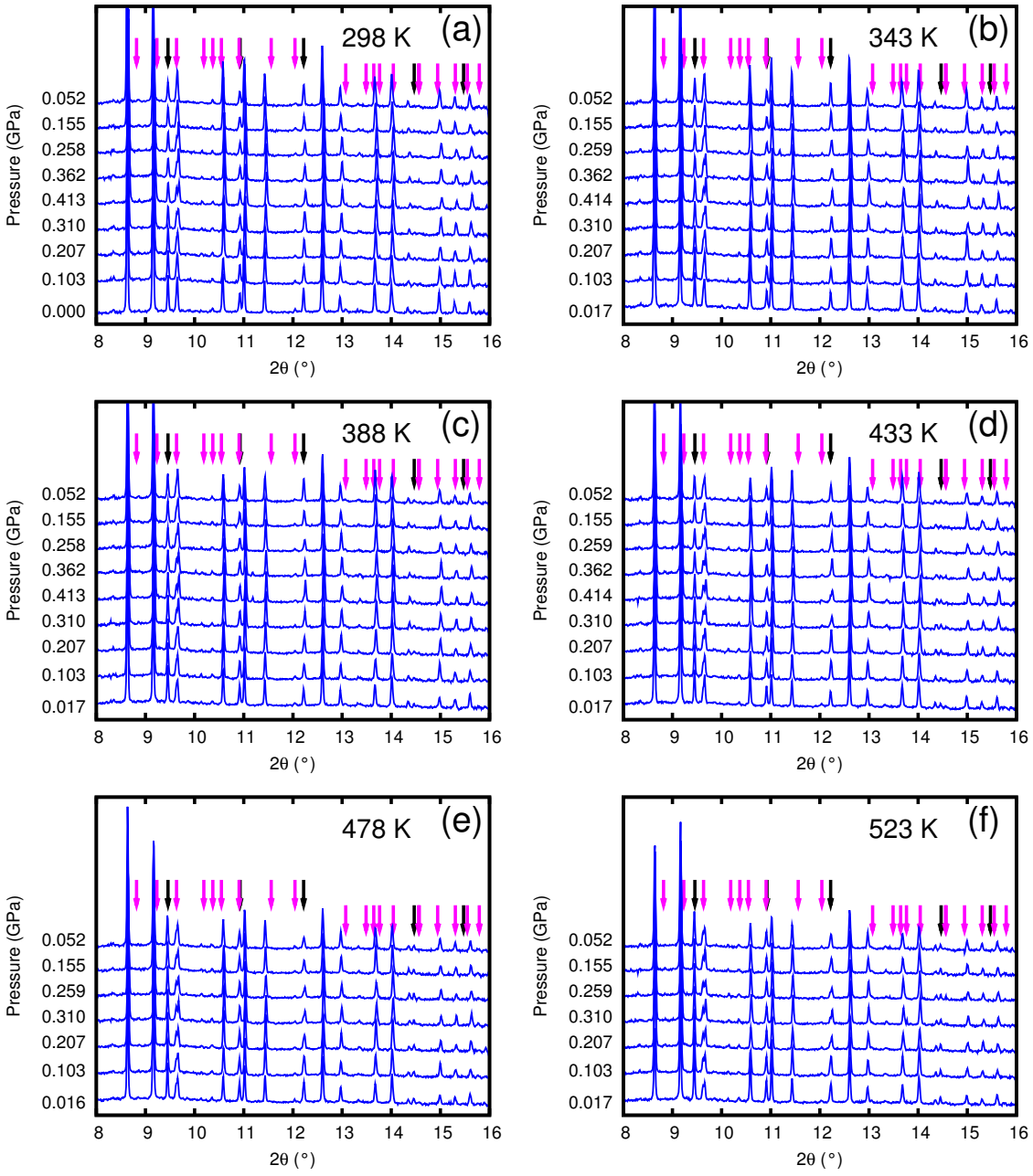

Figure D.12: Variable-pressure/temperature PXRD data for $Sc_{0.95}Al_{0.05}F_3$. Each panel represents a particular temperature, and the patterns within each panel were collected at different pressures, arranged in order of collection from bottom to top. A cubic model was fit to all patterns. Peaks from the tungsten BRIM body and rhenium blade are marked by black and magenta arrows, respectively. Reproduced from ref. [248].

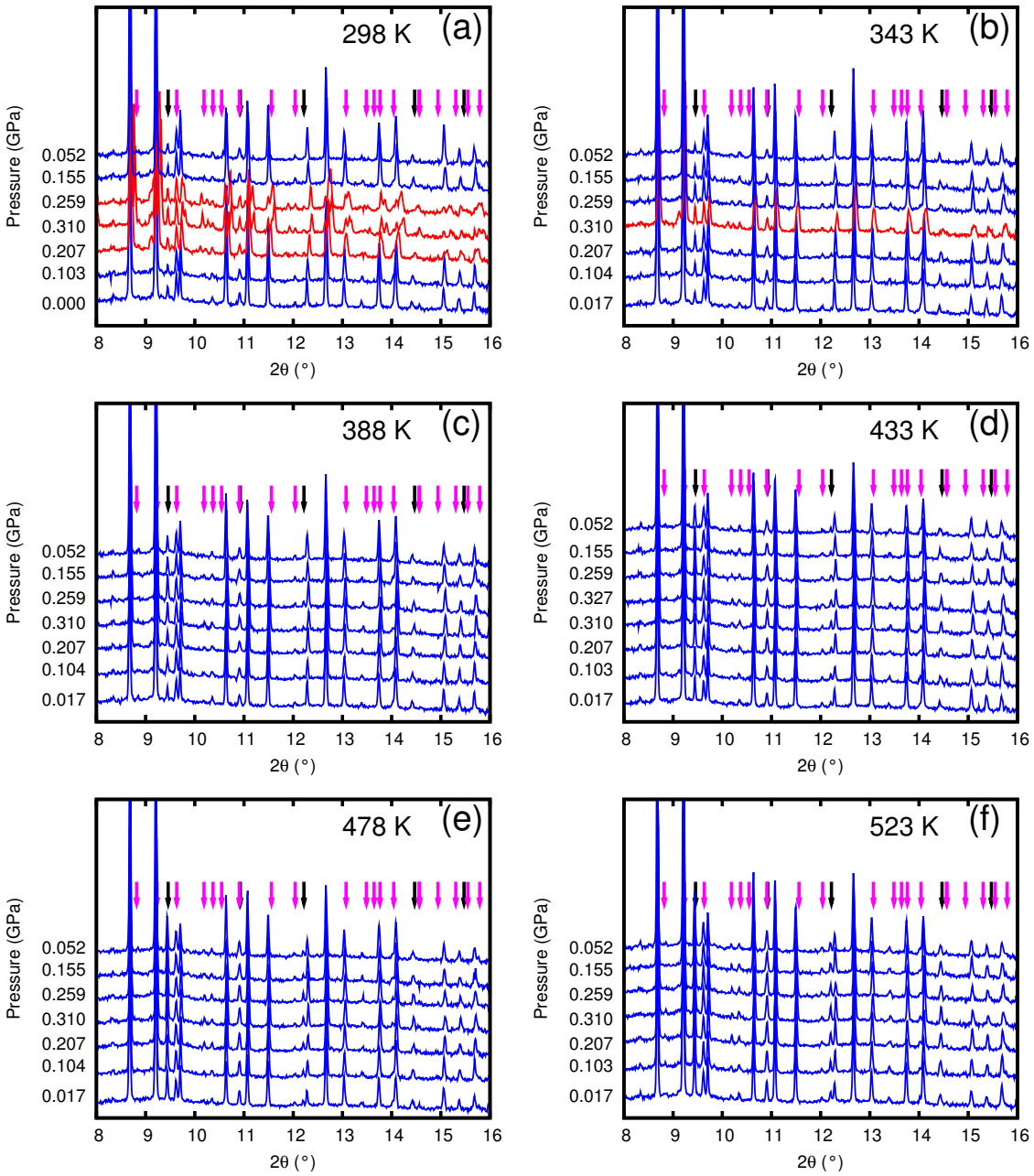

Figure D.13: Variable-pressure/temperature PXRD data for $Sc_{0.90}Al_{0.10}F_3$. Each panel represents a particular temperature, and the patterns within each panel were collected at different pressures, arranged in order of collection from bottom to top. A cubic model was fit to blue patterns, while a rhombohedral model was fit to red ones. Peaks from the tungsten BRIM body and rhenium blade are marked by black and magenta arrows, respectively. Reproduced from ref. [248].

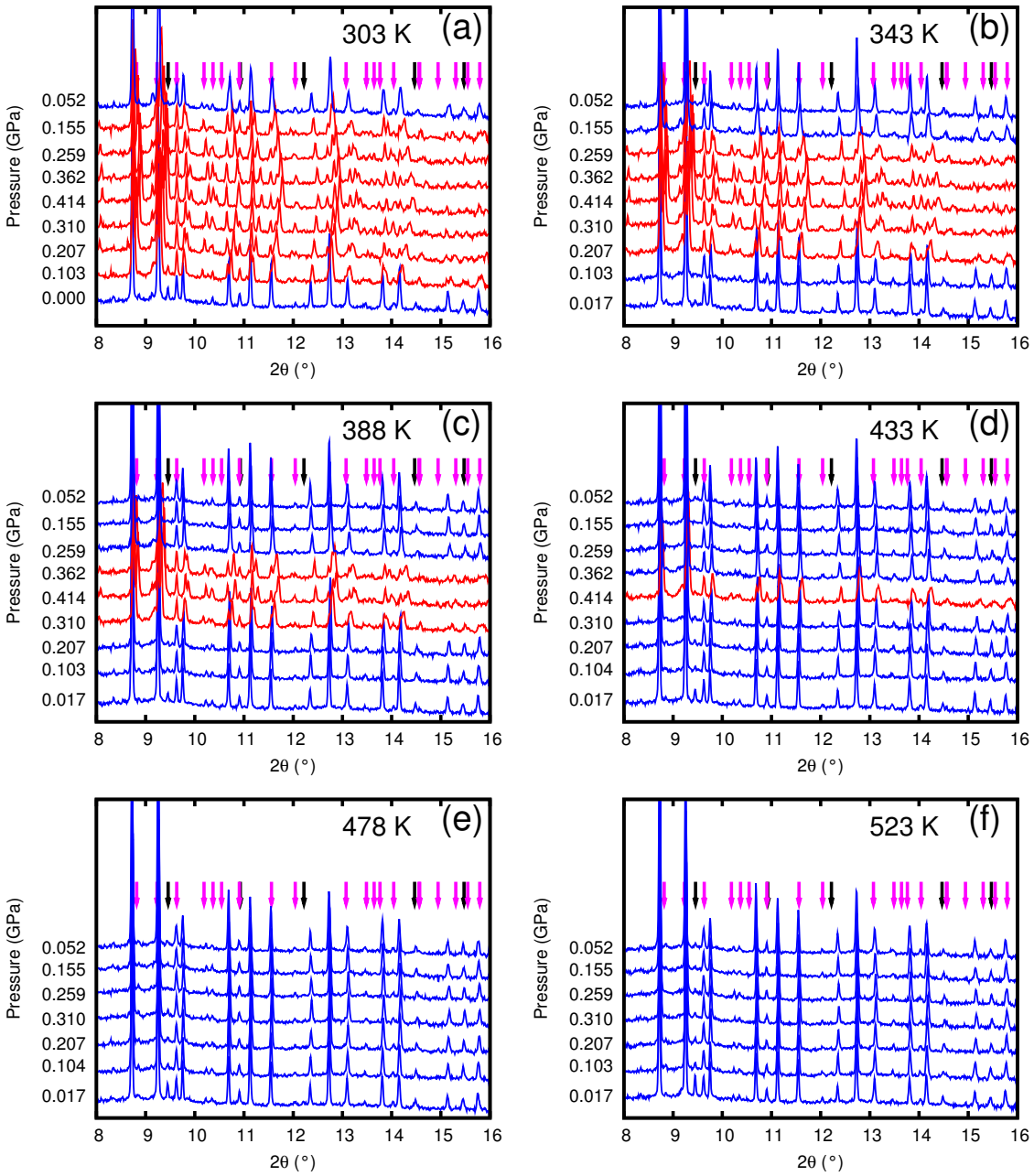

Figure D.14: Variable-pressure/temperature PXRD data for $Sc_{0.85}Al_{0.15}F_3$. Each panel represents a particular temperature, and the patterns within each panel were collected at different pressures, arranged in order of collection from bottom to top. A cubic model was fit to blue patterns, while a rhombohedral model was fit to red ones. Peaks from the tungsten BRIM body and rhenium blade are marked by black and magenta arrows, respectively. Reproduced from ref. [248].

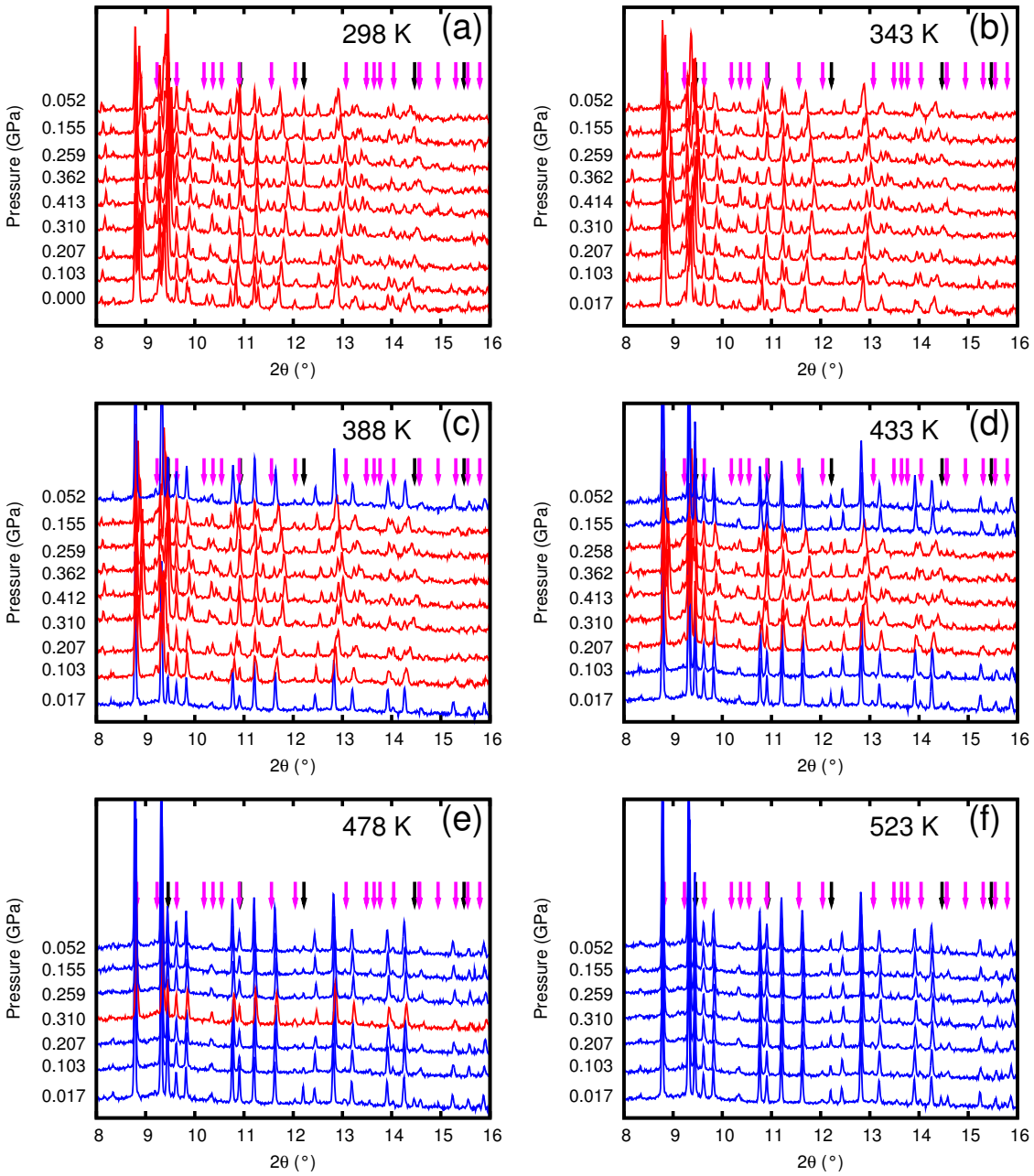

Figure D.15: Variable-pressure/temperature PXRD data for $Sc_{0.80}Al_{0.20}F_3$. Each panel represents a particular temperature, and the patterns within each panel were collected at different pressures, arranged in order of collection from bottom to top. A cubic model was fit to blue patterns, while a rhombohedral model was fit to red ones. Peaks from the tungsten BRIM body and rhenium blade are marked by black and magenta arrows, respectively. Reproduced from ref. [248].

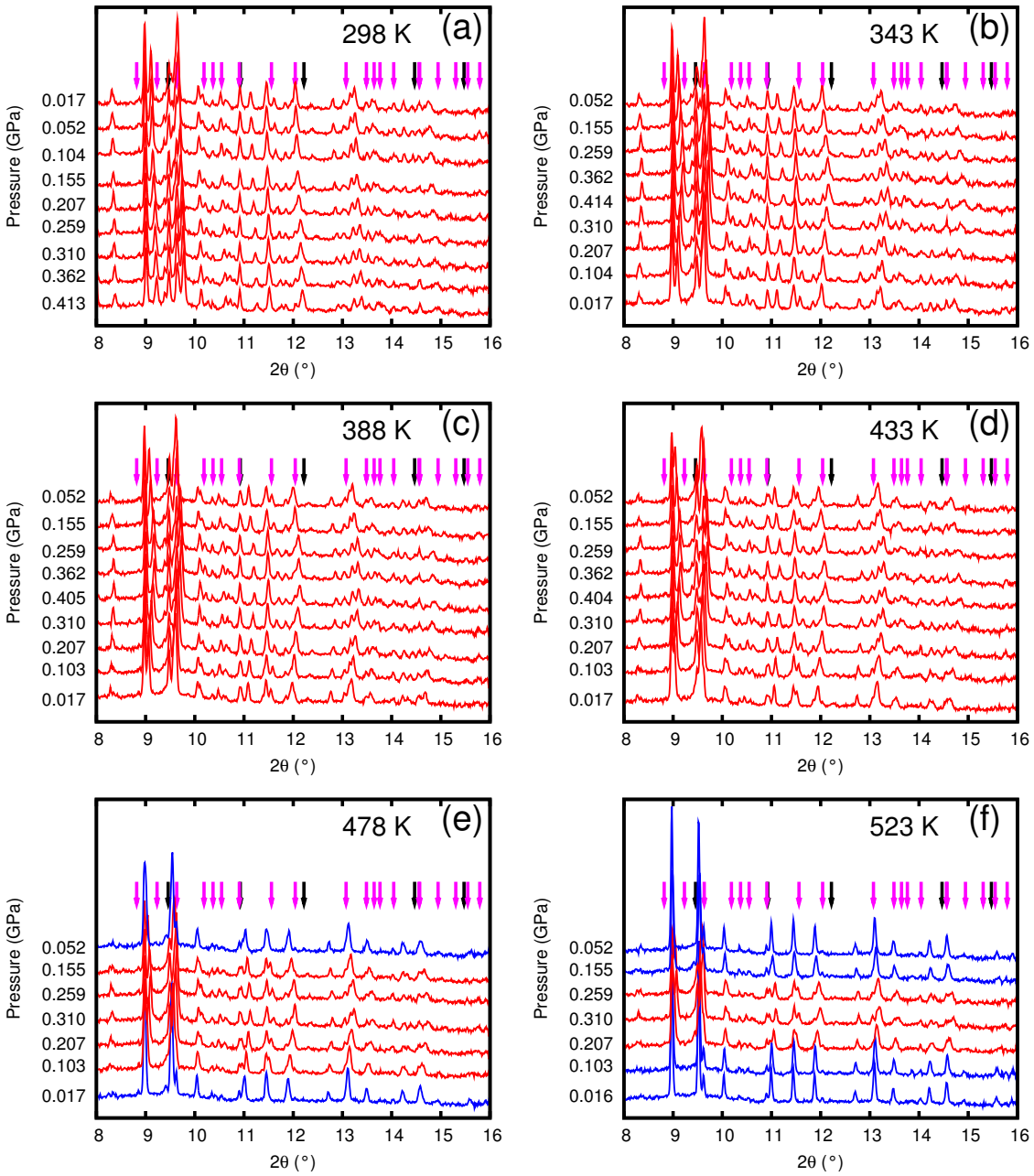

Figure D.16: Variable-pressure/temperature PXRD data for $Sc_{0.60}Al_{0.40}F_3$. Each panel represents a particular temperature, and the patterns within each panel were collected at different pressures, arranged in order of collection from bottom to top. A cubic model was fit to blue patterns, while a rhombohedral model was fit to red ones. Peaks from the tungsten BRIM body and rhenium blade are marked by black and magenta arrows, respectively. Reproduced from ref. [248].

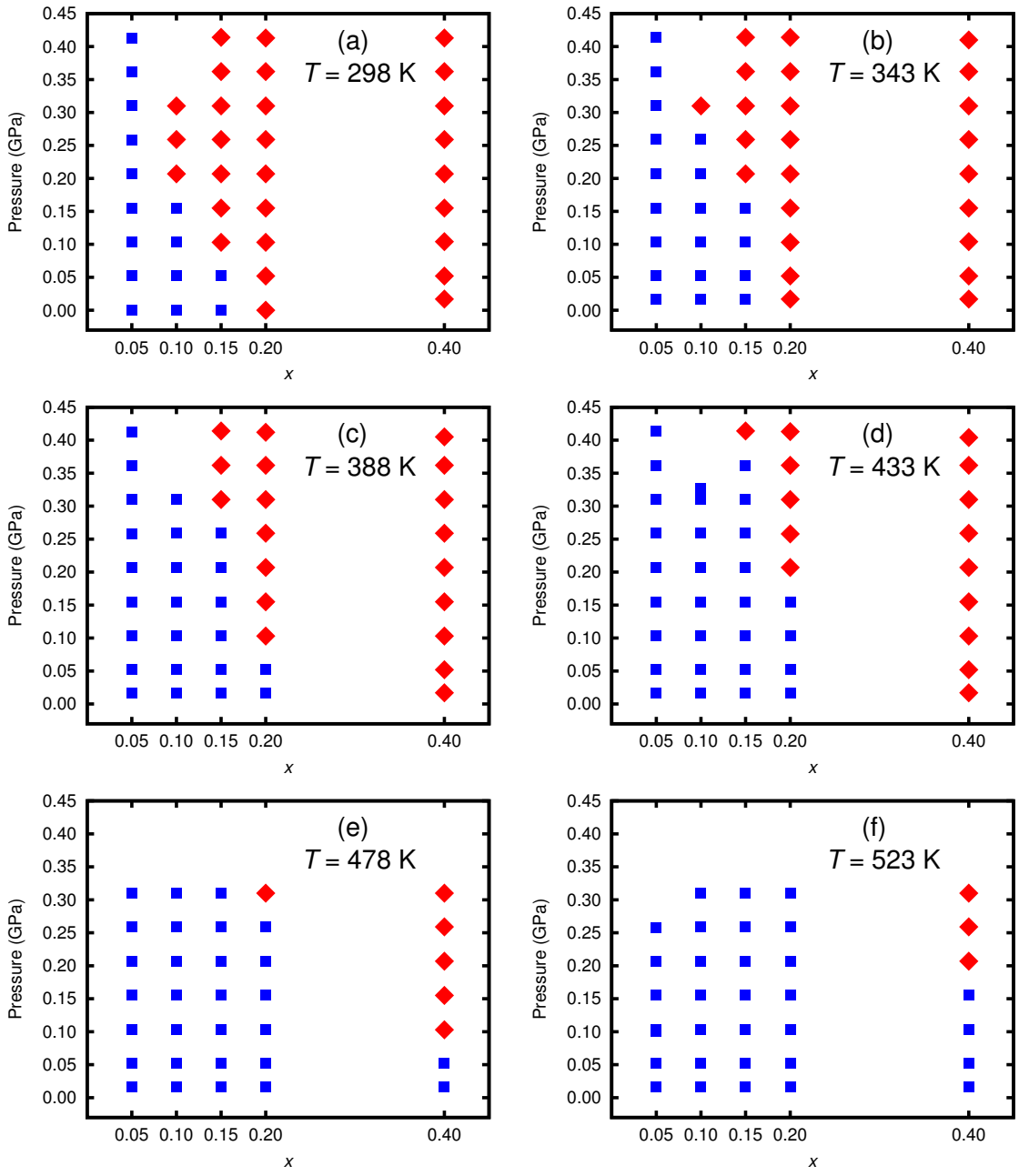

Figure D.17: Pressure-composition phase diagrams at constant temperature for $Sc_{1-x}Al_xF_3$. Blue squares (red diamonds) indicate that the structure of the material is cubic (rhombohedral) at the specified conditions. Reproduced from ref. [248].

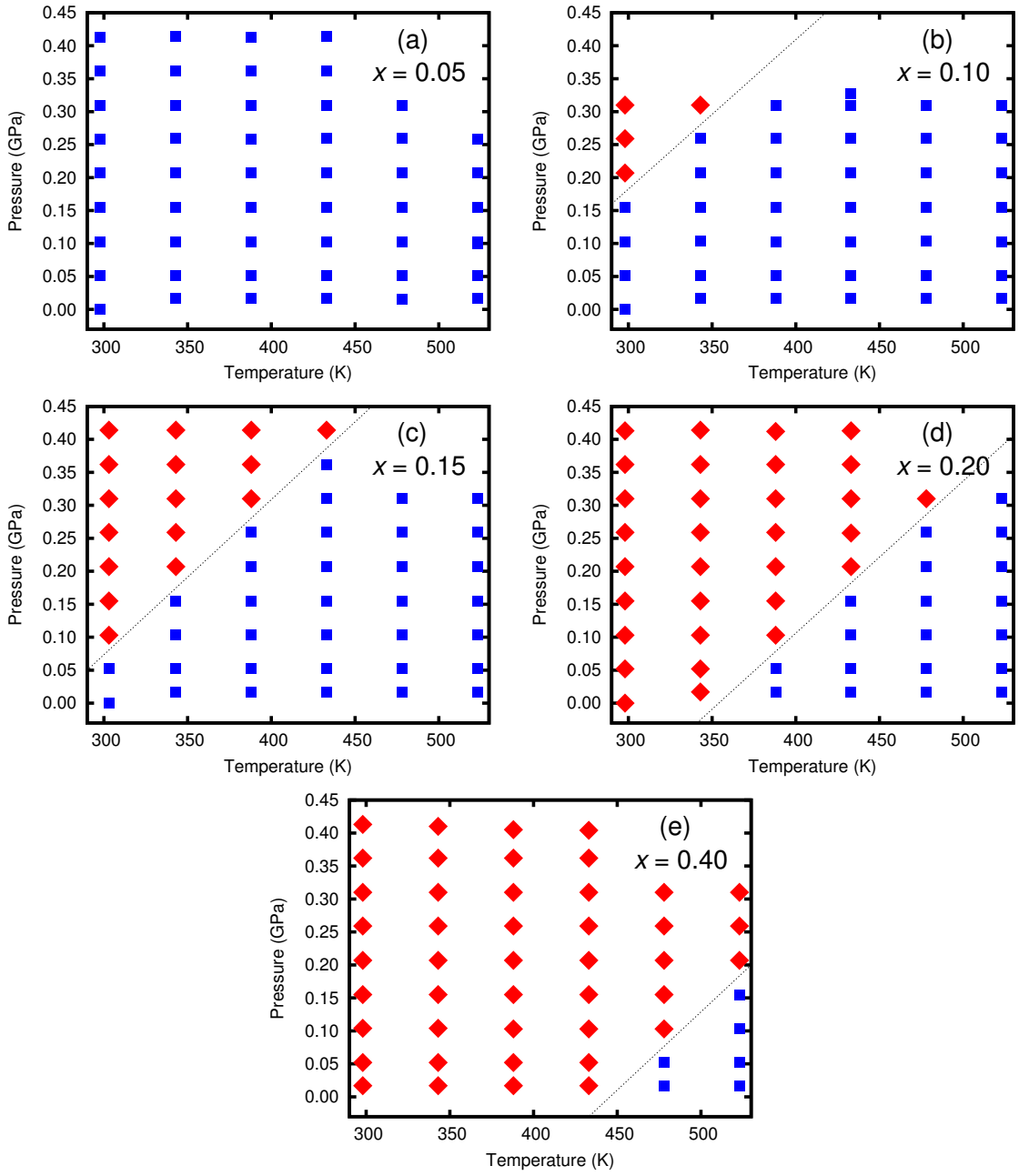

Figure D.18: Pressure-temperature phase diagrams for various $Sc_{1-x}Al_xF_3$ compositions. Blue squares (red diamonds) indicate that the structure of the material is cubic (rhombohedral) at the specified conditions. Dashed lines indicate estimated phase boundaries. Reproduced from ref. [248].

APPENDIX E

CHAPTER 9 SUPPORTING MATERIAL

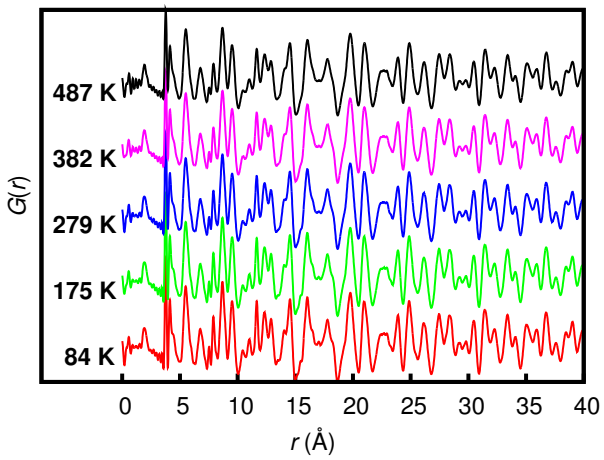

Figure E.1: Pair distribution functions $G(r)$ of TaO_2F, calculated from X-ray total scattering data collected at selected temperatures. The high-r portion changes little with temperature due to the very high level of static disorder that is present even at low temperatures. Reproduced from ref. [218].

E.1 Peak fitting to variable-temperature pair distribution functions

Peak fitting to the variable-temperature pair distribution functions (PDFs) was accomplished using *Fityk* [273]. A linear background and a total of seven Gaussian functions were fit to each PDF; these fits used a fixed r range of 1.5 to 4.6 Å. The eight functions below were used in the fit, which first refined functions 1, 2, and 3; the other functions were refined subsequently:

1. Linear background with negative slope and y-intercept of zero;
2. Ta–O correlation peak = Gaussian centered ∼1.856 Å, constrained to have the same width as Peak 3 but twice its height;
3. Ta–F correlation peak = Gaussian centered ∼2.056 Å, constrained to have the same width as Peak 2 but half its height;

4. Ta–(O)–Ta correlation peak = Gaussian centered ∼3.766 Å, constrained to have the same width as Peak 5 but twice its height;

5. Ta–(F)–Ta correlation peak = Gaussian centered ∼4.112 Å, constrained to have the same width as Peak 4 but half its height;

6. Shoulder from next-nearest-neighbor Ta–(O/F) correlations = Gaussian centered ∼4.303 Å, constrained to have the same width as Peak 7;

7. Shoulder from next-nearest-neighbor Ta–(O/F) correlations = Gaussian centered ∼4.503 Å, constrained to have the same width as Peak 6;

8. Broad peak to model ripples between Peaks 3 and 4 = Gaussian of fixed center (2.7 Å) and width (FWHM = 0.8 Å) but refined height.

E.2 Supercell model for the local structure of TaO_2F

The necessary parameters for constructing the supercell model are summarized in Table E.1. The lattice constant of the average structure for TaO_2F was determined as a function of temperature using *PDFgui* [272], and the temperature-averaged lattice constant a (80-487 K) was used for supercell construction. The unit cell dimension for the supercell is simply $3a$. As described above, peak fitting with *Fityk* [273] to the variable-temperature PDFs yielded temperature-averaged values for Ta–X and Ta–(X)–Ta separations (80-487 K), and from those values, the average displacements δ_O and δ_F of the anions perpendicular to the Ta$\cdots$Ta bond axis were calculated using geometry. The displacements of atoms along one-dimensional chains were calculated using the displacement factor σ, equal to the difference between a and the Ta–(O)–Ta separation. For construction of the supercell, the displacement factors were converted to fractions of $3a$, as summarized in Table E.1. The fractional coordinates of the atoms in the final supercell model are given in Table E.2, and a view of the structure is given in Figure E.2.

As *PDFgui* does not allow for partial occupancies, the 25% site-occupied O/F were modeled as 100% site-occupied helium atoms. Also, Ta and He were assigned separate U_{xx} parameters for the refinement, with the helium atoms representing oxygen having a different

U parameter than those representing fluorine. This model was used for the fits shown in parts c and d of Figure 9.1.

During the fits of the supercell model to the PDF, the unit cell constant, scale factor, low-r peak sharpening factor (*sratio*), resolution damping factor (*Qdamp*), and isotropic atomic displacement parameters (U_{xx}) for each atom type (Ta, He representing O, and He representing F) were refined.

Table E.1: Parameters used to construct the supercell model for the local structure of TaO_2F (derived from variable-temperature PDFs).

Parameter	**Length (Å)**	**Fraction of supercell lattice constant (3a)**
a	3.884	—
$3a$	11.65	—
Ta–O–Ta	3.773	—
$\sigma = a-$ (Ta–O–Ta)	0.111	0.01
δ_F	0.45	0.039
δ_O	0.13	0.011

Table E.2: Fractional coordinates and site occupancies of the atoms in the TaO_2F supercell model.

Atom #	**Atom type**	x	y	z	**Site occupancy**
1	Ta	0	0	0	1
2	Ta	0	0	0.32381	1
3	Ta	0	0	0.64761	1
4	Ta	0	0.32381	0	1
5	Ta	0	0.35239	0.32381	1
6	Ta	0	0.32381	0.67619	1
7	Ta	0	0.67619	0	1
8	Ta	0	0.67619	0.35239	1
9	Ta	0	0.64761	0.67619	1
10	Ta	0.35239	0	0	1

Table E.2: *Continued on next page*

Table E.2: *Continued from previous page*

Atom #	**Atom type**	x	y	z	**Site occupancy**
11	Ta	0.32381	0	0.32381	1
12	Ta	0.32381	0	0.64761	1
13	Ta	0.35239	0.32381	0	1
14	Ta	0.32381	0.35239	0.32381	1
15	Ta	0.32381	0.32381	0.67619	1
16	Ta	0.35239	0.67619	0	1
17	Ta	0.32381	0.67619	0.35239	1
18	Ta	0.32381	0.64761	0.67619	1
19	Ta	0.67619	0	0	1
20	Ta	0.64761	0	0.32381	1
21	Ta	0.67619	0	0.64761	1
22	Ta	0.67619	0.32381	0	1
23	Ta	0.64761	0.35239	0.32381	1
24	Ta	0.67619	0.32381	0.67619	1
25	Ta	0.67619	0.67619	0	1
26	Ta	0.64761	0.67619	0.35239	1
27	Ta	0.67619	0.64761	0.67619	1
28	O	0.01116	0	0.1619	0.25
29	O	0	0.01116	0.1619	0.25
30	O	-0.0112	0	0.1619	0.25
31	O	0	-0.0112	0.1619	0.25
32	O	0.01116	0	0.48571	0.25
33	O	0	0.01116	0.48571	0.25
34	O	-0.0112	0	0.48571	0.25
35	O	0	-0.0112	0.48571	0.25
36	F	0.03862	0	0.82381	0.25

Table E.2: *Continued on next page*

Table E.2: *Continued from previous page*

Atom #	**Atom type**	x	y	z	**Site occupancy**
37	F	0	0.03862	0.82381	0.25
38	F	-0.0386	0	0.82381	0.25
39	F	0	-0.0386	0.82381	0.25
40	O	0.01116	0.3381	0.1619	0.25
41	O	0	0.34925	0.1619	0.25
42	O	-0.0112	0.3381	0.1619	0.25
43	O	0	0.32694	0.1619	0.25
44	F	0.03862	0.3381	0.5	0.25
45	F	0	0.37672	0.5	0.25
46	F	-0.0386	0.3381	0.5	0.25
47	F	0	0.29948	0.5	0.25
48	O	0.01116	0.32381	0.8381	0.25
49	O	0	0.33496	0.8381	0.25
50	O	-0.0112	0.32381	0.8381	0.25
51	O	0	0.31265	0.8381	0.25
52	F	0.03862	0.67619	0.17619	0.25
53	F	0	0.71481	0.17619	0.25
54	F	-0.0386	0.67619	0.17619	0.25
55	F	0	0.63757	0.17619	0.25
56	O	0.01116	0.6619	0.51429	0.25
57	O	0	0.67306	0.51429	0.25
58	O	-0.0112	0.6619	0.51429	0.25
59	O	0	0.65075	0.51429	0.25
60	O	0.01116	0.6619	0.8381	0.25
61	O	0	0.67306	0.8381	0.25
62	O	-0.0112	0.6619	0.8381	0.25

Table E.2: *Continued on next page*

Table E.2: *Continued from previous page*

Atom #	**Atom type**	x	y	z	**Site occupancy**
63	O	0	0.65075	0.8381	0.25
64	O	0.34925	0	0.1619	0.25
65	O	0.3381	0.01116	0.1619	0.25
66	O	0.32694	0	0.1619	0.25
67	O	0.3381	-0.0112	0.1619	0.25
68	O	0.33496	0	0.48571	0.25
69	O	0.32381	0.01116	0.48571	0.25
70	O	0.31265	0	0.48571	0.25
71	O	0.32381	-0.0112	0.48571	0.25
72	F	0.37672	0	0.82381	0.25
73	F	0.3381	0.03862	0.82381	0.25
74	F	0.29948	0	0.82381	0.25
75	F	0.3381	-0.0386	0.82381	0.25
76	O	0.34925	0.3381	0.1619	0.25
77	O	0.3381	0.34925	0.1619	0.25
78	O	0.32694	0.3381	0.1619	0.25
79	O	0.3381	0.32694	0.1619	0.25
80	F	0.36243	0.3381	0.5	0.25
81	F	0.32381	0.37672	0.5	0.25
82	F	0.28519	0.3381	0.5	0.25
83	F	0.32381	0.29948	0.5	0.25
84	O	0.34925	0.32381	0.8381	0.25
85	O	0.3381	0.33496	0.8381	0.25
86	O	0.32694	0.32381	0.8381	0.25
87	O	0.3381	0.31265	0.8381	0.25
88	F	0.37672	0.67619	0.17619	0.25

Table E.2: *Continued on next page*

Table E.2: *Continued from previous page*

Atom #	**Atom type**	x	y	z	**Site occupancy**
89	F	0.3381	0.71481	0.17619	0.25
90	F	0.29948	0.67619	0.17619	0.25
91	F	0.3381	0.63757	0.17619	0.25
92	O	0.33496	0.6619	0.51429	0.25
93	O	0.32381	0.67306	0.51429	0.25
94	O	0.31265	0.6619	0.51429	0.25
95	O	0.32381	0.65075	0.51429	0.25
96	O	0.34925	0.6619	0.8381	0.25
97	O	0.3381	0.67306	0.8381	0.25
98	O	0.32694	0.6619	0.8381	0.25
99	O	0.3381	0.65075	0.8381	0.25
100	O	0.67306	0	0.1619	0.25
101	O	0.6619	0.01116	0.1619	0.25
102	O	0.65075	0	0.1619	0.25
103	O	0.6619	-0.0112	0.1619	0.25
104	O	0.67306	0	0.48571	0.25
105	O	0.6619	0.01116	0.48571	0.25
106	O	0.65075	0	0.48571	0.25
107	O	0.6619	-0.0112	0.48571	0.25
108	F	0.71481	0	0.82381	0.25
109	F	0.67619	0.03862	0.82381	0.25
110	F	0.63757	0	0.82381	0.25
111	F	0.67619	-0.0386	0.82381	0.25
112	O	0.67306	0.3381	0.1619	0.25
113	O	0.6619	0.34925	0.1619	0.25
114	O	0.65075	0.3381	0.1619	0.25

Table E.2: *Continued on next page*

Table E.2: *Continued from previous page*

Atom #	**Atom type**	x	y	z	**Site occupancy**
115	O	0.6619	0.32694	0.1619	0.25
116	F	0.70052	0.3381	0.5	0.25
117	F	0.6619	0.37672	0.5	0.25
118	F	0.62328	0.3381	0.5	0.25
119	F	0.6619	0.29948	0.5	0.25
120	O	0.68735	0.32381	0.8381	0.25
121	O	0.67619	0.33496	0.8381	0.25
122	O	0.66504	0.32381	0.8381	0.25
123	O	0.67619	0.31265	0.8381	0.25
124	F	0.70052	0.67619	0.17619	0.25
125	F	0.6619	0.71481	0.17619	0.25
126	F	0.62328	0.67619	0.17619	0.25
127	F	0.6619	0.63757	0.17619	0.25
128	O	0.67306	0.6619	0.51429	0.25
129	O	0.6619	0.67306	0.51429	0.25
130	O	0.65075	0.6619	0.51429	0.25
131	O	0.6619	0.65075	0.51429	0.25
132	O	0.68735	0.6619	0.8381	0.25
133	O	0.67619	0.67306	0.8381	0.25
134	O	0.66504	0.6619	0.8381	0.25
135	O	0.67619	0.65075	0.8381	0.25
136	O	0.01116	0.1619	0	0.25
137	O	0	0.1619	0.01116	0.25
138	O	-0.0112	0.1619	0	0.25
139	O	0	0.1619	-0.0112	0.25
140	F	0.03862	0.5	0	0.25

Table E.2: *Continued on next page*

Table E.2: *Continued from previous page*

Atom #	**Atom type**	x	y	z	**Site occupancy**
141	F	0	0.5	0.03862	0.25
142	F	-0.0386	0.5	0	0.25
143	F	0	0.5	-0.0386	0.25
144	O	0.01116	0.8381	0	0.25
145	O	0	0.8381	0.01116	0.25
146	O	-0.0112	0.8381	0	0.25
147	O	0	0.8381	-0.0112	0.25
148	F	0.03862	0.17619	0.32381	0.25
149	F	0	0.17619	0.36243	0.25
150	F	-0.0386	0.17619	0.32381	0.25
151	F	0	0.17619	0.28519	0.25
152	O	0.01116	0.51429	0.3381	0.25
153	O	0	0.51429	0.34925	0.25
154	O	-0.0112	0.51429	0.3381	0.25
155	O	0	0.51429	0.32694	0.25
156	O	0.01116	0.8381	0.3381	0.25
157	O	0	0.8381	0.34925	0.25
158	O	-0.0112	0.8381	0.3381	0.25
159	O	0	0.8381	0.32694	0.25
160	O	0.01116	0.1619	0.6619	0.25
161	O	0	0.1619	0.67306	0.25
162	O	-0.0112	0.1619	0.6619	0.25
163	O	0	0.1619	0.65075	0.25
164	O	0.01116	0.48571	0.67619	0.25
165	O	0	0.48571	0.68735	0.25
166	O	-0.0112	0.48571	0.67619	0.25

Table E.2: *Continued on next page*

Table E.2: *Continued from previous page*

Atom #	**Atom type**	x	y	z	**Site occupancy**
167	O	0	0.48571	0.66504	0.25
168	F	0.01116	0.82381	0.6619	0.25
169	F	0	0.82381	0.70052	0.25
170	F	-0.0112	0.82381	0.6619	0.25
171	F	0	0.82381	0.62328	0.25
172	O	0.36354	0.1619	0	0.25
173	O	0.35239	0.1619	0.01116	0.25
174	O	0.34123	0.1619	0	0.25
175	O	0.35239	0.1619	-0.0112	0.25
176	F	0.39101	0.5	0	0.25
177	F	0.35239	0.5	0.03862	0.25
178	F	0.31377	0.5	0	0.25
179	F	0.35239	0.5	-0.0386	0.25
180	O	0.36354	0.8381	0	0.25
181	O	0.35239	0.8381	0.01116	0.25
182	O	0.34123	0.8381	0	0.25
183	O	0.35239	0.8381	-0.0112	0.25
184	F	0.36243	0.17619	0.32381	0.25
185	F	0.32381	0.17619	0.36243	0.25
186	F	0.28519	0.17619	0.32381	0.25
187	F	0.32381	0.17619	0.28519	0.25
188	O	0.33496	0.51429	0.3381	0.25
189	O	0.32381	0.51429	0.34925	0.25
190	O	0.31265	0.51429	0.3381	0.25
191	O	0.32381	0.51429	0.32694	0.25
192	O	0.33496	0.8381	0.3381	0.25

Table E.2: *Continued on next page*

Table E.2: *Continued from previous page*

Atom #	**Atom type**	x	y	z	**Site occupancy**
193	O	0.32381	0.8381	0.34925	0.25
194	O	0.31265	0.8381	0.3381	0.25
195	O	0.32381	0.8381	0.32694	0.25
196	O	0.33496	0.1619	0.6619	0.25
197	O	0.32381	0.1619	0.67306	0.25
198	O	0.31265	0.1619	0.6619	0.25
199	O	0.32381	0.1619	0.65075	0.25
200	O	0.33496	0.48571	0.67619	0.25
201	O	0.32381	0.48571	0.68735	0.25
202	O	0.31265	0.48571	0.67619	0.25
203	O	0.32381	0.48571	0.66504	0.25
204	F	0.36243	0.82381	0.6619	0.25
205	F	0.32381	0.82381	0.70052	0.25
206	F	0.28519	0.82381	0.6619	0.25
207	F	0.32381	0.82381	0.62328	0.25
208	O	0.68735	0.1619	0	0.25
209	O	0.67619	0.1619	0.01116	0.25
210	O	0.66504	0.1619	0	0.25
211	O	0.67619	0.1619	-0.0112	0.25
212	F	0.71481	0.5	0	0.25
213	F	0.67619	0.5	0.03862	0.25
214	F	0.63757	0.5	0	0.25
215	F	0.67619	0.5	-0.0386	0.25
216	O	0.68735	0.8381	0	0.25
217	O	0.67619	0.8381	0.01116	0.25
218	O	0.66504	0.8381	0	0.25

Table E.2: *Continued on next page*

Table E.2: *Continued from previous page*

Atom #	**Atom type**	x	y	z	**Site occupancy**
219	O	0.67619	0.8381	-0.0112	0.25
220	F	0.68623	0.17619	0.32381	0.25
221	F	0.64761	0.17619	0.36243	0.25
222	F	0.60899	0.17619	0.32381	0.25
223	F	0.64761	0.17619	0.28519	0.25
224	O	0.65877	0.51429	0.3381	0.25
225	O	0.64761	0.51429	0.34925	0.25
226	O	0.63646	0.51429	0.3381	0.25
227	O	0.64761	0.51429	0.32694	0.25
228	O	0.65877	0.8381	0.3381	0.25
229	O	0.64761	0.8381	0.34925	0.25
230	O	0.63646	0.8381	0.3381	0.25
231	O	0.64761	0.8381	0.32694	0.25
232	O	0.68735	0.1619	0.6619	0.25
233	O	0.67619	0.1619	0.67306	0.25
234	O	0.66504	0.1619	0.6619	0.25
235	O	0.67619	0.1619	0.65075	0.25
236	O	0.68735	0.48571	0.67619	0.25
237	O	0.67619	0.48571	0.68735	0.25
238	O	0.66504	0.48571	0.67619	0.25
239	O	0.67619	0.48571	0.66504	0.25
240	F	0.71481	0.82381	0.6619	0.25
241	F	0.67619	0.82381	0.70052	0.25
242	F	0.63757	0.82381	0.6619	0.25
243	F	0.67619	0.82381	0.62328	0.25
244	F	0.17619	0.03862	0	0.25

Table E.2: *Continued on next page*

Table E.2: *Continued from previous page*

Atom #	**Atom type**	x	y	z	**Site occupancy**
245	F	0.17619	0	0.03862	0.25
246	F	0.17619	-0.0386	0	0.25
247	F	0.17619	0	-0.0386	0.25
248	O	0.51429	0.01116	0	0.25
249	O	0.51429	0	0.01116	0.25
250	O	0.51429	-0.0112	0	0.25
251	O	0.51429	0	-0.0112	0.25
252	O	0.8381	0.01116	0	0.25
253	O	0.8381	0	0.01116	0.25
254	O	0.8381	-0.0112	0	0.25
255	O	0.8381	0	-0.0112	0.25
256	O	0.1619	0.01116	0.32381	0.25
257	O	0.1619	0	0.33496	0.25
258	O	0.1619	-0.0112	0.32381	0.25
259	O	0.1619	0	0.31265	0.25
260	O	0.48571	0.01116	0.32381	0.25
261	O	0.48571	0	0.33496	0.25
262	O	0.48571	-0.0112	0.32381	0.25
263	O	0.48571	0	0.31265	0.25
264	F	0.82381	0.03862	0.32381	0.25
265	F	0.82381	0	0.36243	0.25
266	F	0.82381	-0.0386	0.32381	0.25
267	F	0.82381	0	0.28519	0.25
268	O	0.1619	0.01116	0.64761	0.25
269	O	0.1619	0	0.65877	0.25
270	O	0.1619	-0.0112	0.64761	0.25

Table E.2: *Continued on next page*

Table E.2: *Continued from previous page*

Atom #	**Atom type**	x	y	z	**Site occupancy**
271	O	0.1619	0	0.63646	0.25
272	F	0.5	0.03862	0.64761	0.25
273	F	0.5	0	0.68623	0.25
274	F	0.5	-0.0386	0.64761	0.25
275	F	0.5	0	0.60899	0.25
276	O	0.8381	0.01116	0.64761	0.25
277	O	0.8381	0	0.65877	0.25
278	O	0.8381	-0.0112	0.64761	0.25
279	O	0.8381	0	0.63646	0.25
280	F	0.17619	0.36243	0	0.25
281	F	0.17619	0.32381	0.03862	0.25
282	F	0.17619	0.28519	0	0.25
283	F	0.17619	0.32381	-0.0386	0.25
284	O	0.51429	0.33496	0	0.25
285	O	0.51429	0.32381	0.01116	0.25
286	O	0.51429	0.31265	0	0.25
287	O	0.51429	0.32381	-0.0112	0.25
288	O	0.8381	0.33496	0	0.25
289	O	0.8381	0.32381	0.01116	0.25
290	O	0.8381	0.31265	0	0.25
291	O	0.8381	0.32381	-0.0112	0.25
292	O	0.1619	0.36354	0.32381	0.25
293	O	0.1619	0.35239	0.33496	0.25
294	O	0.1619	0.34123	0.32381	0.25
295	O	0.1619	0.35239	0.31265	0.25
296	O	0.48571	0.36354	0.32381	0.25

Table E.2: *Continued on next page*

Table E.2: *Continued from previous page*

Atom #	**Atom type**	x	y	z	**Site occupancy**
297	O	0.48571	0.35239	0.33496	0.25
298	O	0.48571	0.34123	0.32381	0.25
299	O	0.48571	0.35239	0.31265	0.25
300	F	0.82381	0.39101	0.32381	0.25
301	F	0.82381	0.35239	0.36243	0.25
302	F	0.82381	0.31377	0.32381	0.25
303	F	0.82381	0.35239	0.28519	0.25
304	O	0.1619	0.33496	0.67619	0.25
305	O	0.1619	0.32381	0.68735	0.25
306	O	0.1619	0.31265	0.67619	0.25
307	O	0.1619	0.32381	0.66504	0.25
308	F	0.5	0.36243	0.67619	0.25
309	F	0.5	0.32381	0.71481	0.25
310	F	0.5	0.28519	0.67619	0.25
311	F	0.5	0.32381	0.63757	0.25
312	O	0.8381	0.33496	0.67619	0.25
313	O	0.8381	0.32381	0.68735	0.25
314	O	0.8381	0.31265	0.67619	0.25
315	O	0.8381	0.32381	0.66504	0.25
316	F	0.17619	0.71481	0	0.25
317	F	0.17619	0.67619	0.03862	0.25
318	F	0.17619	0.63757	0	0.25
319	F	0.17619	0.67619	-0.0386	0.25
320	O	0.51429	0.68735	0	0.25
321	O	0.51429	0.67619	0.01116	0.25
322	O	0.51429	0.66504	0	0.25

Table E.2: *Continued on next page*

Table E.2: *Continued from previous page*

Atom #	**Atom type**	x	y	z	**Site occupancy**
323	O	0.51429	0.67619	-0.0112	0.25
324	O	0.8381	0.68735	0	0.25
325	O	0.8381	0.67619	0.01116	0.25
326	O	0.8381	0.66504	0	0.25
327	O	0.8381	0.67619	-0.0112	0.25
328	O	0.1619	0.68735	0.35239	0.25
329	O	0.1619	0.67619	0.36354	0.25
330	O	0.1619	0.66504	0.35239	0.25
331	O	0.1619	0.67619	0.34123	0.25
332	O	0.48571	0.68735	0.35239	0.25
333	O	0.48571	0.67619	0.36354	0.25
334	O	0.48571	0.66504	0.35239	0.25
335	O	0.48571	0.67619	0.34123	0.25
336	F	0.82381	0.71481	0.35239	0.25
337	F	0.82381	0.67619	0.39101	0.25
338	F	0.82381	0.63757	0.35239	0.25
339	F	0.82381	0.67619	0.31377	0.25
340	O	0.1619	0.65877	0.67619	0.25
341	O	0.1619	0.64761	0.68735	0.25
342	O	0.1619	0.63646	0.67619	0.25
343	O	0.1619	0.64761	0.66504	0.25
344	F	0.5	0.68623	0.67619	0.25
345	F	0.5	0.64761	0.71481	0.25
346	F	0.5	0.60899	0.67619	0.25
347	F	0.5	0.64761	0.63757	0.25
348	O	0.8381	0.65877	0.67619	0.25

Table E.2: *Continued on next page*

Table E.2: *Continued from previous page*

Atom #	**Atom type**	x	y	z	**Site occupancy**
349	O	0.8381	0.64761	0.68735	0.25
350	O	0.8381	0.63646	0.67619	0.25
351	O	0.8381	0.64761	0.66504	0.25

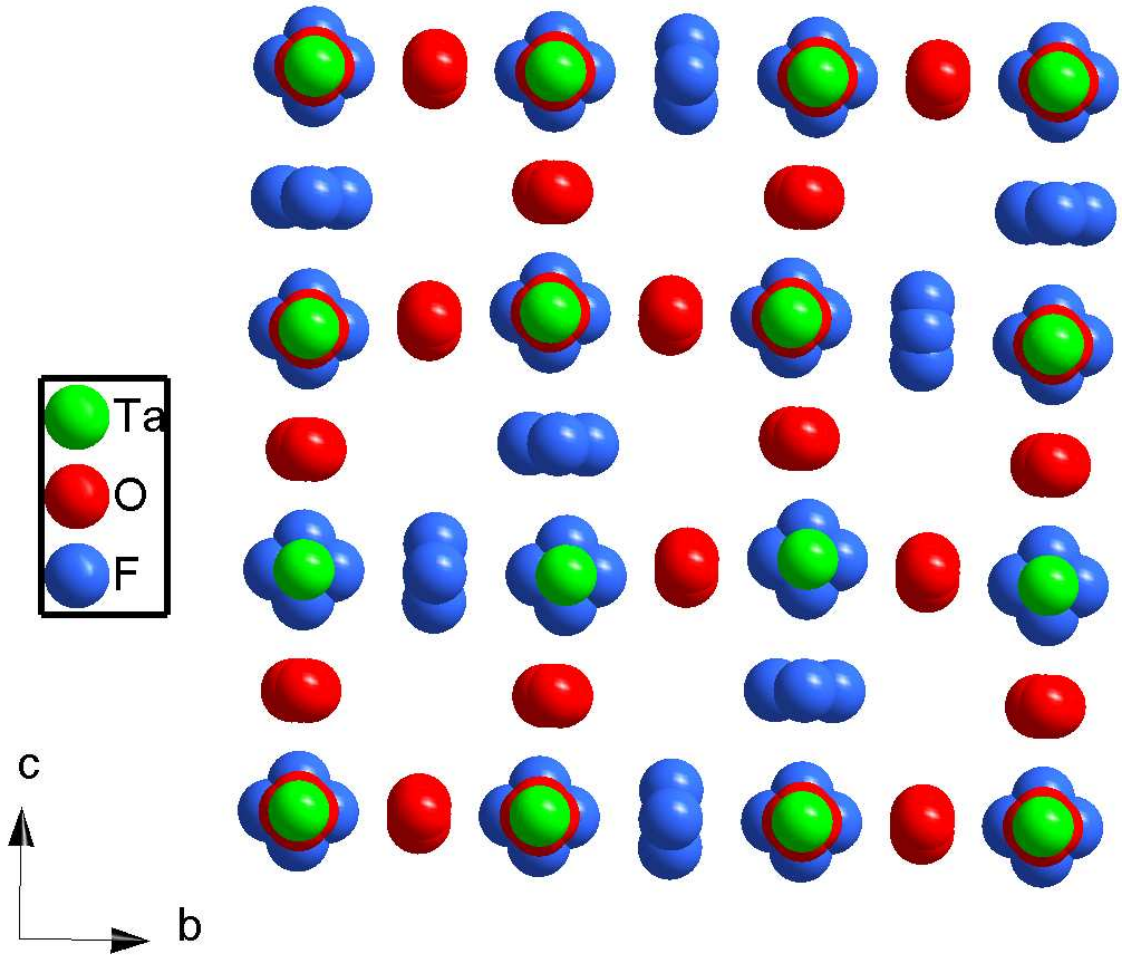

Figure E.2: TaO_2F supercell model, viewed down the crystallographic a–axis. This figure emphasizes the magnitude of the displacements of the F atoms relative to those of the O atoms. Reproduced from ref. [218].

Table E.3: Cubic lattice constant a, Ta–X and Ta–(X)–Ta (X = O, F; denoted NN_X in the table) separations, Ta–X–Ta bond angles (denoted BA_X), and anion off-axis displacement δ_X in TaO_2F at various temperatures T (80-487 K). Lattice constants were determined by fitting the simple cubic structural model to variable-temperature PDFs with *PDFgui* [272]. Interatomic separations were determined by fitting Gaussian peaks to the PDFs with *Fityk* [273], as described above. Bond angles and displacements were calculated by geometry from the interatomic separations. Estimated standard deviations (ESDs) from the least-squares fits for the interatomic separations are generally on the order of 0.001, except for those for the Ta–F separations, which are on the order of 0.01. ESDs for the lattice constant are all ∼0.0006.

T (K)	a (Å)	Ta–O (Å)	Ta–F (Å)	NN_O (Å)	NN_F (Å)	BA_O (°)	BA_F (°)	δ_O (Å)	δ_F (Å)
80	3.8839	1.89035	2.09973	3.77244	4.12003	172.4238	157.6771	0.124889	0.406453
84.2	3.88361	1.88849	2.09442	3.77273	4.11825	174.5634	158.9329	0.089563	0.382883
88.3	3.88354	1.88903	2.10296	3.77273	4.12492	173.9124	157.4743	0.100307	0.41073
92.5	3.88359	1.88788	2.09438	3.77287	4.11797	175.5162	158.9028	0.07385	0.383417
96.6	3.8836	1.88694	2.09692	3.77302	4.11793	177.5536	158.1642	0.040281	0.397161
100.8	3.88361	1.88839	2.09841	3.77296	4.11897	174.8456	157.894	0.084912	0.402301

Table E.3: *Continued on next page*

Table E.3: *Continued from previous page*

T (K)	a (Å)	Ta—O (Å)	Ta—F (Å)	NN_O (Å)	NN_F (Å)	BA_O (°)	BA_F (°)	δ_O (Å)	δ_F (Å)
104.9	3.88363	1.88985	2.09955	3.7728	4.1179	173.0748	157.428	0.114141	0.410895
107.9	3.88363	1.89186	2.09699	3.77293	4.11795	171.3439	158.1473	0.142773	0.397478
111	3.88364	1.89171	2.10354	3.77285	4.11801	171.4323	156.3782	0.141306	0.430557
114	3.88365	1.89233	2.10716	3.7728	4.11827	170.9258	155.4879	0.149693	0.44731
117.1	3.88367	1.89291	2.1073	3.77289	4.11887	170.5265	155.5297	0.156312	0.446588
120.1	3.8838	1.89344	2.11157	3.77299	4.1185	170.1823	154.4377	0.162024	0.467137
123.1	3.88384	1.89369	2.1074	3.77293	4.11922	169.9869	155.5496	0.165262	0.446253
126.2	3.88393	1.89342	2.11188	3.77318	4.11915	170.2639	154.4433	0.160678	0.467106
129.2	3.88396	1.89257	2.11212	3.77305	4.11929	170.8387	154.4031	0.151144	0.467882
133.3	3.88401	1.89362	2.10911	3.77318	4.11928	170.1228	155.132	0.163018	0.454123
137.5	3.88402	1.89367	2.10878	3.77312	4.11996	170.0669	155.2997	0.163943	0.451038
141.6	3.88404	1.89309	2.10866	3.77323	4.1192	170.5196	155.233	0.15644	0.452211
145.8	3.88403	1.89306	2.10932	3.7732	4.11914	170.5305	155.0627	0.156258	0.455414
149.9	3.88404	1.89326	2.10893	3.77326	4.1201	170.4072	155.2802	0.158306	0.45142
154.1	3.88389	1.89287	2.10862	3.77321	4.11944	170.6742	155.2733	0.153878	0.451477
158.2	3.88383	1.89286	2.10531	3.77307	4.11948	170.6296	156.1144	0.154611	0.435662

Table E.3: *Continued on next page*

Table E.3: *Continued from previous page*

T (K)	a (Å)	Ta—O (Å)	Ta—F (Å)	NN_O (Å)	NN_F (Å)	BA_O (°)	BA_F (°)	δ_O (Å)	δ_F (Å)
162.4	3.8838	1.89177	2.10732	3.77306	4.11788	171.469	155.398	0.140706	0.448958
166.5	3.88376	1.89212	2.10627	3.77306	4.11873	171.1894	155.7713	0.145336	0.442028
170.7	3.88375	1.89242	2.10495	3.77281	4.11923	170.8611	156.1743	0.150763	0.434512
174.8	3.88374	1.89238	2.1046	3.77293	4.11887	170.9374	156.2172	0.149505	0.433669
178.9	3.88376	1.89256	2.10602	3.77287	4.1186	170.7783	155.8179	0.152139	0.441139
183.1	3.88377	1.89229	2.1095	3.77275	4.11884	170.9372	154.9808	0.149502	0.456924
187.2	3.88378	1.89393	2.1058	3.77279	4.11815	169.7748	155.8153	0.168774	0.441139
191.4	3.88379	1.89186	2.10747	3.77283	4.11911	171.3039	155.5179	0.143432	0.446837
195.5	3.8838	1.89142	2.10184	3.77288	4.11777	171.6827	156.7931	0.137163	0.422758
199.7	3.8838	1.89096	2.10532	3.77299	4.11816	172.1237	155.9389	0.12987	0.438819
203.8	3.88379	1.89149	2.10588	3.77295	4.11814	171.6536	155.7937	0.137646	0.441544
208	3.88379	1.89215	2.10497	3.77311	4.11806	171.1855	156.0154	0.145402	0.437372
212.1	3.8838	1.89053	2.10706	3.77294	4.11756	172.4887	155.4221	0.123833	0.448472
216.3	3.88381	1.89052	2.10531	3.77302	4.11701	172.5351	155.7917	0.123069	0.44146
220.4	3.88383	1.8905	2.10406	3.77304	4.11763	172.563	156.193	0.122607	0.433992
224.6	3.88383	1.89042	2.10593	3.77321	4.1171	172.7187	155.6465	0.120039	0.444199

Table E.3: *Continued on next page*

Table E.3: *Continued from previous page*

T (K)	a (Å)	Ta—O (Å)	Ta—F (Å)	NN_O (Å)	NN_F (Å)	BA_O (°)	BA_F (°)	δ_O (Å)	δ_F (Å)
228.7	3.88383	1.89134	2.10701	3.77312	4.11788	171.8513	155.4755	0.134381	0.447501
232.8	3.88383	1.8914	2.1034	3.77308	4.1176	171.7835	156.3602	0.135502	0.430853
237	3.88384	1.89071	2.10551	3.77298	4.11701	172.3424	155.741	0.126253	0.442413
241.1	3.88384	1.88969	2.10431	3.77301	4.11784	173.3459	156.1561	0.109669	0.434706
245.3	3.88385	1.89045	2.10428	3.77307	4.11803	172.6239	156.1889	0.121601	0.43411
249.4	3.88385	1.88953	2.10388	3.77303	4.11778	173.5257	156.2594	0.106699	0.432762
253.6	3.88386	1.88948	2.10254	3.77288	4.11724	173.4988	156.5369	0.107139	0.427502
257.7	3.88386	1.88908	2.10498	3.77316	4.11792	174.104	155.9945	0.097155	0.437749
261.9	3.88386	1.88885	2.10542	3.7732	4.1178	174.4062	155.8665	0.092167	0.440141
266	3.88387	1.88969	2.10287	3.77329	4.11796	173.4938	156.5468	0.107233	0.427392
270.2	3.88388	1.8901	2.10492	3.77317	4.11833	173.0104	156.0636	0.115217	0.436495
274.3	3.88388	1.88967	2.10515	3.77311	4.1184	173.4194	156.0138	0.108457	0.437438
278.6	3.88391	1.88922	2.1064	3.77315	4.1179	173.9356	155.6312	0.099935	0.444574
282.9	3.884	1.88941	2.10473	3.77331	4.11776	173.811	156.0376	0.101995	0.436923
287.2	3.88408	1.88953	2.10519	3.77337	4.11682	173.7109	155.7975	0.10365	0.441331
291.6	3.88414	1.89083	2.10424	3.77333	4.11847	172.3927	156.2574	0.125432	0.432871

Table E.3: *Continued on next page*

Table E.3: *Continued from previous page*

T (K)	a (Å)	Ta—O (Å)	Ta—F (Å)	NN_O (Å)	NN_F (Å)	BA_O (°)	BA_F (°)	δ_O (Å)	δ_F (Å)
295.9	3.88421	1.89051	2.10612	3.77341	4.11749	172.7284	155.6489	0.119885	0.444196
300.2	3.88426	1.89083	2.10611	3.7732	4.11763	172.3336	155.6695	0.126406	0.443824
304.5	3.88429	1.88988	2.10428	3.77341	4.11792	173.3567	156.1744	0.109502	0.434371
308.8	3.8843	1.89024	2.10452	3.77356	4.11886	173.0655	156.2365	0.114317	0.433304
313.1	3.88432	1.88943	2.10778	3.77349	4.11797	173.8902	155.295	0.100693	0.450907
317.5	3.88431	1.89069	2.11011	3.77341	4.1177	172.5587	154.6903	0.12269	0.462278
321.8	3.88418	1.89075	2.10887	3.77358	4.11744	172.5822	154.9595	0.122307	0.45717
326.1	3.88411	1.89077	2.10999	3.77356	4.11755	172.5542	154.7007	0.12277	0.462064
330.4	3.88405	1.89086	2.1111	3.77337	4.1173	172.3837	154.403	0.125584	0.467657
334.7	3.88402	1.89086	2.11204	3.77332	4.11757	172.3609	154.2122	0.125959	0.471293
339.1	3.88399	1.89072	2.11044	3.77337	4.11814	172.5122	154.665	0.123458	0.462804
343.4	3.88398	1.88927	2.11084	3.77318	4.11733	173.8957	154.4689	0.100595	0.466416
347.7	3.88397	1.89022	2.11056	3.77332	4.11804	172.966	154.6237	0.115956	0.463573
352	3.88398	1.88988	2.11315	3.77333	4.11752	173.315	153.9446	0.110189	0.476351
356.3	3.88397	1.89004	2.11057	3.77334	4.11738	173.156	154.5398	0.112816	0.465082
360.6	3.88399	1.88989	2.11138	3.77332	4.11704	173.2994	154.3044	0.110446	0.46949

Table E.3: *Continued on next page*

Table E.3: *Continued from previous page*

T (K)	a (Å)	Ta—O (Å)	Ta—F (Å)	NN_O (Å)	NN_F (Å)	BA_O (°)	BA_F (°)	δ_O (Å)	δ_F (Å)
365	3.88399	1.89007	2.11286	3.77329	4.11768	173.1004	154.032	0.113733	0.474716
369.3	3.884	1.89071	2.1108	3.77348	4.1184	172.5728	154.6103	0.12246	0.463866
373.6	3.88401	1.88957	2.10982	3.77331	4.11828	173.6341	154.8327	0.104918	0.459655
377.9	3.88403	1.88919	2.11109	3.77328	4.11802	174.0455	154.4937	0.098124	0.466024
382.1	3.88404	1.88917	2.10724	3.77343	4.11759	174.1574	155.381	0.09628	0.449248
386.3	3.88406	1.88893	2.11091	3.7733	4.11791	174.3692	154.5234	0.092781	0.465452
390.5	3.88406	1.88927	2.11099	3.77331	4.1181	173.9701	154.5276	0.099368	0.465394
394.7	3.88409	1.88968	2.11184	3.77314	4.11756	173.4247	154.2585	0.10837	0.470418
398.9	3.8841	1.89029	2.11192	3.77338	4.11718	172.9267	154.1933	0.116607	0.471607
403.1	3.88412	1.89025	2.11064	3.77323	4.11829	172.8923	154.6353	0.11717	0.463382
407.3	3.88412	1.89053	2.11448	3.77319	4.11723	172.6052	153.6004	0.121914	0.482835
411.4	3.88414	1.89135	2.11733	3.77315	4.11738	171.8556	152.968	0.134312	0.494855
415.6	3.88414	1.89396	2.11568	3.77299	4.11731	169.8225	153.3341	0.167991	0.487895
419.8	3.88417	1.89379	2.11669	3.77312	4.11653	169.9837	153.0138	0.165324	0.493884
424	3.8842	1.89392	2.11683	3.77299	4.11762	169.8497	153.1088	0.16754	0.49221
428.2	3.88425	1.89354	2.1213	3.77297	4.1181	170.105	152.1706	0.163304	0.510124

Table E.3: *Continued on next page*

Table E.3: *Continued from previous page*

T **(K)**	a **(Å)**	**Ta—O (Å)**	**Ta—F (Å)**	NN_O **(Å)**	NN_F **(Å)**	BA_O **(°)**	BA_F **(°)**	δ_O **(Å)**	δ_F **(Å)**
432.4	3.88428	1.89337	2.11765	3.77315	4.11804	170.2888	152.9724	0.160265	0.494852
436.6	3.88431	1.89208	2.11634	3.77311	4.11717	171.2407	153.1674	0.144489	0.491043
440.8	3.88434	1.89169	2.1152	3.77312	4.11602	171.5589	153.2924	0.139221	0.488534
445	3.8844	1.89095	2.11419	3.77305	4.11692	172.159	153.6307	0.129288	0.482226
449.2	3.88444	1.891	2.11576	3.77305	4.11745	172.115	153.3323	0.130017	0.487946
453.4	3.88447	1.89095	2.11617	3.77316	4.11847	172.2079	153.3584	0.128483	0.487572
457.6	3.88451	1.89062	2.114	3.77317	4.11726	172.512	153.7152	0.123455	0.480665
461.8	3.88457	1.89036	2.11282	3.77301	4.1171	172.6805	153.9714	0.120664	0.475794
466	3.88473	1.89149	2.12002	3.77318	4.11738	171.7499	152.3696	0.136061	0.506241
470.2	3.88485	1.89176	2.11766	3.77348	4.11912	171.6501	153.0955	0.137725	0.492642
474.3	3.88487	1.89257	2.12218	3.77321	4.11805	170.8996	151.9739	0.150143	0.513872
478.5	3.88497	1.89252	2.11848	3.77358	4.11988	171.0806	152.9986	0.147158	0.494575
482.7	3.88507	1.89262	2.11694	3.77347	4.11841	170.961	153.1759	0.149136	0.491029
486.9	3.88508	1.89245	2.12042	3.77353	4.1188	171.1156	152.4425	0.146577	0.505027

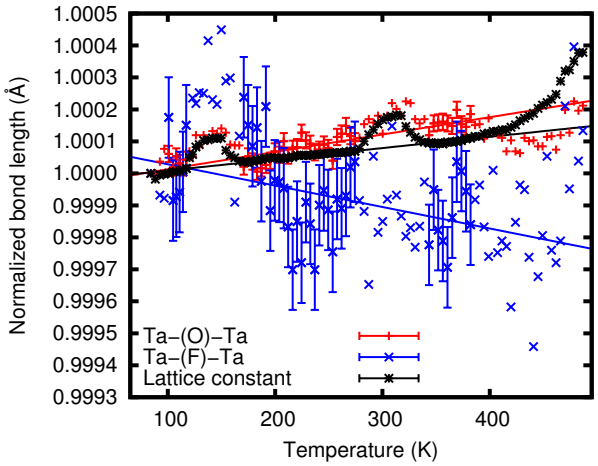

Figure E.3: Temperature dependence of the lattice constant, estimated by fits to the PDFs, and the interatomic separations Ta–(X)–Ta (X = O, F) in TaO_2F, normalized to 84 K. The anomalous "waves" in the lattice constant values are due to X-ray wavelength instability. Similar anomalies were also observed in the lattice constants extracted by Rietveld analysis. The straight lines, which serve as guides to the eye, were fit to the data over the same temperature range used to calculate coefficients of thermal expansion in Table E.4; the regions showing fluctuations in lattice constant due to wavelength instability were not included in these fits. The error bars shown for the Ta–O–Ta and Ta–F–Ta separations are the standard deviations of the estimated Ta–(X)–Ta values from the least-squares fits. Error bars are only shown for the temperature intervals used in the linear fits. While the slopes of these lines appear dramatically different due to the scaling of this plot, they correspond to differences in linear CTE of only $\sim$1 ppm·K^{-1}. The quite large fluctuations in the best estimates for the Ta–(F)–Ta separation are believed to be due to correlations amongst model-fitting parameters, as the peak in $G(r)$ corresponding to the Ta–(F)–Ta separation, unlike that for the Ta–(O)–Ta separation, significantly overlaps with other peaks (see Figure 9.1). Reproduced from ref. [218].

Table E.4: Average linear coefficients of thermal expansion for the Ta–(X)–Ta (X = O, F) linkages and lattice constant of TaO_2F. These average coefficients were calculated over the temperature range 101-382 K by fitting a line to bond length *versus* T data, excluding the two anomalous "wave" regions at 120-167 K and 279-339 K (see Figure E.3), and dividing by the average bond length over that temperature range. Numbers in parentheses are estimated standard deviations from these least-squares fits.

	Linear CTE, ppm·K^{-1}
Lattice constant, a	+0.353(7)
Ta–O–Ta	+0.54(5)
Ta–F–Ta	-0.7(2)

APPENDIX F

COPYRIGHT AGREEMENT LETTERS

Permission for Figure 1.5 in Chapter 1

Title: Pronounced Negative Thermal Expansion from a Simple Structure: Cubic ScF3

Author: Benjamin K. Greve, Kenneth L. Martin, Peter L. Lee, Peter J. Chupas, Karena W. Chapman, and Angus P. Wilkinson

Publication: Journal of the American Chemical Society

Publisher: American Chemical Society

Date: Nov 1, 2010

PERMISSION/LICENSE IS GRANTED FOR YOUR ORDER AT NO CHARGE

This type of permission/license, instead of the standard Terms & Conditions, is sent to you because no fee is being charged for your order. Please note the following:

- Permission is granted for your request in both print and electronic formats, and translations.
- If figures and/or tables were requested, they may be adapted or used in part.
- Please print this page for your records and send a copy of it to your publisher/graduate school.
- Appropriate credit for the requested material should be given as follows: "Reprinted (adapted) with permission from (COMPLETE REFERENCE CITATION). Copyright (YEAR) American Chemical Society." Insert appropriate information in place of the capitalized words.
- One-time permission is granted only for the use specified in your request. No additional uses are granted (such as derivative works or other editions). For any other uses, please submit a new request.

If credit is given to another source for the material you requested, permission must be obtained from that source.

Permission for Figure 1.8 in Chapter 1 and portions of Chapter 4, including Figures 4.3 and 4.6-4.9

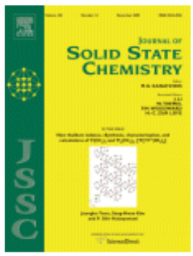

Title: Thermal expansion and phase transitions of α-AlF3
Author: Cody R. Morelock,Justin C. Hancock,Angus P. Wilkinson
Publication: Journal of Solid State Chemistry
Publisher: Elsevier
Date: November 2014

Order Completed

Thank you very much for your order.

This is a License Agreement between Cody R Morelock ("You") and Elsevier ("Elsevier"). The license consists of your order details, the terms and conditions provided by Elsevier, and the payment terms and conditions.

Get the printable license.

License Number	3444400217393
License date	Aug 08, 2014
Licensed content publisher	Elsevier
Licensed content publication	Journal of Solid State Chemistry
Licensed content title	Thermal expansion and phase transitions of α-AlF3
Licensed content author	Cody R. Morelock,Justin C. Hancock,Angus P. Wilkinson
Licensed content date	November 2014
Licensed content volume number	219
Licensed content issue number	n/a
Number of pages	5
Type of Use	reuse in a thesis/dissertation
Portion	full article
Format	both print and electronic
Are you the author of this Elsevier article?	Yes
Will you be translating?	No
Title of your thesis/dissertation	Thermal Expansion, Compressibility, and Local Structure of Fluorides and Oxyfluorides with the Rhenium Trioxide Structure
Expected completion date	Aug 2014
Estimated size (number of pages)	300
Elsevier VAT number	GB 494 6272 12
Permissions price	0.00 USD
VAT/Local Sales Tax	0.00 USD / 0.00 GBP
Total	0.00 USD

Permission for Figure 1.9 in Chapter 1 and portions of Chapter 6 and Appendix B, including Figures 6.2-6.9 and B.1-B.6

Title:	Evolution of Negative Thermal Expansion and Phase Transitions in Sc1-xTixF3
Author:	Cody R. Morelock, Leighanne C. Gallington, and Angus P. Wilkinson
Publication:	Chemistry of Materials
Publisher:	American Chemical Society
Date:	Mar 1, 2014

PERMISSION/LICENSE IS GRANTED FOR YOUR ORDER AT NO CHARGE

This type of permission/license, instead of the standard Terms & Conditions, is sent to you because no fee is being charged for your order. Please note the following:

- Permission is granted for your request in both print and electronic formats, and translations.
- If figures and/or tables were requested, they may be adapted or used in part.
- Please print this page for your records and send a copy of it to your publisher/graduate school.
- Appropriate credit for the requested material should be given as follows: "Reprinted (adapted) with permission from (COMPLETE REFERENCE CITATION). Copyright (YEAR) American Chemical Society." Insert appropriate information in place of the capitalized words.
- One-time permission is granted only for the use specified in your request. No additional uses are granted (such as derivative works or other editions). For any other uses, please submit a new request.

Permission for portions of Section 2.2.2

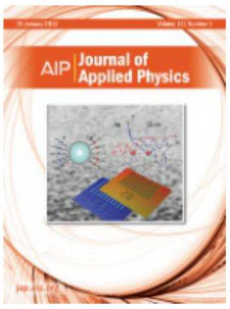

Title:	Dramatic softening of the negative thermal expansion material HfW2O8 upon heating through its WO4 orientational order-disorder phase transition
Author:	Leighanne C. Gallington,Karena W. Chapman,Cody R. Morelock, et al.
Publication:	Journal of Applied Physics
Volume/Issue	115/5
Publisher:	AIP Publishing LLC
Date:	Feb 4, 2014
Page Count:	5

Order Completed

Thank you very much for your order.

Click here for Payment Terms and Conditions.

Get a printable version for your records.

License Number	3444400781378
Order Date	Aug 08, 2014
Publisher	AIP Publishing LLC
Publication	Journal of Applied Physics
Article Title	Dramatic softening of the negative thermal expansion material HfW2O8 upon heating through its WO4 orientational order-disorder phase transition
Author	Leighanne C. Gallington,Karena W. Chapman,Cody R. Morelock, et al.
Online Publication Date	Feb 4, 2014
Volume number	115
Issue number	5
Type of Use	Thesis/Dissertation
Requestor type	Author (original article)
Format	Print and electronic
Portion	Excerpt (> 800 words)
Will you be translating?	No
Title of your thesis / dissertation	Thermal Expansion, Compressibility, and Local Structure of Fluorides and Oxyfluorides with the Rhenium Trioxide Structure
Expected completion date	Aug 2014
Estimated size (number of pages)	300
Total	0.00 USD

Permission for portions of Chapter 7 and Appendix C, including Figures 7.1, 7.2a, 7.4-7.10, and C.1-C.14

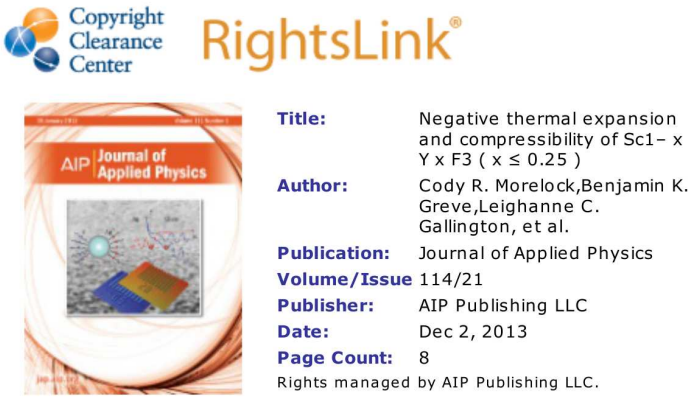

Title:	Negative thermal expansion and compressibility of Sc1− x Y x F3 (x ≤ 0.25)
Author:	Cody R. Morelock,Benjamin K. Greve,Leighanne C. Gallington, et al.
Publication:	Journal of Applied Physics
Volume/Issue	114/21
Publisher:	AIP Publishing LLC
Date:	Dec 2, 2013
Page Count:	8

Order Completed

Thank you very much for your order.

Click here for Payment Terms and Conditions.

Get a printable version for your records.

License Number	3444401080730
Order Date	Aug 08, 2014
Publisher	AIP Publishing LLC
Publication	Journal of Applied Physics
Article Title	Negative thermal expansion and compressibility of Sc1− x Y x F3 (x ≤ 0.25)
Author	Cody R. Morelock,Benjamin K. Greve,Leighanne C. Gallington, et al.
Online Publication Date	Dec 2, 2013
Volume number	114
Issue number	21
Type of Use	Thesis/Dissertation
Requestor type	Author (original article)
Format	Print and electronic
Portion	Excerpt (> 800 words)
Will you be translating?	No
Title of your thesis / dissertation	Thermal Expansion, Compressibility, and Local Structure of Fluorides and Oxyfluorides with the Rhenium Trioxide Structure
Expected completion date	Aug 2014
Estimated size (number of pages)	300
Total	0.00 USD

Permission for portions of Chapter 9 and Appendix E, including Figures 9.1-9.3 and E.1-E.3

Title:	Role of Anion Site Disorder in the Near Zero Thermal Expansion of Tantalum Oxyfluoride
Author:	Cody R. Morelock, Benjamin K. Greve, Mehmet Cetinkol, Karena W. Chapman, Peter J. Chupas, and Angus P. Wilkinson
Publication:	Chemistry of Materials
Publisher:	American Chemical Society
Date:	May 1, 2013

PERMISSION/LICENSE IS GRANTED FOR YOUR ORDER AT NO CHARGE

This type of permission/license, instead of the standard Terms & Conditions, is sent to you because no fee is being charged for your order. Please note the following:

- Permission is granted for your request in both print and electronic formats, and translations.
- If figures and/or tables were requested, they may be adapted or used in part.
- Please print this page for your records and send a copy of it to your publisher/graduate school.
- Appropriate credit for the requested material should be given as follows: "Reprinted (adapted) with permission from (COMPLETE REFERENCE CITATION). Copyright (YEAR) American Chemical Society." Insert appropriate information in place of the capitalized words.
- One-time permission is granted only for the use specified in your request. No additional uses are granted (such as derivative works or other editions). For any other uses, please submit a new request.

REFERENCES

[1] C. P. Romao, K. J. Miller, C. A. Whitman, M. A. White, and B. A. Marinkovic. *Negative Thermal Expansion (Thermomiotic) Materials*, volume 4, pages 128–151. Oxford, Elsevier, 2013.

[2] R. Roy, D. K. Agrawal, and H. A. McKinstry. Very Low Thermal Expansion Coefficient Materials. *Annu. Rev. Mater. Sci.*, 19(1):59–81, 1989.

[3] A. W. Sleight. Thermal contraction. *Endeavour*, 19(2):64–68, 1995.

[4] A. W. Sleight. Compounds That Contract on Heating. *Inorg. Chem.*, 37(12):2854–2860, 1998.

[5] J. S. O. Evans. Negative thermal expansion materials. *J. Chem. Soc., Dalton Trans.*, (19):3317–3326, 1999.

[6] W. Miller, C. W. Smith, D. S. Mackenzie, and K. E. Evans. Negative thermal expansion: a review. *J. Mater. Sci.*, 44(20):5441–5451, 2009.

[7] K. Takenaka. Negative thermal expansion materials: technological key for control of thermal expansion. *Sci. Technol. Adv. Mater.*, 13(1):013001, 2012.

[8] C. Lind. Two Decades of Negative Thermal Expansion Research: Where Do We Stand? *Materials*, 5(6):1125–1154, 2012.

[9] G. K. White. Solids: Thermal expansion and contraction. *Contemp. Phys.*, 34(4):193–204, 1993.

[10] G. D. Barrera, J. A. O. Bruno, T. H. K. Barron, and N. L. Allan. Negative Thermal Expansion. *J. Phys.: Condens. Matter*, 17(4):R217–R252, 2005.

[11] N. W. Ashcroft and N. D. Mermin. *Solid State Physics*. Saunders College, 1976.

[12] P. Atkins and J. de Paula. *Physical Chemistry, Seventh Edition*. W. H. Freeman and Company, New York, 2002.

[13] E. Grüneisen. Zustand des festen körpers. *Handb. Phys.*, 10:1–59, 1926.

[14] E. Grüneisen. Theorie des festen Zustandes einatomiger elemente. *Ann. Phys., Ser. 4*, 39:257–306, 1912.

[15] J. Chadwick. Possible Existence of a Neutron. *Nature*, 129(3252):312, 1932.

[16] B. E. Warren. *X-Ray Diffraction*. Dover Publications, Inc., New York, 1990.

[17] J. D. James, J. A. Spittle, S. G. R. Brown, and R. W. Evans. A review of measurement techniques for the thermal expansion coefficient of metals and alloys at elevated temperatures. *Meas. Sci. Technol.*, 12(3):R1–R15, 2001.

[18] M. A. White. *Physical Properties of Materials*. CRC Press, Boca Raton, FL, 2012.

[19] J. S. O. Evans, T. A. Mary, and A. W. Sleight. Negative Thermal Expansion in a Large Molybdate and Tungstate Family. *J. Solid State Chem.*, 133(2):580–583, 1997.

[20] J. S. O. Evans, T. A. Mary, and A. W. Sleight. Negative Thermal Expansion in $Sc_2(WO_4)_3$. *J. Solid State Chem.*, 137(1):148–160, 1998.

[21] J. S. O. Evans, T. A. Mary, T. Vogt, M. A. Subramanian, and A. W. Sleight. Negative Thermal Expansion in ZrW_2O_8 and HfW_2O_8. *Chem. Mater.*, 8(12):2809–2823, 1996.

[22] S. LaPlaca and B. Post. Thermal expansion of ice. *Acta Cryst.*, 13(6):503–505, 1960.

[23] R. M. Buffington and W. M. Latimer. The Measurement of Coefficients of Expansion at Low Temperatures: Some Thermodynamic Applications of Expansion Data. *J. Am. Chem. Soc.*, 48(1):2305–2319, 1926.

[24] M. E. Straumanis. Neubestimmung der Gitterparameter, Dichten und thermischen Ausdehnungskoeffizienten von Silber und Gold, und Vollkommenheit der Struktur. *Montash. Chem.*, 102(5):1377–1386, 1971.

[25] J. Z. Tao and A. W. Sleight. Very low thermal expansion in TaO_2F. *J. Solid State Chem.*, 173(1):45–48, 2003.

[26] S. E. Tallentire, F. Child, I. Fall, L. Vella-Zarb, I. R. Evans, M. G. Tucker, D. A. Keen, C. Wilson, and J. S. O. Evans. Systematic and Controllable Negative, Zero, and Positive Thermal Expansion in Cubic $Zr_{1-x}Sn_xMo_2O_8$. *J. Am. Chem. Soc.*, 135(34):12849–12856, 2013.

[27] Pyrex® Glass Code 7740, Industrial Supplies. Technical report, Corning Glass Works, Corning, NY, USA, 1987.

[28] C. A. Swenson. Recommended Values for the Thermal Expansivity of Silicon from 0 to 1000 K. *J. Phys. Chem. Ref. Data*, 12:179, 1983.

[29] G. J. F. Holman and C. A. ten Seldam. A Critical Evaluation of the Thermophysical Properties of Mercury. *J. Phys. Chem. Ref. Data*, 23:807–827, 1994.

[30] R. S. Krishnan. Thermal Expansion of Diamond. *Nature*, 154(3911):486–487, 1944.

[31] W. F. Schlosser, G. M. Graham, and P. P. M. Meincke. The temperature and magnetic field dependence of the forced magnetostriction and thermal expansion of Invar. *J. Phys. Chem. Solids*, 32(5):927–938, 1971.

[32] T. Chatterji, P. F. Henry, R. Mittal, and S. L. Chaplot. Negative thermal expansion of ReO_3: Neutron diffraction experiments and dynamical lattice calculations. *Phys. Rev. B*, 78(13):134105, 2008.

[33] K. W. Chapman, P. J. Chupas, and C. J. Kepert. Compositional Dependence of Negative Thermal Expansion in the Prussian Blue Analogues $M^{II}Pt^{IV}(CN)_6$ (M = Mn, Fe, Co, Ni, Cu, Zn, Cd). *J. Am. Chem. Soc.*, 128(21):7009–7014, 2006.

[34] S. Margadonna, K. Prassides, and A. N. Fitch. Zero Thermal Expansion in a Prussian Blue Analogue. *J. Am. Chem. Soc.*, 126(47):15390–15391, 2004.

[35] B. K. Greve, K. L. Martin, P. L. Lee, P. J. Chupas, K. W. Chapman, and A. P. Wilkinson. Pronounced Negative Thermal Expansion from a Simple Structure: Cubic ScF_3. *J. Am. Chem. Soc.*, 132(44):15496–15498, 2010.

[36] J. S. O. Evans, W. I. F. David, and A. W. Sleight. Structural investigation of the negative-thermal-expansion material ZrW_2O_8. *Acta Cryst. B*, 55(3):333–340, 1999.

[37] A. L. Goodwin and C. J. Kepert. Negative thermal expansion and low-frequency modes in cyanide-bridged framework materials. *Phys. Rev. B*, 71(14):140301, 2005.

[38] I. Yamada, K. Tscuhida, K. Ohgushi, N. Hayashi, J. Kim, N. Tsuji, R. Takahashi, M. Matsushita, N. Nishiyama, T. Inoue, T. Irifune, K. Kato, M. Takata, and M. Takano. Giant Negative Thermal Expansion in the Iron Perovskite $SrCu_3Fe_4O_{12}$. *Angew. Chem. Int. Ed.*, 50(29):6579–6582, 2011.

[39] M. Azuma, W. Chen, H. Seki, M. Czapski, S. Olga, K. Oka, M. Mizumaki, T. Watanuki, N. Ishimatsu, N. Kawamura, S. Ishiwata, M. G. Tucker, Y. Shimakawa, and J. P. Attfield. Colossal negative thermal expansion in $BiNiO_3$ induced by intermetallic charge transfer. *Nat. Commun.*, 2(347):1–5, 2011.

[40] H. Holzer and D. C. Dunand. Phase transformation and thermal expansion of Cu/ZrW_2O_8 metal matrix composites. *J. Mater. Res.*, 14(3):780–789, 1999.

[41] S. Yilmaz. Phase transformations in thermally cycled Cu/ZrW_2O_8 composites investigated by synchrotron x-ray diffraction. *J. Phys.: Condens. Matter.*, 14(3):365–375, 2002.

[42] S. Yilmaz. Thermal mismatch stress development in Cu-ZrW_2O_8 composite investigated by synchrotron x-ray diffraction. *Compos. Sci. Technol.*, 62(14):1835–1839, 2002.

[43] S. Yilmaz and D. C. Dunand. Finite-element analysis of thermal expansion and thermal mismatch stresses in a Cu 60vol% ZrW_2O_8 composite. *Compos. Sci. Technol.*, 64(12):1895–1898, 2004.

[44] C. R. Morelock, M. R. Suchomel, and A. P. Wilkinson. A cautionary tale on the use of GE-7031 varnish: low-temperature thermal expansion studies of ScF_3. *J. Appl. Cryst.*, 46(3):823–825, 2013.

[45] K. Scheel. Versuche ueber die Ausdehnung Fester Korper, insbesondere von Quarz in Richtung der Hauptachse, Platin, Palladium und Quarzglas bei der Temperatur der Fluessigen Luft (Experiments on the expansion of solid bodies, in particular of quartz in the major axis direction, platinum, palladium, and silica glass at the temperature of liquid air). *Verh. Deutsch Phys. Ges.*, 9:3–23, 1907.

[46] K. Scheel. Ueber die Ausdehnung des Quarzglases (Concerning the expansion of quartz glass). *Verh. Deutsch Phys. Ges.*, 9:718–721, 1907.

[47] M. E. Milberg and H. D. Blair. Thermal Expansion of Cordierite. *J. Am. Ceram. Soc.*, 60(7-8):372–373, 1977.

[48] J. D. Lee and J. L. Pentecost. Properties of Flux-Grown Cordierite Single Crystals. *J. Am. Ceram. Soc.*, 59(3-4):183–184, 1976.

[49] D. L. Evans, G. R. Fischer, J. E. Geiger, and F. W. Martin. Thermal Expansions and Chemical Modifications of Cordierite. *J. Am. Ceram. Soc.*, 63(11-12):629–634, 1980.

[50] F. A. Hummel. Thermal expansion properties of natural lithia minerals. *Foote Prints*, 20:3–11, 1948.

[51] F. A. Hummel. Thermal Expansion Properties of Some Synthetic Lithia Minerals. *J. Am. Ceram. Soc.*, 34(8):235–239, 1951.

[52] F. H. Gillery and E. A. Bush. Thermal Contraction of β-Eucryptite ($Li_2O{\cdot}Al_2O_3{\cdot}2SiO_2$) by X-Ray and Dilatometer Methods. *J. Am. Ceram. Soc.*, 42(4):175–177, 1959.

[53] W. Ostertag, G. R. Fischer, and J. P. Williams. Thermal Expansion of Synthetic β-Spodumene and β-Spodumene–Silica Solid Solutions. *J. Am. Ceram. Soc.*, 51(11):651–654, 1968.

[54] V. Korthuis, N. Khosrovani, A. W. Sleight, N. Roberts, R. Dupree, and W. W. Warren. Negative Thermal Expansion and Phase Transitions in the $ZrV_{2-x}P_xO_7$ Series. *Chem. Mater.*, 7(2):412–417, 1995.

[55] T. A. Mary, J. S. O. Evans, T. Vogt, and A. W. Sleight. Negative Thermal Expansion from 0.3 to 1050 Kelvin in ZrW_2O_8. *Science*, 272(5258):90–92, 1996.

[56] A. K. A. Pryde, K. D. Hammonds, M. T. Dove, V. Heine, J. D. Gale, and M. C. Warren. Origin of the negative thermal expansion in ZrW_2O_8 and ZrV_2O_7. *J. Phys.: Condens. Matter*, 8(50):10973, 1996.

[57] J. S. O. Evans, Z. Hu, J. D. Jorgensen, D. N. Argyriou, S. Short, and A. W. Sleight. Compressibility, Phase Transitions, and Oxygen Migration in Zirconium Tungstate, ZrW_2O_8. *Science*, 275(5296):61–65, 1997.

[58] A. P. Giddy, M. T. Dove, G. S. Pawley, and V. Heine. The determination of rigid-unit modes as potential soft modes for displacive phase transitions in framework crystal structures. *Acta Cryst. A*, 49(5):697–703, 1993.

[59] J. Z. Tao and A. W. Sleight. The role of rigid unit modes in negative thermal expansion. *J. Solid State Chem.*, 173(2):442–448, 2003.

[60] K. D. Hammonds, M. T. Dove, V. Heine, and B. Winkler. Rigid-unit phonon modes and structural phase transitions in framework silicates. *Am. Miner.*, 81(5):1057–1079, 1996.

[61] R. L. Withers, Y. Tabira, J. S. O. Evans, I. J. King, and A. W. Sleight. A New Three-Dimensional Incommensurately Modulated Cubic Phase (in ZrP_2O_7) and Its Symmetry Characterization via Temperature-Dependent Electron Diffraction. *J. Solid State Chem.*, 157(1):186–192, 2001.

[62] B. A. Marinkovic, M. Ari, R. R. de Avillez, F. Rizzo, F. F. Ferreira, K. J. Miller, M. B. Johnson, and M. A. White. Correlation between AO_6 Polyhedral Distortion and Negative Thermal Expansion in Orthorhombic $Y_2Mo_3O_{12}$ and Related Materials. *Chem. Mater.*, 21(13):2886–2894, 2009.

[63] A. M. Glazer and S. Mabud. Powder profile refinement of lead zirconate titanate at several temperatures. II. Pure $PbTiO_3$. *Acta Cryst. B*, 34(4):1065–1070, 1979.

[64] J. Chen, X. R. Xing, R. B. Yu, and G. R. Liu. Structure and enhancement of negative thermal expansion in the $PbTiO_3$-$CdTiO_3$ system. *Appl. Phys. Lett.*, 87(23):231915, 2005.

[65] J. Chen, X. R. Xing, G. R. Liu, J. H. Li, and Y. T. Liu. Structure and negative thermal expansion in the $PbTiO_3$-$BiFeO_3$ system. *Appl. Phys. Lett.*, 89(10):101914–3, 2006.

[66] J. Chen, X. Xing, C. Sun, P. Hu, R. Yu, X. Wang, and L. Li. Zero Thermal Expansion in $PbTiO_3$-Based Perovskites. *J. Am. Chem. Soc.*, 130(4):1144–1145, 2008.

[67] P. Hu, J. Chen, J. Deng, and X. Xing. Thermal Expansion, Ferroelectric and Magnetic Properties in $(1-x)PbTiO_3$–$xBi(Ni_{1/2}Ti_{1/2})O_3$. *J. Am. Chem. Soc.*, 132(6):1925–1928, 2010.

[68] J. Chen, K. Nittala, J. S. Forrester, J. L. Jones, J. X. Deng, R. B. Yu, and X. R. Xing. The Role of Spontaneous Polarization in the Negative Thermal Expansion of Tetragonal $PbTiO_3$-Based Compounds. *J. Am. Chem. Soc.*, 133(29):11114–11117, 2011.

[69] J. P. Boilot and J. P. Salanié. Phase transformation in $Na_{1+x}Si_xZr_2P_{3-x}O_{12}$ compounds. *Mater. Res. Bull.*, 14(11):1469–1477, 1979.

[70] C.-Y. Huang, D. K. Agrawal, and H. A. McKinstry. Thermal expansion behaviour of $M'Ti_2P_3O_{12}$ (M' = Li, Na, K, Cs) and $M''Ti_4P_6O_{24}$ (M'' = Mg, Ca, Sr, Ba) compounds. *J. Mater. Sci.*, 30(13):3509–3514, 1995.

[71] D. A. Woodcock, P. Lightfoot, and C. Ritter. Mechanism of low thermal expansion in the cation-ordered Nasicon structure. *Chem. Commun.*, (1):107–108, 1998.

[72] D. A. Woodcock, P. Lightfoot, and R. I. Smith. Negative Thermal Expansion Behaviour in The NZP Phase $NbTi(PO_4)_3$. *MRS Proceedings*, 547:191–196, 1999.

[73] J. H. Burge, T. Peper, and S. F. Jacobs. Thermal Expansion of Borosilicate Glass, Zerodur, Zerodur M, and Unceramized Zerodur at Low Temperatures. *Appl. Optics*, 38(34):7161–7162, 1999.

[74] J. Arvanitidis, K. Papagelis, S. Margadonna, K. Prassides, and A. N. Fitch. Temperature-induced valence transition and associated lattice collapse in samarium fulleride. *Nature*, 425(6958):599–602, 2003.

[75] Y. W. Long, N. Hayashi, T. Saito, M. Azuma, S. Muranaka, and Y. Shimakawa. Temperature-induced A-B intersite charge transfer in an A-site-ordered $LaCu_3Fe_4O_{12}$ perovskite. *Nature*, 458(7234):60–63, 2009.

[76] Y. W. Long and Y. Shimakawa. Intermetallic charge transfer between A-site Cu and B-site Fe in A-site-ordered double perovskites. *New J. Phys.*, 12(6):063029, 2010.

[77] J. R. Salvador, F. Guo, T. Hogan, and M. G. Kanatzidis. Zero thermal expansion in YbGaGe due to an electronic valence transition. *Nature*, 425(6959):702–705, 2003.

[78] D. Gignoux, D. Givord, F. Givord, and R. Lemaire. Invar properties in the rare earth-3d transition metal alloys. *J. Magn. Magn. Mater.*, 10(2-3):288–293, 1979.

[79] H. Nakamura, H. Wada, K. Yoshimura, M. Shiga, Y. Nakamura, J. Sakurai, and Y. Komura. Effect of chemical pressure on the magnetism of YMn_2: magnetic properties of $Y_{1-x}Sc_xMn_2$ and $Y_{1-x}La_xMn_2$. *J. Phys. F: Met. Phys.*, 18(5):981–991, 1988.

[80] Y. Hao, Y. Gao, B. Wang, J. Qu, Y. Li, J. Hu, and J. Deng. Negative thermal expansion and magnetic properties of $Y_2Al_3Fe_{14-x}Mn_x$ compounds. *Appl. Phys. Lett.*, 78(21):3277–3279, 2001.

[81] Y. Hao, X. Zhang, B. Wang, Y. Yuang, and F. Wang. Anomalous thermal expansion and magnetic properties of $Tm_2Fe_{17-x}Cr_x$ compounds. *J. Appl. Phys.*, 108(2):023915, 2010.

[82] K. Takenaka and H. Takagi. Giant negative thermal expansion in Ge-doped antiperovskite manganese nitrides. *Appl. Phys. Lett.*, 87(26):261902, 2005.

[83] K. Takenaka and H. Takagi. Magnetovolume Effect and Negative Thermal Expansion in $Mn_3Cu_{1-x}Ge_xN$. *Mater. Trans.*, 47(3):471–474, 2006.

[84] K. Takenaka, K. Asano, M. Misawa, and H. Takagi. Negative thermal expansion in Ge-free antiperovskite manganese nitrides: Tin-doping effect. *Appl. Phys. Lett.*, 92(1):011927, 2008.

[85] R. Huang, Y. Liu, W. Fan, J. Tan, F. Xiao, L. Qian, and L. Li. Giant Negative Thermal Expansion in $NaZn_{13}$-Type La(Fe, Si, Co)$_{13}$ Compounds. *J. Am. Chem. Soc.*, 135(31):11469–11472, 2013.

[86] Z. H. Sun, X. Y. Song, F. X. Yin, L. X. Sun, X. K. Yuan, and X. M. Liu. Giant negative thermal expansion in ultrafine-grained $Mn_3Cu_{1-x}Ge_xN$ (x=0.5) bulk. *J. Phys. D: Appl. Phys.*, 42(12):122004, 2009.

[87] Z. Hu, J. D. Jorgensen, S. Teslic, S. Short, D. N. Argyriou, J. S. O. Evans, and A. W. Sleight. Pressure-induced phase transformation in ZrW_2O_8 Compressibility and thermal expansion of the orthorhombic phase. *Physica B: Condens. Matter*, 241-243:370–372, 1997.

[88] C. Verdon and D. C. Dunand. High-temperature reactivity in the ZrW_2O_8–Cu system. *Scripta Mater.*, 36(9):1075–1080, 1997.

[89] D. K. Balch and D. C. Dunand. Copper-zirconium tungstate composites exhibiting low and negative thermal expansion influenced by reinforcement phase transformations. *Metall. Mater. Trans. A*, 35(3):1159–1165, 2004.

[90] A. Grzechnik and W. A. Crichton. Structural transformations in cubic $ZrMo_2O_8$ at high pressures and high temperatures. *Solid State Sci.*, 4(9):1137–1141, 2002.

[91] A. P. Wilkinson, B. K. Greve, C. J. Ruschman, K. W. Chapman, and P. J. Chupas. Pressure induced amorphization of $ZrMo_2O_8$ and its relaxation on decompression as seen by in situ total x-ray scattering. *J. Appl. Phys.*, 112(2):023511, 2012.

[92] C. Lind, D. G. VanDerveer, A. P. Wilkinson, J. Chen, M. T. Vaughan, and D. J. Weidner. New High-Pressure Form of the Negative Thermal Expansion Materials Zirconium Molybdate and Hafnium Molybdate. *Chem. Mater.*, 13(2):487–490, 2001.

[93] L. C. Gallington, K. W. Chapman, C. R. Morelock, P. J. Chupas, and A. P. Wilkinson. Orientational order-dependent thermal expansion and compressibility of ZrW_2O_8 and $ZrMo_2O_8$. *Phys. Chem. Chem. Phys.*, 15(45):19665–19672, 2013.

[94] T. Varga, A. P. Wilkinson, A. C. Jupe, C. Lind, W. A. Bassett, and C.-S. Zha. Pressure-induced amorphization of cubic ZrW_2O_8 studied *in situ* and *ex situ* by synchrotron x-ray absorption spectroscopy and diffraction. *Phys. Rev. B*, 72(2):024117, 2005.

[95] L. C. Gallington, K. W. Chapman, C. R. Morelock, P. J. Chupas, and A. P. Wilkinson. Dramatic softening of the negative thermal expansion material HfW_2O_8 upon heating through its WO_4 orientational order-disorder phase transition. *J. Appl. Phys.*, 115(5):053512, 2014.

[96] T. Varga, A. P. Wilkinson, C. Lind, W. A. Bassett, and C.-S. Zha. In situ high-pressure synchrotron x-ray diffraction study of $Sc_2W_3O_{12}$ at up to 10 GPa. *Phys. Rev. B*, 71(21):214106, 2005.

[97] T. Varga, A. P. Wilkinson, J. D. Jorgensen, and S. Short. Neutron powder diffraction study of the orthorhombic to monoclinic transition in $Sc_2W_3O_{12}$ on compression. *Solid State Sci.*, 8(34):289–295, 2006.

[98] M. Maczka, W. Paraguassu, A. G. Souza Filho, P. T. C. Freire, J. Mendes Filho, F. E. A. Melo, and J. Hanuza. High-pressure Raman study of $Al_2(WO_4)_3$. *J. Solid State Chem.*, 177(6):2002–2006, 2004.

[99] T. Varga, A. P. Wilkinson, C. Lind, W. A. Bassett, and C.-S. Zha. High pressure synchrotron x-ray powder diffraction study of $Sc_2Mo_3O_{12}$ and $Al_2W_3O_{12}$. *J. Phys.: Condens. Matter*, 17(27):4271–4283, 2005.

[100] H. J. McSkimin and W. L. Bond. Elastic Moduli of Diamond. *Phys. Rev.*, 105(1):116–121, 1957.

[101] O. Anderson. *Equations of state of solids for geophysics and ceramic science*. Oxford University Press, Oxford, 1995.

[102] J. Garai and A. Laugier. The temperature dependence of the isothermal bulk modulus at 1 bar pressure. *J. Appl. Phys.*, 101(2):023514, 2007.

[103] J. B. Wachtman, W. E. Tefft, D. G. Lam, and C. S. Apstein. Exponential Temperature Dependence of Young's Modulus for Several Oxides. *Phys. Rev.*, 122(6):1754–1759, 1961.

[104] O. L. Anderson. Derivation of Wachtman's Equation for the Temperature Dependence of Elastic Moduli of Oxide Compounds. *Phys. Rev.*, 144(2):553–557, 1966.

[105] C. Pantea, A. Migliori, P. B. Littlewood, Y. Zhao, H. Ledbetter, J. C. Lashley, T. Kimura, J. Van Duijn, and G. R. Kowach. Pressure-induced elastic softening of monocrystalline zirconium tungstate at 300 K. *Phys. Rev. B*, 73(21):214118, 2006.

[106] K. W. Chapman and P. J. Chupas. Pressure Enhancement of Negative Thermal Expansion Behavior and Induced Framework Softening in Zinc Cyanide. *J. Am. Chem. Soc.*, 129(33):10090–10091, 2007.

[107] H. Fang and M. T. Dove. Pressure-induced softening as a common feature of framework structures with negative thermal expansion. *Phys. Rev. B*, 87:214109, 2013.

[108] H. Fang, M. T. Dove, L. H. N. Rimmer, and A. J. Misquitta. Simulation study of pressure and temperature dependence of the negative thermal expansion in $Zn(CN)_2$. *Phys. Rev. B*, 88:104306, 2013.

[109] H. Fang, A. E. Phillips, M. T. Dove, M. G. Tucker, and A. L. Goodwin. Temperature-dependent pressure-induced softening in $Zn(CN)_2$. *Phys. Rev. B*, 88:144103, 2013.

[110] H. Fang and M. T. Dove. A phenomenological expression to describe the temperature dependence of pressure-induced softening in negative thermal expansion materials. *J. Phys.: Condens. Matter*, 26:115402, 2014.

[111] J. S. O. Evans, T. A. Mary, and A. W. Sleight. Negative thermal expansion materials. *Physica B: Condens. Matter*, 241-243:311–316, 1998.

[112] J. Graham, A. D. Wadsley, J. H. Weymouth, and L. S. Williams. A New Ternary Oxide, ZrW_2O_8. *J. Am. Ceram. Soc.*, 42(11):570, 1959.

[113] C. Martinek and F. A. Hummel. Linear Thermal Expansion of Three Tungstates. *J. Am. Ceram. Soc.*, 51(4):227–228, 1968.

[114] C. Lind, A. P. Wilkinson, Z. Hu, S. Short, and J. D. Jorgensen. Synthesis and Properties of the Negative Thermal Expansion Material Cubic $ZrMo_2O_8$. *Chem. Mater.*, 10(9):2335–2337, 1998.

[115] Y. Yamamura, N. Nakajima, and T. Tsuji. Calorimetric and x-ray diffraction studies of α-to-β structural phase transitions in HfW_2O_8 and ZrW_2O_8. *Angew. Chem. Int. Ed.*, 64(18):184109, 2001.

[116] S. Allen and J. S. O. Evans. Negative thermal expansion and oxygen disorder in cubic $ZrMo_2O_8$. *Phys. Rev. B*, 68(13):134101, 2003.

[117] C. Lind. *Negative Thermal Expansion Materials Related to Cubic Zirconium Tungstate*. PhD thesis, 2001.

[118] C. De Meyer, F. Bouree, J. S. O. Evans, K. De Buysser, E. Bruneel, I. Van Driessche, and S. Hoste. Structure and phase transition of Sn-substituted $Zr_{(1-x)}Sn_xW_2O_8$. *J. Mater. Chem.*, 14(20):2988–2994, 2004.

[119] K. De Buysser, I. Van Driessche, B. Vande Putte, P. Vanhee, J. Schaubroeck, and S. Hoste. Study of Negative Thermal Expansion and Shift in Phase Transition Temperature in Ti^{4+}- and Sn^{4+}-Substituted ZrW_2O_8 Materials. *Inorg. Chem.*, 47(2):736–741, 2008.

[120] N. Nakajima, Y. Yamamura, and T. Tsuji. Synthesis and physical properties of negative thermal expansion materials $Zr_{1-x}M_xW_2O_{8-y}$ (M = Sc, In, Y) substituted for Zr(IV) sites by M(III) ions. *Solid State Commun.*, 128(5):193–196, 2003.

[121] T. Hashimoto, J. Kuwahara, T. Yoshida, M. Nashimoto, Y. Takahashi, K. Takahashi, and Y. Morito. Thermal conductivity of negative-thermal-expansion oxide, $Zr_{1-x}Y_xW_2O_8$ (x = 0.00, 0.01) – temperature dependence and effect of structural phase transition. *Solid State Commun.*, 131(3-4):217–221, 2004.

[122] T. Tsuji, Y. Yamamura, and N. Nakajima. Thermodynamic properties of negative thermal expansion materials ZrW_2O_8 substituted for Zr site. *Thermochim. Acta*, 416(1-2):93–98, 2004.

[123] Y. Yamamura, N. Nakajima, and T. Tsuji. Drastic lowering of the order-disorder phase transition temperatures in $Zr_{1-x}M_xW_2O_{8-y}$ (M = Sc, Y, In) solid solutions. *Phys. Rev. B*, 70(10):104107, 2004.

[124] H.-H. Li, J.-S. Han, H. Ma, L. Huang, and X.-H. Zhao. $Zr_{1-x}Ln_xW_2O_{8-x/2}$ (Ln = Eu, Er, Yb): Solid solutions of negative thermal expansion—synthesis, characterization and limited solid solubility. *J. Solid State Chem.*, 180(3):852–857, 2007.

[125] C. A. Perottoni and J. A. H. da Jornada. Pressure-Induced Amorphization and Negative Thermal Expansion in ZrW_2O_8. *Science*, 280(5365):886–889, 1998.

[126] J. D. Jorgensen, Z. Hu, S. Teslic, D. N. Argyriou, S. Short, J. S. O. Evans, and A. W. Sleight. Pressure-induced cubic-to-orthorhombic phase transition in ZrW_2O_8. *Phys. Rev. B*, 59(1):215–225, 1999.

[127] J. D. Jorgensen, Z. Hu, S. Short, A. W. Sleight, and J. S. O. Evans. Pressure-induced cubic-to-orthorhombic phase transformation in the negative thermal expansion material HfW_2O_8. *J. Appl. Phys.*, 89(6):3184–3188, 2001.

[128] T. Varga, A. P. Wilkinson, C. Lind, W. A. Bassett, and C.-S. Zha. Pressure-induced amorphization of cubic $ZrMo_2O_8$ studied in situ by X-ray absorption spectroscopy and diffraction. *Solid State Commun.*, 135(11-12):739–744, 2005.

[129] E. R. Losilla, A. Cabeza, S. Bruque, M. A. G. Aranda, J. Sanz, J. E. Iglesias, and J. A. Alonso. Syntheses, Structures, and Thermal Expansion of Germanium Pyrophosphates. *J. Solid State Chem.*, 156(1):213–219, 2001.

[130] R. K. B. Gover, N. D. Withers, S. Allen, R. L. Withers, and J. S. O. Evans. Structure and Phase Transitions of SnP_2O_7. *J. Solid State Chem.*, 166(1):42–48, 2002.

[131] G. W. Stinton, M. R. Hampson, and J. S. O. Evans. The 136-Atom Structure of ZrP_2O_7 and HfP_2O_7 from Powder Diffraction Data. *Inorg. Chem.*, 45(11):4352–4358, 2006.

[132] H. Birkedal, A. M. Krogh Andersen, A. Arakcheeva, G. Chapuis, P. Norby, and P. Pattison. The Room-Temperature Superstructure of ZrP_2O_7 Is Orthorhombic: There Are No Unusual 180° P–O–P Bond Angles. *Inorg. Chem.*, 45(11):4346–4351, 2006.

[133] K. M. White, P. L. Lee, P. J. Chupas, K. W. Chapman, E. A. Payzant, A. C. Jupe, W. A. Bassett, C.-S. Zha, and A. P. Wilkinson. Synthesis, Symmetry, and Physical Properties of Cerium Pyrophosphate. *Chem. Mater.*, 20(11):3728–3734, 2008.

[134] G. Wallez, P. E. Raison, N. Dacheux, N. Clavier, D. Bykov, L. Delevoye, K. Popa, D. Bregiroux, A. N. Fitch, and R. J. M. Konings. Triclinic-Cubic Phase Transition and Negative Expansion in the Actinide IV (Th, U, Np, Pu) Diphosphates. *Inorg. Chem.*, 51(7):4314–4322, 2012.

[135] S. Carlson and A. M. Krogh Andersen. High-pressure properties of TiP_2O_7, ZrP_2O_7 and ZrV_2O_7. *J. Appl. Cryst.*, 34(1):7–12, 2001.

[136] K. E. Lipinska-Kalita, M. B. Kruger, S. Carlson, and A. M. Krogh Andersen. High-pressure studies of titanium pyrophosphate by Raman scattering and infrared spectroscopy. *Physica B: Condens. Matter*, 337(1-4):221–229, 2003.

[137] E. A. Petruska, D. V. S. Muthu, S. Carlson, A. M. Krogh Andersen, L. Ouyang, and M. B. Kruger. High-pressure Raman and infrared spectroscopic studies of ZrP_2O_7. *Solid State Commun.*, 150(5-6):235–239, 2010.

[138] U. L. C. Hemamala, F. El-Ghussein, D. V. S. Muthu, A. M. Krogh Andersen, S. Carlson, L. Ouyang, and M. B. Kruger. High-pressure Raman and infrared study of ZrV_2O_7. *Solid State Commun.*, 141(12):680–684, 2007.

[139] U. L. C. Hemamala, F. El-Ghussein, A. M. Goedken, B. Chen, Ch. Leroux, and M. B. Kruger. High-pressure x-ray diffraction and Raman spectroscopy of HfV_2O_7. *Phys. Rev. B*, 70(21):214114, 2004.

[140] T. A. Mary and A. W. Sleight. Bulk thermal expansion for tungstate and molybdates of the type $A_2M_3O_{12}$. *J. Mater. Res.*, 14(3):912–915, 1999.

[141] S. C. Abrahams and J. L. Bernstein. Crystal Structure of the Transition-Metal Molybdates and Tungstates. II. Diamagnetic $Sc_2(WO_4)_3$. *J. Chem. Phys.*, 45(8):2745–2752, 1966.

[142] K. Nassau, H. J. Levinstein, and G. M. Loiacono. A comprehensive study of trivalent tungstates and molybdates of the type $L_2(MO_4)_3$. *J. Phys. Chem. Solids*, 26(12):1805–1816, 1965.

[143] A. W. Sleight and L. H. Brixner. A new ferroelastic transition in some $A_2(MO_4)_3$ molybdates and tungstates. *J. Solid State Chem.*, 7(2):172–174, 1973.

[144] Y. Zhou, S. Adams, R. P. Rao, D. D. Edwards, A. Neiman, and N. Pestereva. Charge Transport by Polyatomic Anion Diffusion in $Sc(WO_4)_3$. *Chem. Mater.*, 20(20):6335–6345, 2008.

[145] N. Imanaka, M. Hiraiwa, G. Adachi, H. Dabkowska, and A. Dabkowski. Thermal contraction behavior in $Al_2(WO_4)_3$ single crystal. *J. Crystal Growth*, 220:176–179, 2000.

[146] P. M. Forster and A. W. Sleight. Negative thermal expansion in $Y_2W_3O_{12}$. *Int. J. Inorg. Mater.*, 1(2):123–127, 1999.

[147] T. Suzuki and A. Omote. Zero Thermal Expansion in $(Al_{2x}(HfMg)_{1-x})(WO_4)_3$. *J. Am. Ceram. Soc.*, 89(2):691–693, 2006.

[148] J. S. O. Evans and T. A. Mary. Structural phase transitions and negative thermal expansion in $Sc_2(MoO_4)_3$. *Int. J. Inorg. Mater.*, 2(1):143–151, 2000.

[149] M. Cetinkol, A. P. Wilkinson, and C. Lind. In situ high-pressure synchrotron x-ray diffraction study of $Zr_2(WO_4)(PO_4)_2$ up to 16 GPa. *Phys. Rev. B*, 79(22):224118, 2009.

[150] T. G. Amos, A. Yokochi, and A. W. Sleight. Phase Transition and Negative Thermal Expansion in Tetragonal $NbOPO_4$. *J. Solid State Chem.*, 141(1):303–307, 1998.

[151] T. G. Amos and A. W. Sleight. Negative Thermal Expansion in Orthorhombic $NbOPO_4$. *J. Solid State Chem.*, 160(1):230–238, 2001.

[152] J. Wang, J. Deng, R. Yu, J. Chen, and X. Xing. Coprecipitation synthesis and negative thermal expansion of $NbVO_5$. *Dalton Trans.*, 40(13):3394–3397, 2011.

[153] X. Wang, Q. Huang, J. Deng, R. Yu, J. Chen, and X. Xing. Phase Transformation and Negative Thermal Expansion in $TaVO_5$. *Inorg. Chem.*, 50(6):2685–2690, 2011.

[154] W. Tiano, M. Dapiaggi, and G. Artioli. Thermal expansion in cuprite-type structures from 10 K to decomposition temperature: Cu_2O and Ag_2O. *J. Appl. Cryst.*, 36(6):1461–1463, 2003.

[155] K. W. Chapman and P. J. Chupas. Anomalous Thermal Expansion of Cuprites: A Combined High Resolution Pair Distribution Function and Geometric Analysis. *Chem. Mater.*, 21(2):425–431, 2009.

[156] P. Tschaufeser and S. C. Parker. Thermal Expansion Behavior of Zeolites and $AlPO_4$s. *J. Phys. Chem.*, 99(26):10609–10615, 1995.

[157] J. W. Couves, R. H. Jones, S. C. Parker, P. Tschaufeser, and C. R. A. Catlow. Experimental verification of a predicted negative thermal expansivity of crystalline zeolites. *J. Phys. Condens. Matter*, 5(27):L329–L332, 1993.

[158] M. P. Attfield and A. W. Sleight. Strong negative thermal expansion in siliceous faujasite. *Chem. Commun.*, (5):601–602, 1998.

[159] M. P. Attfield and A. W. Sleight. Exceptional Negative Thermal Expansion in $AlPO_4$-17. *Chem. Mater.*, 10(7):2013–2019, 1998.

[160] I. Bull, P. Lightfoot, L. A. Villaescusa, L. M. Bull, R. K. B. Gover, J. S. O. Evans, and R. E. Morris. An X-ray Diffraction and MAS NMR Study of the Thermal Expansion Properties of Calcined Siliceous Ferrierite. *J. Am. Chem. Soc.*, 125(14):4342–4349, 2003.

[161] P. Lightfoot, D. A. Woodcock, M. J. Maple, L. A. Villaescusa, and P. A. Wright. The widespread occurrence of negative thermal expansion in zeolites. *J. Mater. Chem.*, 11(1):212–216, 2001.

[162] D. J. Williams, D. E. Partin, F. J. Lincoln, J. Kouvetakis, and M. O'Keeffe. The Disordered Crystal Structures of $Zn(CN)_2$ and $Ga(CN)_3$. *J. Solid State Chem.*, 134(1):164–169, 1997.

[163] A. E. Phillips, A. L. Goodwin, G. J. Halder, P. D. Southon, and C. J. Kepert. Nanoporosity and Exceptional Negative Thermal Expansion in Single-Network Cadmium Cyanide. *Angew. Chem. Int. Ed.*, 47(8):1396–1399, 2008.

[164] K. W. Chapman, P. J. Chupas, and C. J. Kepert. Direct Observation of a Transverse Vibrational Mechanism for Negative Thermal Expansion in $Zn(CN)_2$: An Atomic Pair Distribution Function Analysis. *J. Amer. Chem. Soc.*, 127(44):15630–15636, 2005.

[165] J. W. Zwanziger. Phonon dispersion and Grüneisen parameters of zinc dicyanide and cadmium dicyanide from first principles: Origin of negative thermal expansion. *Phys. Rev. B*, 76(5):052102, 2007.

[166] R. Mittal, M. Zbiri, H. Schober, E. Marelli, S. J. Hibble, A. M. Chippindale, and S. L. Chaplot. Relationship between phonons and thermal expansion in $Zn(CN)_2$ and $Ni(CN)_2$ from inelastic neutron scattering and ab initio calculations. *Phys. Rev. B*, 83(2):024301, 2011.

[167] S. J. Hibble, A. M. Chippindale, A. H. Pohl, and A. C. Hannon. Surprises from a Simple Material-The Structure and Properties of Nickel Cyanide. *Angew. Chem. Int. Ed.*, 46(37):7116–7118, 2007.

[168] A. L. Goodwin, K. W. Chapman, and C. J. Kepert. Guest-Dependent Negative Thermal Expansion in Nanoporous Prussian Blue Analogues $M^{II}Pt^{IV}(CN)_6 \cdot x(H_2O)$ ($0 \leq x \leq 2$; M = Zn, Cd). *J. Am. Chem. Soc.*, 127(51):17980–17981, 2005.

[169] S. Adak, L. L. Daemen, M. Hartl, D. Williams, J. Summerhill, and H. Nakotte. Thermal expansion in 3d-metal Prussian Blue Analogs–A survey study. *J. Solid State Chem.*, 184(11):2854–2861, 2011.

[170] A. L. Goodwin, M. Calleja, M. J. Conterio, M. T. Dove, J. S. O. Evans, D. A. Keen, L. Peters, and M. G. Tucker. Colossal Positive and Negative Thermal Expansion in the Framework Material $Ag_3[Co(CN)_6]$. *Science*, 319(5864):794–797, 2008.

[171] A. L. Goodwin, D. A. Keen, M. G. Tucker, M. T. Dove, L. Peters, and J. S. O. Evans. Argentophilicity-Dependent Colossal Thermal Expansion in Extended Prussian Blue Analogues. *J. Am. Chem. Soc.*, 130(30):9660–9661, 2008.

[172] H. Li, M. Eddaoudi, M. O'Keefe, and O. M. Yaghi. Design and synthesis of an exceptionally stable and highly porous metal-organic framework. *Nature*, 402(6759):276–279, 1999.

[173] J. L. C. Rowsell, E. C. Spencer, J. Eckert, J. A. K. Howard, and O. M. Yaghi. Gas adsorption sites in a large-pore metal-organic framework. *Science*, 309(5739):1350–1354, 2005.

[174] D. Dubbeldam, K. S. Walton, D. E. Ellis, and R. Q. Snurr. Exceptional Negative Thermal Expansion in Isoreticular Metal-Organic Frameworks. *Angew. Chem. Int. Ed.*, 46(24):4496–4499, 2007.

[175] S. S. Han and W. A. Goddard. Metal-Organic Frameworks Provide Large Negative Thermal Expansion Behavior. *J. Phys. Chem. C*, 111(42):15185–15191, 2007.

[176] W. Zhou, H. Wu, T. Yildirim, J. R. Simpson, and A. R. Hight Walker. Origin of the exceptional negative thermal expansion in metal-organic framework-5 Zn_4O(1,4-benzenedicarboxylate)$_3$. *Phys. Rev. B*, 78(5):054114, 2008.

[177] S. S.-Y. Chui, S. M.-F. Lo, J. P. H. Charmant, A. G. Orpen, and I. D. Williams. A Chemically Functionalizable Nanoporous Material $[Cu_3(TMA)_2(H_2O)_3]_n$. *Science*, 283(5405):1148–1150, 1999.

[178] Y. Wu, A. Kobayashi, G. J. Halder, V. K. Peterson, K. W. Chapman, N. Lock, P. D. Southon, and C. J. Kepert. Negative Thermal Expansion in the Metal-Organic Framework Material Cu_3(1,3,5-benzenetricarboxylate)$_2$. *Angew. Chem. Int. Ed.*, 47(46):8929–8932, 2008.

[179] V. K. Peterson, G. J. Kearley, Y. Wu, A. J. Ramirez-Cuesta, E. Kemner, and C. J. Kepert. Local Vibrational Mechanism for Negative Thermal Expansion: A Combined Neutron Scattering and First-Principles Study. *Angew. Chem. Int. Ed.*, 49(3):585–588, 2010.

[180] Y. Wu, V. K. Peterson, E. Luks, T. A. Darwish, and C. J. Kepert. Interpenetration as a Mechanism for Negative Thermal Expansion in the MetalOrganic Framework $Cu_3(btb)_2$ (MOF-14). *Angew. Chem.*, 126, 2014.

[181] W. Hume-Rothery and H. M. Powell. On the Theory of Super-Lattice Structures in Alloys. *Z. Kristallogr.*, 91(1):23–47, 1935.

[182] J. S. O. Evans, P. A. Hanson, R. M. Ibberson, N. Duan, U. Kameswari, and A. W. Sleight. Low-Temperature Oxygen Migration and Negative Thermal Expansion in $ZrW_{2-x}Mo_xO_8$. *J. Am. Chem. Soc.*, 122(36):8694–8699, 2000.

[183] L. Huang, Q. Xiao, H. Ma, G. Li, F. Liao, C. Qi, and X. Zhao. Phase Behaviors of the $ZrMo_{2-x}W_xO_8$ (x = 0.2-2.0) System and the Preparation of an Mo-Rich Cubic Phase. *Eur. J. Inorg. Chem.*, 2005(22):4521–4526, 2005.

[184] M. Dapiaggi and A. N. Fitch. Negative (and very low) thermal expansion in ReO_3 from 5 to 300 K. *J. Appl. Cryst.*, 42(2):253–258, 2009.

[185] T. Chatterji, T. C. Hansen, M. Brunelli, and P. F. Henry. Negative thermal expansion of ReO_3 in the extended temperature range. *Appl. Phys. Lett.*, 94(24):241902–3, 2009.

[186] E. E. Rodriguez, A. Llobet, T. Proffen, B. C. Melot, R. Seshadri, P. B. Littlewood, and A. K. Cheetham. The role of static disorder in negative thermal expansion in ReO_3. *J. Appl. Phys.*, 105(11):114901–6, 2009.

[187] A. Ferretti, D. B. Rogers, and J. B. Goodenough. The relation of the electrical conductivity in single crystals of rhenium trioxide to the conductivities of Sr_2MgReO_6 and Na_xWO_3. *J. Phys. Chem. Solids*, 26(12):2007–2011, 1965.

[188] C. N. King, H. C. Kirsch, and T. H. Geballe. The low temperature heat capacity and electrical resistivity of ReO_3. *Solid State Commun.*, 9(12):907–910, 1971.

[189] N. Matsuno, M. Yoshimi, S. Ohtake, T. Akahane, and N. Tsuda. Thermal Expansion of ReO_3. *J. Phys. Soc. Jpn.*, 45(5):1542–1544, 1978.

[190] D. Taylor. Thermal expansion V. Miscellaneous binary oxides. *Br. Ceram. Soc. Trans. J.*, 84(1):9–14, 1985.

[191] F. S. Razavi, Z. Altounian, and W. R. Datars. A pressure induced anomaly in the Fermi surface of ReO_3. *Solid State Commun.*, 28(2):217–220, 1978.

[192] J. E. Schirber and B. Morosin. "Compressibility Collapse" Transition in ReO_3. *Phys. Rev. Lett.*, 42(22):1485–1487, 1979.

[193] B. Batlogg, R. G. Maines, M. Greenblatt, and S. DiGregorio. Novel p-V relationship in ReO_3 under pressure. *Phys. Rev. B*, 29(6):3762–3764, 1984.

[194] J. E. Schirber, B. Morosin, R. W. Alkire, A. C. Larson, and P. J. Vergamini. Structure of ReO_3 above the "compressibility collapse" transition. *Phys. Rev. B*, 29(7):4150–4152, 1984.

[195] J. D. Axe, Y. Fujii, B. Batlogg, M. Greenblatt, and S. DiGregorio. Neutron scattering study of the pressure-induced phase transformation in ReO_3. *Phys. Rev. B*, 31(2):663–667, 1985.

[196] J.-E. Jørgensen, J. D. Jorgensen, B. Batlogg, J. P. Remeika, and J. D. Axe. Order parameter and critical exponent for the pressure-induced phase transitions in ReO_3. *Phys. Rev. B*, 33(7):4793–4798, 1986.

[197] T. Chatterji and G. J. McIntyre. Pressure-induced structural phase transition in ReO_3. *Solid State Commun.*, 139(1):12–15, 2006.

[198] T. I. Dyuzheva, N. A. Bendeliani, and S. S. Kabalkina. New high-pressure phases of ReO_3. *J. Less-Comm. Met.*, 133(2):313–317, 1987.

[199] T. I. Dyuzheva, N. A. Bendeliani, A. N. Glushko, and S. S. Kabalkina. Phase Diagram of ReO_3 up to 10 GPa. *Phys. Scr.*, 39(3):341–342, 1989.

[200] J.-E. Jørgensen, J. S. Olsen, and L. Gerward. Phase transitions in ReO_3 studied by high-pressure X-ray diffraction. *J. Appl. Cryst.*, 33(2):279–284, 2000.

[201] E. Suzuki, Y. Kobayashi, S. Endo, and T. Kikegawa. Structural phase transition in ReO_3 under high pressure. *J. Phys.: Condens. Matter*, 14(44):10589–10593, 2002.

[202] J.-E. Jørgensen, W. G. Marshall, R. I. Smith, J. S. Olsen, and L. Gerward. High-pressure neutron powder diffraction study of the $Im\bar{3}$ phase of ReO_3. *J. Appl. Cryst.*, 37(6):857–861, 2004.

[203] T. I. Dyuzheva, N. A. Bendeliani, A. N. Glushko, and S. S. Kabalkina. Compressibility and phase transition of δ-UO_3 under high pressure. *J. Alloys Compd.*, 315(1-2):59–61, 2001.

[204] L. K. Frevel and H. W. Rinn. The crystal structure of NbO_2F and TaO_2F. *Acta Cryst.*, 9(8):626–627, 1956.

[205] A. P. Wilkinson, R. E. Josefsberg, L. C. Gallington, C. R. Morelock, and C. M. Monaco. History-dependent thermal expansion in NbO_2F. *J. Solid State Chem.*, 213:38–42, 204.

[206] S. Sawhill and E. Savrun. A near zero coefficient of thermal expansion ceramic: Tantalum oxyfluoride. *Ceram. Int.*, 38(3):1981–1989, 2012.

[207] B. L. Chamberland. A new oxyfluoride perovskite, $KTiO_2F$. *Mater. Res. Bull.*, 6(5):311–315, 1971.

[208] R. L. Needs and M. T. Weller. A New 2+/3+ Perovskite: The Synthesis and Structure of $BaScO_2F$. *J. Solid State Chem.*, 139(2):422–423, 1998.

[209] F. J. Berry, F. C. Coomer, C. Hancock, Ö. Helgason, E. A. Moore, P. R. Slater, A. J. Wright, and M. F. Thomas. Structure and magnetic properties of the cubic oxide fluoride $BaFeO_2F$. *J. Solid State Chem.*, 184(6):1361–1366, 2011.

[210] F. J. Berry, R. Heap, Ö. Helgason, E. A. Moore, S. Shim, P. R. Slater, and M. F. Thomas. Magnetic order in perovskite-related $SrFeO_2F$. *J. Phys.: Condens. Matter*, 20(21):215207, 2008.

[211] T. Katsumata, M. Nakashima, H. Umemoto, and Y. Inaguma. Synthesis of the novel perovskite-type oxyfluoride $PbScO_2F$ under high pressure and high temperature. *J. Solid State Chem.*, 181(10):2737–2740, 2008.

[212] Y. Inaguma, J.-M. Greneche, M.-P. Crosnier-Lopez, T. Katsumata, Y. Calage, and J.-L. Fourquet. Structure and Mössbauer Studies of F-O Ordering in Antiferromagnetic Perovskite $PbFeO_2F$. *Chem. Mater.*, 17(6):1386–1390, 2005.

[213] F. J. Brink, R. L. Withers, and L. Norén. An Electron Diffraction and Crystal Chemical Investigation of Oxygen/Fluorine Ordering in Niobium Oxyfluoride, NbO_2F. *J. Solid State Chem.*, 166(1):73–80, 2002.

[214] F. J. Brink, L. Norén, and R. L. Withers. Electron diffraction evidence for continuously variable, composition-dependent O/F ordering in the ReO_3 type, $Nb^{V}_{1-x}Nb^{IV}_{x}O_{2-x}F_{1+x}$, $0 \leq x \leq 0.48$, solid solution. *J. Solid State Chem.*, 177(6):2177–2182, 2004.

[215] R. L. Withers, F. J. Brink, L. Norén, T. R. Welberry, and Y. Liu. Local Strain, Structured Diffuse Scattering and Oxygen/Fluorine Ordering in Transition Metal Oxyfluorides. *Ferroelectrics*, 305(1):123–126, 2004.

[216] F. J. Brink, R. L. Withers, S. Cordier, and M. Poulain. An electron diffraction and bond valence sum investigation of oxygen/fluorine ordering in $Nb_nO_{2n-1}F_{n+2}$, $n = 3$. *J. Solid State Chem.*, 179:341–348, 2006.

[217] R. L. Withers, F. J. Brink, Y. Liu, and L. Norén. Cluster chemistry in the solid state: Structured diffuse scattering, oxide/fluoride ordering and polar behaviour in transition metal oxyfluorides. *Polyhedron*, 26(2):290–299, 2007.

[218] C. R. Morelock, B. K. Greve, M. Cetinkol, K. W. Chapman, P. J. Chupas, and A. P. Wilkinson. Role of Anion Site Disorder in the Near Zero Thermal Expansion of Tantalum Oxyfluoride. *Chem. Mater.*, 25(9):1900–1904, 2013.

[219] S. Carlson, A.-K. Larsson, and F. E. Rohrer. High-pressure transformations of NbO_2F. *Acta Cryst. B*, 56(2):189–196, 2000.

[220] S. Carlson. High-pressure studies of the cubic to rhombohedral transformation in NbO_2F. *J. Appl. Cryst.*, 33(4):1175–1176, 2000.

[221] M. Cetinkol, A. P. Wilkinson, C. Lind, W. A. Bassett, and C.-S. Zha. High-pressure powder diffraction study of TaO_2F. *J. Phys. Chem. Solids*, 68(4):611–616, 2007.

[222] K. Kamali, T. R. Ravindran, and T. N. Sairam. High pressure Raman spectroscopic study of phase transformation in TaO_2F. *Vib. Spec.*, 71:12–17, 2014.

[223] B. K. Greve. *Exploring the Thermal Expansion of Fluorides and Oxyfluorides with ReO_3-type Structures: From Negative to Positive Thermal Expansion.* PhD thesis, 2011.

[224] K. Vorres and J. Donohue. The structure of titanium oxydifluoride. *Acta. Cryst.*, 8(1):25–26, 1955.

[225] S. Shian and K. H. Sandhage. Hexagonal and cubic $TiOF_2$. *J. Appl. Cryst.*, 43(4):757–761, 2010.

[226] A. Mogus-Milankovic, J. Ravez, J. P. Chaminade, and P. Hagenmuller. Ferroelastic properties of TF_3 compounds (T = Ti, V, Cr, Fe, Ga). *Mater. Res. Bull.*, 20(1):9–17, 1985.

[227] P. Daniel, A. Bulou, M. Rousseau, J. Nouet, and M. Leblanc. Raman-scattering study of crystallized MF_3 compounds (M = Al, Cr, Ga, V, Fe, In): An approach to the short-range-order force constants. *Phys. Rev. B*, 42(16):10545–10552, 1990.

[228] B. J. Kennedy and T. Vogt. Powder X-ray diffraction study of the rhombohedral to cubic phase transition in TiF_3. *Mater. Res. Bull.*, 37(1):77–83, 2002.

[229] P. Daniel, A. Bulou, M. Leblanc, M. Rousseau, and J. Nouet. Structural and vibrational study of VF_3. *Mater. Res. Bull.*, 25(4):413–420, 1990.

[230] K. H. Jack and V. Gutmann. The Crystal Structure of Vanadium Trifluoride, VF_3. *Acta Cryst.*, 4(3):246–249, 1951.

[231] P. J. Chupas, X. Qiu, J. C. Hanson, P. L. Lee, C. P. Grey, and S. J. L. Billinge. In Situ X-ray Diffraction and Solid-State NMR Study of the Fluorination of γ-Al_2O_3 with HCF_2Cl. *J. Am. Chem. Soc.*, 123(8):1694–1702, 2001.

[232] P. Daniel, A. Bulou, M. Rousseau, J. Nouet, J. L. Fourquet, M. Leblanc, and R. Burriel. A study of the structural phase transitions in AlF_3: X-ray powder diffraction, differential scanning calorimetry (DSC) and Raman scattering investigations of the lattice dynamics and phonon spectrum. *J. Phys.: Condens. Matter*, 2(26):5663–5677, 1990.

[233] Y.-R. Chen, V. Perebeinos, and P. B. Allen. Density-functional study of the cubic-to-rhombohedral transition in α-AlF_3. *Phys. Rev. B*, 69(5):054109, 2004.

[234] S. Chaudhuri, P. J. Chupas, M. Wilson, P. Madden, and C. P. Grey. Study of the Nature and Mechanism of the Rhombohedral-to-Cubic Phase Transition in α-AlF_3 with Molecular Dynamics Simulations. *J. Phys. Chem. B*, 108(11):3437–3445, 2004.

[235] P. J. Chupas, S. Chaudhuri, J. C. Hanson, X. Qiu, P. L. Lee, S. D. Shastri, S. J. L. Billinge, and C. P. Grey. Probing Local and Long-Range Structure Simultaneously: An In Situ Study of the High-Temperature Phase Transition of α-AlF_3. *J. Am. Chem. Soc.*, 126(15):4756–4757, 2004.

[236] J. Ravez, A. Mogusmilankovic, J. P. Chaminade, and P. Hagenmuller. Ferroelastic properties of AlF_3. *Mater. Res. Bull.*, 19(10):1311–1316, 1984.

[237] C. R. Morelock, J. C. Hancock, and A. P. Wilkinson. Thermal expansion and phase transitions of α-AlF_3. *J. Solid State Chem.*, 219:143–147, 2014.

[238] C. R. Morelock, L. C. Gallington, and A. P. Wilkinson. Evolution of negative thermal expansion and phase transitions in $Sc_{1-x}Ti_xF_3$. *Chem. Mater.*, 26(5):1936–1940, 2014.

[239] H. Sowa and H. Ahsbahs. Pressure-Induced Octahedron Strain in VF_3-Type Compounds. *Acta Cryst. B*, 54(5):578–584, 1998.

[240] J.-E. Jorgensen and R. I. Smith. On the compression mechanism of FeF_3. *Acta Cryst. B*, 62(6):987–992, 2006.

[241] J.-E. Jorgensen, J. S. Olsen, and L. Gerward. Compression mechanism of GaF_3 and FeF_3: a high-pressure X-ray diffraction study. *High Pressure Res.*, 30(4):634–642, 2010.

[242] J.-E. Jorgensen, W. G. Marshall, and R. I. Smith. The compression mechanism of CrF_3. *Acta Cryst. B*, 60(6):669–673, 2004.

[243] C. W. Li, X. Tang, J. A. Muñoz, J. B. Keith, S. J. Tracy, D. L. Abernathy, and B. Fultz. Structural Relationship between Negative Thermal Expansion and Quartic Anharmonicity of Cubic ScF_3. *Phys. Rev. Lett.*, 107(19):195504, 2011.

[244] K. S. Aleksandrov, V. N. Voronov, A. N. Vtyurin, A. S. Krylov, M. S. Molokeev, M. S. Pavlovskii, S. V. Goryainov, A. Yu. Likhavcheva, and A. I. Ancharov. Pressure-Induced Phase Transition in the Cubic ScF_3 Crystal. *Phys. Solid State*, 51(4):810–816, 2009.

[245] K. S. Aleksandrov, V. N. Voronov, A. N. Vtyurin, S. V. Goryainov, N. G. Zamkova, V. I. Zinenko, and A. S. Krylov. Lattice dynamics and hydrostatic-pressure-induced phase transitions in ScF_3. *J. Exp. Theor. Phys.*, 94(5):977–984, 2002.

[246] K. S. Aleksandrov, V. N. Voronov, A. N. Vtyurin, S. V. Goryainov, N. G. Zamkova, V. I. Zinenko, and A. S. Krylov. Pressure-Induced Phase Transitions in ScF_3 Crystal–Raman Spectra and Lattice Dynamics. *Ferroelectrics*, 284(1):31–45, 2003.

[247] C. R. Morelock, B. K. Greve, L. C. Gallington, K. W. Chapman, and A. P. Wilkinson. Negative thermal expansion and compressibility of $Sc_{1-x}Y_xF_3$ ($x \leq 0.25$). *J. Appl. Phys.*, 114(21):213501, 2013.

[248] C. R. Morelock, L. C. Gallington, P. J. Chupas, K. W. Chapman, and A. P. Wilkinson. Solid solubility, phase transitions, thermal expansion, and compressibility in $Sc_{1-x}Al_xF_3$. *Manuscript submitted for publication*, 2014.

[249] S. D. Shastri, R. J. Dejus, D. R. Haeffner, and J. C. Lang. Performance of Advanced Photon Source insertion devices at high photon energies (50-300 keV). *Rev. Sci. Instrum.*, 67(9):3346, 1996.

[250] P. J. Chupas, K. W. Chapman, C. Kurtz, J. C. Hanson, P. L. Lee, and C. P. Grey. A versatile sample-environment cell for non-ambient X-ray scattering experiments. *J. Appl. Cryst.*, 41(4):822–824, 2008.

[251] Oxford Cryosystems, Oxford, UK. *Cryostream 700 Series*. `http://www.oxcryo.com/wp/wp-content/uploads/2010/10/cryostream700series.pdf`.

[252] J. Wang, B. H. Toby, P. L. Lee, L. Ribaud, S. M. Antao, C. Kurtz, M. Ramanathan, R. B. Von Dreele, and M. A. Beno. A dedicated powder diffraction beamline at the Advanced Photon Source: Commissioning and early operational results. *Rev. Sci. Instrum.*, 79(8):085105–7, 2008.

[253] P. L. Lee, D. Shu, M. Ramanathan, C. Preissner, J. Wang, M. A. Beno, R. B. Von Dreele, L. Ribaud, C. Kurtz, S. M. Antao, X. Jiao, and B. H. Toby. A twelve-analyzer detector system for high-resolution powder diffraction. *J. Synchrotron Rad.*, 15(5):427–432, 2008.

[254] A. P. Wilkinson, C. R. Morelock, B. K. Greve, A. C. Jupe, K. W. Chapman, P. J. Chupas, and C. Kurtz. Reducing the background from pressure vessels using a BRIM. *J. Appl. Cryst.*, 44(5):1047–1053, 2011.

[255] A. P. Hammersley, S. O. Svensson, M. Hanfland, A. N. Fitch, and D. Hausermann. Two-dimensional detector software: From real detector to idealised image or two-theta scan. *High Pressure Res.*, 14(4-6):235–248, 1996.

[256] S. J. L. Billinge and M. G. Kanatzidis. Beyond crystallography: the study of disorder, nanocrystallinity and crystallographically challenged materials with pair distribution functions. *Chem. Commun.*, (7):749–760, 2004.

[257] P. J. Chupas, X. Qiu, J. C. Hanson, P. L. Lee, C. P. Grey, and S. J. L. Billinge. Rapid-acquisition pair distribution function (RA-PDF) analysis. *J. Appl. Cryst.*, 36(6):1342–1347, 2003.

[258] P. J. Chupas, K. W. Chapman, and P. L. Lee. Applications of an amorphous silicon-based area detector for high-resolution, high-sensitivity and fast time-resolved pair distribution function measurements. *J. Appl. Cryst.*, 40(3):463–470, 2007.

[259] K. W. Chapman, P. J. Chupas, G. J. Halder, J. A. Hrljac, C. Kurtz, B. K. Greve, C. J. Ruschman, and A. P. Wilkinson. Optimizing high-pressure pair distribution function measurements in diamond anvil cells. *J. Appl. Cryst.*, 43(2):297–307, 2010.

[260] J. H. Lee, C. C. Aydiner, J. Almer, J. Bernier, K. W. Chapman, P. J. Chupas, D. Haeffner, K. Kump, P. L. Lee, U. Lienert, A. Miceli, and G. Vera. Synchrotron applications of an amorphous silicon flat-panel detector. *J. Synchrotron Rad.*, 15(5):477–488, 2008.

[261] J. C. Lashley, M. F. Hundley, A. Migliori, J. L. Sarrao, P. G. Pagliuso, T. W. Darling, M. Jaime, J. C. Cooley, W. L. Hults, L. Morales, D. J. Thoma, J. L. Smith, J. Boerio-Goates, B. F. Woodfield, G. R. Stewart, R. A. Fisher, and N. E. Phillips. Critical examination of heat capacity measurements made on a Quantum Design physical property measurement system. *Cryogenics*, 43(6):369–378, 2003.

[262] C. A. Kennedy, M. Stancescu, R. A. Marriott, and M. A. White. Recommendations for accurate heat capacity measurements using a Quantum Design physical property measurement system. *Cryogenics*, 47(2):107–112, 2007.

[263] B. Toby. CMPR–a powder diffraction toolkit. *J. Appl. Cryst.*, 38(6):1040–1041, 2005.

[264] S. W. Freiman and N. M. Trahey. National Institute of Standards and Technology Certificate: Standard Reference Material 660a. Technical report, National Institute of Standards and Technology, 2000.

[265] H. M. Rietveld. A Profile Refinement Method for Nuclear and Magnetic Structures. *J. Appl. Cryst.*, 2(2):65–71, 1969.

[266] P. Thompson, D. E. Cox, and J. B. Hastings. Rietveld refinement of Debye-Scherrer synchrotron X-ray data from Al_2O_3. *J. Appl. Cryst.*, 20(2):79–83, 1987.

[267] G. Caglioti, A. Paoletti, and F. P. Ricci. Choice of collimators for a crystal spectrometer for neutron diffraction. *Nucl. Instrum.*, 3(4):223–228, 1958.

[268] L. B. McCusker, R. B. Von Dreele, D. E. Cox, D. Louër, and P. Scardi. Rietveld refinement guidelines. *J. Appl. Cryst.*, 32(1):36–50, 1999.

[269] A. C. Larson and R. B. Von Dreele. General Structure Analysis System (GSAS). Technical report, Los Alamos National Laboratory, 2000.

[270] B. Toby. EXPGUI, a graphical user interface for GSAS. *J. Appl. Cryst.*, 34(2):210–213, 2001.

[271] X. Qiu, J. W. Thompson, and S. J. L. Billinge. PDFgetX2: a GUI-driven program to obtain the pair distribution function from X-ray powder diffraction data. *J. Appl. Cryst.*, 37(4):678, 2004.

[272] C. L. Farrow, P. Juhas, J. W. Liu, D. Bryndin, E. S. Božin, J. Bloch, T. Proffen, and S. J. L. Billinge. PDFfit2 and PDFgui: computer programs for studying nanostructure in crystals. *J. Phys.: Condens. Matter*, 19(33):335219, 2007.

[273] M. Wojdyr. Fityk: a general-purpose peak fitting program. *J. Appl. Cryst.*, 43(5):1126–1128, 2010.

[274] T. C. Hansen, P. F. Henry, H. E. Fischer, J. Torregrossa, and P. Convert. The D20 instrument at the ILL: a versatile high-intensity two-axis neutron diffractometer. *Meas. Sci. Technol.*, 19(3):034001, 2008.

[275] K. Yaoita, Y. Katayama, K. Tsuji, T. Kikegawa, and O. Shimomura. Angle-dispersive diffraction measurement system for high-pressure experiments using a multichannel collimator. *Rev. Sci. Instrum.*, 68(5):2106–2110, 1997.

[276] M. Mezouar, P. Faure, W. Crichton, N. Rambert, B. Sitaud, S. Bauchau, and G. Blattmann. Multichannel collimator for structural investigation of liquids and amorphous materials at high pressures and temperatures. *Rev. Sci. Instrum.*, 73(10):3570–3574, 2002.

[277] A. Katrusiak. High-pressure crystallography. *Acta Cryst. A*, 64(1):135–148, 2007.

[278] F. Birch. Equation of state and thermodynamic parameters of NaCl to 300 kbar in the high-temperature domain. *J. Geophys. Res.: Solid Earth*, 91(B5):4949–4954, 1986.

[279] C. Michel, J. M. Moreau, and W. J. James. Structural relationships in compounds with $R\bar{3}c$ symmetry. *Acta Cryst. B*, 27(2):501–503, 1971.

[280] M. Vlasse, J.-C. Massies, and B. L. Chamberland. Etude structurale de l'oxyfluorure d'indium. *Acta. Cryst. B*, 29(3):627–631, 1973.

[281] P. W. Stephens. Phenomenological model of anisotropic peak broadening in powder diffraction. *J. Appl. Cryst.*, 32(2):281–289, 1999.

[282] Y. Zhao, D. J. Weidner, J. B. Parise, and D. E. Cox. Thermal expansion and structural distortion of perovskite – data for $NaMgF_3$ perovskite. Part I. *Phys. Earth Planet. In.*, 76(1-2):1–16, 1993.

[283] J. C. Wheatley, D. F. Griffing, and T. L. Estle. Thermal Contact and Insulation below 1 K. *Rev. Sci. Instrum.*, 27(12):1070–1077, 1956.

[284] N. E. Phillips. Heat Capacity of Aluminum between 0.1 K and 4.0 K. *Phys. Rev.*, 114(3):676–685, 1959.

[285] T. Ashworth and M. Rechowicz. Properties of materials–I. application of adhesives. *Cryogenics*, 8(6):361–363, 1968.

[286] J. H. McTaggart and G. A. Slack. Thermal conductivity of General Electric No. 7031 varnish. *Cryogenics*, 9(5):384–385, 1969.

[287] J. L. Cude and L. Finegold. Specific heat of GE 7031 varnish (4-18 K). *Cryogenics*, 11(5):394–395, 1971.

[288] J. T. Heessels. Specific heat of General Electric 7031 varnish from 2 to 80 K. *Cryogenics*, 11(6):483–484, 1971.

[289] R. B. Stephens. The thermal properties of sample addenda used in T<1 K specific heat measurements: 1 – specific heat and thermal conductivity of General Electric 7031 varnish. *Cryogenics*, 15(7):420–422, 1975.

[290] K. D. Jayasuriya, A. M. Stewart, and S. J. Campbell. The specific heat capacity of GE varnish (200-400K). *J. Phys. E: Sci. Instrum.*, 15(9):885, 1982.

[291] D. E. Tsatis. Thermal diffusivity of GE-7031 varnish. *J. Appl. Phys.*, 62(1):302, 1987.

[292] F. Ye, Y. Ren, Q. Huang, J. A. Fernandez-Baca, P. Dai, J. W. Lynn, and T. Kimura. Spontaneous spin-lattice coupling in the geometrically frustrated triangular lattice antiferromagnet $CuFeO_2$. *Phys. Rev. B*, 73(22):220404, 2006.

[293] M. V. Speight and R. C. Lobb. Elastic stress at a particle-matrix interface. *Metallurg. Trans.*, 3(3):737, 1972.

[294] I. I. Perepechko. *Low-temperature properties of polymers.* Moscow, Mir Publishers, 1980.

[295] M. Poulain, M. Poulain, and M. Matecki. Verres au fluorure de scandium. *Mater. Res. Bull.*, 17(5):661–669, 1982.

[296] M. Poulain and M. Poulain. Trivalent Fluoride Glasses. *Mater. Sci. Forum*, 32-33:137–141, 1988.

[297] M. Poulain and M. Poulain. Magnesium in fluoride glasses. *J. Non-Cryst. Solids*, 140:87–91, 1992.

[298] P. P. Fedorov, V. I. Kalinin, and B. P. Sobolev. *Russ. J. Inorg. Chem.*, 27(7):1065, 1982.

[299] P. P. Fedorov, G. A. Lovetskaya, and B. P. Sobolev. Phase Diagram of the ScF_3-LuF_3 System. *Russ. J. Inorg. Chem.*, 40(9):1504, 1995.

[300] R. D. Shannon. Revised effective ionic radii and systematic studies of interatomic distances in halides and chalcogenides. *Acta Cryst. A*, 32(5):751–767, 1976.

[301] V. Perebeinos and T. Vogt. Jahn-Teller transition in TiF_3 investigated using density-functional theory. *Phys. Rev. B*, 69(11):115102–7, 2004.

[302] B. A. Hunter, B. J. Kennedy, and T. Vogt. Magnetostriction in a simple trivalent manganese perovskite. *Phys. Rev. B*, 69(2):020410(R), 2004.

[303] S. A. Hayward and E. K. H. Salje. Low-temperature phase diagrams: non-linearities due to quantum mechanical saturation of order parameters. *J. Phys.: Condens. Matter*, 10(6):1421–1430, 1998.

[304] C. P. Romao, C. R. Morelock, M. B. Johnson, A. P. Wilkinson, and M. A. White. The Role of Dispersion in the Heat Capacities of Thermomiotic ScF_3 and ScF_3–YF_3 Solid Solutions. *Manuscript submitted for publication*, 2014.

[305] P. Egger, N. Peters, and J. Hulliger. The Copper Ampoule: A New Reactor for the Solid-State Synthesis of Complex Lanthanide Fluorides. *J. Solid State Chem.*, 142(1):152–155, 1999.

[306] C. J. Howard and H. T. Stokes. Group-Theoretical Analysis of Octahedral Tilting in Perovskites. *Acta Cryst. B*, 54(6):782–789, 1998.

[307] A. M. Glazer. The classification of tilted octahedra in perovskites. *Acta Cryst. B*, 28(11):3384–3392, 1972.

[308] P. B. Allen, Y. R. Chen, S. Chaudhuri, and C. P. Grey. Octahedral tilt instability of ReO_3-type crystals. *Phys. Rev. B*, 73(17):172102, 2006.

[309] M. Cetinkol and A. P. Wilkinson. Pressure dependence of negative thermal expansion in $Zr_2(WO_4)(PO_4)_2$. *Solid State Commun.*, 149(11-12):421, 2009.

[310] B. Fultz. Vibrational thermodynamics of materials. *Prog. Mater. Sci.*, 55(4):247–352, 2010.

[311] G. A. Samara, T. Sakudo, and K. Yoshimitsu. Important Generalization Concerning the Role of Competing Forces in Displacive Phase Transitions. *Phys. Rev. Lett.*, 35(26):1767–1769, 1975.

[312] P. Bouvier and J. Kreisel. Pressure-induced phase transition in $LaAlO_3$. *J. Phys.: Condens. Matter*, 14(15):3981–3991, 2002.

[313] R. J. Angel, J. Zhao, and N. L. Ross. General Rules for Predicting Phase Transitions in Perovskites due to Octahedral Tilting. *Phys. Rev. Lett.*, 95(2):025503, 2005.

[314] R. Ernstorfer, M. Harb, C. T. Hebeisen, G. Sciaini, T. Dartigalongue, and R. J. D. Miller. The Formation of Warm Dense Matter: Experimental Evidence for Electronic Bond Hardening in Gold. *Science*, 323(5917):1033–1037, 2009.

[315] H. Fang, M. T. Dove, and A. E. Phillips. Common origin of negative thermal expansion and other exotic properties in ceramic and hybrid materials. *Phys. Rev. B*, 89:214103, 2014.

[316] N. E. Brese and M. O'Keeffe. Bond-valence parameters for solids. *Acta Cryst. B*, 47(2):192–197, 1991.

[317] J. C. Bertolini. Hydrofluoric acid: A review of toxicity. *J. Emerg. Med.*, 10(2):163–168, 1992.

[318] D. Peters and R. Miethchen. Symptoms and treatment of hydrogen fluoride injuries. *J. Fluorine Chem.*, 79(2):161–165, 1996.

[319] E. B. Segal. First aid for a unique acid: HF. *Chem. Health Saf.*, 5:25–28, 1998.

[320] E. B. Segal. First aid for a unique acid, HF: A sequel. *Chem. Health Saf.*, 7(1):18–23, 2000.

[321] S. G. Ebbinghaus, H.-P. Abicht, R. Dronskowski, T. Mller, A. Reller, and A. Weidenkaff. Perovskite-related oxynitrides – Recent developments in synthesis, characterisation and investigations of physical properties. *Prog. Solid State Chem.*, 37(23):173–205, 2009.

[322] K. Page, M. W. Stoltzfus, Y.-I. Kim, T. Proffen, P. M. Woodward, A. K. Cheetham, and R. Seshadri. Local Atomic Ordering in $BaTaO_2N$ Studied by Neutron Pair Distribution Function Analysis and Density Functional Theory. *Chem. Mater.*, 19(16):4037–4042, 2007.

[323] M. Yang, J. Oró-Solé, J. A. Rodgers, A. B. Jorge, A. Fuertes, and J. P. Attfield. Anion order in perovskite oxynitrides. *Nat. Chem.*, 3(1):47–52, 2011.

VITA

Cody Reeves Morelock was born on September 25, 1986, in Kingsport, Tennessee, to Jeffrey and Lisa (Sparks) Morelock, and graduated from Dobyns-Bennett High School in Kingsport in 2005. He received his Bachelor of Science degree *magna cum laude* in chemistry in 2009 from Furman University, Greenville, South Carolina, USA, where he worked in the laboratory of Prof. Laura L. Wright. Cody's graduate work was conducted at the Georgia Institute of Technology, Atlanta, Georgia, USA, under the supervision of Prof. Angus P. Wilkinson. Upon successful defense of this thesis in 2014, Cody received his Doctor of Philosophy degree in chemistry.